

**CO₂ capture through sorption onto activated carbons derived
from biomass**



UNIVERSITY OF LEEDS

Antonio Salituro

Submitted in accordance with the requirements for the degree of
Doctor of Philosophy

The University of Leeds
School of Process and Chemical Engineering

January 2016

The candidate confirms that the work submitted is his own and that appropriate credit has been given where reference has been made to the work of others.

This copy has been supplied on the understanding that it is copyright material and that no quotation from the thesis may be published without proper acknowledgement

© 2016 The University of Leeds and Antonio Salituro

Acknowledgements

First, a special thanks to Aidan Westwood, Andrew Ross, and Rik Brydson, who gave me valuable guidance throughout my PhD course.

I would also like to thank Robert Simpson, Surjit Singh, Adrian Cunliffe, Stuart Micklethwaite, Simon Lloyd, Tim Comyn, Mohammed Javed, and Diane Cochrane for giving technical assistance.

I acknowledge the National EPSRC XPS Users Service for the performance of X-ray photoelectron spectroscopy.

Thanks to the University of Leeds for financial support in carrying out this project.

Finally, many thanks to all people who supported me during this challenging experience, in particular to my family, my girlfriend Sarah and my friends.

Abstract

In this study, activated carbons (ACs) were synthesized and tested as CO₂ sorbents. In-house ACs were prepared starting both from a traditional biomass (i.e. oak wood) and from an unconventional macroalgal seaweed (i.e. *Laminaria hyperborea*). In addition to this, a biomass-derived commercial AC was studied as a sorbent on which polyethylenimine (PEI) was impregnated.

Biochars were produced both by pyrolysis at 800 °C and by hydrothermal carbonization (HTC) at 250 °C. Pyrolysis chars generally had higher fixed carbon and lower volatile content compared to hydrochars. Moreover, seaweed-derived chars exhibited significantly larger ash content than that measured for oak wood-based chars. Pyrolyzed and HTC-treated biomass were then activated either by physical (CO₂) or chemical (KOH) treatment. Limited texture development of the biochars was observed after CO₂ activation, yet this treatment proved to be more suitable for the creation of narrower micropores. By contrast, KOH activation, followed by HCl washing, led to a more dramatic texture enhancement (but to lower narrow micropore volumes) and higher purity of the ACs due to a significant demineralization of the chars. The morphology of all materials was examined by Scanning Electron Microscopy (SEM) which revealed the creation of larger pores after KOH activation, whereas chars and CO₂-ACs generally showed an undeveloped porous matrix along with particles anchored onto the carbon structure. Furthermore, Energy-Dispersive X-ray spectroscopy (EDX) analyses corresponding to the SEM micrographs proved that these particles were inorganic. In particular, Ca compounds predominated in oak wood-based samples. For macroalgae-derived materials, a significant proportion of alkali (i.e. Na, K), alkaline-earth (i.e. Ca, Mg) metal ions and Cl was detected, along with high levels of Cl. Conversely, reduced or negligible levels of inorganic fractions were detected for all KOH-ACs, which confirmed that demineralization occurred upon HCl washing. The identity of inorganic species was revealed by X-Ray Diffraction (XRD) patterns. In particular, calcium oxalate and Ca(OH)₂ were identified in oak wood chars, whereas CO₂-activated derivatives had CaCO₃ as their main crystalline phase. For macroalgae-based materials, KCl and NaCl were found to be the dominant crystalline phases. In addition, MgO was also identified in pyrolyzed seaweed and in its CO₂-activated counterpart. By contrast, a partial or total lack of crystalline phases was found for all KOH-ACs, thus offering further evidence of the loss of inorganic species after HCl rinsing. The intrinsic alkalinity of biomass-derived chars and CO₂-ACs was corroborated by the great amount of basic surface groups, whose number was lower for KOH-ACs.

CO₂ sorptions by chars and ACs were initially measured at T=35 °C, P_{CO2}=1 bar, and P_{tot}=1 bar by using Thermogravimetric Analysis (TGA). Sorbents showing promising behaviour were then tested for capture of CO₂ under simulated post-combustion conditions (T=53 °C, P_{CO2}=0.15 bar, and P_{tot}=1 bar). Unmodified ACs showed relatively high sorption capacity (up to 70

mg CO₂·g⁻¹) at higher partial pressure and lower temperature. Nonetheless, the ACs' sorption capability dramatically decreased at lower partial pressure and higher temperature. However, the biomass feedstocks included in this work proved to be advantageous precursors for sustainable synthesis of CO₂-selective sorbents under post-combustion conditions. In particular, Ca(OH)₂ and MgO intrinsically incorporated within the raw materials enabled production of highly basic "CO₂-philic" sorbents without applying any chemical modifications. The best virgin ACs also exhibited fast adsorption kinetics, excellent regeneration capacity and good durability over ten Rapid Temperature Swing Adsorption (RTSA) cycles. On the other hand, the CO₂ uptake of optimally-PEI modified commercial AC was up to 4 times higher than that achieved by the best performing unmodified AC. PEI impregnation was optimized to maximize post-combustion uptakes. In particular, the influence of various parameters (i.e. PEI loading, stirring time of the PEI/solvent/AC mixture, solvent type and sorption temperature) on the post-combustion capture capacity of the PEI-modified ACs was assessed. Interestingly, longer agitation engendered efficient dispersion of the polymer through the porous network. Additionally, a more environmentally friendly (i.e. aqueous) impregnation enabled uptakes nearly as large as those attained when the impregnation solvent was methanol, despite using lower amounts of polymer and shorter impregnation runs. In addition, when measuring uptakes under simulated post-combustion conditions but at 77 °C, optimization of aqueous PEI impregnation led to a sorption capacity larger than those achieved by the best performing PEI-loaded ACs impregnated using methanol as solvent. The use of an oak wood-derived carbon support or monoethanolamine (MEA) as impregnating agent did not lead to any significant improvement of the CO₂ sorption capacity. On the other hand, tetraethylenepentamine (TEPA)-impregnated AC slightly outperformed the optimally-PEI loaded sorbent, but the use of PEI was preferred because of its thermal stability. The addition of glycerol to the PEI/solvent/AC blend resulted in lower CO₂ uptakes but moderately faster adsorption/desorption kinetics along with comparable "amine efficiency". In addition, PEI-loaded AC showed larger CO₂ uptakes and faster kinetics than those attained, for comparison purposes, by Zeolite-13X (Z13X). Furthermore, amine-containing ACs were found to be durable and easy to regenerate by RTSA at 120 °C. This CO₂ desorption required ca. one third of the energy needed to regenerate a 30% MEA solution (i.e. the state of the art capture technique), thus potentially implying a lower energy penalty for the PEI-based technology in post-combustion power plant.

Overall, at higher partial pressure of carbon dioxide, textural properties were the dominant parameter governing CO₂ capture, especially at lower temperatures. This CO₂ physisorption appeared to be governed by a combination of narrow microporosity and surface area. In contrast, at increased temperature and lower partial pressure, basic (alkali metal or amine-containing) functionalities were the key factor for promoting selective chemisorption of CO₂.

Table of contents

Acknowledgements	i
Abstract	ii
Table of contents	iv
List of Tables	xi
List of Figures	xiv
1 Introduction and overall context	1
1.1 Thesis framework	1
1.2 Chapter outline	1
1.3 Problem overview	2
1.3.1 Greenhouse effect and global warming	2
1.3.2 Policies and Regulations	4
1.4 The CCS chain	5
1.4.1 CO ₂ Capture	5
1.4.1.1 Pre-combustion	5
1.4.1.2 Post-combustion	6
1.4.1.3 Oxy-fuel combustion	7
1.4.1.4 Chemical Looping Combustion	8
1.4.2 Post-capture steps.....	9
1.4.2.1 CO ₂ transport	9
1.4.2.2 CO ₂ storage and utilization	10
1.5 Post-combustion CO ₂ capture onto solid sorbents	11
1.5.1 Physisorbents	12
1.5.1.1 Zeolites	12
1.5.1.2 Metal organic frameworks	13
1.5.1.3 Virgin ACs	14
1.5.2 Chemisorbents	16
1.5.2.1 N-doped sorbents	16
1.5.2.1.1 In situ-doping	16
1.5.2.1.2 Post-doping	17
1.5.2.2 Alkali-based sorbents.....	19
1.5.2.2.1 Regenerable alkali-metal carbonates	19
1.5.2.2.2 Metal oxide carbonates.....	20
2 Scientific background	21
2.1 Outline.....	21

2.2	Precursors for activated carbons production	21
2.3	Carbonization of biomass	23
2.3.1	Dry pyrolysis	23
2.3.2	Hydrothermal carbonization (HTC)	24
2.4	Activation of biochars	26
2.4.1	Physical treatment	26
2.4.1.1	Mechanism of physical activation.....	26
2.4.1.2	Effect of activating agent.....	28
2.4.1.3	Effect of CO ₂ activation temperature.....	29
2.4.1.4	Effect of CO ₂ activation dwell time	30
2.4.2	Chemical treatment.....	31
2.4.2.1	Mechanism of chemical activation with KOH	32
2.4.2.2	Effect of KOH activation temperature.....	33
2.4.2.3	Effect of KOH:solid ratio.....	34
2.5	Preparation of activated carbon from oak wood	35
2.5.1	Carbonization of oak wood	35
2.5.1.1	Pyrolysis of oak wood	35
2.5.1.2	HTC of oak wood	36
2.5.2	Activation of oak wood-derived chars	37
2.5.2.1	CO ₂ activation of oak wood-derived chars	37
2.5.2.2	KOH activation of oak wood-derived chars	38
2.6	Synthesis of activated carbons from <i>Laminaria hyperborea</i>	39
2.6.1	Carbonization of macroalgae	39
2.6.1.1	Pyrolysis of macroalgae	39
2.6.1.2	HTC of macroalgae	40
2.6.2	Activation of macroalgae-based chars.....	41
2.7	Use of biomass-derived ACs as CO ₂ sorbents	42
2.8	CO ₂ capture through amine-modified solid sorbents	44
2.8.1	Mechanism of CO ₂ chemisorption onto amines under dry or wet conditions.....	44
2.8.2	The CO ₂ sorption performance of PEI-modified sorbents.....	45
2.8.2.1	The influence of PEI loading and sorption temperature.....	46
2.8.2.2	The influence of solvent amount and type.....	48
2.8.2.3	The influence of other preparation conditions	49

2.8.2.4	The influence of water on the CO ₂ capture performances of PEI-modified sorbents.....	50
2.8.2.4.1	The effect of moisture in the simulated post-combustion flue gas.....	50
2.8.2.4.2	The effect of the addition of OH-containing species to PEI-modified sorbents.....	50
2.8.2.5	Regeneration strategy.....	51
2.9	Main objectives.....	52
3	Experimental.....	53
3.1	Outline.....	53
3.2	Materials.....	53
3.2.1	Biomass feedstock.....	53
3.2.2	Commercial carbons.....	54
3.3	Synthesis of biochars.....	54
3.3.1	Dry pyrolysis.....	54
3.3.1.1	Horizontal ceramic tube furnace.....	54
3.3.1.2	Stainless steel vertical furnace.....	56
3.3.2	Hydrothermal carbonization.....	58
3.3.3	Repeatability of carbonization process.....	59
3.4	Activation step.....	59
3.4.1	CO ₂ activation.....	59
3.4.2	KOH activation.....	60
3.5	Amine wet impregnation of activated carbons: procedure optimization.....	61
3.5.1	Primary optimization.....	61
3.5.2	Influence of additional factors.....	62
3.5.2.1	Use of a different carbon substrate.....	63
3.5.2.2	Use of alternative N-containing compounds.....	63
3.5.2.3	Addition of glycerol.....	65
3.6	Gas adsorption (porosity and surface area measurements).....	65
3.6.1	Sample degassing.....	65
3.6.2	Gas isotherm construction.....	66
3.6.3	N ₂ adsorption/desorption data reduction.....	68
3.6.3.1	Brunauer-Emmett-Teller (BET) method - Surface area of non-microporous materials.....	68
3.6.3.1.1	Multipoint approach.....	69
3.6.3.1.2	Single-point approach.....	70

3.6.3.2	BET method - Surface area of microporous materials	71
3.6.3.3	Total pore volume - Gurvitsch's rule	72
3.6.3.4	Mesopore volume - Barrett-Joyner-Halenda (BJH) model and choice of the isotherm leg	72
3.6.3.5	Micropore volume - Dubinin-Radushkevich (DR) model	73
3.6.3.6	Pore size distribution (PSD) - Non-local density functional theory (NLDFT) model	74
3.6.4	CO ₂ adsorption data reduction	75
3.7	Chemical, morphological and structural analyses	76
3.7.1	Elemental analysis (CHNS)	76
3.7.2	Proximate analysis	77
3.7.3	X-Ray Diffraction (XRD)	78
3.7.4	Scanning Electron Microscope (SEM) and Energy-Dispersive X-ray (EDX) spectroscopy	79
3.7.5	Boehm titrations	80
3.7.6	Fourier Transform Infrared (FTIR) spectroscopy	81
3.7.7	X-ray Photoelectron Spectroscopy (XPS)	81
3.8	CO ₂ capture performance	82
3.8.1	Calculation of CO ₂ sorption capacity - TGA programmes	82
3.8.2	Calculation of heat of adsorption/desorption - DSC data	83
4	Eco-friendly synthesis of selective CO₂ sorbents for post-combustion capture: the key role of basicity	84
4.1	Outline	84
4.2	Carbonization of oak wood	85
4.2.1	Repeatability of dry pyrolysis and HTC	85
4.3	Activation of oak wood-based chars	87
4.3.1	CO ₂ activation of oak wood-based chars - Optimal conditions	87
4.3.1.1	The effect of the temperature	88
4.3.1.1.1	Hydrothermally carbonized wood (OW250)	88
4.3.1.1.2	Pyrolyzed wood (OW800)	90
4.3.1.2	The effect of the dwell time	92
4.3.1.2.1	Hydrothermally carbonized wood (OW250)	92
4.3.1.2.2	Pyrolyzed wood (OW800)	94
4.3.2	KOH activation of oak wood-based chars	96
4.3.2.1	The effect of the washing procedure	97
4.3.2.2	Repeatability of the optimal run	100

4.4	Texture evolution of raw oak wood	102
4.4.1	N ₂ adsorption isotherms	102
4.4.1.1	Study of isotherm hysteresis	107
4.4.2	CO ₂ adsorption isotherms.....	110
4.5	Chemical and structural properties of raw oak wood and its derivatives	113
4.5.1	Elemental and proximate analyses	113
4.5.2	SEM and EDX analyses	115
4.5.3	XRD patterns	120
4.5.4	Boehm titration for selected samples.....	123
4.6	Assessment of CO ₂ sorption performance	123
4.6.1	CO ₂ uptake programmes	123
4.6.1.1	35 °C, 100% CO ₂	124
4.6.1.2	53 °C, 15% CO ₂	126
4.6.2	First screening	127
4.6.3	Simulated post-combustion performance	132
4.7	Chapter Conclusions	134
5	Sustainable and regenerable alkali metal-containing carbons derived from seaweed for post-combustion capture of CO₂	138
5.1	Outline.....	138
5.2	Carbonization of <i>Laminaria hyperborea</i>	139
5.2.1	Repeatability of dry pyrolysis and HTC.....	139
5.3	Activation of macroalgae-based chars - Optimal conditions.....	142
5.3.1	CO ₂ activation.....	142
5.3.1.1	The effect of the temperature.....	142
5.3.1.1.1	Hydrothermally carbonized <i>Laminaria hyperborea</i> (LH_S250)	142
5.3.1.1.2	Pyrolyzed <i>Laminaria hyperborea</i> (LH_S800)	145
5.3.1.2	The effect of the dwell time	147
5.3.1.2.1	Hydrothermally carbonized <i>Laminaria hyperborea</i> (LH_S250)	147
5.3.1.2.2	Pyrolyzed <i>Laminaria hyperborea</i> (LH_S800)	149
5.3.2	KOH activation.....	150
5.3.2.1	The effect of the temperature.....	151
5.3.2.1.1	Hydrothermally carbonized <i>Laminaria hyperborea</i> (LH_S250)	151

5.3.2.1.2	Pyrolyzed <i>Laminaria hyperborea</i> (LH_S800)	154
5.3.2.2	The effect of the KOH/char ratio	156
5.3.2.2.1	Hydrothermally carbonized <i>Laminaria hyperborea</i> (LH_S250)	156
5.3.2.2.2	Pyrolyzed <i>Laminaria hyperborea</i> (LH_S800)	158
5.4	Texture development of raw <i>Laminaria hyperborea</i>	160
5.4.1	N ₂ adsorption isotherms	160
5.4.2	CO ₂ adsorption isotherms.....	164
5.5	Chemical and structural characterization of raw <i>Laminaria hyperborea</i> and its derived products	168
5.5.1	Elemental and proximate analyses	168
5.5.1.1	Insight regarding TGA as a method for proximate analyses.....	171
5.5.2	Scanning Electron Microscope (SEM) and Energy-Dispersive X-ray (EDX) analyses	173
5.5.3	Further characterization for selected samples	178
5.5.3.1	XRD patterns	178
5.5.3.2	Boehm titration.....	181
5.6	CO ₂ uptake measurements	182
5.6.1	First screening	182
5.6.2	Simulated post-combustion performance	187
5.7	Chapter Conclusions	195
6	Chemical modification of activated carbons: Optimized wet impregnation of amines	198
6.1	Outline.....	198
6.2	Optimization of the PEI impregnation procedure	199
6.2.1	Effect of PEI loading (methanol, 53 °C)	199
6.2.2	Effect of stirring time (methanol, 53 °C).....	204
6.2.2.1	Optimal PEI loading	204
6.2.2.2	Non-optimal PEI loadings.....	206
6.2.3	Effect of solvent type and sorption temperature	211
6.2.3.1	Optimization of aqueous impregnation at 53 °C.....	213
6.2.3.1.1	Effect of PEI loading (water, 53 °C)	213
6.2.3.1.2	Effect of stirring time (water, 53 °C).....	216
6.2.3.2	Optimization of aqueous impregnation at 77 °C.....	219
6.2.3.2.1	Effect of PEI loading (water, 77 °C)	219

6.2.3.2.2 Effect of stirring time (water, 77 °C)	220
6.2.4 Influence of the carbon support	223
6.2.5 Influence of the impregnating agent.....	226
6.2.6 Influence of OH group-containing additive	230
6.3 Detection of PEI on the optimally PEI-impregnated carbon.....	235
6.4 Sorption kinetics modeling.....	239
6.5 Assessment of CO ₂ capture performance of the optimally PEI-impregnated carbon	242
6.5.1 Comparison with virgin AC and benchmark sorbent (Z13X) ..	242
6.5.1.1 35 °C, 100 % CO ₂	242
6.5.1.2 Simulated post-combustion performance.....	243
6.5.2 Cyclic post combustion capture for the optimally PEI-impregnated carbon.....	249
6.6 Chapter Conclusions	251
7 Conclusions	255
7.1 Biomass feedstocks	255
7.2 Carbonization routes	256
7.3 Activation methods	257
7.4 Chemical modification of carbons.....	259
7.5 The mechanism of CO ₂ uptake onto virgin and chemically-modified activated carbons	262
7.6 Directions for future work.....	264
List of References.....	266
List of abbreviations and symbols	287
Appendix A.....	291
Appendix B.....	293
Appendix C.....	296

List of Tables

Table 3-1 Primary optimization - PEI impregnation of commercial carbon (AR) - NL stands for Nominal Loading, as % calculated from g of PEI/(g of PEI + g of carbon). “Me” and “W” represent the solvent used and stand for Methanol and Water respectively	62
Table 3-2 Physical properties and amine types for impregnating agents used - I, II, and III stand for primary, secondary and tertiary amines respectively.....	64
Table 3-3 Impregnation conditions when adding glycerol (Gly)	65
Table 4-1 Repeatability of carbonization processes for raw oak wood	87
Table 4-2 Effect of CO ₂ activation temperature (T) on burn-off and textural parameters of hydrothermally carbonized wood; t represents the activation dwell time.	89
Table 4-3 Effect of CO ₂ activation temperature on burn-off and textural parameters of pyrolyzed wood	91
Table 4-4 Effect of CO ₂ activation dwell time on burn-off and textural parameters of hydrothermally carbonized wood	93
Table 4-5 Effect of CO ₂ activation dwell time on burn-off and textural parameters of pyrolyzed wood	95
Table 4-6 Yield and textural parameters of oak wood chars after KOH activation	97
Table 4-7 Repeatability of chemical activation of pyrolyzed oak wood (OW800CA) in terms of yield and textural parameters	101
Table 4-8 Repeatability of N ₂ adsorption measurements for OW800CA (run 2).....	101
Table 4-9 Gas adsorption data for key oak wood-based samples and commercial carbon.....	108
Table 4-10 Hysteresis case studies - Mesoporous volume and degassing temperature	108
Table 4-11 - Elemental and proximate analyses for key oak wood-based samples and commercial carbon	114
Table 4-12 - Details about inorganic elements (“Others” Figure 4-21) detected by EDX analyses for key oak wood-based samples and commercial carbon	119
Table 4-13 CO ₂ uptakes measured at a total pressure of 1 bar for oak wood derivatives (chars and activated carbons) and commercial carbon (GAC)	131
Table 5-1 Repeatability of carbonization processes of <i>Laminaria hyperborea</i> . SD is the standard deviation of the three measurements.	141

Table 5-2 Effect of CO ₂ activation temperature on burn off and textural parameters of hydrothermally carbonized <i>Laminaria hyperborea</i>	143
Table 5-3 Effect of CO ₂ activation temperature on burn off and textural parameters of pyrolyzed <i>Laminaria hyperborea</i>	146
Table 5-4 Effect of CO ₂ activation dwell time on burn off and textural parameters of hydrothermally carbonized <i>Laminaria hyperborea</i>	147
Table 5-5 Effect of CO ₂ activation dwell time on burn off and textural parameters of pyrolyzed <i>Laminaria hyperborea</i>	149
Table 5-6 Effect of activation temperature on activation yield and textural parameters of hydrothermally carbonized <i>Laminaria hyperborea</i>	152
Table 5-7 Effect of activation temperature on activation yield and textural parameters of pyrolyzed <i>Laminaria hyperborea</i>	155
Table 5-8 Effect of KOH:char ratio on activation yield and textural parameters of hydrothermally carbonized <i>Laminaria hyperborea</i>	157
Table 5-9 Effect of KOH:char ratio on activation yield and textural parameters of pyrolyzed <i>Laminaria hyperborea</i>	159
Table 5-10 Gas adsorption data for key <i>Laminaria hyperborea</i> -based samples and magnesium oxide. NM stands for not measured....	163
Table 5-11 Elemental and proximate analyses for isotherms for key <i>Laminaria hyperborea</i> -based samples.....	170
Table 5-12 Details about inorganic elements (see “Others” Figure 5-26) detected by EDX analyses for for key <i>Laminaria hyperborea</i> -based samples	177
Table 5-13 CO ₂ uptakes measurement at a total pressure of 1 bar for key <i>Laminaria hyperborea</i> -based samples.....	185
Table 6-1 Primary optimization - Impregnation efficiency and Nitrogen content.....	200
Table 6-2 Primary optimization - Textural parameters.....	201
Table 6-3 Primary optimization - CO ₂ uptakes at 53 or 77 °C and 0.15 bar (total pressure of 1 bar)	204
Table 6-4 Effect of stirring time for non-optimal PEI loadings - Impregnation efficiency and Nitrogen content.....	208
Table 6-5 Effect of stirring time for non-optimal PEI loadings - Textural parameters	209
Table 6-6 Effect of stirring time for non-optimal loadings - CO ₂ uptakes at 0.15 bar (total pressure of 1 bar) and 53 °C	210
Table 6-7 Optimization of aqueous impregnation - Impregnation efficiency and Nitrogen content	214
Table 6-8 Optimization of aqueous impregnation - Textural parameters	215

Table 6-9 Optimization of aqueous impregnation - CO ₂ uptakes at 53 or 77 °C and 0.15 bar (total pressure of 1 bar)	215
Table 6-10 Main optimal conditions as identified by maximization of the CO ₂ sorption capacity of PEI-impregnated carbons - Optimal values of PEI loading and stirring time are reported for each sorption temperature and solvent type used	223
Table 6-11 Effect of the carbon support - Textural parameters, actual loading and N content	223
Table 6-12 Effect of the impregnating agent - Textural parameters, actual loading and N content.....	227
Table 6-13 Effect of glycerol addition - Actual loading and elemental analysis; the actual loading measured for the glycerol-containing samples refers to the PEI/glycerol mixture. Gly stands for Glycerol.	230
Table 6-14 Effect of glycerol addition - CO ₂ uptakes (CO _{2, ads max}) at 53 °C and 0.15 bar (total pressure of 1 bar), and amine efficiency. N* represents the amount of nitrogen actually incorporated after impregnation of PEI or PEI/glycerol blend onto the carbon support, and is calculated by subtracting the N content of AR (see Table 6-1) from the N levels measured for impregnated samples (see Table 6-13). The CO _{2, ads max} /N* molar ratio is then calculated as (CO _{2, ads max} /N*)·(MW _(N) /MW _(CO₂)), where CO _{2, ads max} is expressed as wt%.	231
Table 6-15 Effect of glycerol addition - Textural parameters	233
Table 6-16 Kinetic model parameters for CO ₂ sorption onto virgin (AR) and PEI-modified commercial carbon (AR-PEI).....	241
Table 6-17 Differential Scanning Calorimetry (DSC) data related to the adsorption of CO ₂ - Total enthalpy was calculated as the integral of heat flow for 0<t<30 min. Heat of adsorption was calculated as total enthalpy divided by adsorbed moles of gas.	248
Table 6-18 DSC data related to desorption of CO ₂ and pure N ₂ . Total enthalpy was calculated as the integral of heat flow for 30<t<40 min. Heat of desorption was calculated as total enthalpy divided by desorbed moles of gas.....	248

List of Figures

Figure 1-1 CO ₂ emissions shares by fossil fuel (1971-2012) [3]	2
Figure 1-2 Total CO ₂ Emissions Excluding Land-Use Change and Forestry between 1850 and 2012 [4].	3
Figure 2-1 Commercial use of various precursors for ACs production	22
Figure 2-2 Pressure - temperature phase diagram of water with associated hydrothermal processes [147]	25
Figure 3-1 (a) Raw oak wood (OW) and (b) <i>Laminaria hyperborea</i> summer (LH_S) used as precursor for activated carbons (ACs) preparation	53
Figure 3-2 Dry pyrolysis of biomass - setup 1 (ceramic horizontal tube furnace): a) exhaust system on the left hand side, b) gas feed connection on the right hand side, and c) furnace controller.	55
Figure 3-3 Dry pyrolysis of biomass - setup 1 – schematic representation.....	55
Figure 3-4 Dry pyrolysis of biomass - setup 1 (Stainless steel rig): a) vertical furnace, b) traps for collection of HCl and further volatiles, and c) furnace controller.	56
Figure 3-5 Dry pyrolysis of biomass - setup 2 – schematic representation.....	57
Figure 3-6 HTC of biomass: a) reactor setup, and b) temperature controller	58
Figure 3-7 Glycerol molecule	65
Figure 3-8 Scheme representing the interference of an incident X-ray (wavelength λ) scattered from two parallel atomic layers (hkl) separated by an interplanar distance d.	78
Figure 4-1 N ₂ adsorption isotherms - Effect of temperature on CO ₂ activation of hydrothermally carbonized oak wood	90
Figure 4-2 NLDFT pore size distributions - Effect of temperature on CO ₂ activation of hydrothermally carbonized oak wood.....	90
Figure 4-3 N ₂ adsorption isotherms - Effect of temperature on CO ₂ activation of pyrolyzed oak wood	91
Figure 4-4 NLDFT pore size distributions - Effect of temperature on CO ₂ activation of pyrolyzed oak wood.....	92
Figure 4-5 - N ₂ adsorption isotherms - Effect of dwell time on CO ₂ activation of hydrothermally carbonized oak wood	93
Figure 4-6 NLDFT pore size distributions - Effect of dwell time on CO ₂ activation of hydrothermally carbonized oak wood	94
Figure 4-7 - N ₂ adsorption isotherms - Effect of dwell time on CO ₂ activation of pyrolyzed oak wood	95

Figure 4-8 - NLDFT pore size distributions - Effect of dwell time on CO ₂ activation of pyrolyzed oak wood.....	96
Figure 4-9 Influence of the washing procedure on textural parameters of pyrolyzed wood after KOH activation (OW800CA)	99
Figure 4-10 Influence of the washing procedure on FTIR spectra of OW800CA	100
Figure 4-11 Influence of the washing procedure on EDX chemical compositions of OW800CA.....	100
Figure 4-12 N ₂ adsorption isotherms for key oak wood-based samples and commercial carbon	102
Figure 4-13 N ₂ NLDFT pore size distributions for key oak wood-based samples and commercial carbon	103
Figure 4-14 Isotherms hysteresis – case study 1 (“D” stands for desorption).....	109
Figure 4-15 Isotherms hysteresis - case study 2 (“D” stands for desorption).....	110
Figure 4-16 CO ₂ adsorption isotherms for key oak wood-based samples and commercial carbon	111
Figure 4-17 CO ₂ NLDFT pore size distributions for key oak wood-based samples and commercial carbon.....	112
Figure 4-18 Correlation between CO ₂ uptake at 273 K and 1 bar, and the narrow micropore volume (d<0.7 nm) determined by applying the NLDFT method to the CO ₂ adsorption isotherms measured for key oak wood-based samples and commercial carbon.....	112
Figure 4-19 Correlation between CO ₂ uptake at 273 K and 1 bar, and the narrow micropore volume (d<0.7 nm) determined by applying the DR method to the CO ₂ adsorption isotherms measured for key oak wood-based samples and commercial carbon.....	113
Figure 4-20 SEM images at 5000x magnification for (a) OW, (b) OW250, (c) OW800, (d) OW250PA, (e) OW800PA, (f) OW250CA, (g) OW800CA and (h) GAC.....	117
Figure 4-21 EDX chemical composition for key oak wood-based samples and commercial carbon	118
Figure 4-22 XRD patterns and standard stick patterns for raw oak wood (a), oak wood-derived chars (b), physically-activated chars (c), chemically- activated chars (d) and commercial carbon (e)..	122
Figure 4-23 Boehm titration for selected samples	123
Figure 4-24 CO ₂ uptakes programme (100% CO ₂ , 35 °C) for representative sample (OW800PA): (a) before amendment and (b) after amendment	125
Figure 4-25 CO ₂ uptakes programme (100% CO ₂ , 35 °C) - Blank run ..	126

Figure 4-26 CO ₂ uptakes programme (15% CO ₂ , 53 °C) for representative sample (OW800PA)	127
Figure 4-27 CO ₂ uptakes programme (15% CO ₂ , 53 °C) - Blank run	127
Figure 4-28 CO ₂ kinetics measured at 35 °C and 1 bar (total pressure of 1 bar) for all samples.....	129
Figure 4-29 CO ₂ kinetics measured at 35 °C and 1 bar (total pressure of 1 bar) and normalized by surface area for best performing samples	130
Figure 4-30 Regeneration (single rapid temperature swing adsorption (RTSA) cycle, 35-100 °C) for best performing samples	130
Figure 4-31 15% CO ₂ adsorption kinetics at 53 °C and 0.15 bar (total pressure of 1 bar) measured for best performing samples	132
Figure 4-32 Regeneration (single RTSA, 53-100 °C) for best performing samples	133
Figure 4-33 (a) Regeneration performance and (b) CO ₂ sorption capacity over ten RTSA cycles for the physically-activated wood (OW800PA)	134
Figure 4-34 Zoom of the first 2 RTSA cycle for the physically-activated wood (OW800PA)	134
Figure 5-1 N ₂ adsorption isotherms - Effect of temperature on CO ₂ activation of hydrothermally carbonized <i>Laminaria hyperborea</i> .	144
Figure 5-2 Non-local density functional theory (NLDFT) pore size distributions by volume - Effect of temperature on CO ₂ activation of hydrothermally carbonized <i>Laminaria hyperborea</i> .	144
Figure 5-3 N ₂ adsorption isotherms - Effect of temperature on CO ₂ activation of pyrolyzed <i>Laminaria hyperborea</i>	146
Figure 5-4 NLDFT Pore size distributions by volume - Effect of temperature on CO ₂ activation of pyrolyzed <i>Laminaria hyperborea</i>	147
Figure 5-5 N ₂ adsorption isotherms - Effect of dwell time on CO ₂ activation of hydrothermally carbonized <i>Laminaria hyperborea</i> .	148
Figure 5-6 NLDFT Pore size distributions by volume - Effect of dwell time on CO ₂ activation of hydrothermally carbonized <i>Laminaria hyperborea</i>	148
Figure 5-7 N ₂ adsorption isotherms - Effect of dwell time on CO ₂ activation of pyrolyzed <i>Laminaria hyperborea</i>	150
Figure 5-8 NLDFT Pore size distributions by volume - Effect of dwell time on CO ₂ activation of pyrolyzed <i>Laminaria hyperborea</i>	150
Figure 5-9 N ₂ adsorption isotherms - Effect of temperature on chemical activation of hydrothermally carbonized <i>Laminaria hyperborea</i>	153

Figure 5-10 NLDFT Pore size distributions by volume - Effect of temperature on chemical activation of hydrothermally carbonized <i>Laminaria hyperborea</i>	154
Figure 5-11 N ₂ adsorption isotherms - Effect of temperature on chemical activation of pyrolyzed <i>Laminaria hyperborea</i>	155
Figure 5-12 NLDFT Pore size distributions by volume - Effect of temperature on chemical activation of pyrolyzed <i>Laminaria hyperborea</i>	156
Figure 5-13 N ₂ adsorption isotherms - Effect of KOH:char ratio on chemical activation of hydrothermally carbonized <i>Laminaria hyperborea</i>	157
Figure 5-14 NLDFT Pore size distributions by volume - Effect of KOH:char ratio on chemical activation of hydrothermally carbonized <i>Laminaria hyperborea</i>	158
Figure 5-15 N ₂ adsorption isotherms - Effect of KOH:char ratio on chemical activation of pyrolyzed <i>Laminaria hyperborea</i>	159
Figure 5-16 NLDFT Pore size distributions by volume - Effect of KOH:char ratio on chemical activation of pyrolyzed <i>Laminaria hyperborea</i>	160
Figure 5-17 N ₂ adsorption isotherms for key <i>Laminaria hyperborea</i> -based samples.	164
Figure 5-18 NLDFT pore size distribution for key <i>Laminaria hyperborea</i> -based samples.	164
Figure 5-19 CO ₂ adsorption isotherms for key <i>Laminaria hyperborea</i> -based samples	166
Figure 5-20 NLDFT pore size distribution for key <i>Laminaria hyperborea</i> -based samples	166
Figure 5-21 Linear correlation between CO ₂ uptake at 273 K and 1 bar, and the narrow micropore volume (d<0.7 nm) determined by applying the NLDFT method to the CO ₂ adsorption isotherms for key <i>Laminaria hyperborea</i> -based samples.....	167
Figure 5-22 Correlation between CO ₂ uptake at 273 K and 1 bar, and the narrow micropore volume (d<0.7 nm) determined by applying the DR method to the CO ₂ adsorption isotherms for key <i>Laminaria hyperborea</i> -based samples.....	167
Figure 5-23 Proximate analyses determined by TGA for pyrolyzed <i>Laminaria hyperborea</i> (LH_S800).....	172
Figure 5-24 Comparison between TGA and DTGA curves for pyrolyzed <i>Laminaria hyperborea</i> (LH_S800)	172
Figure 5-25 SEM images at 5000x magnification for (a) LH_S, (b) LH_S250, (c) LH_S800, (d) LH_S250PA, (e) LH_S800PA, (f) LH_S250CA and (g) LH_S800CA	175

Figure 5-26 EDX chemical compositions acquired on the micrographs shown in Figure 5-25 for for key <i>Laminaria hyperborea</i> -based samples	176
Figure 5-27 XRD Patterns for (a) raw macroalgae (LH_S), (b) pyrolyzed macroalgae (LH_S800) and physically-activated counterpart (LH_S800PA), and (c) chemically-activated counterpart (LH_S800CA)	181
Figure 5-28 Basic and acidic functionalities measured by Boehm's titration for pyrolyzed macroalgae (LH_S800), physically-activated counterpart (LH_S800PA), and chemically-activated counterpart (LH_S800CA)	182
Figure 5-29 CO ₂ adsorption kinetic at 35 °C and 1 bar for key <i>Laminaria hyperborea</i> -based samples.....	184
Figure 5-30 Regeneration (rapid temperature swing adsorption (RTSA), 35-100 °C) for key <i>Laminaria hyperborea</i> -based samples.....	186
Figure 5-31 CO ₂ adsorption kinetic at 53 °C and 0.15 bar (total pressure of 1 bar) measured for pyrolyzed macroalgae (LH_S800), physically-activated counterpart (LH_S800PA), chemically-activated counterpart (LH_S800CA), and magnesium oxide (MgO).....	187
Figure 5-32 CO ₂ adsorption progress at 53 °C and 0.15 bar (total pressure of 1 bar) measured for pyrolyzed macroalgae (LH_S800), physically-activated counterpart (LH_S800PA), and magnesium oxide (MgO).....	188
Figure 5-33 Regeneration (RTSA, 53-100 °C) for pyrolyzed macroalgae (LH_S800), physically-activated counterpart (LH_S800PA), chemically-activated counterpart (LH_S800CA), and magnesium oxide (MgO).....	192
Figure 5-34 CO ₂ desorption progress (RTSA, 53-100 °C) for pyrolyzed macroalgae (LH_S800), physically-activated counterpart (LH_S800PA), and magnesium oxide (MgO).....	192
Figure 5-35 (a) Recyclability and (b) sorption capacity over ten RTSA cycles for pyrolyzed <i>Laminaria</i> (LH_S800).....	193
Figure 5-36 1 st RTSA cycle for pyrolyzed <i>Laminaria</i> (LH_S800)	193
Figure 5-37 (a) Recyclability and (b) sorption capacity over ten RTSA cycles for physically-activated <i>Laminaria</i> (LH_S800PA).....	194
Figure 5-38 1 st RTSA cycle for physically-activated <i>Laminaria</i> (LH_S800PA)	194
Figure 6-1 Effect of PEI loading: (a) N ₂ Adsorption Isotherms and (b) non-local density functional theory (NLDFT) Pore size distributions (PSDs) by volume. A stirring time of 0.5 h and methanol solvent were used to impregnate these samples.....	202

- Figure 6-2 Effect of PEI loading: (a) N content and pore volume reduction, and (b) CO₂ uptakes at 53 °C and 0.15 bar (total pressure of 1 bar). A stirring time of 0.5 h and methanol solvent were used to impregnate these samples. Error bars represent standard error (n=3).....203**
- Figure 6-3 Effect of PEI loading: CO₂ adsorption kinetics at 53 °C and 0.15 bar (total pressure of 1 bar). A stirring time of 0.5 h and methanol solvent were used to impregnate these samples.....203**
- Figure 6-4 Effect of stirring time: (a) N content and pore volume reduction, and (b) CO₂ uptakes at 53 °C and 0.15 bar (total pressure of 1 bar). Optimal nominal PEI loading (44 wt%) and methanol solvent were used to impregnate these samples. Error bars represent standard error (n=3).....205**
- Figure 6-5 Effect of stirring time: CO₂ adsorption kinetics at 53 °C and 0.15 bar (total pressure of 1 bar). Optimal nominal PEI loading (44 wt%) and methanol solvent samples were used to prepare these samples.....206**
- Figure 6-6 Effect of stirring time: (a) N content and pore volume reduction, and (b) CO₂ uptakes at 53 °C and 0.15 bar (total pressure of 1 bar). Nominal PEI loading of 38 wt% and methanol solvent were used to impregnate these samples.208**
- Figure 6-7 Effect of stirring time: (a) N content and pore volume reduction, and (b) CO₂ uptakes at 53 °C and 0.15 bar (total pressure of 1 bar). Nominal PEI loading of 50 wt% and methanol solvent were used to impregnate these samples.209**
- Figure 6-8 Effect of stirring time: CO₂ adsorption kinetics at 53 °C and 0.15 bar (total pressure of 1 bar). Nominal PEI loading of (a) 38 wt% or (b) 50 wt% and methanol solvent were used to prepare these samples.....211**
- Figure 6-9 Effect of solvent type and sorption temperature: CO₂ adsorption kinetics at 0.15 bar (total pressure of 1 bar) for 53 °C and 77 °C; samples were prepared using optimal values of nominal PEI loading (44 wt%) and stirring time (8 h).....213**
- Figure 6-10 Effect of PEI loading: (a) N content and pore volume reduction, and (b) CO₂ uptakes at 53 °C and 0.15 bar (total pressure of 1 bar). A stirring time of 0.5 h and water solvent were used to impregnate these samples.....216**
- Figure 6-11 Effect of PEI loading: CO₂ adsorption kinetics at 53 °C and 0.15 bar (total pressure of 1 bar). A stirring time of 0.5 h and water solvent were used to impregnate these samples.216**
- Figure 6-12 Effect of stirring time: (a) N content and pore volume reduction, and (b) CO₂ uptakes at 53 °C and 0.15 bar (total pressure of 1 bar). Optimal nominal PEI loading (38 wt%) and water as solvent were used to prepare the samples.218**

Figure 6-13 Effect of stirring time: CO ₂ adsorption kinetics at 53 °C and 0.15 bar (total pressure of 1 bar); samples were prepared using an optimal value of nominal PEI loading (38 wt%) and water as solvent.....	218
Figure 6-14 Effect of PEI loading: (a) N content and pore volume reduction, and (b) CO ₂ uptakes at 77 °C and 0.15 bar (total pressure of 1 bar). A stirring time of 8 h and water as solvent were used to impregnate these samples.....	219
Figure 6-15 Effect of PEI loading: CO ₂ adsorption kinetics at 77 °C and 0.15 bar (total pressure of 1 bar). A stirring time of 8 h and water solvent were used to impregnate these samples.....	220
Figure 6-16 Effect of stirring time: (a) N content and pore volume reduction, and (b) CO ₂ uptakes at 77 °C and 0.15 bar (total pressure of 1 bar). An optimal value of nominal PEI loading (50 wt%) and water as solvent were used to prepare these samples.....	222
Figure 6-17 Effect of stirring time: CO ₂ adsorption kinetics at 77 °C and 0.15 bar (total pressure of 1 bar); samples were prepared using an optimal value of nominal PEI loading (50 wt%) and water solvent.....	222
Figure 6-18 Effect of the carbon support - N ₂ adsorption isotherms ..	224
Figure 6-19 Effect of the carbon support - NLDFIT PSDs by volume ...	224
Figure 6-20 Effect of the carbon support – Basic and acidic functionalities measured by Boehm titrations	225
Figure 6-21 Effect of the carbon support - CO ₂ uptakes at 53 °C and 0.15 bar (total pressure of 1 bar)	225
Figure 6-22 Effect of the carbon support - CO ₂ adsorption kinetics at 53 °C and 0.15 bar (total pressure of 1 bar).....	226
Figure 6-23 Effect of impregnating agent - N ₂ adsorption isotherms..	228
Figure 6-24 Effect of impregnating agent - NLDFIT PSDs by volume ..	228
Figure 6-25 Effect of impregnating agent - CO ₂ uptakes at 53 °C and 0.15 bar (total pressure of 1 bar)	228
Figure 6-26 Effect of impregnating agent - CO ₂ adsorption kinetics at 53 °C and 0.15 bar (total pressure of 1 bar).....	229
Figure 6-27 Effect of impregnating agent - Regeneration (RTSA, 53-100 °C)	230
Figure 6-28 Effect of glycerol addition - CO ₂ adsorption kinetics at 53 °C and 0.15 bar (total pressure of 1 bar).....	231
Figure 6-29 Effect of glycerol addition - N ₂ adsorption isotherms. 4:1, 2:1 and 1:1 are the PEI:Glycerol ratios examined.....	233
Figure 6-30 Effect of glycerol addition - CO ₂ adsorption progress at 53 °C and 0.15 bar (total pressure of 1 bar). Inset shows the first 3 min of the CO ₂ adsorption step.	234

Figure 6-31 Effect of the glycerol addition: (a) CO ₂ desorption kinetics and (b) CO ₂ desorption progress at 53-100 °C and 0.15 bar (total pressure of 1 bar)	235
Figure 6-32 N ₂ (a) and CO ₂ (b) adsorption isotherms for virgin and optimally PEI-impregnated carbons.....	236
Figure 6-33 Back-scattered SEM micrographs at 1 Kx magnification of the cross-section of (a) virgin and (b) optimally PEI-impregnated carbons	236
Figure 6-34 (a) TGA and (b) DTGA of virgin and optimally PEI-impregnated carbons	237
Figure 6-35 Surface functional group concentrations assayed for virgin and optimally PEI-impregnated carbon.....	238
Figure 6-36 Comparison of X-ray Photoelectron Spectroscopy (XPS) survey scan spectra measured for virgin and optimally PEI-impregnated carbons. C/S indicates the counts per second. Inset shows the deconvoluted N1s spectra for the PEI-modified carbon.....	238
Figure 6-37 Sorption kinetics fitting for (a) virgin commercial carbon (AR) and (b) PEI-modified commercial carbon (AR-PEI)	240
Figure 6-38 CO ₂ uptakes measured at 35 °C and 1 bar (total pressure of 1 bar): comparison of virgin carbon, optimally PEI-impregnated carbon and Z13X	242
Figure 6-39 Regeneration (RTSA, 35-100 °C): comparison of virgin carbon, optimally PEI-impregnated carbon and Z13X.....	243
Figure 6-40 CO ₂ uptakes at 53 °C and 0.15 bar (total pressure of 1 bar): comparison of virgin carbon, optimally PEI-impregnated carbon and Z13X.....	244
Figure 6-41 Pure N ₂ uptakes measured at 53 °C and 1 bar: comparison of virgin carbon, optimally PEI-impregnated carbon and Z13X.....	245
Figure 6-42 Preliminary adsorption of nitrogen during 22 min cooling stage prior to measuring CO ₂ uptakes at 53 °C and 0.15 bar (total pressure of 1 bar)	245
Figure 6-43 Regeneration (RTSA, 53-100 °C): comparison of virgin carbon, optimally PEI-impregnated carbon and Z13X.....	246
Figure 6-44 Heat flow related to adsorption and desorption of CO ₂ under simulated post-combustion conditions: comparison of virgin carbon and optimally PEI-impregnated carbon.....	247
Figure 6-45 Heat flow related to adsorption and desorption of N ₂ under simulated post-combustion conditions: comparison of virgin carbon and optimally PEI-impregnated carbon.....	247

- Figure 6-46 Illustration of RTSA cycling experiment (first 2 cycles only) carried out for the optimally PEI-impregnated carbon under simulated post-combustion conditions ($T \approx 53\text{ }^{\circ}\text{C}$, $P_{\text{CO}_2} = 0.15\text{ bar}$, $P_{\text{tot}} = 1\text{ bar}$).....250**
- Figure 6-47 Heat flow related to adsorption and desorption of CO_2 under simulated post combustion conditions during the first RTSA cycle.....250**
- Figure 6-48 (a) Regeneration performance and (b) Cyclic capacity over ten RTSA cycles for the optimally PEI-impregnated carbon.....251**

1 Introduction and overall context

1.1 Thesis framework

The present thesis consists of seven chapters. The current chapter (Chapter 1) attempts to put the entire work into context. Chapter 1 includes a brief introduction of the problem to be addressed (i.e. reduction of CO₂ emission), and gives information concerning the current status of the existing technologies which can potentially tackle this issue, with a particular focus on the route pursued in this work, i.e. sorption onto solid materials.

Chapter 2 provides the scientific background related to the fabrication of the selected sorbents (i.e. biomass-derived activated carbons (ACs)) and their previous application for CO₂ capture. In addition to this, the primary objectives of the study are also outlined.

Details related to the materials used and the methods applied for their synthesis and characterizations are given in Chapter 3.

Results obtained and relevant discussion are grouped in three chapters (4 to 6), referring to the performance of CO₂ sorbents derived from oak wood, *Laminaria hyperborea* and to the chemical modification of commercial carbon respectively.

Overall conclusions along with directions for future works are summarized in Chapter 7.

1.2 Chapter outline

The environmental impact caused by greenhouse and the relevant legislation are briefly discussed in section 1.3.

Following, a comprehensive description of the carbon capture and storage (CCS) chain is given in section 1.4, with specific emphasis on the capture stage.

Section 1.5 focuses on the application of solid sorbents for CO₂ capture under post-combustion conditions as alternative to the state of the art technology (chemical absorption onto liquid amines-based solvents).

1.3 Problem overview

1.3.1 Greenhouse effect and global warming

To date, the greenhouse effect is a well-recognized phenomenon that concerns the entire community. This problem is mostly caused by increasing emissions of greenhouse gases (GHGs), such as carbon dioxide, methane and other minor compounds. Quadrelli and Peterson [1] not only underlined the dominant role of the energy production at increasing GHGs emissions, but also that carbon dioxide represents the greater portion of these gases. The CO₂ footprints are mainly due to the use of unrenovable energy sources (fossil fuels) such as coal, employed in stationary power plants for electricity generation, and oil, whose derivatives are used for motor transport [1].

The CO₂ molecule has been proven very harmful to the ecosystem, due to its long lifetime in the atmosphere, as it is estimated to live around 30 - 95 years [2].

As quantified by the International Energy Agency (IEA) [3], coal was the predominant fossil source at determining the increase of the CO₂ emissions in the recent years (1971-2012, see Figure 1-1), and coal combustion was found to generate the largest share of CO₂ emissions in 2012. According to the data reported by the World Resources Institute (WRI) Climate Analysis Indicators Tool (CAIT) [4], the global CO₂ footprint has been increasing over the last 150 years at an exponential rate (see Figure 1-2), reaching over 30 Gt in 2012.

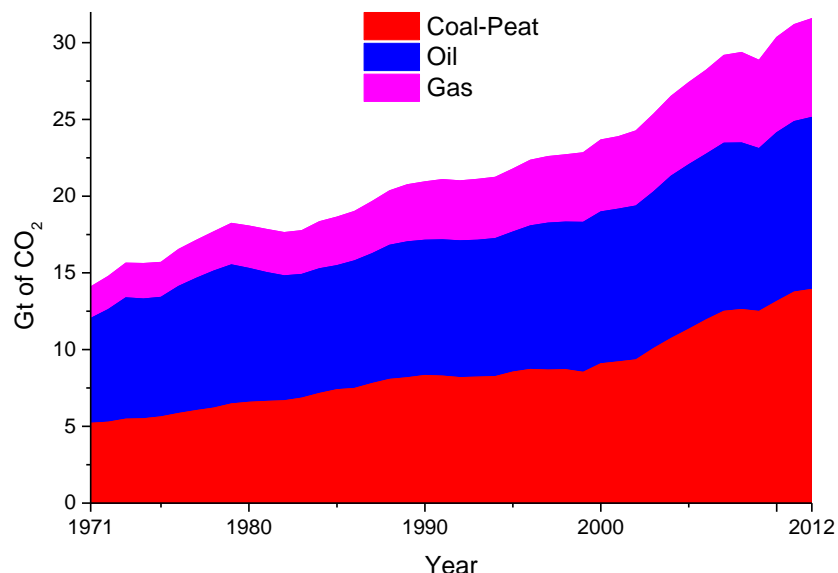


Figure 1-1 CO₂ emissions shares by fossil fuel (1971-2012) [3]

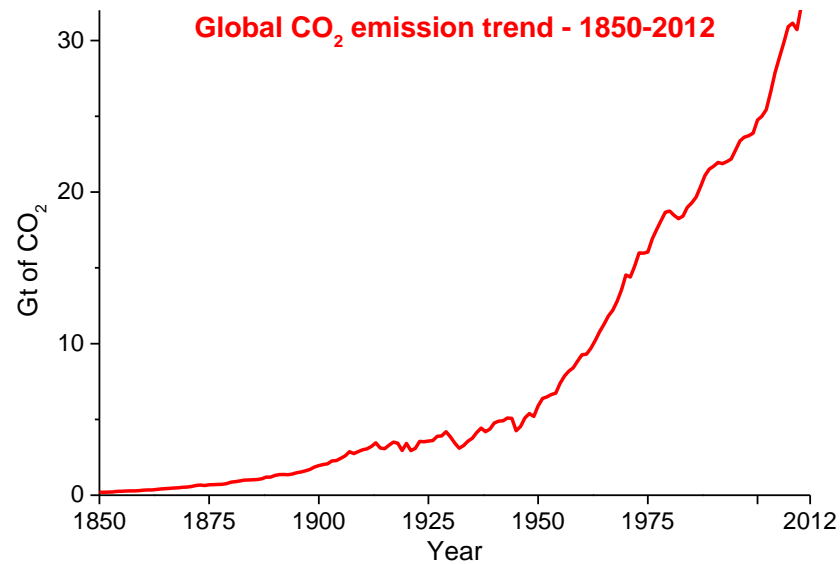


Figure 1-2 Total CO₂ Emissions Excluding Land-Use Change and Forestry between 1850 and 2012 [4].

This progressive increase in the CO₂ level affecting the atmosphere appears to be strongly linked to the global climate change. Because of the greenhouse effect, the global surface temperature has already increased by 0.8 °C in the 20th Century, and is expected to rise further by 1.4-5.8 °C during the 21st Century [5].

According to the most recent (2014) synthetic report published by the Intergovernmental Panel on Climate Change (IPCC) [6], the higher concentration of carbon dioxide in the atmosphere seems to be the main driver for the climate change. This was inferred based upon a series of climate change indicators (e.g. increase of the temperature of atmosphere, surface and ocean, reduction of snow and ice with consequent rise of sea levels, change in the global water cycle and extreme events, ocean acidification, etc.). This report clearly correlated human influence to the drastic change in climate system. In particular, the continuous increase of anthropogenic emissions since the industrial revolution (see also Figure 1-1) led to unprecedentedly high levels of greenhouse gases (i.e. carbon dioxide, methane and nitrous oxide) in the atmosphere. This is believed to be the predominant cause of the global warming phenomenon. One of the most visible impacts of the climate change was reflected in the increased frequency of extreme weather events (heat waves, heavy precipitations, cyclones) over a wider proportion of land regions, which has been detected since 1950. The same report forecasted increasing trends in GHGs emissions, which will probably amplify the magnitude of all the aforementioned impacts on the global climate. In particular, the variation of the global surface temperature by the end of the 21st century is likely to exceed 1.5 °C compared to that measured between 1850 and 1900 for all GHGs emission scenarios except the lowest considered.

1.3.2 Policies and Regulations

In order to mitigate the risks involved by global warming, increasingly strict measures have been imposed to the major developed nations in terms of anthropogenic emissions. Regulations in matter of carbon footprint were introduced for the first time by the Kyoto Protocol in 1997 [7], and after this, with the Copenhagen Accord in 2009 [8]. These were both established by the United Nations Framework Convention on Climate Change (UNFCCC).

The first international agreement imposed to all the ratifying countries to match specific targets in terms of CO₂ concentrations emitted, which should have been met within 2012 by all the parties involved. In attempt to reduce the carbon dioxide emissions level, three different approaches were suggested, in particular Emissions Trading, Joint Implementation and the Clean Development Mechanism. These aimed to encourage green investment (i.e. use of renewable resources) and lead governments to conform to their emission targets in a cost-effective way.

Negotiations following the ratification of the Kyoto protocol led to a second accord, which was drafted during the 15th Conference of Parties (COP). This included the participation of US and developing states (such as China, India, Brazil, and South Africa), which had a significant role in the ratification of the Copenhagen Accord. The latter pledged to limit greenhouse gas concentrations in the atmosphere as to alleviate the negative impacts to the global climate. In other words, the emissions amount should have been restrained to an extent involving a rise of the global temperature below 2 °C. In addition, developed states committed to gather economic aids for the developing countries with the purpose to enable them to exercise mitigation actions against the climatic changes. The greater part of the financial support was supposed to be provided through the Copenhagen Green Climate Fund [8]. Nevertheless, according to the analysis of Lau *et al.* [9], the Copenhagen Accord was considered not as binding as the Kyoto Protocol, and funding supplied by the Copenhagen Green Climate Fund is believed to be limited. Moreover, the same study stated that, although the goal defined by the Kyoto protocol is presumed to be achievable, it would probably not suffice to arrest increasing emissions trend. The same applies to the Copenhagen Accord. Therefore, it is clear that a more stringent target and a full commitment from all parties are needed for a substantial reduction of the CO₂ footprint.

Recently, the European Council endorsed a target of 40% reduction of greenhouse gas emissions to be achieved by 2030 [10]. A more extensive exploitation of renewable energies and increasing investments in CCS systems were indicated as the main countermeasures to be taken in order to meet this ambitious target.

Indeed, although renewable energy technologies (RETs) and biofuels utilization have been significantly developed over the last decades, their use on a larger scale in the short-term is hindered by a number of issues, mostly represented by higher costs compared to use of fossil fuels and a low level of readiness [11]. In addition to that, the inherent intermittent nature of some renewables (e.g. wind, solar, tides) and the limited availability of land for the cultivation of biomass specifically intended for biofuels production dictate the integration of RETs with complementary technologies, such as nuclear and/or CCS chain [11]. The latter consists of three main steps: capture, transport and storage, which were thoroughly discussed in the following sections.

1.4 The CCS chain

1.4.1 CO₂ Capture

CO₂ capture approaches can be divided into four main categories [12]: oxy-fuel processes (oxy-firing or oxy-combustion), chemical-looping combustion (CLC), pre-combustion (gasification or reforming) and post-combustion processes. These configurations are briefly described below.

1.4.1.1 Pre-combustion

Pre-combustion strategy involves the capture of CO₂ prior to energy production. This approach is typically applied to integrated gasification combined cycle (IGCC) power plants [12]. An elementary block diagram of the process is reported by [13]. First, the fuel (coal, natural gas, crude oil, etc.) reacts with steam (solid fuels) or oxygen (liquid or gaseous fuels) at elevated temperature (1400 °C) and pressure (34–55 bar). This reaction yields the synthesis gas (syngas), which mainly consists of CO and H₂ [14]. Following, the carbon monoxide contained within the syngas is converted to CO₂ and additional H₂ in a catalytic reactor (shift converter) by means of a water-gas shift (WGS) reaction [15], which increases the partial pressure of CO₂ in the gas stream. The latter will then be a CO₂/H₂ mixture, and is normally characterized by high pressure (ca. 15-40 bar) and intermediate CO₂-concentration (15-40%) [12]. Under these conditions, the preferred solution for separating CO₂ from hydrogen was reported to be physical absorption onto solvents (e.g. Selexol, Rectisol, etc.).

Physical solvents do not involve any chemical reaction but rely on the solubility of CO₂ into the liquid phase [12]. Regeneration technique depends on the type of solvent. This is normally performed by flash desorption or stripping. Both systems refer to the application of a drastic pressure reduction to release CO₂ from the solvent. However, stripping implies a further purification of the solvent by using an inert (N₂) gas flow. After the separation stage, the CO₂ is

recompressed prior to be transported to storage site, whereas the H₂ concentrated syngas is fed to the combustion chamber for energy conversion.

Chemical solvents could also be used for pre-combustion capture of CO₂ [16], but these offer better performance at lower pressure (post-combustion conditions, see also section 1.4.1.2) and imply high penalty for the efficiency of the power plant.

Cryogenic distillation was also applied for syngas separation [17], but this system is more suitable for a highly CO₂ concentrated gas stream (like that produced by oxy-fuel combustion, see 1.4.1.3) and needs a substantial amount of energy for refrigeration.

However, emerging approaches have been also developed. For instance, as described in the review of Scholes *et al.* [18], different types of CO₂ or H₂-selective membranes were tested for separation of gas stream produced in an IGCC process, which showed interesting prospective for pre-combustion capture of CO₂. In spite of this, the cost-effectiveness of the process is still limited by a series of disadvantages.

In addition to this, adsorption onto solid adsorbents (e.g. AC [19, 20], zeolite [21]) was also considered as potential pre-combustion application. The most efficient regeneration strategy for solid sorbents would be a pressure swing adsorption (PSA), as this gives a trade-off between the CO₂ recovery and the CO₂ purity [22]. Optimization of PSA process was reported by [23], where an activated carbon was used as adsorbent because of its low-cost and good cycling performance. Nonetheless, as suggested by [19], using temperature swing adsorption (TSA) route for the regeneration of the activated carbons could be potentially more convenient. Indeed, an efficient desorption of CO₂ was reported when increasing the temperature up to 170 °C. Moreover, the use of a TSA configuration would allow preserving a high-pressure condition for the CO₂ enriched gas stream, thereby avoiding the energy penalty associated with the re-compression of the CO₂ captured.

The major advantage of the pre-combustion approach over the post-combustion route is the higher CO₂ partial pressure in the initial flue gas, which implies an easier and more efficient capture of the gas [24]. On the other way, IGCC plants involve high investments and operational costs [25], whereas a technology retrofitting to existing plants would be more expensive and complex compared to the post-combustion configuration [12].

1.4.1.2 Post-combustion

Post-combustion technology currently has a higher level of readiness among all available capture approaches, as it can retrofit to existing power plants [26].

A basic representation of the post-combustion route can be found elsewhere [13]. In a typical coal-fired power plant, post-combustion capture of CO₂ is accomplished once combustion has occurred. Particularly, CO₂ separation unit would be normally placed after flue gas desulfurization (FGD) unit. At this stage, the low pressure (1 bar) gas stream is normally cooled down at ca. 50 °C, and features low carbon dioxide concentration (10-14%) [27].

At present, absorption of CO₂ onto liquid amines (wet scrubbing [28]) appears to be the most viable capture technique. In particular, monoethanolamine (MEA) is typically used owing to its fast CO₂ absorption rate and high capture capacity, enabling use of shorter absorption columns [29]. Absorption mechanism requires an intimate contact between the gas (i.e. carbon dioxide) and the absorbent or solvent (i.e. 30% MEA liquid solution [30]). CO₂ molecules are then trapped within the liquid solvent. A schematic flow diagram related to the post-combustion capture of CO₂ through chemical absorption was illustrated by [12]. Once CO₂ is captured, the loaded amine solution is sent to a stripping column for regeneration. This is accomplished by feeding a steam flow pre-heated at 100-200 °C in countercurrent to the desorber unit [31]. Heating process allows decomposing the intermediate compounds (i.e. carbamate or bicarbonate) formed after reaction of CO₂ with MEA [31]. Water vapor is then condensed and a highly concentrated (over 99%) CO₂ stream is obtained, which is pressurized to be ready for transport until storage site, whereas the CO₂ lean solvent is recycled back to the absorber.

Nonetheless, the use of amine aqueous solutions poses several drawbacks that hinder its industrial implementation. Firstly, the large volumes of liquid solvent require a great amount of heat for full regeneration and this decreases the energy efficiency of the power plant [32]. Moreover, amines tend to degrade over time [33], leading to a drop in their capture capacity and harmful emissions into the environment. Furthermore, the SO₂ concentration needs to be limited to ca. 10 ppm [34], as it reacts with amines to form heat-stable salts, thus reducing the absorption capacity of the solvent. Finally, the corrosive nature of the amines damages the capture unit [35].

Novel liquid solvents and process developments have been recently investigated in an attempt to tackle these issues, with specific emphasis on the reduction of regeneration energy [26, 32, 36]. However, the competitiveness of other techniques has been also examined. In particular, adsorption onto solid sorbents appeared to be the most promising scenario (see section 1.5).

1.4.1.3 Oxy-fuel combustion

The oxy-firing technique entails combusting the fuel under an oxygen/carbon dioxide mixture rather than under air. A simplified sketch of the oxy-fuel combustion system can be found elsewhere [13].

The presence of an upstream unit (i.e. air separation unit (ASU) [12]) allows separating nitrogen and oxygen. The main advantage of using an ASU is the significant reduction (50%) of NO_x emissions compared to those implied by combustion in air [37]. However, among the possible separation techniques, only cryogenic distillation seems to be an economically viable option to be applied in fossil fuel burning power plants [14, 38]. In addition to this, ASU is believed to cause an energy penalty of 15% for the power plant [24].

After N₂/O₂ separation, pure oxygen is combined with recycled flue gas rich in CO₂ prior to be sent to the combustion chamber where fuel is supplied. The addition of carbon dioxide permits the reduction of the furnace temperature to values typical of combustion chambers used in fossil-fueled power plants. Combustion then gives rise to a flue gas composed of CO₂ (75-80%), H₂O, and other trace impurities (mainly SO₂, and minimal levels of particulate and NO_x). Nevertheless, oxy-firing exhaust gas needs to go through sequential purification steps. These include: an electrostatic precipitator (ESP) for removal of particulate matter, an FGD unit to eliminate SO₂, and a final condensation stage in order to reduce water vapor down to 50 - 100 ppm. It was reported that the purification treatment required by flue gas produced after oxy-combustion is the most expensive out of all existing CO₂ capture technologies [39]. Once impurities are removed, CO₂ can reach a concentration of up to 90%. Exhaust gas rich in carbon dioxide is then dried, compressed, and further purified before transport and storage [14, 39].

The near absence of N₂ in the oxy-combustion process allows producing an outlet flue gas having high concentration of CO₂, thereby implying an easier capture step with efficiency close to 100% [14]. Despite this, oxy-fuel approach is still not mature as it has a number of shortcomings. First, technology retrofitting is hindered by the high combustion temperatures. Secondly, the large volume of oxygen needed for the process implies a high capital cost for the ASU equipment and high energy required during its operations [12]. This would then imply an overall cost as high as that of the post-combustion treatment [40].

1.4.1.4 Chemical Looping Combustion

Unlike the aforementioned techniques, this emerging process avoids direct contact between the fuel and the oxidizing agent (air or pure oxygen). An explanatory scheme of the CLC strategy was outlined by Ryden and Lyngfelt [41]. Essentially, an oxidized metal (such as Fe₂O₃, NiO, CuO or Mn₂O₃) is normally used as carrier for transferring O₂ from a first reactor (containing air) to the second unit (containing fuel) [12, 40]. This system prevents the formation of NO_x (usually produced by fuel combustion in air) in the flue gas. In fact, the reaction of the oxygen carrier (i.e. MeO) with the fuel gives rise to a gas mixture only composed by CO₂, H₂O and the reduced form of the metal oxide (i.e. Me)

[42]. Accordingly, the reduced metal oxide is recycled to the air rig to be reoxidized, whereas CO₂ can be easily recovered from the flue gas by condensation [43]. After water removal, the residual CO₂ is converted into the liquid phase by compression, and a final purity of at least 99% v/v can be obtained [44]. The metal oxidation in the air reactor generates an exhaust gas mostly composed of N₂ and any excess of air, whereas the carrier (MeO) is cycled back to the fuel chamber to ignite combustion. This loop is repeated as long as the oxygen carrier is functional.

CLC is a promising approach as it poses a series of benefits [12, 40] compared to traditional combustion, such as no energy penalty associated with the capture process [45], a higher purity of flue gas and consequent easier CO₂ separation, much lower or no NO_x emissions (as well as oxy-fuel process), and high flexibility in terms of fuel application [46].

In spite of this, this technology also implies several disadvantages [12], like a complex operation of the fluidized bed reactors and a decrease of the efficiency of the metal oxide reduction after the first cycle [47]. Furthermore, residual carbon particles, which do not combust, might lay on the metal oxide surface, thus reducing its effectiveness [46]. The commercial development of CLC is still very limited, especially because the possible integration and/or retrofitting of this technology to existing plants has not been investigated [46]. Nevertheless, significant advancements on CLC technology for different applications (CO₂ separation, fuel combustion and novel energy development) have been achieved over the recent years [42, 43, 46].

1.4.2 Post-capture steps

Although beyond the scope of this study, the current section briefly describes the post-capture stages (transport, storage and utilization), which are key features for a successful implementation of the CCS technology.

1.4.2.1 CO₂ transport

As concerns CO₂ transport, the use of carbon steel pipelines is normally the most convenient solution, unless CO₂ would need to be carried over very long distances (>1000 km) or over large bodies of water, where transport by ship may result more economical [48].

Transport efficiency by pipelines is maximized when CO₂ is held above its critical point (i.e. 31.1 °C and 74 bar), implying a stable single phase through the pipeline [48]. Accordingly, as temperature is more difficult to control, it is essential to place intermediate pumping stations along the pipelines in order to compensate pressure drops due to the hydraulic head loss. This will avoid giving rise to a two-phase (gas-liquid) which would reduce the CO₂ flow.

However, the stability of a single phase can also be negatively affected by the presence of impurities having lower critical temperature and pressure than those featured by CO₂, such as H₂, N₂, CH₄, O₂, CO and Ar [49]. These shift the pressure range wherein CO₂ is in a supercritical state, and accordingly a higher minimum operating pressure would be required to avoid two-phase flows [48].

Contaminations are also responsible for density reduction of the CO₂ flow [49]. As a result, the operating pressure required for carrying a given amount of CO₂ will increase with increasing concentration of impurities. This will cause a rise of the pipeline cost, as thicker tubes will need to be used.

Additional issues are involved by the presence of water within the CO₂ flow. For instance, moisture levels higher than 50 ppm may lead to the formation of carbonic acid, thus causing corrosion of carbon steel pipelines [50]. The presence of water vapours in the flow composition also accounts for gas hydrate and ice formation, thereby blocking pipelines and compressors. Nevertheless, their production is negligible if the water concentration is maintained below standard levels [51].

1.4.2.2 CO₂ storage and utilization

As mentioned in section 1.4.2.1, the type of carrier used to transport CO₂ will depend upon the distance between the capture and the storage site. The latter will need to be identified at an earlier stage and has to accommodate and retain CO₂ over time.

The most common practice for CO₂ storage is to inject the gas at high pressures into geological formations [48]. CO₂ is usually injected into saline aquifers, having a high storage capacity, or in oil fields, for enhanced oil recovery (EOR), which has been largely applied, especially in US, and could potentially represent the main driver for increasing the CO₂ utilization market [52].

As reported by [48], EOR has a predominant role within carbon dioxide re-use (CDR) technologies, whereas the second most extensive application of CO₂ is urea production [53]. Furthermore, CO₂ can be also potentially converted into plastics or fuels [48]. Other minor uses of CO₂ comprise: food and beverage industry (carbonation, refrigeration), pH solution control, fire extinguishers, etc.. CO₂ recycle through CDR technologies is believed to be an alternative solution to gas storage, yet the limited demand of carbon dioxide would not satisfy the substantially larger supply of CO₂.

CO₂ storage involves a high level of uncertainty in terms of secure confinement of the gas inside the underground sites. Indeed, geological and hydrogeological characterizations of the probable sites must be conducted prior to injection in order to verify its suitability for safe storage. Moreover, the

injection process has to be monitored in order to control overpressure buildup, which might cause rock failure and consequent gas escape towards the surface [48]. Although the risk of gas leakage decreases with time (i.e. overpressure due to injection dissipates, thus reducing the CO₂ mobility), further monitoring over the migration of the CO₂ plume needs to be carried out to ensure a long-term safe storage of the gas within the site.

A different option in terms of storage would be the sequestration of CO₂ through ex situ carbonation of alkali metals-containing materials (e.g. CaO, MgO) [48]. The fixation of CO₂ onto minerals would give rise to a permanent and safer storage, without requiring any subsequent monitoring [54]. Furthermore, this approach would avoid injecting CO₂ into deep underground. On the other hand, MgO and CaO are naturally found as silicates and their carbonation kinetics at room temperature is very slow [55]. Moreover, the provision of a large quantity of this type of feedstock to be used on an industrial scale would require a high amount of energy [48].

Nevertheless, as concerns the CO₂ injection into the underground, carbon dioxide can be potentially retained according to four trapping mechanisms, including physical confinement underneath an impermeable or low-permeability caprock (e.g. shale), dissolution (brine formation), precipitation (reaction with minerals to form stable carbonates), and capillarity (adhesion of CO₂ bubbles to the pore walls of the porous substrate) [56].

The research efforts in the storage field has mostly focused on the study of the aforementioned trapping mechanisms, on the migration of CO₂ plume, and on the enhancement of the fail-safe storage for a wide variety of sites [48]. However, despite several potentially secure storage volumes were identified worldwide, further work is required for the procedure standardization related to the assessment of the storage sites.

1.5 Post-combustion CO₂ capture onto solid sorbents

As earlier discussed in section 1.4.1.2, among CCS technologies, post-combustion approach is the most ready-to-use, and for this reason, it was considered in the present study.

Although chemical absorption onto liquid amines seems to be the leading option for post-combustion capture of CO₂, its scale-up is hindered by a variety of shortcoming. This has encouraged researchers to direct their attention towards alternative post-combustion approaches for CO₂ capture.

In particular, adsorption onto solid sorbents has been a focus of this research. Mangano *et al.* [57] tested various types of materials (e.g. activated carbons, silica, metal organic frameworks (MOFs), etc.) for carbon dioxide

sorption, comparing their performances with that of zeolite Z-13X (Z13X), which is the current benchmark for CO₂ adsorption. They showed that MOFs, especially those containing Mg, can offer CO₂ sorption capacities larger than that of the commercial reference.

Solid sorbents can be grouped in two broad categories, i.e. physisorbents and chemisorbents [58]. Physisorption mechanism relies on weak physical interactions between the carbon dioxide molecule and the adsorbent surface, such as Van der Waals forces [59], or other types of electrostatic forces (i.e. pole-ion and pole-pole interactions). These are caused by the interaction between the permanent quadrupole moment of CO₂ and the ionic and/or polar surface sites featured by solid adsorbents [60]. Conversely, a chemisorption process implies the formation of a covalent bond between the solid sorbent and the carbon dioxide molecule. Accordingly, physisorption is normally accompanied by a lower heat of reaction than chemisorption (less than and higher than 50 kJ·mol⁻¹ respectively [58]).

The most extensively used CO₂ solid sorbents are described in the following sections.

1.5.1 Physisorbents

The most interesting CO₂ physisorbents for post-combustion applications include: zeolites, MOFs, and ACs [12].

1.5.1.1 Zeolites

Zeolites naturally occur as aluminosilicate minerals, but they are also artificially synthesized. The typical structure of zeolite can be described as a three-dimensional tetrahedral network in which each center (atom) can either be silica or aluminium, and whose vertices are oxygen atoms bridging adjacent tetrahedral structures [61]. In particular, aluminium atom typically exists in the 3⁺-oxidation state (Al³⁺), so that aluminium-oxygen tetrahedra form centres that are electrically deficient one electron. Consequently, zeolite frameworks are typically anionic and charge is compensated with exchangeable (often alkali metal) cations in the pore space. This gives zeolite an excellent ionic exchange capacity.

Zeolite is characterized by small and uniform pores in the range of 0.5 nm to 1.2 nm [62], thus implying shape-selective catalysis [63] and molecular sieving properties. The latter allow selective adsorption of gas pollutants such as ammonia [64].

Moreover, Z13X was found to show outstanding CO₂ sorption potential [65-68]. The great affinity towards CO₂ exhibited by Z13X was ascribed to the interaction between the permanent quadrupole moment of carbon dioxide and

the electric field induced by the cations present within the zeolite network [69]. This electrostatic force outweighs Van der Waals interactions [59] typical of activated carbons. One of the main advantages associated with the use of these molecular sieves in adsorbing carbon dioxide, consists of achieving quite high adsorption capacity at mild operating conditions (0-100 °C, 0.1-1 bar), therefore being suitable for post combustion gas streams. On the other hand, the presence of impurities (NO_x, SO_x, and H₂O) significantly inhibits the zeolites' sorption performance [12]. For instance, zeolites are more hydrophilic than carbons. Accordingly, the presence of moisture in the post-combustion flue gas hinders zeolites' CO₂ capture potential as water competes with carbon dioxide for sorption sites [70].

1.5.1.2 Metal organic frameworks

MOFs are microporous crystalline solids having a 2D or 3D porous network. The latter is formed by metal-based nodes (Al³⁺, Cr³⁺, Cu²⁺, Zn²⁺, etc.) which are joined together through organic bridging ligands (e.g., carboxylate, pyridyl, etc.) [71]. MOFs have a uniform porous structure with pore diameters typically ranging between 3 and 20 Å.

A reticular synthesis [72] has been adopted to produce a great variety of MOFs. This methodology entailed combining different metals ions and organic moieties through the formation of strong bonds. The flexible and modular synthesis of MOFs allows an ample control over their pore geometry and the chemical features of their surface, thus leading to high selectivity and sorption potential [58, 73]. MOFs' surface areas reported in the literature range from 1000 to 10,000 m²·g⁻¹ [73].

The measurement of CO₂ adsorption isotherms for the Mg-based MOF-74 showed uptakes of 37 wt% at 298 K and 1 bar [74], and of 23.6 wt% at 296 K and 0.1 bar [75]. The excellent CO₂ capture performance of this sorbent was explained through the great affinity between the oxygen lone pair orbitals of carbon dioxide and the metal cations present within the structure of the MOF-74 [76]. Nevertheless, the abovementioned studies did not report any data referring to the CO₂/N₂ selectivity of the MOF-74, which is a crucial parameter under post-combustion conditions. In addition, the CO₂ sorption capacity of MOFs was found to be lower at temperature higher than 298 K [12]. This would imply cooling the flue gas down to room temperature prior to capturing CO₂ when using MOFs. Moreover, although MOFs exhibit large sorption capacity when flue gas is pressurized (i.e. pre-combustion application), their performance is poorer compared to that of other solid sorbents (i.e. zeolite, activated carbons) at atmospheric pressure (post-combustion case) [12, 58, 73]. Furthermore, the application of MOFs as CO₂ sorbents on an industrial scale is limited by additional drawbacks [73]. For instance, MOFs' synthesis is often costly and complex, and their sorption performance declines over time. In addition to that,

MOFs are negatively affected by moisture, whose absorption causes structural defects to the crystal lattice, thereby implying a reduction of their mechanical strength [12, 73]. Finally, further tests on the cyclic performance and the suitability of regeneration strategies (PSA, TSA) for these materials need to be conducted [12].

1.5.1.3 Virgin ACs

Activated carbons are well-known adsorbent materials, and, unlike zeolite and MOFs, present an amorphous structure [77, 78]. This can be seen as a disordered form of graphite (i.e. non-graphitizing carbon), wherein graphite-like sheets run parallel rather than being orientated as in the typical crystalline structure [79]. As also stated by [80], the ACs' structure can be envisaged as a twisted network of defective graphitic layers cross-linked by aliphatic bridging groups. The space between graphite layers (<2nm) constitutes the slit-shaped micropores of carbons [81], which mostly account for their exceptional surface area and adsorption properties, especially for non-polar adsorbates.

Amorphous carbons usually have different types of hybridized carbon atoms (sp^3 , sp^2 and sp^1 in some cases) within their framework, which might also include hetero-atoms such as hydrogen, oxygen, nitrogen or boron [82]. In particular, as explained in the review of Boehm [83], a number of oxygen surface functionalities can be bound to the edges of the carbon layers. ACs always contain both acidic (e.g. Lactone, Carboxyl, Carbonyl, etc.) and basic (chromene and γ -pyrone-like structures) O-based functionalities. The proportion of surface oxides will vary based on the treatments applied to produce the carbons. Moreover, inorganic fractions (ash) are also present within the carbon matrix. Ash amount and composition will be obviously affected by the nature of the precursor used for developing the carbons, and by the synthetic process (e.g. demineralization after activation). Both oxygen groups and inorganic fractions might enhance the sorption of polar adsorbates onto the carbons surface [84].

ACs can be produced in different forms, including powder, granules or pellets [85]. Pelletized carbons having regular shape are generally preferred to irregular granules for gas treatment because the former materials experience a lower pressure drop [86] and have higher mechanical strength.

Activated carbons have been extensively used for environmental applications, such as water treatment (e.g. removal of heavy metals [87] or organic matter [88]) and air purification (e.g. NO_x sorption [89, 90]). This class of solid sorbents has gained increasingly interest for CO_2 capture due to a number of benefits over the adsorbents earlier described. For instance, ACs are less sensitive than zeolite and MOFs to water [58], thereby implying a less dramatic

impact of moisture when capturing CO₂ from post-combustion gas stream. Additionally, the carbon fabrication process is more facile than that of zeolite or MOFs, and can lead to an exceptional microporous structure, with surface areas of up to 3000 m²·g⁻¹ [91] or even larger [92]. This ensures high sorption capacity, especially at high partial pressure and low temperature (i.e. pre-combustion scenario). For instance, Sevilla *et al.* [93] prepared efficient CO₂ sorbents from the KOH activation of hydrothermally-carbonized chars derived from sawdust. They reported the highest uptake ever measured (ca. 212 mg CO₂·g⁻¹) for ACs at room temperature and under pure CO₂. This excellent performance was mainly attributed to the remarkable textural properties of the carbons, with specific regard to the ultramicropore (d<0.7 nm) volume (0.52 cm³·g⁻¹).

Importantly, carbons normally exhibit high thermal stability and fast CO₂ sorption kinetics, which imply their potential application in rapid temperature swing adsorption (RTSA). In particular, Plaza *et al.* [94] successfully regenerated a commercial AC by simulating faster TSA cycles (adsorption/desorption cycle time of 14 min) as opposed to the conventional systems (regeneration time of hours [12]) for the capture of CO₂ under post-combustion conditions. Rapid TSA is considered a promising technology for the capture of CO₂ under post-combustion conditions, as it could offer some advantages over the conventional systems (e.g. PSA or TSA) [95, 96]. For instance, in contrast to PSA, RTSA does not require the pressurization of the flue gas, which hinders the economic feasibility of the pressure swing adsorption approach, especially when large amounts of gas feed need to be treated [96]. In addition to this, in comparison to traditional TSA, a faster temperature swing allows performing more frequent cycles, thus reducing the adsorption unit size (i.e. smaller amounts of sorbent would be required) and therefore its cost [95]. However, a detailed discussion on the possible adsorption/desorption configurations for post-combustion capture of CO₂ can be found elsewhere [12, 96].

In addition, the raw materials used as AC precursor (e.g. biomass [92, 97-99] or waste [100, 101]) have low-cost and are widely available. In this regard, the current study considered the use of biomass feedstock (in particular, oak wood and *Laminaria hyperborea*) for a low-cost synthesis of the activated carbons.

Further types of carbonaceous materials (i.e. activated carbon fibre, graphene, carbon nanotubes) have been recently developed and could be potentially tested for CO₂ capture [12, 58, 73]. However, the inclusion of these materials for comparison purposes was outside the scope of this work.

Nevertheless, the CO₂ sorption performance of virgin activated carbons is adversely affected by higher temperature [102] and lower gas partial pressure [58], as physisorption normally becomes ineffective under these conditions. In

addition to this, the relatively low CO₂ partial pressure in the flue gas dictates the need for high selectivity in the capture process. Accordingly, the porous structure of the carbon assumes a secondary role when looking at competitive CO₂ capture capacities under post-combustion conditions (ca. 50 °C, P_{CO₂}=0.15 bar [103]). By contrast, the effect of an increased basicity of the carbons becomes fundamental to offset the lack of physisorption performance, as it ensures a selective sorption of CO₂. Indeed, this can be achieved by exploiting the interactions between basic species (electron donor) and the acidic molecule of CO₂ (electron acceptor).

1.5.2 Chemisorbents

As highlighted above, the greater part of the solid physisorbents fails at capturing CO₂ under post-combustion conditions (i.e. low CO₂ partial pressure (0.15 bar), low total pressure (1 bar), and temperature higher than ambient (ca. 50 °C)). Thus, researchers have focused on the chemical modification of porous solid supports with the aim of introducing basic sites. The latter incorporation implies a base-like behaviour of the solid materials, thereby enhancing the affinity with the acidic CO₂ molecule. The main modifying agents used for the fabrication of basic solid sorbents are N-containing (e.g. N-rich biomass, NH₃, amines, etc.) and alkali-based (i.e. oxide, carbonates) compounds, and the relevant modification procedures are following described.

1.5.2.1 N-doped sorbents

Successful attempts at increasing the basicity of physisorbents were achieved by applying different nitrogenation methods [104]. As concerns ACs, nitrogen-based functional groups can be incorporated into the structure of the support materials through two main approaches, such as “In-situ doping” or “Post-doping” [105].

1.5.2.1.1 In situ-doping

The first route, which might be also referred as “pre-doping” (with respect to the activation stage), involves the preparation of basic solid sorbents directly from feedstock naturally containing N-based functionalities.

Particular attention was directed toward the hydrothermal carbonization (HTC) of N-rich biomass (in particular algae) as first step in the generation of ACs intended for CO₂ capture [106, 107]. HTC is a novel and sustainable carbonization technique, and biomass-based feedstock are greener and less expensive compared to other precursors (poly(aniline), melamine, etc.) [105]. In addition, co-HTC of N-rich precursors and carbohydrates (e.g. glucose) was

reported to give rise to the formation of stable aromatic N-containing compounds via Maillard reaction [108].

Nonetheless, N-modified ACs generated through the “In situ doping” method showed relatively high sorption capacity at high CO₂ partial pressure and low temperature [106], but low uptakes under post-combustion conditions [107]. Additionally, aforementioned works showed no clear correlation between CO₂ sorption capacity and N groups. By contrast, CO₂ uptake process appeared to be entirely due to the textural properties of the carbons. This might be because some of the N functionalities were inevitably removed after chemical (KOH) activation, whereas the more stable N moieties (e.g. pyridine, pyrrole, etc.) retained within the structure of the final activated carbons (i.e. after activation treatment) have a lower basicity in comparison with amines [106].

1.5.2.1.2 Post-doping

“Post-doping” methodology consists of modifying the conventionally synthesized carbons with N-containing reagents.

For instance, ACs have been extensively modified either by impregnation with liquid ammonia solution [109, 110] or by heat-treatment under NH₃ atmosphere at high temperature. The latter process is also known as amination, and further details regarding its mechanism and previous applications can be found in the review of Shafeeyan *et al.* [111]. Briefly, during the amination process NH₃ molecule decomposes to free radicals such as NH₂, NH, atomic hydrogen and nitrogen. These species then attack the carbon structure, thereby leading to the incorporation of N within the carbon framework.

Interestingly, the same group showed that, when performing a preliminary oxidation of the carbon support prior to the amination process, the CO₂ capture capacity increased [112]. Apparently, the oxygen surface groups, created during the first oxidative step, decompose when heat-treated at high temperature under ammonia atmosphere (amination), thus leading to the formation of oxygenated anchoring sites. These are then attacked by the free radicals arisen from the NH₃ breakdown, thus enhancing the development of N-based functionalities. This amination variant, referred as ammoxidation, was also applied by Plaza *et al.* [113], who reported that ammoxidized carbons exhibited larger CO₂ uptake compared to that of the parent material at 100 °C.

However, although the aforementioned reports revealed that N groups seemed to play a key role in retaining CO₂ with increasing temperature, the sorption capacity of the unmodified carbons was not significantly increased. In addition to this, CO₂ sorption was measured at high partial pressure (i.e. pure CO₂ flow and atmospheric pressure of the system), which is not representative of the realistic post-combustion flue gas. On the other hand, another study of Plaza *et al.* [114] showed that the effect of the N moieties incorporated through

amination process became more determining under simulated post-combustion conditions (i.e. $T=40\text{ }^{\circ}\text{C}$, $P_{\text{CO}_2}=0.15\text{ bar}$, and $P_{\text{tot}}=1\text{ bar}$). Nevertheless, the CO_2 uptakes attained by the aminated samples were relatively low, probably because the majority of the N-based groups introduced by amination process (i.e. amides, imides, imines and pyridine or pyrrole-like functionalities [111]) are not as effective (basic) as amines. Moreover, it is worth pointing out that treatment conditions (ammonia atmosphere, high temperature) inherent to amination and/or ammoxidation processes inevitably imply high costs and are unsafe.

Consequently, most of the research contributions have devoted their attention over the use of carbons as a substrate for amines impregnation [115, 116]. In fact, in spite of pore blockage of the solid support [117, 118] and amine leaching during cyclic regeneration [119], this nitrogenation route normally leads to dramatically larger CO_2 capacity under post-combustion conditions compared to those attained by applying the abovementioned treatments.

It is worth mentioning that the use of silica-based supports was found to outperform amine-modified carbons in terms of CO_2 capture capacity [30, 120-123]. This could be ascribed to the higher amine loading that it is possible to accommodate within mesoporous silica supports. Nevertheless, the synthesis of ACs is easier and potentially more convenient than that of silica-based materials, especially when starting from low-cost precursors (i.e. widely available biomass or waste materials). Furthermore, mesoporous silica exhibits lower thermal stability at high temperature and under moist conditions, whereas carbons are usually more thermally stable and hydrophobic [58].

In contrast to the simple physical impregnation, amines can also be immobilized through grafting methods [58]. In particular, the conventional grafting procedure (“grafting-to” [30]) entails anchoring (i.e. by covalent tethering) an aminosilane to a solid support through the use of oxides as ligands. This is achieved through a two-steps modification including a preliminary oxidation prior to amine fixation [124]. However, according to results reported in the review of Samanta *et al.* [58], amine-grafted mesoporous silica generally attain lower CO_2 sorption capacity than those achieved through physically-impregnated analogues. Conversely, the “grafting-from” approach implies the in situ synthesis (polymerization) of amine-containing polymers. As shown by [30], this technique led to unprecedentedly higher CO_2 sorption capacity (around $12\text{ mmol CO}_2\cdot\text{g}^{-1}$) under simulated flue gas conditions, and grafted samples exhibited durability over multiple working cycles. This was mostly attributed to the higher stability of the amines introduced onto the solid support through the grafting technique, which minimized the amine leaching. On the other way, as reported by [125], amine-grafted mesoporous silica require a more energy demanding regeneration (i.e. higher enthalpy of desorption) compared to that exhibited by physically-impregnated materials. In addition, grafting procedures are more complex and time consuming than physical

impregnation, thus involving a longer and costly production process of the CO₂ chemisorbents.

Therefore, a post-doping approach, with particular regard to the physical impregnation of amines, was chosen for the nitrogenation of the virgin ACs synthesized in this work.

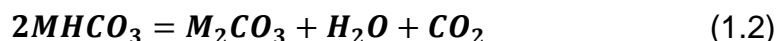
1.5.2.2 Alkali-based sorbents

1.5.2.2.1 Regenerable alkali-metal carbonates

CO₂ can be chemisorbed by using alkali-metals (in particular, Na and K) carbonates at relatively low temperature (60-110 °C) and in presence of moisture [58]. The chemisorption mechanism follows the carbonation reaction (1.1) [58], thereby leading to the formation of alkali-metal bicarbonates, which are easily regenerated through a mild temperature swing at 100-200 °C. Bicarbonates breakdown gives rise to a gas stream composed of CO₂ and water vapor (decarbonation, see (1.2) [58]). Thus, CO₂ can be easily obtained following to moisture condensation.



where, M stands for metal (i.e. Na or K)



The high theoretical capacities of Na₂CO₃ and K₂CO₃ (9.43 mmol CO₂·g⁻¹ and 7.23 mmol CO₂·g⁻¹ respectively [58]) and the relatively low enthalpy (ΔH) associated with the CO₂ sorption process (135 kJ·mol⁻¹ for Na-based carbonates and 141 kJ·mol⁻¹ for K-based carbonates [73]), make these materials particularly attractive as CO₂ captors in post-combustion applications.

The first review on the application of regenerable alkali metal-based materials as CO₂ sorbent for post-combustion capture was reported by Zhao *et al.* [126]. Na and K-based carbonates are usually embedded within various solid supports (ACs, alumina (Al₂O₃), silica (SiO₂), TiO₂, MgO, and zeolites). In particular, K₂CO₃/AC and K₂CO₃/Al₂O₃ exhibited the largest CO₂ capture capacities and the fastest carbonation kinetics out of all materials studied. The use of activated carbons as support was found to be more suitable for cyclic fixed-bed operations for the recovery of CO₂ under moist conditions, whereas the incorporation of potassium carbonated onto alumina appeared to give better performance in a fluidized-bed configuration.

The comprehensive overview of Zhao *et al.* [126] also highlighted the great interest of a variety of research institutions from all over the world in the improvement of the sorbents performance. Indeed, thanks to the moderate

operating temperature of the process and the relatively low-cost synthesis, this technique is believed to be potentially more cost-effective than the state of the art technology (30% MEA solution) for post-combustion capture of CO₂.

Nevertheless, prior to achieving the implementation of this route for the capture of CO₂ from coal-fired flue gas, a series of challenges need to be solved. These mostly refer to the influence of the process conditions (temperature, pressure, gas composition) on the CO₂ sorption capacity of the materials. Additional issues concern the continuous operation and the economic feasibility of the process. All these aspects are thoroughly discussed by [126], and ongoing research is focusing on their optimization.

1.5.2.2.2 Metal oxide carbonates

Metal oxides like CaO ([127, 128]) and MgO [129, 130] are well known to give rise to reversible chemisorption of CO₂ through carbonation/calcination cycles. Carbonation reaction normally occurs at moderate (150-400 °C for MgO [129]) or high temperature (550-650 °C for CaO [128]) and produces stable carbonates, which are then reconverted to the oxide phase through temperature swing (calcination). The calcination temperatures of CaCO₃ and MgCO₃ are ca. 750 °C and ca. 385 °C respectively [128].

Interestingly, Bhagiyalakshmi *et al.* [131] tested the CO₂ capacity of a MgO-based mesoporous carbon under post-combustion conditions. In particular, these authors incorporated MgO particles both within the carbon framework and within the pores of the support. Sorbents showed excellent recyclability and were fully regenerated at low temperature (200 °C). The reversion of MgCO₃ at low temperature was explained through the weak intensity of the chemisorption of CO₂ attained by the MgO present in the non-framework of material. Nevertheless, the capture capacity of the MgO-containing carbon was relatively low (63 mg CO₂·g⁻¹) under conditions typical of post-combustion flue gas (50 °C and P_{CO₂}=0.15 bar). This was probably because at low temperature a limited conversion of CO₂ was achieved.

2 Scientific background

2.1 Outline

The current chapter aims to review the literature relative to the materials and the methodologies used in this work.

In particular, section 2.2 briefly describes the most commonly used feedstock for the production of activated carbons (ACs).

After this, the background related to carbonization (dry pyrolysis and hydrothermal synthesis) of biomass and activation (physical and chemical processes) of biomass-derived chars (biochars) is given in section 2.3 and 2.4 respectively.

Following, section 2.5 and 2.6 report previous contributions concerning the fabrication of activated carbons starting from the precursors selected in this study, i.e. oak wood and *Laminaria hyperborea* correspondingly.

In addition to this, section 2.7 focuses on the application of biomass-derived carbons as CO₂ sorbents, with specific emphasis on those prepared starting from similar feedstock to those tested in the present work.

Furthermore, section 2.8 gives insights on the application of amine-modified solid adsorbents for CO₂ capture, directing particular attention to the wet impregnation of polyethyleneimine (PEI) onto activated carbons.

Finally, the main objectives of this thesis were defined in section 2.9.

2.2 Precursors for activated carbons production

The choice of a good candidate for conversion to activated carbon should be made by considering the following criteria [132]:

- Prospective in generating a valuable activated carbon (e.g. high carbon content);
- (Minimal) Proportion of inorganics (ash);
- (Large) Available amount and (low) cost;
- (Long) Lifetime once stored;
- (High) Easiness of activation.

Among the conventional feedstocks used for manufacturing ACs on an industrial scale, wood has been the most largely applied (see Figure 2-1). In particular, pine-derived wood accounted for more than half of the total production [132].

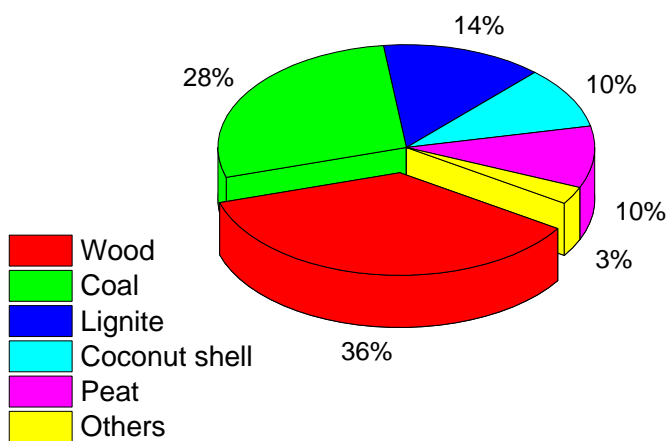


Figure 2-1 Commercial use of various precursors for ACs production

The intrinsic properties of a given raw material affect the characteristics of the resulting carbon and its applications [132]. For instance, the low density and high fraction of volatiles present within wood and lignin imply the production of light powdered carbons having large pore volume. These characteristics make the final carbons particularly suitable for removal of pollutants present within aqueous phases. By contrast, despite having a high proportion of volatiles, vegetable-derived wastes (e.g. nutshells, fruit stones) also have a high density. As a result, these kinds of raw materials normally give rise to hard granular carbons featuring high micropore volume. Granular AC are usually apt to both liquid and vapour phase applications. Similar carbons can be produced by using semihard and hard coal, and are specifically used for gas adsorption.

Nevertheless, in alternative to the use of traditional feedstocks, much attention has been given to the exploitation of waste materials because of its low cost and wide availability. In addition to this, the recycle of by-products implies a more environmentally friendly production of carbons, as it would also contribute to the disposal of waste in excess. Indeed, the increasing amount of landfilled solid waste poses a series of environmental drawbacks, such as water and soil contamination, along with localized air pollution [100]. Therefore, in an attempt to reduce waste landfilling, research has focused on alternative disposal solutions, like the reuse of by-products for the preparation of valuable materials, such as activated carbons. As reported in the review of Olivares-Marin and Maroto-Valer [100], a number of waste materials have been converted into activated carbon, which were then applied for CO₂ capture. These include: waste derived from coal utilization, wastewater treatment by-products (i.e. sludge), household residues, and biomass waste. The latter category mostly comprises agricultural residues (i.e. lignocellulosic materials), which showed great potential as precursor for the production of ACs, thanks to their low cost, large availability and relatively high carbon content [101].

On the other hand, the use of N-rich and/or alkali metals-containing precursors is highly attractive for the preparation of basic carbons suitable for

post-combustion capture of CO₂ [58, 73, 104]. For instance, compared to terrestrial biomass, macroalgae (kelp or seaweed) intrinsically contain high levels of nitrogen [133] and alkali metals [134]. In addition to this, unlike agricultural crops, cultivation of aquatic biomass (i.e. macroalgae) does not require any land. Additionally, seaweed abundantly grows in brackish and salt water. For these reasons, an extensive use of macroalgae would not imply any competition for land and fresh water, which are already utilized for food production [135].

Furthermore, seaweed species are fast growing marine and freshwater plants, and are both wildy harvested and cultivated at farm sites, thereby implying quick and wide availability along with easy access [134]. Therefore, the use of naturally grown and abundantly available biomass would allow a sustainable synthesis of carbon materials, especially on an industrial scale when large amount of precursor are required [106]. In particular, the macroalgae considered in this study is *Laminaria hyperborea* (Curvie), which belongs to the family of brown algae, and was collected from the beds found along the west coast of Scotland.

Macroalgae have been largely used for food and colloid production [136]. Moreover, the generation of macroalgae-derived bio-fuels (e.g. biogas [137], bio-oil [138]) has already been reported. In addition, investigations on the macroalgae potential for activated carbons fabrication have recently intensified [107, 133, 139-142], with few reports concerning the application of macroalgae-derived carbons as CO₂ sorbents [107, 141]. However, according to the author's best knowledge, no reports related to *Laminaria hyperborea*-derived activated carbons have been found in the available literature.

Hence, in light of this, along with a conventional biomass (i.e. oak wood), this study has devoted its attention to the utilization of macroalgae (i.e. *Laminaria hyperborea*) for the synthesis of carbon materials.

2.3 Carbonization of biomass

2.3.1 Dry pyrolysis

As defined by Maschio *et al.* [143], the pyrolysis of biomass refers to its thermal treatment in the absence of oxygen, and gives rise to three phases: solid (charcoal), liquid (tar and an aqueous solution of organics) and gaseous products.

Pyrolysis processes can be classified into three subcategories based upon the operating conditions: conventional (slow) pyrolysis, fast pyrolysis and flash pyrolysis. Process conditions (i.e. heating rate (HR), temperature, residence time, composition of feedstock, particle size) significantly affect the

product distribution obtained at the end of the treatment [143-145]. In particular, high heating rates ($1000-10000\text{ }^{\circ}\text{C}\cdot\text{s}^{-1}$ for flash pyrolysis), coupled with moderate temperatures ($<650\text{ }^{\circ}\text{C}$) and short residence times maximize the production of liquid fractions at the expense of the solid product (char). By contrast, low temperatures, slow heating rates and longer dwell times favour char formation. In addition, high temperature ($>650\text{ }^{\circ}\text{C}$) along with fast heating rates and longer residence times boost the gasification of biomass (i.e. volatiles production).

Fast and flash-pyrolysis processes are very attractive for the production of biofuels, as pyrolysis oil has a high calorific value along with typical advantages associated with liquid fuels (i.e. easy handling and storage) [144, 145]. In addition to this, pyrolysis oil fraction would imply higher energy efficiency compared to that of fossil fuelled technologies when considering smaller operational scales associated with bioenergy systems [144]. Nevertheless, as one of this study's foci was to maximize char production, low heating rate and residence time were applied (i.e. conventional pyrolysis).

As shown by Maschio *et al.* [143], the conventional pyrolysis of biomass occurs through three sequential stages. The first stage (pre-pyrolysis), taking place between 120 and 200°C , is associated with the rearrangement of the internal structure of the material mostly due to moisture evaporation, bond cleavage and formation of functional groups (carbonyl, carboxyl and hydroperoxide). Along with water vapour, CO and CO₂ are also present within gas fraction produced. The second stage represents the main pyrolysis process, which is characterized by a high reactivity, especially between 300 and $600\text{ }^{\circ}\text{C}$. The last stage concerns the material decomposition according to a very slow rate. During this final stage, biomass is continuously devolatilized due to removal of heteroatoms (mostly O and H, along with minor contributions from N and S [146]) after further breaking of chemical bonds with C. H and O-based species are removed as volatiles, and consequently the final product (i.e. char) enriches its carbon fraction. The latter results to be composed by stacks of defective (including non-hexagonal aromatic rings) graphitic layers which are randomly arranged, and the space left between them (pores) is filled by residual tar and disorganized carbon formed during pyrolysis [146]. Therefore, the porosity of the char needs to be developed (activated) through further treatments [84] (see section 2.4).

2.3.2 Hydrothermal carbonization (HTC)

Hydrothermal processes usually include liquefaction, catalytic gasification, and high-temperature gasification [147]. These occur depending upon the temperature and the pressure of the system, which affect both the state of the water (see Figure 2-2) during the reaction and the product distribution.

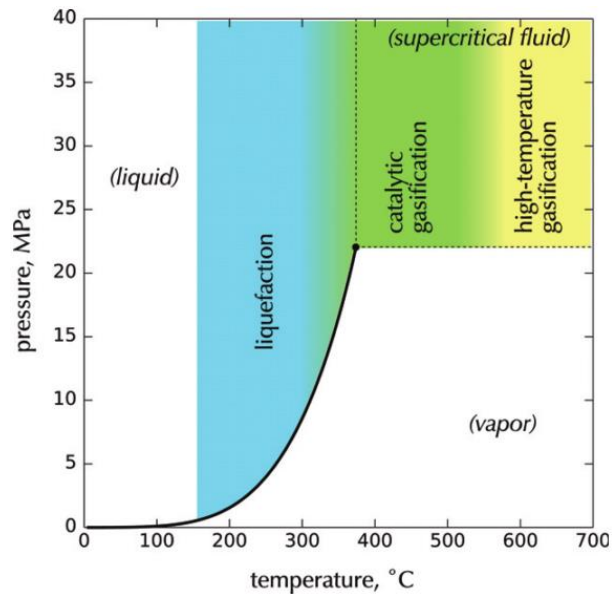


Figure 2-2 Pressure - temperature phase diagram of water with associated hydrothermal processes [147]

Specifically, liquefaction normally arises between ca. 200 and 370 °C, with pressures between ca. 4 and 20 MPa. Under these conditions, biomass is mostly converted in liquid hydrocarbons and water is in a liquid phase. However, at milder temperature (below 250 °C [148]) and relevant autogenous pressure, corresponding to the lower region of liquefaction process (subcritical water), solid fraction (char) formation is enhanced [147-149]. These operating conditions refer to the hydrothermal carbonization or also called wet pyrolysis [148, 149].

Beyond its critical point (ca. 374 °C and ca. 22 MPa) water behaves as supercritical fluid. In the supercritical region, for temperatures below 500 °C gasification occurs with the aid of a catalyst and gives rise to an H₂-rich product, whereas for temperature higher than 500 °C gasification does not require any catalytic enhancement and leads to a methane-rich gas phase [147].

This work has focused its attention on the application of HTC in subcritical water (i.e. 250 °C and relevant autogenous pressure up to ca. 40 bar) in an attempt to enhance the conversion of biomass into hydrochar (i.e. solid fraction). This was done in order to investigate the HTC potential as first step of the ACs fabrication in comparison with dry pyrolysis.

Carbonization of wet biomass (wet animal manures, municipal solid waste (MSW), algae) through HTC is particularly promising, as it can potentially lead to char yields similar to those obtained after dry pyrolysis without requiring energy-intensive drying process [149].

2.4 Activation of biochars

The activation procedure aims to develop porosity within the carbon structure of the biochars.

Depending upon the nature of the activating agent, active sites (pores) can be formed by pursuing either a physical or a chemical methodology. Note that, although activation with CO₂ or steam is considered as a chemical treatment, this methodology will be referred as physical activation throughout this chapter (and in the rest of the thesis) for convenient comparison with chemical (e.g. KOH) activation.

In addition to that, activated carbons can be produced by adopting two different configurations, namely a single step or a two steps process [84]. Regarding the first approach, carbonization and activation stages are performed at the same time. This is normally apt for chemical activation procedure, as compounds typically used favor biomass dehydration during carbonization, thus increasing the proportion of carbon at the expense of tar [84, 150]. In a typical synthesis, the raw biomass is first impregnated with a solution of the chemical agent (see section 2.4.2) prior to heat-treatment (i.e. carbonization and activation occurs simultaneously) at relatively lower temperatures (<800 °C [91]) compared to those required by physical activation [150, 151]. By contrast, the second route (two steps) entails applying the activation treatment (second step) following to the carbonization (pyrolysis or HTC, first step) of the initial precursor (i.e. biomass). This is more suitable for a physical route, as a preliminary removal of organic matter (i.e. evaporation of volatiles during carbonization) is needed in order to obtain a significant development of porosity through the activation stage [91, 150].

Despite the single-step approach involves more simple operations and lower temperatures when performing chemical activation, the two-steps method was adopted in this study for both physical and chemical route in an attempt to make a direct comparison of the activation products.

2.4.1 Physical treatment

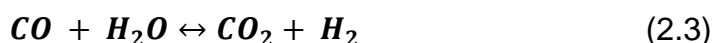
2.4.1.1 Mechanism of physical activation

Physical activation, also called partial gasification [146], is generally performed by exposing carbonized materials (chars) to steam or carbon dioxide [84, 152]. Accordingly, the carbon fraction of the chars is gradually removed (burned off as carbon monoxide, and hydrogen in presence of water vapour), thus creating porous sites. Simplified reactions related to the mechanism of physical activation are reported as follows:



Reactions (2.1) and (2.2) are both endothermic, with enthalpies of +117 KJ mol⁻¹ and +159 KJ mol⁻¹ respectively. This signifies that activation requires heat to occur. Indeed, this process is usually accomplished at high temperature (800-1000 °C [84]).

When using steam as activating agent, water vapour further reacts with CO previously formed through reaction (2.2), according to an exothermic reaction (see reaction (2.3), water gas shift reaction) which is in equilibrium and has an enthalpy of -41 KJ mol⁻¹ [84, 146].



The physical activation with CO₂ and steam also gives rise to the chemisorption of oxygen and hydrogen functionalities onto the carbon surface (see reactions (2.4) and respectively (2.5)), whose chemistry mostly depends on the temperature of formation [84].



where, C(O) represents a generic surface oxygen complex.



where, C(H) represents a generic surface hydrogen complex.

The formation of oxygen and hydrogen functionalities is an intermediate step during the activation process. O and H complexes compete with CO₂ and H₂O for carbon surface sites, thus decreasing the reaction kinetic. Activation mechanism is also inhibited by the amount of reaction products (CO and H₂) [84].

Overall, activation process occurs through two main stages [132]. First, tar and disorganized carbon are burnt off, thus unblocking the pores of the char. After this, activation proceeds by attacking the aromatic carbon rings, thereby causing the formation of additional pores and the widening of existing interstices.

Literature data concerning the influence of the main parameters (i.e. activating agent, activation temperature and reaction dwell time) affecting the physical activation of chars are reported in the following sections.

2.4.1.2 Effect of activating agent

Previous reports [152, 153] found that, for a similar temperature, activation kinetic with steam (see reaction (2.2)) was faster than that achieved when using CO₂. This would suggest that steam activation might require the application of a lower intensity of activation (i.e. lower temperature/shorter durations) in order to achieve the same efficiency. This was confirmed by results reported by [154]. As stated by Wigmans [146], the higher reactivity of steam was ascribed to the smaller dimension of the H₂O molecule compared to that of carbon dioxide, whose diffusion through the carbon porous structure is slower [155] and limited to larger pores (i.e. restricted access to micropores) [156]. The lack of diffusion of carbon dioxide within the smaller pores was corroborated by experimental results reported by Wigmans [146], who measured a moderately higher development of mesopores when activating carbonized peat with CO₂ compared to that attained through activation with steam.

As reported by Kuhl *et al.* [157], the influence of the activating agent (CO₂ or steam) on the porosity of coke-derived carbons appeared to be affected by the type of pre-treatment of the precursors.

The influence of the activating agents on the porosity evolution of olive stone-derived chars was investigated by Rodriguez and Molina [152]. These authors compared activated carbons obtained through activation with carbon dioxide and steam. Activation with water vapour was performed under different conditions, by varying the temperature and/or the concentration of the activating agent. Essentially, Rodriguez and Molina found higher activation rates when using steam, but higher proportion of micropore volume for the CO₂-activated carbons, which is in contrast to the expected behaviour proposed by Wigmans [146]. In particular, for a common carbon burn-off, the use of water vapour generally implied a widening of the entire fraction of microporosity since the beginning of the process, whereas CO₂ caused a first opening of the ultramicropores ($d < 0.7$ nm), which were following widen to form supermicropores ($d < 0.7$ nm). In addition to that, carbons activated with CO₂ exhibited larger microporosity than that of steam-activated carbons, especially when using a pure water vapour atmosphere and lower activation temperature. Furthermore, steam-activated carbons presented a broader pore size distribution with more marked contributions from meso and macropores, whereas CO₂-ACs mostly contained micropores.

Rodriguez and Molina [152] attempted to interpret their observations by proposing two different explanations. First, the easier and faster access of the water molecule (smaller than carbon dioxide) to the narrower micropores of the carbonized material might cause their widening at the earliest stage of the process. On the other hand, another possible theory is related to the fact that CO₂ activation leads to the creation of a higher amount of oxygen surface

functionalities compared to those attained by steam. Specifically, O-based groups chemisorbed onto the carbon surface at the beginning of activation process (i.e. when burn-off is low and pores are small) tend to shrink the accessible pore width, thus promoting a selective enhancement of the narrow microporosity. The second assumption was validated by a subsequent study of Molina *et al.* [153], wherein a similarity between porosity and surface functionalities (assayed by measuring CO concentration) evolution was highlighted. In particular, a higher amount of functional groups was measured for the CO₂-activated carbon, which had the largest volume of micropores. This was explained through the fact that the greater part of the carbon surface groups are usually chemisorbed onto the walls of the active sites (micropores).

A larger narrow microporosity for CO₂-activated carbons was also measured by Pastor-Villegas and Durán-Valle [158] when activating rockrose-based chars, especially at low temperature (700-800 °C). By contrast, microporosity was found to be independent of the activating agent at higher temperature because of an increased kinetic reaction.

On the other hand, controversial results concerning the effect of the activating agent on the porosity development of the chars were reported in the literature [91, 154, 158, 159]. However, most of these studies did not include a systematic comparison between steam and CO₂-activated carbons in terms of porosity distribution. Therefore, based on the more reliable analysis carried out by [152, 153], carbon dioxide was selected as oxidizing agent for the physical activation of the biochars tested in an attempt to maximize the narrow microporosity. Hence, literature review regarding the effect of activation temperature (section 2.4.1.3) and duration (section 2.4.1.4) focuses on the CO₂ activation treatment.

2.4.1.3 Effect of CO₂ activation temperature

Higher temperatures normally correspond to increased intensities of the activation treatment. Sánchez *et al.* [160], who CO₂-activated oak wood-derived chars at 800, 840 and 880 °C, plotted the carbon yield versus the activation time for each temperature series. Results showed that, for a given dwell time, the higher the activation temperature, the lower is the carbon yield. In addition to this, the decreasing rate (slope) exhibited by the carbon yield was proportional to the activation temperature. This was corroborated by the gasification rate (defined as the carbon burn-off in the given residence time, i.e. wt%·h⁻¹) which was plotted against the normalized time (i.e. residence time divided by the longest time interval studied). In particular, for each value of dwell time, gasification rate appeared to increase with activation temperature. This signifies that, for the same activation duration, a higher temperature condition allows having a faster degree of carbon removal. The effect of the temperature on the porosity development of the oak wood chars was not

directly assessed. Nevertheless, 840 °C was found to be optimal in terms of surface area and micropore volume (these parameters seemed to be directly related). On the other hand, 800 °C was found to be optimal in terms of ultramicropore volume ($d < 0.7$ nm), whose maximum value was achieved at the lowest intensities of activation (i.e. highest activation yields (>60 wt%)).

Zhang *et al.* [161] applied the CO₂ activation method to chars derived from agricultural and forest residues (i.e. oak wood waste, corn hulls, and corn stover). Chars were activated both at 700 and at 800 °C. Overall, the largest surface area and micropore volume were found at the highest temperature studied. These findings agreed with those obtained by Lua and Guo [162], who performed CO₂ activation of oil-palm shell-derived chars and reported an optimal temperature of 900 °C in terms of surface area. Moreover, Zhang *et al.* [161] noticed that the effect of the activation temperature on the microporosity (i.e. ratio of micropore volume to total pore volume) of the carbons depended upon the type of precursor used for their production. Specifically, for a given activation duration, micropore fraction increased with increasing temperature for corn hulls-based carbons, whereas decreased for the other samples, thus indicating micropore widening at higher temperature.

González *et al.* [154] activated tyres-based chars with CO₂ at three different temperatures (750, 800 and 850 °C). Surface area and microporosity generally increased with increasing temperature, which agreed with above-mentioned contributions

2.4.1.4 Effect of CO₂ activation dwell time

Most of the studies mentioned in section 2.4.1.3 also assessed the effect of the dwell time on the CO₂ activation process. For instance, for each temperature investigated, Sánchez *et al.* [160] varied the severity of the activation treatment (i.e. carbon yield ranging between 18 and 85 wt%) by changing the residence time (from 45 to 300 min). At the same temperature, the overall gasification rate (i.e. carbon yield) linearly decreased with increasing holding time, as activation degree (carbon burn-off) was found to be proportional to the duration of the treatment. Similar trends were also reported by González *et al.* [154], suggesting a constant rate of reaction between chars and CO₂ throughout the process. In spite of this, at the lowest temperatures (800 and 840 °C), Sánchez *et al.* [160] found a different trend when plotting the normalized gasification rate (divided by the relevant residence time) against the normalized dwell time (divided by the highest holding time considered). In fact, the decay of the carbon conversion rate appeared to be higher for lower dwell times (up to 60% of the highest duration studied), whereas a less appreciable drop was observed afterwards. This led to infer that at the lowest temperatures, further increase of duration did not significantly increase the carbon burn-off. This behaviour was emphasized when normalizing the gasification rate by the

exposed Brunauer–Emmett–Teller (BET) surface area (i.e. the surface including available sites for reaction with CO₂). The decrease of reactivity with increasing dwell time was associated with the retarding effect due to the formation of surface carbon/oxygen complexes during the early stage of the CO₂ activation process [84]. These tend to deactivate (occupy) a significant portion of reaction sites, thereby impeding access of CO₂ and then delaying the activation mechanism.

Sánchez *et al.* [160] also showed that, for any activation temperature, microporosity generally increased with increasing residence time (i.e. decreasing carbon yield). Conversely, mesoporosity continuously increased with increasing activation time only at the highest temperatures (840 and 880 °C), whereas at the lowest temperature (800 °C) showed a decreasing trend at the highest intensities of activation (carbon yield < 50 wt%). Nevertheless, at 840 °C (i.e. optimal temperature, see section 2.4.1.3), an holding time of ca. 2 h (corresponding to a carbon burn-off of ca. 68.3 wt%) maximized surface area and microporosity development of the chars. This result was fairly consistent with that found by González *et al.* [154], reporting an optimal dwell time of 3 h (at 850 °C). Moreover, for each given temperature, the narrow micropore:total micropore volume ratio decreased with increasing activation yield (i.e. longer holding time), as ultramicropores were enlarged to form supermicropores ($d > 0.7$ nm) at the highest degrees of activation (longest activation durations).

As shown by Zhang *et al.* [161], the influence of the activation dwell time on the porosity of CO₂-activated carbons resulted to be sample-dependent. In particular, regarding oak wood chars, porosity remained constant (at 700 °C) or increased (at 800 °C) with increasing activation duration. In contrast, a longer residence time had a deleterious effect on the texture of the activation carbons derived from the other precursors tested (i.e. corn-based chars). This might have occurred because, with increasing degree of activation (i.e. treatment duration), the rate of porosity widening/collapsing outweighed that of porosity development.

2.4.2 Chemical treatment

Among the great variety of chemicals that can be potentially used for chemical activation, ZnCl₂, H₃PO₄ and KOH are the most largely applied on an industrial scale [84]. Molina-Sabio and Rodríguez-Reinoso [163] compared the effect of these three chemicals on the one-step activation of lignocellulosic materials (i.e. olive and peach stones). When loading was optimal, these authors reported an outstanding enhancement of microporosity, which was independent of the type of reagent used. On the other hand, at high intensity of treatment (i.e. high chemical loading) the development of porosity resulted to be affected by the type of activating agent. This was mostly ascribed to the different activation mechanism involved by each chemical. However, it worth

mentioning that the use of the first two reagents (ZnCl_2 and H_3PO_4) is less environmentally friendly due to eutrophication issues involved by Zn and P [84, 164].

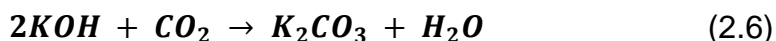
In addition to the aforementioned activating agents, alkali-metals-based compounds other than KOH (i.e. K_2CO_3 [141], NaOH [165], Na_2CO_3 [166]) were effectively used for the production of chemically-activated carbons. On the other hand, reviewing literature revealed potassium hydroxide as one of the most effective activating agents out of the alkali metals-based compounds [150, 167-169]. In addition, KOH was successfully applied for the chemical activation of precursors similar to those examined in this work (wood, algae) [93, 106, 141, 142, 169-171].

Under these premises, KOH was chosen for the preparation of chemically-activated carbons produced in this study. In addition to this, results published by Fierro *et al.* [172] supported the decision of applying a two-steps process also for the chemical activation procedure. In fact, these authors reported that the two-steps KOH activation of biomass (rice straw) led to higher carbon yield and larger surface areas of the resulting ACs compared to those achieved through a 1-step route.

Following subsections attempt to give further information concerning the mechanism of reaction with KOH and the influence of the main parameters affecting the KOH activation procedure (i.e. activation temperature and chemical ratio [150]).

2.4.2.1 Mechanism of chemical activation with KOH

According to the standard chemical activation process, biomass (single step) or char (two steps) is first impregnated with an aqueous solution of the activating agent prior to heat-treatment under nitrogen. However, this would imply a preliminary drying step in air. This, as clearly demonstrated by Illingworth [168], leads to a preliminary carbonation of KOH according to reaction (2.6):

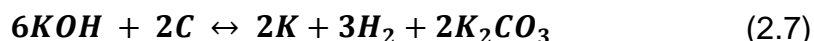


As a result, part of the potassium hydroxide will not be available for reaction with the carbon matrix of biomass (single step) or char (two steps) during the actual activation process (i.e. heat-treatment under N_2), therefore leading to a less dramatic improvement of texture. In particular, Illingworth [168] found larger porosity development for a KOH-impregnated carbon dried under vacuum compared to that measured for the same sample air dried for longer time.

By contrast, an alternative procedure was followed by Fierro *et al.* [169], who ground and physically mixed KOH lentils with raw lignin prior to heat-

treatment. Although these authors did not compare the adopted methodology (i.e. dry physical mixing) to the conventional technique (wet impregnation), final carbons with outstanding surface areas (up to 3000 m² g⁻¹) were obtained, thus demonstrating the efficiency of the former procedure.

Nevertheless, regardless of the chemical addition process, during heat-treatment under N₂ potassium hydroxide attacks the carbon structure that is then oxidized to potassium carbonate (see reaction (2.6)). Additionally, as explained by the global reaction (2.7) proposed by Lillo-Rodenas *et al.* [167, 173], other products such as potassium metal and hydrogen are formed.



Moreover, it is worth mentioning that a secondary activation contribution might arise from the potassium carbonate produced during heat-treatment. In particular, as described in the review of McKee [174], alkali carbonates have a catalytic effect on the gasification reaction occurring between carbon and oxidizing agents (e.g. oxygen, steam or CO₂) formed at the early stage of the heat-treatment. Further details regarding the mechanism of activation with potassium hydroxide are given in the work of Illingworth [168] and reference therein.

2.4.2.2 Effect of KOH activation temperature

Experimental tests conducted by Evans *et al.* [175] revealed that an activation temperature of 400 °C (just above the KOH melting point (i.e. 360 °C)) was insufficient to develop any increase of the surface area of a sucrose-derived char. This was attributed to the fact that, although already melted and penetrated through the char, KOH had not started to react with carbon at such low temperature. In contrast, Evans *et al.* observed that the KOH/char mixture began to release some gaseous products when heated at 540 °C, which could be considered as the onset temperature for chemical activation with KOH. This was largely consistent with results reported by Illingworth [168], who observed most of the porosity development between 450 (onset temperature) and 650 °C when activating pyrolyzed flax fibre with KOH. Illingworth [168] also highlighted that, at the lowest activation temperatures (450-650 °C), micropore development was the main feature of the process, whereas, at higher temperatures (over 700 °C), an enlargement of micropores previously formed at lower temperature occurred. This was ascribed to an increase of severity in the gasification reaction of carbon (i.e. micropore walls) with increasing temperature.

Correlation between porosity evolution and activation temperature found by Illingworth generally agreed with that showed in other studies. For instance, Carvalho *et al.* [176], who chemically-activated cork waste with KOH, reported

that mostly narrow micropores were created between 500 and 700 °C, yet these were widened to form supermicropores at higher temperatures. A decrease of narrow microporosity with increasing activation temperature was also observed by Sevilla *et al.* [93], who KOH-activated some sawdust-based hydrochars. In this study, the authors showed that the knee of the samples' isotherms became broader as activation temperature increased, especially between 700 and 800 °C. Sevilla *et al.* also highlighted a shift in the mode of the samples' pore size distributions with increasing temperature, thus enlightening porosity widening. In another work, the same group [106] measured an increase of average pore width along with a broadening of the pore size distributions with increasing activation temperature when chemically activating microalgae/glucose-derived hydrochars with KOH. On the other hand, for a common chemical ratio of 4, microporosity (and surface area) continuously increased with increasing temperature (from 650 to 750 °C), while ultramicroporosity declined in favour of supermicroporosity.

Oh and Park [177] KOH-activated rice-straws by applying either a one stage or a two stages process and activation temperatures between 500 and 900 °C. As concerns carbons obtained through a two steps route, these authors showed a type I-isotherm when activation temperature was 600 °C, indicating mostly micropores in the porous structure of the carbon. On the other hand, when increasing temperature from 600 to 900 °C, the opening of the isotherms' knee and the appearance of hysteresis loop was observed, thereby suggesting the formation of mesoporosity at the expense of micropores. N₂ adsorption data agreed with those reported by Sevilla *et al.* [93].

The same range of activation temperatures (500-900 °C) was applied by Guo and Lua [178], who obtained chemically-ACs by impregnating palm shell with KOH solutions at different stages. Regardless of the impregnation technique, carbon yield continuously declined with increasing temperature, whereas surface area increased up to 800 °C. The decrease of surface area between 800 and 900 °C was ascribed to the micropore walls burn-off, which led to the formation of meso and macropores.

2.4.2.3 Effect of KOH:solid ratio

Similar to the influence of a higher activation temperature (see section 2.4.2.2), a larger chemical (KOH) addition normally involves a more severe activation treatment. Lozano-Castello *et al.* [167] KOH-activated anthracite-based chars by mixing these with different amount of chemical (KOH:char ratios of 1 to 5). Surface area and microporosity significantly increased with increasing chemical ratio up to a value of 4. On the other hand, a further increase of chemical ratio from 4 to 5 caused a moderate detrimental effect on the textural parameters. In the same study, the authors also noticed a visible broadening of

the knee of the type I isotherms exhibited by all samples with increasing KOH:char ratio. This was attributed to the enlargement of micropores.

Results showed by Lozano-Castello *et al.* were largely consistent with a number of other contributions found in the literature [78, 93, 106, 176]. In particular, Sevilla *et al.* [93] used a KOH:char of 2 (defined as mild activation) or 4 (defined as severe activation) for the chemical activation of sawdust-derived hydrochars. Essentially, for a given temperature, mild activation (i.e. lower chemical addition), gave rise to lower surface areas but higher ultramicroporosity. By contrast, severe treatment (higher KOH:char ratio) maximized the surface area but led to a broader pore size distribution, including larger contributions from meso and macropores. The same group drew similar conclusions in another study [106], wherein the authors activated microalgae/glucose-derived hydrochars using KOH:char ratios of 1, 2 or 4. It is worth noticing that, when considering a temperature of 700 °C, the ultramicropore volume remained constant as chemical ratio increased from 1 to 2. This was probably due to the mild condition of activation. On the other hand, a decrease of narrow micropore volume (widened to form supermicropores) was recorded when further increasing KOH:char ratio from 2 to 4.

In general, a higher KOH:precursor ratio leads to greater overall porosity and surface areas, but to a more heterogeneous pore size distribution. In contrast, lower KOH:solid ratios tend to maximize microporosity, with particular regard to its ultramicroporous fraction.

2.5 Preparation of activated carbon from oak wood

2.5.1 Carbonization of oak wood

2.5.1.1 Pyrolysis of oak wood

Traditional pyrolysis of wood was extensively applied. However, only the most relevant contributions concerning pyrolyzed oak are following reported [160, 161, 179, 180]. Specifically, Sanchez *et al.* [160] carbonized *Quercus agrifolia* wood waste at different temperature (450, 800, 840 and 880 °C) for 2 h in a steel furnace. In this study, the authors reported a decrease of the carbonization yield with increasing temperature. In particular, at 800 °C, a product yield of 26 wt% was measured.

Zhang *et al.* [161] performed a fast pyrolysis of oak wood at ca. 500 °C into a fluidized sand-bed reactor. The wood-based residue was fed to the reactor at a rate of 7 kg·h⁻¹. Despite the mild carbonization, a very low product yield (10 wt%) was recorded for oak wood char. This might be ascribed to the rapid heating process, which may have adversely affected the carbonization yield [181].

Holm and Pyrenean oak were pyrolyzed at 600 °C by Lopez *et al.* [180] in a pilot scale rig. These authors stated that lignin fraction mostly affected the char formation, which was ca. 30 wt% for oak-derived products. It is worth mentioning that pyrolysis was performed in presence of oxygen, which might have contributed to lessen the product yield.

Moreover, Jindo *et al.* [179] carbonized oak tree (i.e. *Quercus serrata* Murray) at different temperatures (from 400 to 800 °C) at a heating rate of 10 °C·min⁻¹ in a ceramic tube furnace. Final temperature was held for 10 h. As expected, this study reported decreasing char yield with increasing pyrolysis temperature. In particular, the product yield after carbonization of raw oak declined from 35.8 wt% (400 °C) to 19.1 wt% (800 °C). In addition to that, the volatile matter was also found to decrease with increasing intensity (i.e. temperature) of carbonization.

It is worth pointing out that all of the abovementioned works, except [179], were finalized to the production of activated carbons.

2.5.1.2 HTC of oak wood

The use of wood-derived biomass (sawdust) for the production of hydrochars was reported in a series of contributions [93, 182, 183]. In addition, hydrothermal carbonization of wood meal (i.e. consisting of a mixture of lignin, cellulose, and hemicellulose), and other types of lignocellulosic feedstock was also performed [184-186]. Temperature and dwell time applied in these studies ranged between 180 and 295 °C, and between 5 and 120 min respectively. In particular, Hoekman *et al.* [185] studied the influence of temperature and dwell time on the hydrochar compositions and on the product yields. In particular, gaseous phase and water production were found to increase with increasing severity of the process (i.e. higher temperature, longer holding time), whereas the solid fraction declined. Furthermore, HTC (200-260 °C) of pine wood was applied by Reza *et al.* [187] as pre-treatment for the preparation of biochars pellets.

However, as concerns oak, few investigations on the application of HTC treatment emerged from the literature survey [188-191]. For instance, Konara oak wood was hydrothermally-treated by Inoue *et al.* [188], who reported an increase of energy density of 11-73% for the hydrochars compared to that of the raw feedstock. Hydrochar energy density generally increases with increasing intensity of the treatment (i.e. more severe temperature, longer residence time), as a result of the increase of the C/O ratio [185].

HTC of oak material was frequently applied as pre-treatment. Specifically, Ishibashi *et al.* [189] examined the influence of the preliminary hydrothermal treatment on the carbonization behaviour of sawtooth oak. Apparently, HTC was found to affect the shrinkage and the formation of carbon

crystallites during the subsequent carbonization step of the woody biomass. The use of HTC as pre-treatment was also pursued by Carrasco *et al.* [190], where oak wood was heat-treated at 230 °C for 4 min. In this case, the preliminary HTC was referred as steam explosion and was applied in an attempt to increase the decomposition (i.e. hydrolysis by dilute acid) kinetic of the cellulose present within raw oak wood. Moreover, a similar application was reported in the study of Szczodrak *et al.* [191], who tried to exploit the effect of HTC to enhance the enzymatic hydrolysis of cellulosic fraction contained within raw oak sawdust. The latter was heat-treated at 200 °C for 10 min.

Note that none of the aforementioned studies referred to the application of HTC of oak as first step of the preparation of activated carbons. On the other hand, it is worth mentioning that, as reported by Salvador *et al.* [192], high-temperature (525-775 °C) HTC (i.e. gasification with supercritical water (SCW)) of pyrolyzed oak wood was successfully applied as activation method, giving rise to carbons featuring an heterogeneous distribution of micropores and a minor presence of mesopores.

2.5.2 Activation of oak wood-derived chars

2.5.2.1 CO₂ activation of oak wood-derived chars

Previous studies related to the optimization of CO₂ activation of pyrolyzed wood were reported. In particular, Sanchez *et al.* [160] heat-treated pyrolyzed wood waste under a CO₂ flow rate of 500 cm³·min⁻¹. As already discussed in detail in section 2.4.1.3 and 2.4.1.4, these authors studied the effect of the activation temperature (800, 840 or 880 °C) and of the residence time (between 45 and 300 min). Optimal conditions were found to be 840 °C and ca. 2 h, corresponding to a burn-off of 68.3 wt%. These conditions led to maximum values of surface area and micropore volume of ca. 1200 m²·g⁻¹ and ca. 0.5 cm³·g⁻¹ respectively.

In addition to this, oak wood waste was pyrolyzed and CO₂-activated by Zhang *et al.* [161]. In this study, char was heat-treated at 700 or 800 °C for 1 or 2 h. In this case, BET surface area of up to 985 m²·g⁻¹ and micropore volume of up to ca. 0.38 cm³·g⁻¹ were achieved at activation temperature of 800 °C and dwell time of 2 h, corresponding to a burn-off of 51.4 wt%.

Two different types of oak wood (Pyrenean and Holm) were physically activated by using CO₂ (flow rate of 74 cm³ min⁻¹) at 800 °C for 6.5 h by López *et al.* [180] after conventional pyrolysis at 600 °C. Surface areas measured for activated derivatives were 722 and 557 m²·g⁻¹ respectively.

Oak-derived cork (i.e. *Quercus suber* L.) was also used as feedstock for the preparation of CO₂-activated carbons [193]. Specifically, after pyrolysis at 750 °C, Mourao *et al.* [193] heat-treated the cork-based char at 750 °C under

CO₂. The activation temperature was held for two different dwell times corresponding to burn-offs of 23 and 48 wt%. The highest carbon burn-off gave rise to the largest surface area (ca. 957 m²·g⁻¹).

The textural development of the CO₂-activated oak obviously depended upon the different activation conditions (temperature and dwell time) applied, which imply various degree of burn-off. In general, temperatures between 750 and 840 °C appeared to be suitable for the heat-treatment of pyrolyzed oak under CO₂.

However, according to the author's best knowledge, the CO₂ activation of hydrothermally-carbonized oak has not been investigated yet. In spite of this, it worth pointing out that Ishibashi *et al.* [194] recently applied hydrothermal carbonization of two different kinds of oak wood (i.e. *Quercus acutissima* Carruth. and *Quercus serrata* Thunb.) as pre-treatment prior to performing dry pyrolysis and carbon dioxide activation. Interestingly, these authors showed that HTC favoured the formation of mesoporosity in the final CO₂-activated carbons.

Therefore, the application of CO₂ activation directly on oak wood-derived hydrochars (i.e. without applying any pyrolysis step) has been performed in this research for the first time (see Chapter 4). In addition, this work has also contributed on the influence of the main parameters (temperature and holding time) on the textural properties of the physically-activated hydrochars.

2.5.2.2 KOH activation of oak wood-derived chars

Different oak derivatives were used as precursor for the preparation of KOH-activated carbons [195-197]. In particular, Zyzlila Figueroa-Torres [195] physically mixed *Quercus agrifolia*-based char with KOH powder (KOH:char of 4) prior to heat-treatment under N₂ at 760 °C in a rotary batch. The influence of the N₂ flow rate was also investigated. A flow rate of 250 cm³·min⁻¹ appeared to maximize all textural parameters of the final carbons, except the mesopore volume.

In addition to this, cork powder (i.e. oak wood residue) was chemically activated with KOH in the study of Cardoso *et al.* [196]. Raw cork was first demineralized with a 10% aqueous solution of H₂SO₄ in order to reduce the ash content of the material. After this, pre-treated cork powder was impregnated with an aqueous solution of KOH (25% (w/w)) according to KOH:solid ratios of 0.25, 0.5, and 1. KOH/cork mixture was then heat-treated under nitrogen flow (2 cm³·s⁻¹) according to a determined temperature programme. Activation temperatures (500, 600, 700, and 800 °C) were hold for 2 h. Following to chemical activation, samples were washed with water until measuring a pH of 7. Largest values of surface area (1300 m²·g⁻¹) and micropore volume (0.56 cm³·g⁻¹) were attained when using the highest chemical ratio (1) and temperature (800 °C).

Moreover, the use of cork oak (*Quercus suber L.*) waste for the production of KOH-activated carbons was tested by Mourao *et al.* [197]. In particular, these authors blended the raw oak residue with solid potassium hydroxide according to a KOH:cork mass ratio of 2. The KOH:precursor mixture was then pyrolyzed under nitrogen (flow rate $85 \text{ cm}^3\cdot\text{min}^{-1}$) at $700 \text{ }^\circ\text{C}$ for 2 h. After heat-treatment, chemically-activated carbons were washed until complete removal of potassium hydroxide in excess. Chemically-activated cork had a surface area of $1616 \text{ m}^2\cdot\text{g}^{-1}$ and a micropore volume of $0.61 \text{ cm}^3\cdot\text{g}^{-1}$.

However, all of the aforementioned studies referred to the chemical activation of raw oak (1 stage) or its pyrolyzed counterpart (2 stages). By contrast, to the best knowledge of the author, no study on the KOH activation of hydrothermally oak has been reported in the open literature. In light of this, the potential of the oak-derived hydrochars for the production of KOH-activated carbons has been first investigated in this work (see Chapter 4).

2.6 Synthesis of activated carbons from *Laminaria hyperborea*

2.6.1 Carbonization of macroalgae

2.6.1.1 Pyrolysis of macroalgae

The pyrolysis behaviour of *Laminaria hyperborea* was previously studied with the aim of characterizing the composition of macroalgae [198, 199]. In particular, Ross *et al.* [198] pyrolyzed *Laminaria hyperborea* before and after demineralization using the pyrolysis-Gas Chromatography/Mass Spectrometry (GC/MS) technique. Flash pyrolysis of raw and pre-treated (demineralized) seaweed was performed at $500 \text{ }^\circ\text{C}$ at a heating rate of $20 \text{ }^\circ\text{C}\cdot\text{ms}^{-1}$. The final temperature was held for a dwell time of 20 s. The analysis of the pyrograms indicated the presence of a series of compounds within the raw macroalgae, such as ketones, pentosans, phenols, and N-containing species. In addition to this, the solid fraction (char) decreased after demineralization, thus confirming the beneficial effect of inorganics at increasing char formation [134, 181, 200, 201]. A similar study was conducted by another group [199], that identified the four main carbohydrates present within *Laminaria hyperborea* (i.e. alginic acid, fucoidan, laminarin and mannitol) using pyrolysis products as markers.

The carbonization of other types of *Laminaria* was also reported in the literature [138, 202]. For instance, Bae *et al.* [138] carbonized *Laminaria japonica* at temperature ranging from 300 to $600 \text{ }^\circ\text{C}$ for 1h in a packed tube reactor. The char yield was found to decrease with increasing temperature from values in excess of 50 wt% ($300 \text{ }^\circ\text{C}$) to ca. 40 wt% ($600 \text{ }^\circ\text{C}$). However, the objective of Bae's study was to produce macroalgae-derived bio-oil.

A far lower char formation was recorded by Stratford *et al.* [202] when pyrolyzing *Laminaria digitata* (oarweed) at 800 °C in a muffle furnace. Yet, in this case, the product yield was determined considering the solid residue following to pyrolysis and acid washing. The latter likely caused the removal of inorganic matter. Interestingly, macroalgae experienced a significant development of porosity after pyrolysis, leading to seaweed-based chars with very high surface area (up to ca. 1500 m²·g⁻¹). This result suggested that further activation treatment of the char could be avoided. In the same report, Stratford *et al.* showed an approximate correlation between the textural properties of the seaweed-derived chars and the overall inorganic content of raw macroalgae, thereby suggesting that ash (with specific regard to K) seemed to act as activating agent. In addition to this, Song *et al.* [133] successfully applied pyrolysis as 1-step production (no subsequent activation) of porous carbons starting from macroalgae (i.e. *Undaria pinnatifida*). These authors pyrolyzed seaweed at temperature ranging from 800 to 1100 °C for 5 h, and pyrolyzed products were acid (HCl) washed (demineralization). The maximum surface area (in excess of 1200 m²·g⁻¹) was attained when pyrolysis temperature was 1000 °C.

Additionally, Ferrera-Lorenzo *et al.* [203] performed the pyrolysis of a macroalgae (*Gelidium sesquipedale*)-derived solid waste to produce a biochar as precursor for activated carbon preparation. In particular, these authors pyrolyzed seaweed in a horizontal tubular furnace at 750 °C for 1 h, using a heating ramp of 5 °C·min⁻¹. Pyrolysis conditions were considered optimal for the production of char (yield of ca. 30 wt%) to be subjected to following activation. Indeed, the same group reported the application of this macroalgae-derived char for the production of chemically-activated carbons in further studies [141, 142] (see section 2.6.2). The two-steps synthesis (i.e. including activation) led to a far higher surface area (up to 2118 m²·g⁻¹) than those obtained after pyrolysis of other kinds of macroalgae.

Nevertheless, the literature search revealed that there is a gap in knowledge regarding the pyrolysis of *Laminaria hyperborea* as first step for activated carbon production. Therefore, further investigation on this aspect is presented in this work (see Chapter 5).

2.6.1.2 HTC of macroalgae

Only one study related to the hydrothermal treatment of *Laminaria hyperborea* was found in the literature [204]. However, in this study Cherad *et al.* carried out HTC under supercritical water conditions (i.e. 600 °C and 35 MPa), corresponding to a gasification regime. Indeed, the scope of their work was to assess the influence of a set of parameters on the gasification behaviour of *Laminaria hyperborea*.

On the other hand, hydrothermal carbonization of macroalgae (other than *Laminaria hyperborea*) was reported in a series of contributions [107, 205-208]. For instance, Xu *et al.* [207] performed HTC for a mixture of seaweed (*Sargassum horneri*) and citric acid (used as catalyst) at temperatures ranging from 180 to 210 °C and dwell times of 2 to 16 h. These authors examined the effect of different reaction parameters on the physiochemical characteristics of the macroalgae-derived hydrochars.

Moreover, Anastasakis and Ross [206] heat-treated *Laminaria saccharina* at 250 °C for 15 min, with a solid fraction (hydrochar) yield of ca. 25 wt%. Yet, this group was mostly interested in the bio-oil production, and therefore their attention was directed to reaction conditions typical of liquefaction regime (250-370 °C). An analogous approach was followed by Xu *et al.* [208], who hydrothermally carbonized another type of macroalgae (i.e. *Enteromorpha prolifera*) at temperature ranging from 250 to 390 °C. In this case, under conditions relevant to the hydrothermal carbonization process (250 °C and 60 min), a hydrochar yield of 15 wt% was measured. The lower solid fraction compared to that reported by Anastasakis and Ross after HTC of *Laminaria saccharina* was probably due to the longer residence time. On the other way, comparable hydrochar yields (below 20 wt%) to those reported by Xu *et al* were measured by Zhou *et al.* [205] when hydrothermally-treating *Enteromorpha prolifera* at temperatures of 240 or 260 °C held for 30 min.

However, according to the review of the open literature, the use of macroalgae-derived hydrochars as precursors for activated carbon preparation has only been reported by Zhang *et al.* [107]. Specifically, these authors hydrothermally treated *Enteromorpha prolifera* at 180 °C for 24 h prior to chemical activation with KOH. The seaweed-derived carbon was then tested for CO₂ capture. Nonetheless, it is worth emphasizing the lack of works related to the application of hydrothermal carbonization of macroalgae emerging from literature review, with particular regard to the fabrication of CO₂ solid sorbents. In addition, according to the best knowledge of the author, hydrothermal carbonization of *Laminaria hyperborea* has been reported in this study for the first time (see Chapter 5).

2.6.2 Activation of macroalgae-based chars

As already highlighted in sections 2.6.1.1 and 2.6.1.2, literature survey has not revealed any previous study concerning the use of raw *Laminaria hyperborea* and its carbonized counterparts as precursors for the manufacture of activated carbons. Therefore, general information related to the activation methods applied for other types of macroalgae are following given.

Reviewing the available literature, no studies regarding the CO₂ activation of any kind of macroalgae were found. By contrast, a number of

investigations related to the KOH activation of pyrolyzed seaweed have been recently performed [141, 142, 170, 209]. In particular, Cho *et al.* [170] chemically-activated a char derived from the fast pyrolysis of *Undaria pinnatifida*. The pyrolyzed macroalgae was impregnated with a 1 M KOH solution using a mass ratio of 1:1. The mixture was then stirred on a hot plate for 4 h in order to remove water but no heat-treatment under N₂ was performed. After this, the dried KOH:char blend was washed with 5 M HCl and H₂O. The final carbon had a surface area of 1287 m²·g⁻¹. In addition to this, as already mentioned in section 2.6.1.1, Ferrera-Lorenzo *et al.* applied KOH activation of *Gelidium sesquipedale*-based precursors [141, 142]. In particular, these authors assessed the effect of a series of parameters on the chemical activation process, including the kind of precursor (i.e. raw macroalgae waste or its pyrolyzed counterpart), the type of heat-treatment (conventional furnace or microwave), the activation temperature and the KOH:precursor ratio [142]. Results showed that the carbon having the highest surface area (2118 m²·g⁻¹) and pore volume (1.14 cm³·g⁻¹) was obtained through conventional activation of raw macroalgae-based waste (1 step activation) carried out at 900 °C and using a KOH:precursor ratio of 0.5:1.

On the other hand, only one study referring to the KOH activation of hydrothermally carbonized macroalgae was found in the open literature [107]. Specifically, Zhang *et al.* activated *Enteromorpha prolifera*-derived hydrochars with KOH. Macroalgae-derived hydrochar was impregnated with a 0.9 M KOH solution. The impregnated hydrochar was first heated to 60 °C for 1.5 h prior to drying at 100 °C for 24 h. The dried KOH:hydrochar blend was then heat-treated under N₂ (heating rate of 2 °C·min⁻¹) up to 600 °C. The final temperature was held for 4 h. Chemically-activated macroalgae was sequentially washed with water, 10 wt% HF and then water again. The KOH-activated carbon exhibited a relatively low surface area (418 m²·g⁻¹) compared to the macroalgae-derived carbons reported in other studies. This could be probably attributed to the partial KOH carbonation during the drying stage [168].

2.7 Use of biomass-derived ACs as CO₂ sorbents

As earlier discussed in section 2.2, the use of widely available biomass precursors for the fabrication of activated carbons has become a preferential practice over the last years. In addition to this, the application of biomass-derived ACs as CO₂ sorbents has gained great interest. Indeed, the conversion of such low-cost feedstock into a CO₂ captor would imply a more sustainable and less costly synthetic process.

A variety of biomass-based materials (i.e. corncob [98], hemp (*Cannabis sativa* L.) stem [92], agricultural waste (palm kernel shell) [210], sugarcane bagasse [211] and further waste biomass [97]) were successfully upgraded into

effective CO₂ sorbents. However, this section aims to give further details concerning the CO₂ capture performance of ACs derived from feedstock similar to those used in this work, such as wood [93, 212, 213] and algae-based [106, 107, 141] materials.

As concerns wood-based biomass, Sevilla *et al.* [93] produced CO₂ sorbents through a two-steps synthesis (i.e. hydrothermal carbonization and chemical activation with KOH) starting from *Eucalyptus* sawdust. In this study, the authors measured the highest CO₂ uptake ever reported (ca. 212 mg CO₂·g⁻¹) for ACs at 25 °C and under pure CO₂ (1 bar). This outstanding CO₂ sorption capacity was mostly attributed to the high ultramicropore volume (up to 0.52 cm³·g⁻¹) of the best performing carbon, which was attained after mild chemical activation (KOH:hydrochar ratio of 2).

Furthermore, highly microporous carbons were prepared from chemical activation (H₃PO₄, ZnCl₂, KOH) of *Eucalyptus camaldulensis* wood by Heidari *et al.* [212]. These authors measured CO₂ uptakes up to 4.10 mmol CO₂·g⁻¹ at 30 °C and 1 bar, which was slightly lower than that reported by Sevilla *et al.*. Yet, in this case, the uptake of CO₂ was measured at moderately higher temperature, which normally has a negative effect on the physisorption capacity of the activated carbons [102]. Nonetheless, the largest CO₂ capacity was achieved when using KOH as activating agent, as this implied the development of the highest surface area (2594 m²·g⁻¹) and the largest microporosity (ca. 98%) out of all the chemically-activated carbons produced.

Additionally, Zhu *et al.* [213] synthesized activated carbons through one-step KOH activation of *Paulownia* sawdust. Interestingly, the largest CO₂ uptake measured at 1 bar was significantly higher (8.0 mmol CO₂·g⁻¹) than that recorded by Sevilla *et al.* [93], but it was attained at a lower temperature (0 °C), which usually favors CO₂ physisorption onto activated carbons [102]. However, the maximum CO₂ uptake was attained when using a KOH:precursor of 4, an activation temperature of 700 °C and a dwell time of 1 h. These conditions led to the highest micropore volume, which was mostly responsible for CO₂ adsorption.

Regarding to the use of algae, Sevilla *et al.* [106] synthesized effective CO₂ sorbents at high partial pressure (1 bar) starting from a mixture of *Spirulina platensis* (microalgae) and glucose. The algae-based precursor was subjected to HTC followed by KOH activation. The highest CO₂ uptake was obtained when using a KOH:hydrochar ratio of 2 and an activation temperature of 700 °C. As expected, the CO₂ sorption capacity of the optimally-activated carbon was negatively affected by the temperature, decreasing from 7.4 mmol CO₂·g⁻¹ (at 0 °C) to 2.8 mmol CO₂·g⁻¹ (at 50 °C). The relatively large CO₂ sorption capacity was exclusively attributed to the high narrow microporosity of the carbons rather than to the larger porosity or to the nitrogen functionalities incorporated.

Only two studies relating to the production of macroalgae-derived CO₂ sorbents were found in the open literature [107, 141]. In particular, Ferrera-Lorenzo *et al.* [141] prepared CO₂ sorbents using a residue (macroalgae meal waste) generated from industrial processing of *Gelidium sesquipedale*. These authors showed that, under simulated pre-combustion conditions (3 MPa, room temperature), macroalgae-derived sorbents exhibited higher selectivity towards CO₂ than towards hydrogen or methane. This suggested a high potential of the materials for pre-combustion capture (CO₂/H₂ separation) through pressure swing adsorption (PSA), or CO₂/CH₄ separation in order to increase the purity of the natural gas, which can be used as fossil fuel.

In addition to this, *Enteromorpha prolifera* was used as a precursor by Zhang *et al.* [107] to produce N-doped carbons. In this report, the authors applied a two-steps route (i.e. hydrothermal carbonization and KOH activation) for the synthesis of the seaweed-derived sorbents. The latter were tested for CO₂ sorption at 25 °C, a CO₂ partial pressure of 0.15 bar and a total pressure of 1 bar (i.e. simulated post-combustion conditions), attaining a sorption capability of up to 61.4 mg CO₂·g⁻¹.

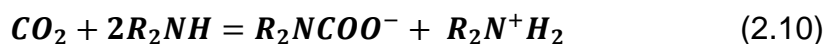
However, except for [107], CO₂ sorption capacities reported by aforementioned studies were measured at high CO₂ partial pressure (1 bar). Moreover, based on the author's best knowledge, literature survey did not show any application of CO₂ sorbents specifically derived from oak wood or *Laminaria hysborea*, which have been first presented in the current study (see Chapter 4 and 5).

2.8 CO₂ capture through amine-modified solid sorbents

2.8.1 Mechanism of CO₂ chemisorption onto amines under dry or wet conditions

The mechanism of CO₂ chemisorption onto primary or secondary amines occurs according to a two-steps reaction [214, 215]. A reaction scheme for primary amines was reported by Li *et al.* [215] (see supporting information) and here readapted for secondary amines.

In particular, during the first step (see reaction (1.1)), 1 mol of CO₂ reacts with 1 mol of amine, giving rise to a zwitterionic intermediate. Following, the latter is deprotonated by a Brønsted base (proton acceptor). Note that, under dry conditions, the proton acceptor is another mol of amine, which enables the conversion of the zwitterionic intermediate to carbamate in the second step (see reaction (2.9)). Therefore, according to the overall reaction (2.10) [116, 216-218], 2 moles of amines are necessary to adsorb 1 mole of CO₂ in absence of water.

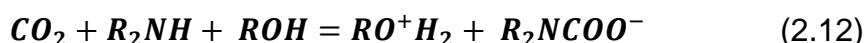


Conversely, under wet conditions (e.g. post-combustion flue gas), H₂O molecule acts as a proton acceptor, and carbamate ion, previously formed by reaction (2.10), further reacts with water and carbon dioxide to form bicarbonates (see reaction (2.11) [217, 218]).



Therefore, it follows that the presence of moisture promotes the consumption of an additional mole of CO₂ (conversion into bicarbonates), thus increasing the moles of CO₂ chemisorbed:moles of amino groups utilized ratio from 1:2 (only reaction (2.10) occurs) to 1:1 (both reaction (2.10) and reaction (2.11) occur).

Similar to water vapour, hydroxyl groups (OH⁻) can also function as a free base to deprotonate the zwitterionic intermediate. Therefore, in presence of OH-containing species, formation of carbamate is believed to occur according to the reaction (2.12) [216].



On this premise, the effect of hydroxyl groups can be considered analogous to that caused by the presence of water vapour, as involves a more favorable CO₂ to N stoichiometry (i.e. conversion of 1 mol of CO₂ requires just 1 mol of amine). However, the influence of hydroxyl groups on the CO₂ chemisorption mechanism onto amines is currently not fully understood.

2.8.2 The CO₂ sorption performance of PEI-modified sorbents

Many types of amines have been impregnated onto solid supports. Of these, the most largely used were reported in the review of Samanta *et al.* [58]. However, literature survey suggested PEI as one of the most promising candidate for improving the CO₂ sorption capacity of the virgin activated carbons. This is mostly due to its high nitrogen density [12] and low vapour pressure [219], which allows minimizing the amine loss over time.

Polyethyleneimine was first deployed by Satyapal *et al.* [218], who anchored PEI onto a polymeric support. The PEI-modified solid sorbent was used for removing CO₂ from space shuttles.

However, Xu *et al.* [120] optimized the application of the amine-containing polymer through the synthesis of the so-called “molecular basket”. These authors performed a wet impregnation method by dissolving PEI in methanol and then dispersing the polymer onto highly mesoporous silica. They measured a CO₂ capacity of up to 127 mg CO₂ · g⁻¹ at 75 °C and 1 bar (pure CO₂ flow). The same group systematically evaluated the effect a series of parameters on the CO₂ sorption performance of the PEI-modified silica in a further work [123] (see following sections).

Several authors [115, 116, 217, 220, 221] successfully used activated carbons as alternative solid support to silica for PEI impregnation. According to the review of Samanta *et al.* [58], the highest pure CO₂ (i.e. 1 bar) uptake (ca. 94 mg CO₂·g⁻¹, i.e. ca. 2 mmol CO₂·g⁻¹) ever measured in the literature for PEI-modified carbons was attained by Maroto-Valer *et al.* [220] at 75 °C. However, a high CO₂ sorption performance of PEI-impregnated ACs was also reported by other authors at the same temperature but under lower CO₂ partial pressure (1.4 mmol CO₂·g⁻¹ at 0.1 bar [116], or 4.82 mmol CO₂·g⁻¹ at 0.15 bar [115]), which is more representative of a post-combustion capture scenario.

Previous studies concerning the effect of a number of variables on the CO₂ sorption performance of the PEI-supported sorbents are reviewed below.

2.8.2.1 The influence of PEI loading and sorption temperature

The PEI loading is probably the most important variable in order to optimize the CO₂ capture capacity of the polymer-coated porous support. The effect of this parameter was first analysed by Xu *et al.* [123], who loaded PEI onto mesoporous silica (pore volume of ca. 1 cm³·g⁻¹) through a wet impregnation procedure. In particular, with increasing PEI loading, the textural properties of the solid support decreased due to pore blocking, whereas CO₂ sorption capacity continuously increased. The largest CO₂ uptake (133 mg CO₂·g⁻¹) was attained at the highest polymer loading considered (i.e. 75 wt%). On the other hand, the polymer loading was found to affect the synergetic effect between the solid support and PEI. This effect was observed for polymer loading larger than 30 wt% (i.e. when mesopores filling began) and was maximized when polymer loading was 50 wt% (i.e. when saturation of mesopore volume of silica occurred). As polymer loading was further increased (from 50 to 75 wt%), the amount of CO₂ per unit of mass of PEI declined. As explained by Xu *et al.*, when PEI loading was higher (i.e. 75 wt%) than the maximum amount of polymer which could be accommodated within the substrate pores (i.e. 50 wt%, considering a PEI density of 1 g·cm⁻³), PEI was

coated onto the external surface of the support. Therefore, they speculated that the outer layer of polymer was less effective than the fraction loaded inside the mesopores of the solid support in terms of CO₂ capture.

As concerns carbon-based supports, the influence of the PEI loading (10, 20, 40 and 60 wt%) on the pure CO₂ sorption capacity measured at 75 °C was evaluated by Arenillas *et al.* [217]. These authors observed a dramatic reduction of the surface area of the support (i.e. fly ash-derived activated carbon) after impregnation of PEI, which was already used up when polymer loading was 40 wt%. CO₂ sorption capacity continuously increased with increasing PEI loading, yet its maximum value was relatively low (up to 45 mg CO₂·g⁻¹ at 75 °C and 1 bar). In addition to this, the sorption speed progressively decreased with increasing amount of polymer loaded onto the carbon, likely because of diffusional limitations. This result was probably due to the very low porosity (surface area of ca. 88 m² g⁻¹) of the carbon support used, which could not easily accommodate a large amount of polymer.

In contrast, much greater CO₂ capture capacity (4.82 mmol CO₂·g⁻¹) was achieved by Wang *et al.* [115] at 75 °C and 0.15 bar, who PEI-impregnated a highly mesoporous carbon (total pore volume of 3.61 cm³·g⁻¹). The superior performance exhibited by the PEI-coated mesoporous carbon was likely due to the far larger available (meso)porosity. The latter enabled admitting a high amount of polymer (optimal loading of 65 wt%) without hindering the CO₂ diffusion through the porous network of the support. On the other hand, excessive pore blocking for loading higher than 65 wt% implied transport limitations of carbon dioxide, with consequent difficult access to the CO₂-capturing sites.

Therefore, as highlighted by the aforementioned studies, the optimal polymer loading will strongly vary depending upon the pore volume/structure of the type of support used. This was corroborated by the work of Wang *et al.* [222], who studied the influence of PEI loading on different solid supports (silica and carbon-based substrates) featuring diverse porous networks. In particular, these authors suggested that solid supports having large mesoporosity and 3-D porous structure are ideal for an efficient loading of a high amount of PEI, and maximize both the CO₂ capture capacity and the sorption kinetics.

However, Wang *et al.* revealed that optimal PEI loading also depends upon the sorption temperature. In particular, they observed that, when loading a low amount of polymer (i.e. 30 wt%), the CO₂ sorption capacity did not significantly improve or decrease with increasing temperature from 30 to 75 °C. This was ascribed to the fact that at lower PEI loadings thermodynamics effect (sorption) is still predominant and its contribution is penalized at higher temperature. In contrast, the same increase of temperature substantially enhanced the CO₂ sorption capacity when a higher PEI loading (65 wt%) was coated onto the solid supports. This was attributed to the beneficial effect of an

increased temperature when CO₂ uptake is diffusion-controlled (i.e. higher degree of pore filling).

Xu *et al.* [120] investigated the effect of the sorption temperature (50, 75 or 100 °C) on the CO₂ performance of PEI-impregnated silica. Specifically, for a polymer loading of 50 wt%, these authors found 75 °C as optimal condition. This finding was generally consistent with those reported by other groups for PEI/silica [223], PEI or tetraethylenepentamine (TEPA)/silica monolith [224] and TEPA/mesoporous silica [225]. Apparently, when CO₂ uptake is measured at 75 °C, a trade-off between thermodynamics (sorption) and diffusion contributions occurs [225]. However, when temperature was further increased from 75 to 100 °C, CO₂ desorption became a dominant feature of the process, thus outweighing the diffusion enhancement [226].

On the other hand, it is worth saying that review of the open literature did not reveal any investigations on the effect of the sorption temperature on the CO₂ capture capacity of PEI-modified materials when using water as solvent.

2.8.2.2 The influence of solvent amount and type

The effect of the support/solvent ratio on the CO₂ sorption performance of PEI-coated mesoporous silica was investigated by Xu *et al.* [123]. In this study, the authors used methanol as carrier and a fixed amount of polymer, whereas solvent:solid support mass ratio was varied (2, 4 or 8). CO₂ uptakes were found to increase with increasing weight ratio.

Moreover, the influence of the same parameter was studied by Arenillas *et al.* [217] when using activated carbons as solid support and methanol as solvent. The optimal value of methanol:carbon ratio agreed with that already reported by Xu *et al.* [123] for silica-based substrates (i.e. 8). In light of this, a solvent:carbon ratio of 8 was used for all impregnation runs carried out in this study.

Xu *et al.* [123] also studied the effect of the solvent type (methanol vs water) on the PEI impregnation of mesoporous silica. These authors used a value of solvent:solid support ratio of 4 and a PEI loading of 50 wt%. However, the kind of solvent appeared not to significantly affect the sorption capacity of the PEI-modified silica.

In addition to this, Egbebi *et al.* [227] used two different solvents (i.e. methanol or a methanol-hexane mixture) to impregnate PEI onto a silica-based support. However, even in this case, the type of solvent did not change the CO₂ capture capacity of the final impregnated sorbents.

Furthermore, Marques *et al.* [228] deposited PEI within the pores of carbon aerogels by using either an aqueous or a methanolic solution. They stated that PEI loading and thermal stability were not affected by the type of

solvent used. On the other way, no information relative to the influence of the solvent type on the CO₂ capture performance of the PEI-modified materials was available.

Therefore, to the author's best knowledge, the study of the effect of the type of solvent on the CO₂ sorption performance of PEI-impregnated activated carbons is unprecedented.

2.8.2.3 The influence of other preparation conditions

In addition to the influence of the abovementioned factors, the effect of other parameters on the CO₂ capture performance of PEI-impregnated materials was also reported.

In particular, Xu *et al.* showed that the wet impregnation method [120] allowed synthesizing more efficient CO₂ sorbents than those obtained through a mechanical mixing method [123]. The same group observed that silica impregnated through a one-step method (i.e. entire amount of PEI loaded in just a single step) exhibited a higher CO₂ uptake than that attained by sorbents prepared using a two-steps impregnation route. The latter entailed loading the first half of the amount of PEI in the first step, while the remaining fraction of polymer was loaded in a second step prior to drying under vacuum at 70 °C.

Furthermore, Arenillas *et al.* [217] studied the effect of the mixing method (i.e. either stirring or shaking) on the CO₂ sorption performance of PEI-impregnated carbons. Yet, these authors stated that this factor did not affect the outcome of the impregnation procedure. Nonetheless, to the best knowledge of the author, no reports have been published yet regarding the effect of the mixing time on the CO₂ capture performance of PEI-supported sorbents.

Moreover, as alternative to the wet impregnation applied by Xu *et al.* [120], a (post-spinning) infusion method was carried out by Labreche *et al.* [229] for the incorporation of PEI onto silica fibers. In particular, these authors studied the effect of the infusion time, showing that the highest CO₂ adsorption capacity was attained at low immersion durations [214, 229]. However, this route appears to be more complex than the wet impregnation, and is probably more appropriate when silica fibers are used as solid support.

In this perspective, a one-step wet impregnation was adopted for the synthesis of the PEI-impregnated carbons. Stirring was selected as mixing method and the effect of the agitation time on the CO₂ sorption capacity of the final impregnated AC was assessed.

2.8.2.4 The influence of water on the CO₂ capture performances of PEI-modified sorbents

2.8.2.4.1 The effect of moisture in the simulated post-combustion flue gas

Prior contributions revealed an increase of CO₂ sorption capacity for PEI-loaded sorbents when exposed to a wet gas feed [214, 230, 231]. For instance, Xu *et al.* [230] measured the CO₂ capture performance of PEI-loaded silica (PEI loading of 50 wt%) under a dry or moist (closer to the real scenario) simulated post-combustion flue gas at 75 °C. These authors observed that, after doping the gas composition with water vapour (ca. 10% by volume), the CO₂ sorption capacity of the chemisorbents was improved. This result was ascribed to the enhancement of the mechanism of CO₂ chemisorption onto amines occurring in presence of water (see section 2.8.1). In the same study, the effect of the moisture concentration (0-16%) in the flue gas on the CO₂ capture behaviour of the PEI-coated silica was also assessed. Specifically, the CO₂ sorption capacity continuously increased with increasing moisture concentration. However, the highest increase rate was attained when moisture and carbon dioxide contents were comparable. These findings are in agreement with those reported in other works for PEI-loaded silica [214, 231].

Moreover, similar observations were reported by Wang *et al.* [115] when measuring the CO₂ sorption capacity of PEI-coated mesoporous AC under anhydrous or moist gas feed simulating post-combustion flue gas. In particular, CO₂ uptakes increased from 4.82 mmol CO₂·g⁻¹ (feed gas containing moisture) to 5.36 mmol CO₂·g⁻¹ (feed gas without moisture).

2.8.2.4.2 The effect of the addition of OH-containing species to PEI-modified sorbents

The introduction of hydroxyl-containing guests within amine-impregnated sorbents was previously found to promote the interaction between CO₂ and amines [123, 214, 216-218, 232]. For instance, Xu *et al.* [123] studied the effect of the addition of polyethylene glycol (PEG) to the PEI/solvent solution prior to adding the solid support (silica). Assuming a theoretical maximum loading of the overall guest of 50 wt%, the amounts of PEI and PEG were fixed to 30 and 20 wt% respectively. The PEG-containing sample not only attained a higher pure CO₂ uptake (1 bar) at 75 °C, but also exhibited faster adsorption and desorption kinetics. This behaviour was attributed to the change in the chemisorption reaction between amines and CO₂ (see section 2.8.1) due to the presence of hydroxyl groups contained within PEG [218].

As concerns activated carbons, similar observations were reported by Arenillas *et al.* [217]. In this case, the same amount of PEG (20 wt%) was added to a series of PEI-impregnated carbons having different polymer loadings (20, 40 and 60 wt%). Results were consistent with those reported by Xu *et al.*

[123]. Indeed, when measuring CO₂ uptakes at 1 bar and 75 °C and for any PEI loading, the additional presence of PEG led to larger CO₂ uptakes and accelerated the adsorption/desorption speed. Arenillas *et al.* [217] also loaded the two guests (PEI and PEG) in either one or two steps, but the authors found no difference in the CO₂ sorption performance of the two final products.

Alternatively to the use of PEG, Labreche *et al.* [214] proposed the addition of glycerol as OH moieties source. This sugar alcohol was chosen as it has a greater number of hydroxyl groups per carbon atom compared to PEG, and because of its higher thermal stability (boiling point of 290 °C), which is a key factor when performing rapid temperature swing adsorption (RTSA) cycles. It was shown that the presence of glycerol as additional guest within the PEI-impregnated silica led to a CO₂ capture capacity at 35 °C nearly twice as large as that attained by the glycerol-free sample. In addition to the increase of the moles of CO₂ chemisorbed:moles of amines ratio, Labreche *et al.* ventured that glycerol plasticized the rigid PEI chain, thus allowing a faster diffusion of CO₂ through the polymer gel.

The favourable effect of glycerol addition on the enhancement of amine efficiency (CO₂/N molar ratio) was also reported by Yue *et al.* [216] when the sugar alcohol was added to TEPA-coated silica. On the other hand, the same authors achieved greater adsorption capacities when using diethanolamine (DEA) as OH group's guest. These results were consistent with those reported by Dao *et al.* [233], showing that the impregnation of a TEPA/DEA mixture on mesoporous silica outweighed the CO₂ adsorption performance obtained when loading TEPA/PEG or TEPA/Glycerol blends. This was attributed to the CO₂ sorption contribution ensured by the amino group contained within DEA molecule amino [233]. Nonetheless, the use of glycerol as additional guest (three OH groups per number of C atoms) allowed achieving a larger CO₂ adsorption capacity than that attained when using PEG (two OH groups per number of C atoms) as additive, thus indicating a beneficial effect of the density of hydroxyl groups.

Nevertheless, to the author's best knowledge, the influence of DEA or glycerol addition on the CO₂ sorption performance of PEI-impregnated AC has not been reported yet. In addition to this, glycerol is more environmentally friendly and has a higher thermal stability than DEA, which plays a key role when applying RTSA cycles. For these reasons, in this study the addition of glycerol as OH groups guest was preferred to the use of DEA.

2.8.2.5 Regeneration strategy

As already discussed in Chapter 1, RTSA cycling is considered as one of the most promising regeneration approach for post-combustion capture of CO₂.

The application of RTSA cycles for the regeneration of PEI-modified silica [234] or hollow polymeric fibers [229] has been reported in the literature.

However, to the author's best knowledge, the regeneration of PEI-modified carbons through rapid TSA cycles has been reported only by Wang *et al.* [235]. On the other hand, these authors regenerated the PEI-loaded carbon by applying a relatively intense temperature swing (25-110 °C) and under nitrogen flow, which tends to facilitate the desorption process (i.e. PSA simulation). Moreover, CO₂ was fully desorbed by holding the regeneration temperature for at least 34 min, which still represents a long desorption step.

2.9 Main objectives

In relation to the literature review reported in the present chapter and to the overall context outlined in Chapter 1, this work has attempted to achieve the following aims:

- Prepare ACs starting from low-cost raw materials, making a comparison between products obtained from a traditional biomass, i.e. oak wood, and those derived from an unconventional and novel feedstock, i.e. *Laminaria hyperborea*.
- Exploit the inherent chemical nature (i.e. alkalinity) and high availability of seaweed for a sustainable synthesis of alkali-metal based sorbents.
- Study the influence of the carbonization process (conventional pyrolysis vs innovative HTC) of biomass on the two steps manufacture of ACs.
- Compare the effect of the activation route (physical (CO₂) vs chemical (KOH)) on the properties of the activated biochars.
- Apply a chemical modification (i.e. amine impregnation) of virgin ACs in an attempt to improve their CO₂ sorption capacity under simulated post-combustion conditions (T=ca. 53 °C, P_{CO₂}=0.15 bar, P_{tot}=1 bar).
- Investigate on the CO₂ sorption mechanism (physisorption vs chemisorption) occurring onto the solid sorbents examined.
- Evaluate the effect of texture and basicity on the CO₂ sorption capacity of physisorbents and chemisorbents tested.
- Examine the influence of the presence of hydroxyl groups (provided by glycerol) on the CO₂ chemisorption mechanism occurring onto PEI-loaded ACs.

3 Experimental

3.1 Outline

In the current chapter, the materials examined and the experimental methodologies adopted are described in detail.

Details about the materials used are given in section 3.2, while section 3.3 describes the synthesis of biomass-derived chars.

Procedures related to the activation of biochars are reported in section 3.4, whereas section 3.5 is concerned with the chemical modification of a commercial carbon.

Characterization techniques conducted on the samples were grouped in three areas. In particular, section 3.6 refers to porosity measurements achieved through gas (i.e. N₂ and CO₂) adsorption. Further analyses related to the chemistry, morphology and structure of the samples are included in section 3.7.

Finally, routines applied for the measurement of the CO₂ sorption performance are explained in section 3.8.

3.2 Materials

3.2.1 Biomass feedstock

Raw materials used for the preparation of the carbons were oak wood and *Laminaria hyperborea* (see Figure 3-1). These were designed as OW and LH_S respectively. Oak wood was obtained from Andalusia, Spain and used as received. The brown macroalgae (*Laminaria hyperborea*) was harvested off Scottish coast of Clachan Sound in the summer season (July). Raw seaweed was ground prior to further treatment.

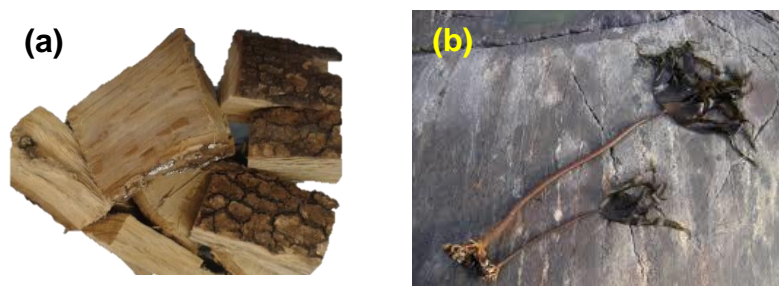


Figure 3-1 (a) Raw oak wood (OW) and (b) *Laminaria hyperborea* summer (LH_S) used as precursor for activated carbons (ACs) preparation

3.2.2 Commercial carbons

Commercial carbons were included in this work and used as reference materials. In particular, a coconut-shell derived carbon, denoted as GAC, was offered by Eurocarb. This was compared with oak wood-derived carbons in Chapter 4. In addition to this, another carbon, referred to as AR, was provided by Chemviron Carbon. The latter sample was employed for the chemical modification procedure following described in section 3.5, and relevant results are reported in Chapter 6.

3.3 Synthesis of biochars

3.3.1 Dry pyrolysis

Conventional pyrolysis of biomass was carried out by using two different types of reactors, in particular a horizontal ceramic tube furnace, and a stainless steel vertical furnace.

3.3.1.1 Horizontal ceramic tube furnace

A known weight of virgin biomass was placed in a ceramic boat. The crucible was then inserted inside the furnace. A metallic rod was used to place the boat within the heating zone (reactor core), thus ensuring that the whole charge was exposed to the same temperature. Afterwards, both ends of the furnace tube were tightly fastened in order to prevent air infiltration. The right hand side (see Figure 3-2(b)) was provided with inlet connections in order to feed the inert gas (nitrogen). Nitrogen was used for an initial purging (5 to 10 min) which allowed excluding oxygen from the internal atmosphere, thereby preventing undesired material burn off. In addition to that, the inert gas flowed at a flow rate of $100 \text{ ml}\cdot\text{min}^{-1}$ during heating and cooling steps in order to sweep the evolved gases from the reaction zone.

The other side of the rig (see Figure 3-2(a)) was connected to an exhaust system. This consisted firstly of an “anti-suck back” trap and oil bubbler (where tars (oil) and condensable liquids tended to collect). Following this, the outlet gas flowed through tubing which worked as an exhaust fume chimney to pull out volatile organic compounds (VOCs) released during heating.

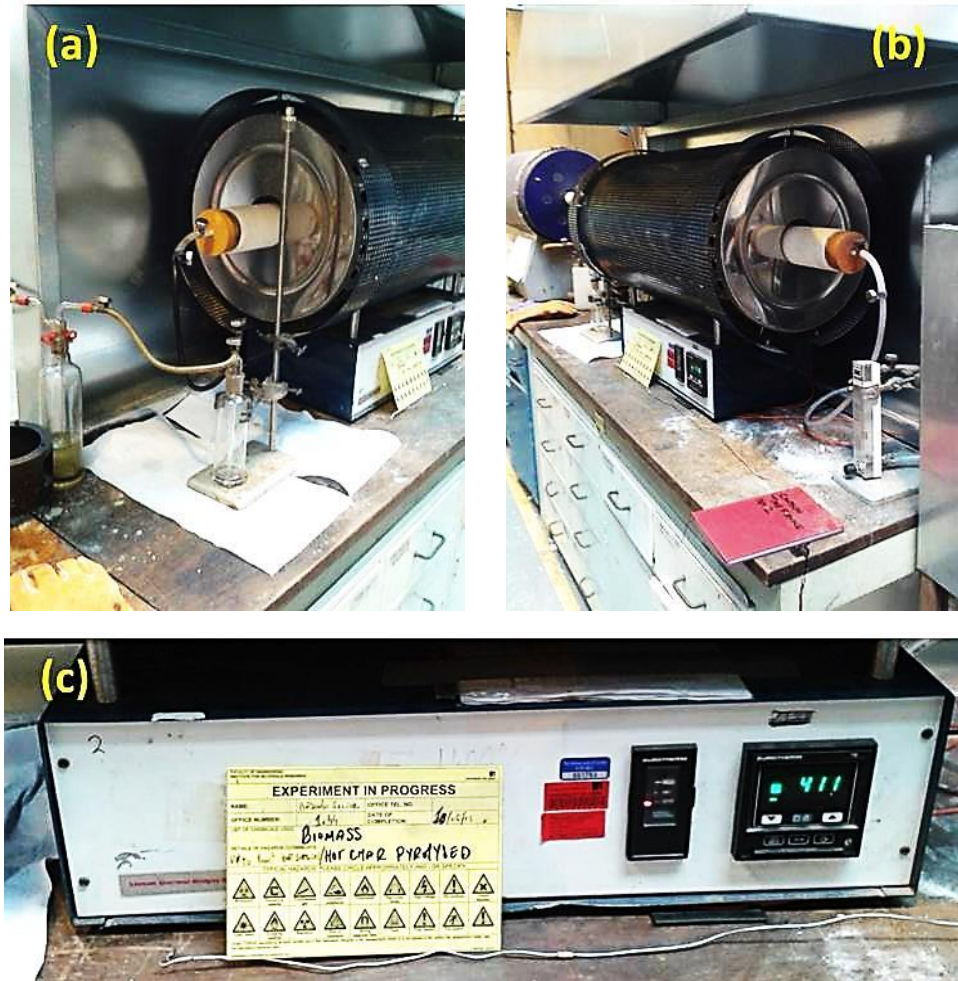


Figure 3-2 Dry pyrolysis of biomass - setup 1 (ceramic horizontal tube furnace): a) exhaust system on the left hand side, b) gas feed connection on the right hand side, and c) furnace controller.

A schematic representation of the reactor setup is provided in Figure 3-3.

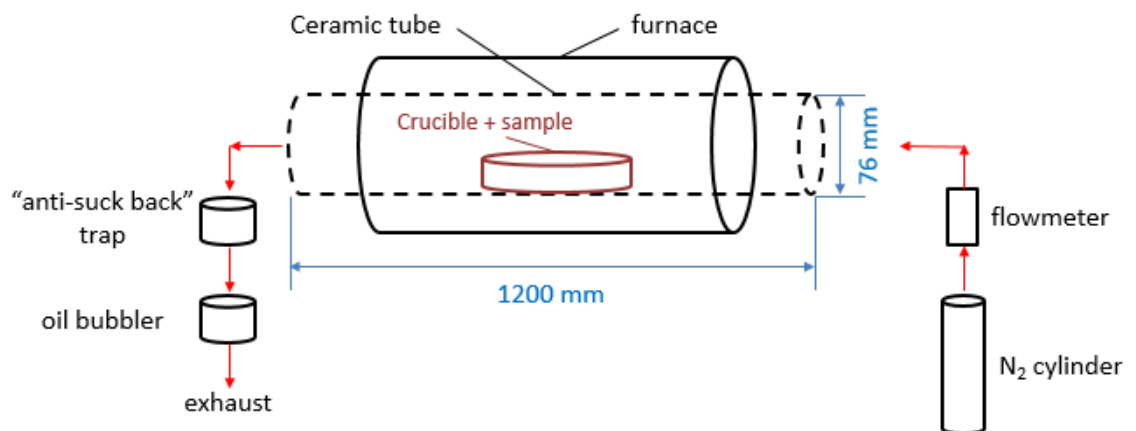


Figure 3-3 Dry pyrolysis of biomass - setup 1 – schematic representation

Carbonization took place by heating the feedstock at a heating rate (HR) determined by the furnace (i.e. average HR of ca. 13 °C·min⁻¹), to a final temperature of 800 °C, which was set by a dedicated controller (see Figure 3-2(c)) and held for 1 h. On completion, furnace was allowed to cool down under nitrogen. Once the sample had reached ambient temperature, the char was then collected and weighed in order to measure the carbonization yield as equation (3.1).

$$\text{Carbon yield (CY)} = (W_{\text{char}}/W_{\text{raw material}}) \cdot 100 \quad (3.1)$$

where, W_{char} and $W_{\text{raw material}}$ are the weights of char and raw material on a dry basis respectively.

3.3.1.2 Stainless steel vertical furnace

A determined amount of raw feedstock was loaded into a basket, which was then inserted within a stainless steel vertical furnace (see Figure 3-4(a) and Figure 3-5). Prior to entering the material into the furnace, a thermocouple was introduced inside the basket such that it was in direct contact with the sample (see Figure 3-5). After this, the basket was anchored on the top ring of the rig by using some chains (see Figure 3-5). The presence of the thermocouple allowed monitoring the sample temperature during the process. The top ring was then sealed through a series of screws, and the top ring fitting was connected to the inlet pipelines allowing the purging gas (N₂) to flow in (flow rate of 1.5 l·min⁻¹).

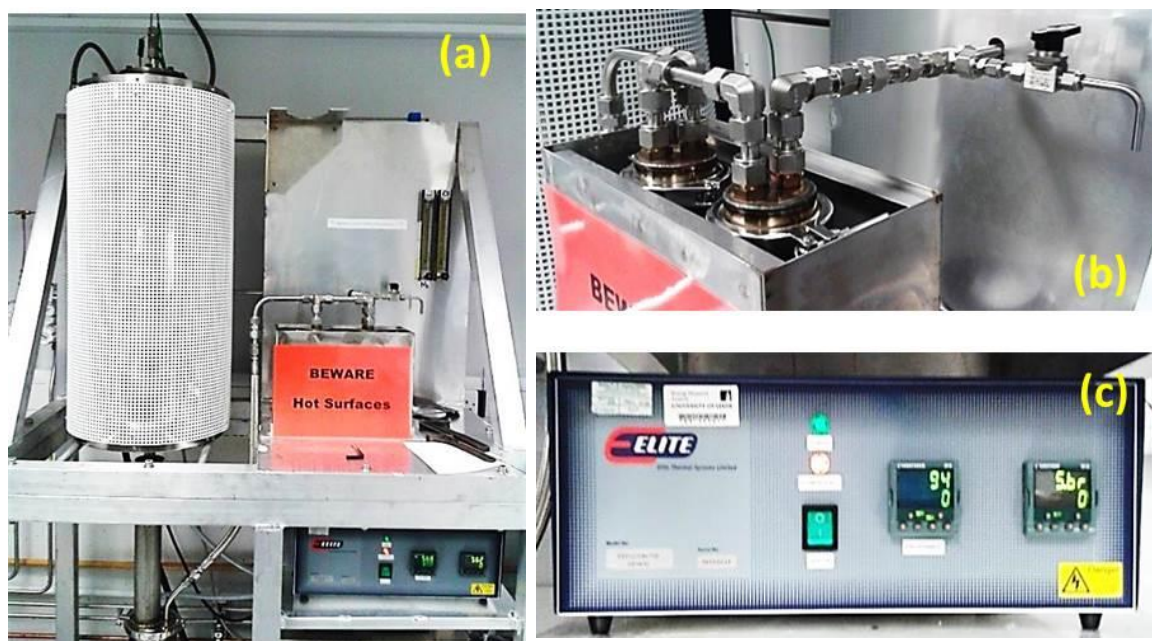


Figure 3-4 Dry pyrolysis of biomass - setup 1 (Stainless steel rig): a) vertical furnace, b) traps for collection of HCl and further volatiles, and c) furnace controller.

As shown in Figure 3-4(a) and Figure 3-5, the outlet fitting at the bottom of the rig was connected to a first condenser to collect condensable oils and vapours. This was maintained at ca. 5 °C by using a chiller. Afterwards, the outlet gas went through two more traps (see Figure 3-4(b) and Figure 3-5). The second trap, containing NaOH, was designed to neutralize any HCl release, especially when pyrolyzing *Laminaria hyperborea*, which normally contains high concentration of Cl (see also results in Chapter 5). Finally, the last trap was used to collect any further volatiles prior to reaching the exhaust.

A schematic representation of the reactor setup is provided in Figure 3-5.

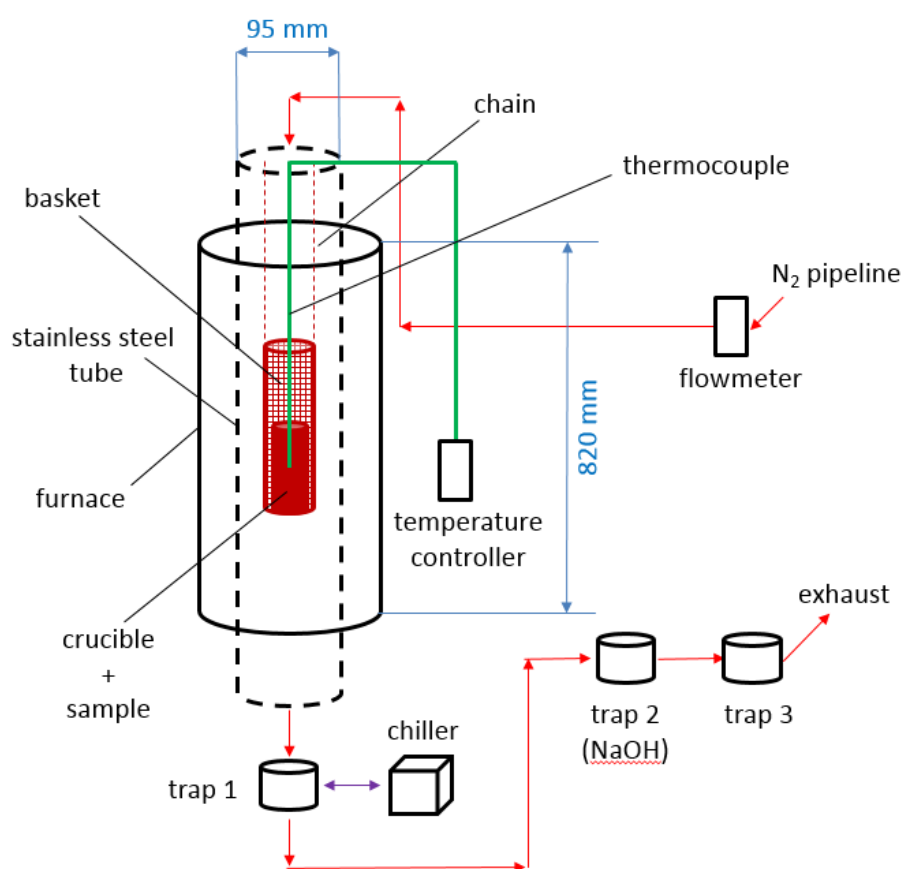


Figure 3-5 Dry pyrolysis of biomass - setup 2 – schematic representation

The reactor was initially purged with N₂ for 10 min. After this, controller (see Figure 3-4(c)) was switched and desired temperature (i.e. 800 °C) was set. Feedstock was then heated up according to a heating rate determined by the furnace. It is worth pointing out that heating ramp was observed to be slower than that implied by the ceramic furnace (i.e. average HR of ca. 8 °C·min⁻¹). As usual, the final temperature was held for 1 h. After cooling down to room temperature, the char was recovered in order to determine the carbonization yield according to equation (3.1).

3.3.2 Hydrothermal carbonization

Hydrothermal synthesis entailed loading 24 g of pristine material along with 220 ml of distilled water in a stainless steel autoclave (see Figure 3-6(a)). Solid and liquid phases were thoroughly mixed and reactor was sealed. The autoclave was then transferred inside a heater, which was attached to a temperature controller (see Figure 3-6(b)). The slurry was then heated at a heating rate (ca. $4\text{ }^{\circ}\text{C}\cdot\text{min}^{-1}$) determined by the reactor up to $250\text{ }^{\circ}\text{C}$, and held at this final temperature for 1 h.



Figure 3-6 HTC of biomass: a) reactor setup, and b) temperature controller

Once the set point was reached, the equilibrium between liquid and gaseous phases (volatiles) was established, and a pressure of 35 to 40 bar was reached inside reactor. This was measured by a pressure gauge connected to the top ring of the hydrothermal rig (see Figure 3-6(a)). At the end of the process, the sample was allowed to cool down to room temperature, and the solid residue was recovered by filtration. The hydrochar obtained was then air-dried and weighed in order to determine the carbonization yield (see equation (3.1)). In addition, a mass balance of the HTC water process was applied to calculate the amount of water lost during the hydrothermal process as given in equation.

$$m_{lost} = m_{initial} - m_{recovered} \quad (3.2)$$

where, $m_{initial}$ is the mass of water initially added to HTC rig, $m_{recovered}$ is the mass of water recovered after HTC process, and m_{lost} is the mass of water lost after HTC process.

3.3.3 Repeatability of carbonization process

The repeatability [236] of carbonization processes for the feedstock chosen is assessed in Chapters 4 and 5 respectively. In order to do this, three runs under the same conditions were carried out. As suggested by Illingworth [168], the accuracy of the repeatability was then estimated using the equation (3.3):

$$SD (\% \text{ Mean}) = (SD/Mean) \cdot 100 \quad (3.3)$$

where, SD is the standard deviation of the three measurements.

The repeatability of the solid yield (see equation (3.1)) was determined for both carbonization processes. In addition, the variability of the HTC water balance (see equation (3.2)) was also assessed.

3.4 Activation step

Chars were activated via two different methods. A heat-treatment step either under CO₂ (physical activation) or N₂ (chemical activation) was performed in a ceramic horizontal tube furnace with a setup similar to that already shown in Figure 3-2, with the exception of using a tube with smaller diameter. In addition to this, the smaller furnace used in this case allowed a greater flexibility in terms of control settings. In fact, the furnace controller enabled pre-defined multi-steps programmes, by manually selecting the heating rate, the set point and the dwell time for each stage.

3.4.1 CO₂ activation

A fixed mass of each char was placed in an alumina crucible. This was centred within a horizontal tube furnace. After closing tightly both ends of the reactor, the system was initially purged with N₂ for ca. 15 min to exclude any presence of oxygen inside the furnace. The sample was heated at a heating rate of 10 °C·min⁻¹, up to the chosen activation temperature. The char was then isothermally held for a certain holding time. CO₂ (flow rate of 0.6 l·min⁻¹) flowed throughout the heating treatment. At the end of the temperature programme, the furnace elements were switched off and allowed to cool down to room

temperature. The resultant activated carbon was then weighed to determine its burn-off according to equation (3.4) and then stored in a desiccator for further characterization experiments.

$$\text{Burn-off (BO)} = \frac{W_{char} - W_{AC}}{W_{char}} \cdot 100 \quad (3.4)$$

where, W_{char} is the mass of the char used for physical activation, and W_{AC} is the mass of carbon following to CO_2 activation. Masses were reported on a dry basis.

3.4.2 KOH activation

Chemical activation was carried out according to the procedure reported by Fierro *et al.* [169]. This entailed grinding some KOH pellets (Sigma Aldrich, P1767) and physically mixing these with a certain amount of char in a mortar according to a desired ratio. This methodology was preferred to the wet impregnation route because it does not require any drying step prior to the heat-treatment under N_2 , thereby avoiding the preliminary carbonation of KOH in air [168] (see also Chapter 2).

Therefore, the procedure adopted in the present study entailed heating the solid dry blend KOH/char up to the determined temperature immediately after physical mixing. The maximum temperature was held for a dwell time of 1 h.

Following heat-treatment under N_2 , the recovered material was washed through a filter in an attempt to remove the residual potassium compounds taking up the pore space. Illingworth [168] highlighted the crucial role of the washing treatment in order to ensure the effectiveness of the KOH activation. In particular, the author used either water or highly concentrated (5 M) hydrochloric acid as washing agents. In the current work, three different washing procedures were applied:

No washing;

1 step - aqueous rinsing with distilled water until constant filtrate pH (ca. 7.0);

2 steps - sequential washing

✓ 1 M HCl (VWR International, 20252.420) until constant filtrate pH (ca. 2.0)

✓ Aqueous rinsing with distilled water until constant filtrate pH (ca. 7.0).

Use of high concentrated acid was avoided, as this would be less economical if washing treatment was to be applied on an industrial scale.

The final activation yield was then calculated as equation (3.5).

$$\text{Activation yield (AY)} = (W_{AC}/W_{char}) \cdot 100 \quad (3.5)$$

where, W_{char} is the dry mass of the char mixed with KOH prior to heat-treatment under N_2 , and W_{AC} is the dry mass of carbon following activation and washing treatments.

3.5 Amine wet impregnation of activated carbons: procedure optimization

3.5.1 Primary optimization

A commercial carbon, designed as AR and provided by Chemviron Carbon, was chemically modified by wet impregnation. The main impregnating agent used was a branched polyethileneimine (PEI), which was purchased from Sigma Aldrich (product number 408719).

PEI was chosen for its high amine concentration (ca. 33% N by weight) [12], due to the numerous primary, secondary and tertiary amines present within its polymeric chain (see Table 3-2). Moreover, its high molecular weight (see Table 3-2) implies a good thermal stability [237], which allows minimizing the loss of amines after regeneration when using rapid temperature swing adsorption (RTSA). This would ensure durable performances over time and avoid the release of toxic substances in the environment.

PEI impregnation was carried out initially using the conditions reported by Xu *et al.* [120]. This entailed dissolving the desired amount of polymer in methanol and stirring for 15 min. After this, mesoporous silica was added as solid support and the mixture stirred for a further 30 min. The amount of solid support was determined in order to have a support/solvent ratio of 1:8.

The aforementioned methodology was adapted to the use of the commercial carbon (AR) as solid support. As summarized in Table 3-1, either 0.4, 0.6, 0.8 or 1 g of pure polymer were added to the desired amount of solvent according to the optimal ratio reported by Xu [123] and stirred for 15 min. Afterwards, 1 g of carbon was added and the final mixture was further stirred for 0.5, 2, 4, 6 or 8 h.

The final slurry was recovered by filtration and air dried until constant weight in order to determine the actual amount of PEI loaded onto the support by mass balance (see equation (3.6)). Oven drying was avoided in order to prevent any amine degradation.

$$\text{Actual Loading (AL)} = (W_{\text{IC}} - W_{\text{C}} / W_{\text{IC}}) \cdot 100 \quad (3.6)$$

where, W_{IC} is the mass of impregnated carbon air-dried until constant weight, and W_{C} is the dry mass of carbon before impregnation.

Table 3-1 Primary optimization - PEI impregnation of commercial carbon (AR) - NL stands for Nominal Loading, as % calculated from g of PEI/(g of PEI + g of carbon). “Me” and “W” represent the solvent used and stand for Methanol and Water respectively

Sample ID	NL wt%	wt. carbon g	wt. PEI g	Stirring time h
AR_PEI_29%_Me_0.5h	29	1	0.4	0.5
AR_PEI_38%_Me_0.5h	38	1	0.6	0.5
AR_PEI_44%_Me_0.5h	44	1	0.8	0.5
AR_PEI_50%_Me_0.5h	50	1	1	0.5
AR_PEI_44%_Me_2h	44	1	0.8	2
AR_PEI_44%_Me_4h	44	1	0.8	4
AR_PEI_44%_Me_6h	44	1	0.8	6
AR_PEI_44%_Me_8h	44	1	0.8	8
AR_PEI_44%_W_8h	44	1	0.8	8

Note that details included in Table 3-1 refer to the main optimization of the PEI wet impregnation. This consisted of three main steps, and entailed assessing the influence of the following parameters on the CO₂ sorption capacity of the impregnated carbons measured under post-combustion conditions (see results reported in Chapter 6):

The nominal loading of polymer with a stirring time of 0.5 h and solvent was methanol;

The stirring time of the mixture PEI/solvent/carbon when the PEI loading was optimal (i.e. 44 wt%, see Table 3-1) and solvent was methanol;

The type of solvent (using water rather than methanol) when the PEI loading and the stirring time were optimal (44 wt% and 8 h respectively). The effect of the solvent type was examined at two different temperatures, i.e. 53 or 77 °C (see Chapter 6 for further discussion).

In addition to the aforementioned steps, the influence of stirring time was also studied for polymer loadings other than the optimal value (i.e. 38 and 50 wt%). Moreover, the use of aqueous impregnation was further optimized by varying the polymer loading and the stirring time independently.

3.5.2 Influence of additional factors

Starting from optimal conditions of PEI loading, stirring time and solvent type, which were determined for maximum CO₂ uptake at 53 °C, the influence

of additional factors on the CO₂ sorption capacity of PEI-loaded carbons was then assessed.

3.5.2.1 Use of a different carbon substrate

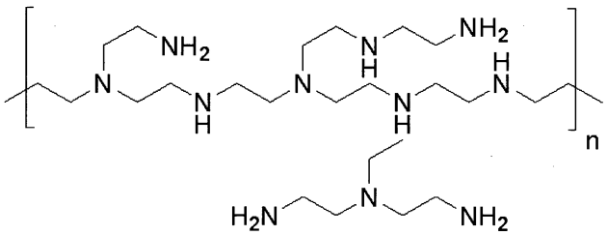
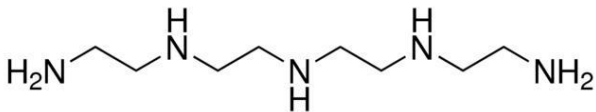
An alternative carbon support was selected for carrying out the PEI impregnation. OW800CA was chosen as best candidate, as this represented a reasonable trade-off between available pore volume and activation yield (see Chapter 4). The alternative carbon substrate was obtained from the KOH activation of pyrolyzed wood.

3.5.2.2 Use of alternative N-containing compounds

The main solid support used, i.e. AR, was impregnated with other types of amines having different characteristics to PEI (see Table 3-2). This was done in an attempt to study the effect of the incorporation of diverse N-based moieties. monoethanolamine (MEA) was chosen because of its smaller size and lower molecular weight. In addition to this, a 30% aqueous solution of this type of amine is the state of the art technology for post-combustion capture of CO₂.

Another compound, in particular tetraethylenepentamine (TEPA), was selected because, according to previous studies [121, 122, 224, 237, 238], TEPA-modified supports were found to outperform PEI-impregnated sorbents in terms of CO₂ sorption capacity. This was mostly attributed to the higher amine density [237] or lower viscosity [121] (see also Table 3-2) of the TEPA molecule as compared to PEI. In particular, the less viscous TEPA implies an improved diffusion of CO₂ through the amine coating/porous channels of the solid support.

Table 3-2 Physical properties and amine types for impregnating agents used - I, II, and III stand for primary, secondary and tertiary amines respectively.

Impregnating agent	Product number	Density at 25 °C g·ml ⁻¹	Molecular weight g·mol ⁻¹	Dynamic Viscosity at 20 °C cP	Amine type	Molecular structure
-	-	-	-	-	-	-
PEI	408719	1.050	600.00	800 - 5000	I, II, III	
MEA	E9508	1.012	61.08	24.1 [239]	I	
TEPA	T11509	0.998	189.30	23.4 [240]	I, II	

3.5.2.3 Addition of glycerol

The addition of an OH-containing compound (i.e. glycerol) to the PEI/methanol mixture was studied. As already reported in Chapter 2, it had already been proved that the presence of hydroxyl groups enhanced the chemisorption mechanism of CO₂ onto amines [115, 216, 217, 232].

Glycerol was chosen because it is a natural, non-toxic compound, and has a higher number of OH groups per number of C atoms (see Figure 3-7) than other compounds previously used such as Polyethylene glycol (PEG) [214]. Furthermore, its higher boiling point (ca. 290 °C) ensures a higher thermal stability. Moreover, according to the author's best knowledge, the influence of glycerol addition on the PEI impregnation of ACs has been examined for the first time in this work.

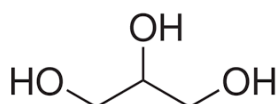


Figure 3-7 Glycerol molecule

Details about impregnation including glycerol addition are given in Table 3-3. In particular, 1 g of carbon was impregnated using the optimal conditions of PEI loading, stirring time and solvent type determined in Chapter 6. The PEI/glycerol ratio was varied from 4:1 to 1:1.

Table 3-3 Impregnation conditions when adding glycerol (Gly)

g AC	g PEI	g Gly	PEI:Gly ratio
1	0.8	0.2	4:1
1	0.8	0.4	2:1
1	0.8	0.8	1:1

3.6 Gas adsorption (porosity and surface area measurements)

3.6.1 Sample degassing

Prior to measuring gas adsorption, all samples were degassed under vacuum. This degassing process is essential for a reliable measurement of porosity as it enables the release of moisture and chemical species from the pore surface of the adsorbents. The instrument allowed the outgassing step to

be conducted at temperatures higher than ambient (up to 350 °C). In order to do this, the sample cell was placed inside a heating mantle, which was connected to a temperature controller. In theory, a material should be degassed at the highest temperature that does not cause any damage to its structure, because the higher the temperature, the more efficient and the shorter the degassing process.

The maximum degassing temperature depended upon the type of sample analysed. In particular, the raw biomass and the chars were degassed at room temperature as these materials kept on releasing a significant amount of volatiles on heating, thus contaminating the outgassing station. On the other hand, degassing these samples at room temperature often led to isotherms characterized by a low-pressure hysteresis (LPH) phenomena, which are further discussed in Chapter 4. In addition to raw materials and carbonized counterparts, amine-modified carbons were also degassed at ambient temperature. In this case, the temperature was not increased to avoid any chemical degradation. Conversely, virgin activated carbons were subjected to a gradual heating process. Initially, ACs were degassed for 30 min at room temperature. After this, the temperature was increased stepwise ($\Delta T < 50$ °C) until reaching a maximum temperature of 100 to 200 °C. As suggested by Tucker [241], a faster heating rate promotes an intense release of a high concentration of volatiles, thus potentially causing contamination problems.

The duration of the degassing process was extended until the final outgassing rate dropped below 20 mm Hg·min⁻¹.

3.6.2 Gas isotherm construction

The porosity of solid materials examined in this study was measured with the aid of a Quantachrome Autosorb 1-C gas sorption analyser. The instrument returned a gas adsorption isotherm as output. This can be defined as the relationship between the amount of gas adsorbed/desorbed onto/from a unit of mass of solid sample and the relative pressure P/P_0 (corresponding to a certain equilibrium vapour pressure) at which the gas is adsorbed onto/desorbed from the material, at a constant temperature.

The construction of the adsorption/desorption isotherm was accomplished by using the static volumetric method. This entails admitting a known amount of adsorptive gas into the sample cell filled with the solid adsorbent. The latter will then adsorb some of the gas admitted, thereby implying a variation in the pressure inside the sample cell, which will change until equilibrium occurs. If equilibrium is not reached, the sample cell is scheduled for another dose of gas. Once equilibrium is established, the amount of gas adsorbed onto the solid sample is then calculated by applying the gas law as the total amount of gas admitted minus the amount of gas filling the dead

space (i.e. space not occupied by solid material) at the equilibrium pressure and at the desired temperature. The sample cell was maintained at $-196\text{ }^{\circ}\text{C}$ (77 K) by using liquid nitrogen when the adsorptive gas was N_2 , whereas an ice bath was used to keep the sample at $0\text{ }^{\circ}\text{C}$ (273 K) when CO_2 was used as the adsorptive gas (see also 3.6.4).

A similar principle is applied for the construction of the desorption leg of the isotherm, with the exception of removing a known amount of adsorptive gas from the sample cell. Therefore, when plotting relative pressure against volume of adsorbate, the graphical isotherm will consist of two legs, i.e. adsorption and desorption. If adsorption is not fully reversible, desorption branch will not follow the same path as the adsorption leg, thus giving rise to the so called hysteresis [242].

The construction of the adsorption-desorption isotherm allows identifying a characteristic pore structure for the analysed solid sorbent. In particular, adsorption isotherms were initially classified into six types according to IUPAC recommendations [242]. However, thanks to the investigation of new porous systems over the last 30 years, this classification has been recently updated by a IUPAC report [243], introducing two more isotherm types. The same report also refined the hysteresis loops classification, adding two new hysteresis types to the four patterns proposed in the first report.

However, the recent IUPAC report recommended the use of Ar at 87 K as the adsorptive gas instead of N_2 at 77 K for porosity measurements. Indeed, adsorption of Ar at 87 K is considered more accurate due to a series of reasons. For instance, thanks to the lack of quadrupole moment and to the higher sorption temperature, Ar is less affected by the structure and functional groups of the adsorbent surface. The use of Ar at 87 K rather than N_2 at 77 K is particularly advantageous for the measurement of microporosity. Indeed, the higher temperature enhances gas diffusion into smaller micropores, which are filled at higher relative pressures, thereby implying faster and higher resolution analysis. Nevertheless, the last IUPAC report was published when most of the current experimental work had already been accomplished. Therefore, the use of Ar as adsorptive gas was not considered in this study.

Whenever possible, the choice of the amount of sample for the analysis was made according to the recommendations given by Quantachrome [244]. In particular, the amount of material weighed for each sample was chosen as to having a presumed total surface area of 5 to 20 m^2 . In particular, sample sizes were 0.02 to 0.03 g for activated carbons. However, although the raw biomass and the chars had significantly lower specific surface areas than those featured by activated carbons, the sample size was maintained below 0.05 g in order to avoid excessive release of volatiles from these materials during the degassing stage (see section 3.6.1). Nonetheless, all measurements were carried out by using the smallest sample cell available ($d=6\text{ mm}$, small bulb), thereby

minimizing the dead space around the solid material. This helped to reduce the buoyancy errors introduced by backfilling sample cell with helium (see further details in the Autosorb manual [244]).

Although the Autosorb 1-C instrument is able to measure gas adsorption/desorption down to relative pressures (P/P_0) of ca. 10^{-7} , in this study N_2 adsorption isotherms were measured by applying a shorter P/P_0 range (10^{-3} to 0.99) because of the long equilibration time required for some of the samples. This was dictated by the high number of samples to be analysed. In addition, previous studies [245-247] pointed out that nitrogen does not enter ultramicropores ($d < 0.7$ nm) as its adsorption is usually kinetically restricted because of diffusional limitations. Under this premise, CO_2 adsorption isotherms (see section 3.6.4) were also measured to provide complementary and more reliable information about narrow microporosity. However, in this case the isotherm was measured until $P/P_0 = 0.03$ in order to prevent condensation of carbon dioxide in mesopores at higher absolute pressures.

The routine used for the construction of the N_2 isotherms implied the measurement of 27 points for the adsorption branch, whereas 10 desorption points were acquired by measuring back down to a partial pressure of 0.1. Adsorption and desorption data were then reduced into a series of parameters by using the AS1Win Version 1.25X Quantachrome software, including a comprehensive library of built-in models (see following sections).

3.6.3 N_2 adsorption/desorption data reduction

3.6.3.1 Brunauer-Emmett-Teller (BET) method - Surface area of non-microporous materials

BET theory [248] is widely accepted as method for the determination of the surface area of solid materials. This methodology is usually suitable for an adsorbent exhibiting isotherms of type II (nonporous or macroporous solid) or type IV (a mesoporous material) [242, 249]. N_2 adsorption data obtained for the aforementioned materials usually yield to the linearization of the BET equation ((3.7) [244]) over the P/P_0 range 0.05-0.3.

$$\frac{1}{W \cdot \left(\frac{P_0}{P} - 1 \right)} = \frac{1}{W_m \cdot C} + \frac{C - 1}{W_m \cdot C} \left(\frac{P}{P_0} \right) \quad (3.7)$$

where, P is the absolute pressure of the adsorbate (i.e. nitrogen), P_0 is the saturation pressure of nitrogen at its boiling point (77 K), W is the weight of gas adsorbed at a relative pressure P/P_0 , W_m is the weight of the adsorbate monolayer formed over the surface of the adsorbent, and C is the BET constant. The latter is proportional to the magnitude of the adsorbent/adsorbate interactions. Low values of this parameter (2 to 50 $m^2 \cdot g^{-1}$) represent a weak adsorption process usually occurring on adsorbents with low surface areas,

such as metals, polymers and organics. Oxides and silicates normally exhibit intermediate values (50 to 200 m²·g⁻¹) of the C constant, whereas activated carbons are generally characterized by C values higher than 200 [250].

The surface area of raw feedstock and chars was determined by applying the multipoint BET approach over the conventional P/P₀ range (0.05-0.3). However, as described in section 3.6.3.1.2, a single point approach could also be applied.

3.6.3.1.1 Multipoint approach

According to equation (3.7), when plotting 1/[W(P₀/P)-1] (y) vs P/P₀ (x), a straight line should best fit the experimental data. As a result, the intercept (y₀) and the slope (m) of the straight line will be defined as in equations (3.8) and (3.9) respectively.

$$y_0 = \frac{1}{W_m \cdot C} \quad (3.8)$$

$$m = \frac{C - 1}{W_m \cdot C} \quad (3.9)$$

Once the intercept y₀ and the slope m have been determined by linear regression, it will be possible to calculate C and W_m by combining equations (3.8) and (3.9). Accordingly, the total surface area (S_t), expressed in m² (after appropriate unit conversion), was determined from equation (3.10).

$$S_t = \frac{W_m \cdot N \cdot A_{cs}}{M} \quad (3.10)$$

where, W_m is the weight of a monolayer, A_{cs} is the cross-sectional area value for nitrogen, assumed to be equal to 0.162 nm², N is the Avogadro's number (6.023·10²³ molecules·mol⁻¹), and M is the molecular weight of the adsorbate (28.013 g·mol⁻¹ for N₂).

The specific surface area (S), expressed as m²·g⁻¹, can be then obtained as equation (3.11)

$$S = \frac{S_t}{W_s} \quad (3.11)$$

where, W_s is the mass of sample analysed.

Note that the software returns a dimensionless value of the intercept (i.e. W_m), which is already normalized by the sample weight. Therefore, the specific surface area can be calculated directly as equation (3.10).

However, the validity of the BET method requires the fulfilment of two criteria:

- a) The BET plot must be linear over the P/P_0 range considered;
- b) The intercept y_0 must be positive, as negative values of this parameter would lead to meaningless values of the constant C .

If, for a certain material, these conditions are not met, the BET equation cannot be applied for that particular sample. Therefore, the P/P_0 range was accurately selected by applying the following procedure [250]:

- i. Acquire as many points as possible within the P/P_0 range 0.05 to 0.3; Preferably acquire even more points and extend the range to P/P_0 =ca. 0.4. However, points above 0.5 should not be considered as the BET model fails at predicting multilayer formation leading to the capillary condensation of the adsorbate within the pores;
- ii. Determine the upper limit of the linear BET range by calculating the single-point (see section 3.6.3.1.2) BET area using each datum point in turn. Normally, the calculated single-point area will increase with increasing P/P_0 up to some maximum, beyond which the calculated value will decrease. That maximum indicates the upper limit for the multi-point range. However, in certain cases, the calculated single-point value never goes through a maximum. This would be evidenced by a gradual decrease in slope in the BET plot.
- iii. Discard points at P/P_0 values above the upper limit found at (“ii”) and/or discard any other P/P_0 values that clearly do not lie on a straight BET line from the multipoint surface area calculation. Refine the BET plot as long as at least three [244] data points are left.

3.6.3.1.2 Single-point approach

As an alternative to the multipoint approach, a simplified procedure can also be applied, which entails using only one data point lying within the linear region of the BET plot. This procedure is based on assuming the intercept of the BET equation is equal to zero (and the slope equal to $1/W_m$). This assumption is acceptable whenever the C value is sufficiently large (e.g. for activated carbons). Accordingly, solving for W_m , equation (3.7) will reduce to equation (3.12). The latter can be used to calculate the monolayer capacity once the amount of nitrogen adsorbed at one relative pressure has been measured (preferably near $P/P_0=0.3$, which usually gives good general agreement with the multi-point estimation).

$$W_m = W \cdot (1 - P/P_0) \quad (3.12)$$

Considering the ideal gas law, equation (3.12) can be rearranged as equation (3.13).

$$W_m = \frac{P \cdot V \cdot M}{R \cdot T} \cdot (1 - P/P_0) \quad (3.13)$$

Finally, by replacing the expression for W_m found from equation (3.13) in equation (3.10), the surface area can be expressed as equation (3.14).

$$S_t = \frac{P \cdot V \cdot N \cdot A_{cs}}{R \cdot T} \cdot (1 - P/P_0) \quad (3.14)$$

3.6.3.2 BET method - Surface area of microporous materials

The BET equation is not rigorously applicable to microporous adsorbents mainly because it is not easy to disentangle the monolayer formation process from micropore filling [251]. In fact, monolayer completion is supposed to occur at around $P/P_0=0.01$, thus overlapping with the standard pressure range used for BET method. As the BET model does not take into account micropore filling, the surface area tends to be underestimated. On the other hand, adsorbate molecules lying at the centre of super-micropores ($d>0.7$ nm) do not touch the adsorbent surface, implying that the surface area will be overestimated [249].

However, an equivalent BET area for microporous materials can still be found by following the procedure recommended by the International Standard Organization (ISO) [249]. This methodology is essentially based on the following criteria:

1. The constant C should be positive (same as criterion b) section 3.6.3.1.1);
2. BET equation should be applied within a P/P_0 range where the term $n_a \cdot (1-P/P_0)$ continuously increases with P/P_0 . Note that, as n_a represents the number of moles of adsorbate, this will be proportional to the weight of the adsorbate W . In other words, it is also possible to consider the increasing trend of the term $W \cdot (1-P/P_0)$. Furthermore, as the single-point surface area is proportional to $W \cdot (1-P/P_0)$, it can be said that the second ISO criterion essentially coincides with the point ("ii") listed in section 3.6.3.1.1.

As the linear region of the BET plot seems to be normally shifted to lower relative pressures for microporous materials, the lower limit of the P/P_0 range was extended down to 0.01. The modified range recommended by ISO was used for the calculation of the surface area of the activated carbons, which generally presented a highly developed microporous structure.

Correlations between surface areas obtained by applying the BET method either over a conventional ($P/P_0=0.05-0.3$) and ISO pressure range ($P/P_0=0.01-0.1$) to selected activated carbons is reported in Appendix B. Samples were grouped in virgin and PEI-modified carbons. For both data series, a linear

relationship was found with a relatively high coefficient of determination (in excess of 0.9996). The linear equations had a slope very close to 1 and intercept near to 0, thus signifying that, for the set of samples analysed, the calculation of surface area was not significantly affected by the BET approach applied (Conventional or ISO).

3.6.3.3 Total pore volume - Gurvitsch's rule

Total pore volumes (V_{tot}) were estimated by applying Gurvitsch's rule [252]. This entailed converting the amount of nitrogen adsorbed (V_{ads}) at saturation ($P/P_0=0.99$ [118]) in the corresponding volume of liquid adsorbate (V_{liq}), expressed as $\text{cm}^3_{liq}\cdot\text{g}^{-1}$, by applying equation (3.15).

$$V_{tot} = V_{liq} = \frac{P_a \cdot V_{ads} \cdot V_m}{R \cdot T} \quad (3.15)$$

where, P_a and T refer to the standard pressure and temperature conditions (1 atm and 273.15 K respectively), V_m is the molar volume of the liquid adsorbate ($34.7 \text{ cm}^3\cdot\text{moles}^{-1}$ for N_2), and R is the universal gas constant ($82.0575 \text{ cm}^3\cdot\text{atm}\cdot\text{K}^{-1}\cdot\text{moles}^{-1}$).

3.6.3.4 Mesopore volume - Barrett-Joyner-Halenda (BJH) model and choice of the isotherm leg

Mesopore size was determined assuming cylindrical geometry of the pores and starting from the (modified) Kelvin equation, which gives the pore radius wherein condensation occurs at a relative pressure P/P_0 [244]. In particular, the BJH [253] model suggested a corrected expression for the actual pore radius (r_p), given by the Kelvin radius (r_K) plus the thickness of the adsorbate layer (t) which is adsorbed onto the pore walls prior to condensation during adsorption, or which remains on pore walls after evaporation during desorption. The thickness of the adsorbed layer also depends upon the relative pressure P/P_0 . The BJH model calculates the pore volume by considering the average values of the Kelvin radius and layer thickness calculated at the upper and lower limits of each P/P_0 increment (adsorption step)/decrement (desorption step). Cumulative values of mesopore volumes were then calculated by integration of the BJH pore size distribution between 2 and 50 nm [242, 254].

The choice of the isotherm leg for the application of the BJH model has been widely argued in the literature. In theory, desorption branch would be more appropriate because, for the same volume of adsorptive gas, it exhibits a lower relative pressure compared to that associated with the adsorption leg. This implies a lower free energy state, which is closer to the true thermodynamic stability [244]. In contrast, Kruk *et al.* [255] showed that their modified form of the Kelvin equation [256] failed at calculating the pore size distributions for a

cylindrical geometry of pores when considering nitrogen desorption at 77 K, in particular for relative pressure (P/P_0) higher than 0.4. This was mostly due to the irreversibility of the isotherms at $P/P_0 > 0.4$ because of the condensation of the adsorbate inside the mesopores. In addition to this, the choice of the isotherm leg depends on the type of hysteresis shown, which is related to the shape of the pores. Most of the isotherms measured in this study were characterized by an H3 hysteresis loop [242]. This type of hysteresis does not exhibit any limiting adsorption near saturation, and is characteristic of aggregates of plate-like particles, thus implying slit-shaped pore geometry. Under these conditions, as suggested by IUPAC recommendations, the application of the BJH model to the adsorption data would give a more accurate estimate of the pore size distribution. Further explanations about the analysis of mesoporosity are also given elsewhere [256, 257].

Nevertheless, for most of samples the hysteresis loop did not close properly, probably due to inefficient degassing, giving rise to LHP. Therefore, in order to have a direct comparison of the mesopore volume for all the samples, the adsorption branch of the N_2 isotherm was chosen in this study for the application of the BJH model. Isotherms hysteresis is compared for few representative samples in Chapter 4. Moreover, mesopore volumes determined by applying the BJH model to the desorption leg of the N_2 isotherm were also calculated. Note that, when measuring the desorption leg of the N_2 isotherm only 10 points were acquired (see section 3.6.2), simulated values of cumulative (meso)pore volumes were generated by interpolating the known data given by the BJH distribution over the target range (2-50 nm).

3.6.3.5 Micropore volume - Dubinin-Radushkevich (DR) model

The DR model is based on the Polanyi potential theory of adsorption [258]. On this premise, Dubinin and Radushkevich [259] assumed that the fractional filling of the micropore volume (V/V_0) can be related to the adsorption potential (A) as in equation (3.16) [244]:

$$\frac{V}{V_0} = e^{-\left(\frac{A}{\beta E_0}\right)^2} \quad (3.16)$$

where, A is given by equation (3.17):

$$A = RT \ln(P/P_0) \quad (3.17)$$

V is the volume occupied by the liquid adsorbate, V_0 is the micropore volume, E_0 is denoted as characteristic energy of adsorption, and β is the affinity coefficient, which is determined as in equation (3.18) [244]:

$$\beta = \frac{v}{v_{C_6H_6}} \quad (3.18)$$

where, v and $v_{C_6H_6}$ are the liquid molar volume of a given adsorbate and benzene (used as the reference liquid) respectively. In this study, a β value of 0.39 was used.

The volume of liquid adsorbate and micropore volume can be converted into their corresponding weights using equations (3.19) and (3.20) respectively [256]:

$$W = V \cdot \rho \quad (3.19)$$

$$W_0 = V_0 \cdot \rho \quad (3.20)$$

where, ρ is the adsorbate liquid density (equal to $0.808 \text{ g}\cdot\text{cm}^{-3}_{\text{liq}}$ for nitrogen). After substituting equations (3.17), (3.19) and (3.20) in equation (3.16), and applying base-10 logarithm to both sides, the latter can be rearranged in a linear form as equation (3.21):

$$\log_{10} W = \log_{10} W_0 - 2.303 \frac{RT}{\beta E_0} \cdot [\log_{10}(P_0/P)]^2 \quad (3.21)$$

where, 2.303 is the conversion factor from natural to base-10 logarithm.

According to equation (3.21), when plotting the N_2 isotherm data as $\log_{10}(W)$ vs $[\log_{10}(P_0/P)]^2$, W_0 and E_0 can be calculated by linear regression. In particular, the DR plot was obtained for $P/P_0 < 0.02$. The micropore volume (W_0) and energy of adsorption (E_0) were then calculated from the intercept and slope of the linear relationship equation (3.21) respectively.

3.6.3.6 Pore size distribution (PSD) - Non-local density functional theory (NLDFT) model

It is widely accepted that the application of theories based on macroscopic approaches and thermodynamics (such as the BJH approach or semi-empirical methods) for the calculation of the pore size distribution lead to an underestimation of pore sizes because of an unrealistic interpretation of the pore filling, especially in the micropore domain [243]. In contrast, the density functional theory (DFT) method allows for a more accurate analysis of micropore size, as it is based on a microscopic approach. In particular, this method relies on the fundamental principles of statistical mechanics in order to describe the adsorption behaviour and the local structure of fluids (i.e. the liquid adsorbate) confined in the pores on a molecular level. Further details related to the DFT methodology have been reported elsewhere [260-262].

However, the (local) DFT method seems to fail at analysing narrow micropores widths [263]. Therefore, NLDFT was introduced as an improved methodology [260] which has been extensively applied for the pore size

analysis of micro and mesoporous carbons [93, 116, 264]. The NLDFT model was used for the calculation of the PSDs of the materials analysed in this study.

As explained by Jagiello and Thommes [265], the key feature of the pore size distribution calculation when using the NLDFT approach is the kernel. Essentially, the latter consists of a set of theoretical isotherms generated by applying non-local density functional theory for each pore size and for a given adsorbate-adsorbent system. The kernel is obtained from the integration of the equilibrium density profiles of the adsorbate in model pores (adsorbent). The calculated isotherms will depend upon a series of parameters characteristic of the given adsorption system (i.e. carbon-N₂ or carbon-CO₂), such as adsorbate/adsorbate and adsorbate/adsorbent interactions as well as pore geometry [263].

The final pore size distribution can be obtained by solving the integral adsorption equation (IAE) [263] also called generalized adsorption isotherm (GAI) equation [243]. The application of this relationship assumes that the experimental isotherms can be calculated via integration of the contributions given by each single reference isotherm (related to a certain pore width) multiplied by their relative pore distribution (weighting function), over a determined range of pore sizes. The solution of the integral is obtained by using a fast non-negative least squares algorithm [263], which minimizes the fitting error of NLDFT calculated isotherms to the experimental isotherm. In other words, the resulting PSD is the contribution by volume from different (ideal) pores of fixed widths, whose combination of ideal isotherms best fit the experimental data.

Micropore and smaller mesopore distributions were determined by selecting the NLDFT N₂-carbon kernel (77K) provided by the software used in this work, which was based on a slit-pore model with graphite-like parallel walls [244, 266].

3.6.4 CO₂ adsorption data reduction

As already mentioned in section 3.6.2, the use of nitrogen at 77 K for the characterization of narrow microporosity is not recommended, as the access of N₂ to smaller pores is restricted by diffusional limitations. In contrast, using CO₂ as the adsorptive gas at 273 K was proved to be a more reliable solution for the assessment of ultramicropores ($d < 0.7$ nm) [245-247]. Although the kinetic diameters of the two adsorptives are similar (0.33 nm and 0.38 nm for CO₂ and N₂ respectively [245]), the higher temperature condition favours the diffusion of carbon dioxide into the smaller pores. In addition to this, at 273 K, the saturation vapour pressure of CO₂ is much higher (ca. 26140 Torr) than that of nitrogen (760 Torr) [266]. Consequently, lower values of absolute pressure are required for the analysis of narrow microporosity compared to those needed when

measuring nitrogen adsorption. For instance, a relative pressure P/P_0 of 10^{-5} (corresponding to the first point acquired for the measurement of the CO_2 adsorption isotherm) yields an absolute pressure of 0.2614 Torr when using CO_2 as the adsorptive gas. Conversely, the same relative pressure would give a significantly lower absolute pressure (i.e. 0.0076 Torr) when using N_2 as the adsorptive. It follows that the ultramicroporous domain (corresponding to the lowest values of relative pressure) is more easily accessed by CO_2 than by N_2 . In fact, higher temperatures and absolute pressures enhance the diffusion of carbon dioxide through the pores of the adsorbent. Accordingly, faster diffusion rates allow easier access to smaller pores and shorter analysis time (ca. 3 h) compared to that observed when using N_2 as the adsorptive (30 h or longer) [266].

On the other hand, when measuring CO_2 adsorption at 273 K it was not possible to produce a full isotherm, as carbon dioxide would have condensed in mesopores for relative pressures P/P_0 higher than 0.03 [246, 262].

Pore size distributions by volume for pores having widths below 1.5 nm were achieved through the application of the NLDFIT model (see section 3.6.3.6) to the CO_2 adsorption data prior to changing kernel to “NLDFIT - CO_2 - carbon equilibrium transition kernel at 273 K”, assuming a slit-pore model [244]. Integration of the NLDFIT PSD for $d < 0.7$ nm allowed calculation of the ultramicropore volume, denoted as $V_{\text{umi, NLDFIT}}$. Additionally, ultramicropore volume was also determined by applying the DR model (see section 3.6.3.5) to the CO_2 adsorption data ($P/P_0 < 0.02$). The latter parameter was designed as $V_{\text{umi, DR}}$.

3.7 Chemical, morphological and structural analyses

3.7.1 Elemental analysis (CHNS)

Elemental analysis (C, H, N, S) of raw biomass, chars and activated carbons was carried out by using an elemental analyser (Flash EA2000). Samples preparation entailed weighing around 2.5 mg of material, which was sealed within a tin capsule. Each sample was prepared in duplicate. Along with the samples, a series of standards and references having known elemental compositions were also included in the analysis for calibration and comparison purposes respectively.

After this, tin capsules were dropped into the combustion chamber of the instrument. Here, a temperature of ca. 900-1000 °C was held and excess oxygen was injected via the helium carrier gas. Once the tin is exposed to the extremely oxidizing atmosphere, a strong exothermic reaction is triggered. The temperature increases up to ca. 1800 °C instantly causing the complete oxidation of the sample. The combustion gaseous products are then swept

through the reduction reactor, where CO₂, H₂O, NO₂ and SO₂ are formed. Afterwards, the reduced gases pass through and separate in a chromatography column. The amount of each gas phase is measured using a thermal conductivity detector (TCD), which is calibrated with the aforementioned standards. Gas concentrations are then converted into weight percentages of carbon (C), hydrogen (H), nitrogen (N) and sulphur (S) by means of dedicated software. Prior to analysis, samples were dried overnight at 105 °C, therefore results were obtained on a dry basis. O content was estimated by difference as in equation (3.22):

$$O = 100 - (C + H + N + S) \quad (3.22)$$

3.7.2 Proximate analysis

Standard procedures recommended by the British Standards Institution (BSI) were used to determine moisture (M) [267], volatile matter (VM) [268] and ash (A) content [269] of raw biomass and chars. Measurements were carried out in duplicate. Fixed carbon (FC) was obtained by difference.

As concerns activated carbons, proximate analyses were carried out via two different methods. Standard methodology recommended by American Society for Testing and Materials (ASTM) [270] allowed the determination of M, VM and A contents, whereas even in this case FC was calculated by difference. However, when only small quantities of sample were available for analysis, the use of a STA 8000 thermogravimetric analyser was preferred to the standard procedure. In fact, Thermogravimetric Analysis (TGA) only requires 10 to 20 milligram of material for each sample, whereas 1 g of sample for each duplicate are used with the standard methods. This applied to the carbons obtained through KOH activation, whose yield was much lower than that obtained after physical (CO₂) activation of the chars (see Chapters 4 and 5). Therefore, a TGA routine was specifically created for the determination of proximate analyses. In particular, few mg of each sample was loaded into a small alumina crucible. Materials were first heated in air at 15 °C·min⁻¹ up to 105 °C and held at this temperature for 10 min. This first step entailed determining the moisture content. Devolatilization of the sample was then achieved by switching the gas atmosphere to N₂ and raising the temperature up to 900 °C at the same heating rate. This allowed the determination of the volatile matter in the material. Finally, the gas flow was changed back to air and samples were held at 900 °C for 30 min in order to burn off the carbon fraction of the sample, thus leaving inorganic material within the crucible. This last step enables the calculation of fixed carbon and residual ash. Data were corrected for the influence of buoyancy by baseline subtraction. The latter was measured by running the same experiment with an empty sample holder.

In addition, STA 8000 instrument produced Differential Thermogravimetric Analysis (DTGA) evolution profiles, which enables identifying the (peak) temperature associated with a particular change in sample mass.

3.7.3 X-Ray Diffraction (XRD)

This non-destructive technique is based on X-ray diffraction theory [271, 272]. In particular, considering the scheme illustrated in Figure 3-8, Bragg's law can be derived as in equation (3.23). This relationship inversely relates the diffraction angle (2θ) between the incident X-ray hitting the first atomic layer (hkl) and the X-ray diffracted from the second atomic layer, to the interplanar spacing (d_{hkl}) between the two parallel atomic layers. It follows that, the larger the space between the crystal planes, the lower the corresponding angle of diffraction of the X-ray radiation.

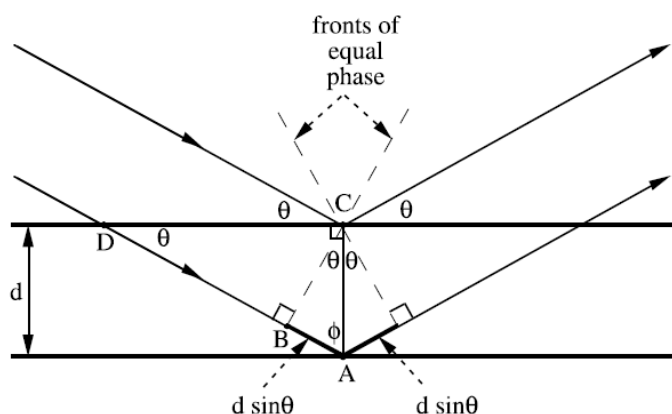


Figure 3-8 Scheme representing the interference of an incident X-ray (wavelength λ) scattered from two parallel atomic layers (hkl) separated by an interplanar distance d .

$$2d \cdot \sin \theta = n\lambda \quad (3.23)$$

where, d is the interplanar spacing, θ is the angle of incidence of an X-ray, n is equal to 1 and λ is the wavelength.

The XRD pattern is obtained by plotting the X-ray diffraction intensity vs. the scattering angle (2θ). The instrument used for recording an XRD pattern is the X-ray powder diffractometer, which normally includes an X-ray source, a goniometer, which allows mounting and orienting of a sample, and a detector, which enables the X-ray intensity to be measured over the desired 2θ diffraction range. Note that X-ray diffraction of powders does not require orientating the sample with respect to the incident beam, as the microcrystalline nature of powder means crystallites are randomly oriented [273].

XRD analyses were conducted in an attempt to investigate the presence of inorganic crystalline compounds within the structure of the materials included in this work. XRD patterns were recorded using a Bruker D8 powder diffractometer system operating with a Cu K α radiation source. The X-ray patterns were acquired by means of the software DIFFRACPlus and recorded in the 2 θ range 10-80°, with a step width of 0.033° and a time per step of 1 s. Prior to measuring XRD patterns, samples were dried at 105 °C overnight.

In order to identify crystalline phases present within the materials, measured XRD patterns were matched to an X-ray diffraction database library provided by the software package Highscore (Panalytic, UK).

In addition, the size of the crystallites was calculated according to the Scherrer equation (equation (3.24)) [274]:

$$\frac{K \cdot \lambda}{FWHM \cdot \cos \theta} \quad (3.24)$$

where, K is the shape factor and was assumed to be 0.9, λ was 0.154 nm, FWHM is the full width at half maximum in radians, and θ was half the Bragg diffraction angle.

3.7.4 Scanning Electron Microscope (SEM) and Energy-Dispersive X-ray (EDX) spectroscopy

A Carl Zeiss EVO MA15 SEM, having a nominal resolution of 3nm at 30kV, was used to examine the surface morphology of the raw biomass, chars and activated carbons. The instrument was operated with a working distance of 8 to 9 mm and an accelerating voltage of 20 kV using an in lens detector. Further specifications about the microscope used in this work are given elsewhere [275].

Samples were normally oven-dried at 105 °C overnight prior to analysis. A small amount of dry powder was then mounted on aluminium stubs, and any excess material was removed by airblowing. Furthermore, in order to make the sample conductive and avoid charging, the specimens were usually gold coated using an Emscope SC500 specimen vacuum gold coater with a 30 nm layer of 99.99% Au at 20 mA. Coated samples were then stored in a desiccator prior to analysis.

Secondary electron images, sensitive to surface topography, were taken at 5000 x magnification for all samples. Moreover, a semi-quantitative analysis of the samples' inorganic components was conducted using the Oxford EDX system integrated with the scanning electron microscope (liquid nitrogen-free X-Max Silicon Drift Detector (SDD) [276]).

EDX technique relies on the detection of the X-rays generated when an inner shell electron is displaced by an incident electron of the microscope beam hitting the sample. As each element gives rise to a specific X-ray energy, EDX analysis allows for elemental identification [276]. AZtec software was used to obtain EDX spectra and maps and relevant elemental compositions.

In addition, the cross section of a virgin commercial carbon (AR) and its optimally-PEI impregnated counterpart (AR-PEI) were also examined by using back-scattered imaging (atomic weight-sensitive). This was done in an attempt to localize the presence of the polymer within the pores of the carbon support. In this case, materials were embedded into a Transoptic resin by using a mounting press. After cooling, specimens were sequentially subjected to grinding and polishing steps in order to expose the cross section.

3.7.5 Boehm titrations

Boehm titrations were carried out according to the methodology reported by Bagreev *et al.* [277]. A gram of each activated carbon was mixed with 50 ml of 0.05 M solutions of either sodium hydroxide (NaOH) or hydrochloric acid (HCl) in vials, which were sealed and shaken for 24 h. Solutions were previously standardized following the procedure suggested by Oickle *et al.* [278]. The content of the vials was filtered and 5 ml of each filtrate was pipetted into a beaker. The excess of base or acid was then titrated with either HCl or NaOH, respectively. The amounts of overall basic and acidic groups were calculated as given in equations (3.25) and (3.26) respectively according to the relationships reported by [279] for direct titrations.

$$\mathbf{Basic} = \frac{[\mathbf{HCl}] \cdot V_{\mathbf{HCl,mix}} - ([\mathbf{NaOH}] \cdot V_{\mathbf{NaOH,cons}} \cdot \mathbf{DF})}{m_{\mathbf{carbon}}} \quad (3.25)$$

$$\mathbf{Acidic} = \frac{[\mathbf{NaOH}] \cdot V_{\mathbf{NaOH,mix}} - ([\mathbf{HCl}] \cdot V_{\mathbf{HCl,cons}} \cdot \mathbf{DF})}{m_{\mathbf{carbon}}} \quad (3.26)$$

where, Basic and Acidic are the mmol of basic and acidic surface groups respectively per unit of mass of carbon (m_{carbon}), [HCl] and [NaOH] are the concentration values of the standardized solutions, V_{HClmix} and V_{NaOHmix} are the volumes of the standardized solutions mixed with the carbon, V_{NaOHcons} and V_{HClcons} are the volumes of the standardized solutions consumed during titration, and DF is a dilution factor equal to 10.

Results were interpreted according to the assumption that NaOH neutralizes all acidic groups (carboxylic, phenolic and lactonic groups) and HCl reacts with all basic groups.

3.7.6 Fourier Transform Infrared (FTIR) spectroscopy

FTIR spectra were collected in attenuated total reflection (ATR) geometry on a Thermo Scientific iS10 FTIR spectrometer, over a wavenumber range of 4000 - 600 cm^{-1} . An environmental background was subtracted every 10 min. FTIR analysis was used to identify any residual inorganic (potassium-based) compounds after chemical treatment of chars (KOH activation followed by washing). This allowed assessment of the efficacy of the washing procedure (see section 3.4.2) for the removal of K-based species. Samples were previously dried at 105 °C overnight prior to acquiring spectra.

A detailed description of this characterization technique can be found elsewhere [280].

3.7.7 X-ray Photoelectron Spectroscopy (XPS)

XPS is a non-destructive surface-sensitive technique. In particular, the electronic states of the atoms present within the outer layer (up to 10 nm) of the specimen's surface are excited by X-ray radiation of a known energy. Inner shell electronic excitation gives rise to the emission of photoelectrons, whose energy is filtered via a hemispherical analyser (HSA) and then measured through an electron energy analyser. The energies of the photoelectrons correspond to a specific binding energy of the electronic states of atoms [281].

XPS spectra are then obtained by recording the energy of the photoelectrons escaped from the sample surface, expressed as counts·sec⁻¹, vs. the correspondent electron binding energy (eV). The peak intensities are proportional to the atomic concentration, whereas peak positions (i.e. binding energies) give indications about the type and the chemical states of the element identified [281].

XPS analysis was conducted in an attempt to identify the type of N-containing functional groups, which were incorporated onto the surface of a commercial carbon (AR) following PEI impregnation. In order to do this, the virgin activated carbon and its PEI-modified counterpart were also analysed.

XPS spectra were measured using the National EPSRC XPS Users Service (NEXUS) facility at the University of Newcastle, with the aid of a Thermo Scientific Theta Probe XPS provided with a microfocused monochromatic aluminium K-alpha X-ray source. The spot size was 400 x 800 μm . Pass energies were 200eV and 40eV for survey and high resolution spectra respectively.

Prior to packing and sending the samples out, materials were accurately immobilized by making a “sandwich” between two layers of indium foil, which reduced charging during measurement.

3.8 CO₂ capture performance

The CO₂ capture performance of the sorbents was assessed by means of a thermogravimetric analyser (Mettler Toledo TGA/Differential Scanning Calorimetry (DSC) 1). CO₂ uptakes were determined thermogravimetrically by creating appropriate routines (see the following section and also Chapter 4). The instrument allowed the temperature to be varied as well as the gas atmosphere. Gas cylinders containing pure (99.8%) or 15% v/v CO₂ in N₂ were purchased from BOC Gases Ltd, whereas the purging gas (nitrogen) was directly piped in. The adsorption gas and temperature conditions for the programmes used in this experimentation are reported below:

- i. Pure CO₂, ca. 35 °C (first screening);
- ii. 15% v/v CO₂ in N₂, ca. 53 °C (simulated post-combustion conditions);
- iii. 15% v/v CO₂ in N₂, ca. 77 °C (simulated post-combustion conditions, higher temperature);
- iv. Pure N₂, ca. 53 °C (correction of programme “ii” for nitrogen adsorption)¹.

All experiments were run at atmospheric pressure. For each programme created, a blank run (empty pan) was first conducted under identical test conditions in order to correct sample data for buoyancy effects (see also Chapter 4).

3.8.1 Calculation of CO₂ sorption capacity - TGA programmes

All samples were initially degassed under nitrogen (flow rate of 50 ml·min⁻¹) at 120 °C for 30 min. Subsequently, materials were cooled down to the desired temperature (35, 53 or 77 °C). At this stage, the gas atmosphere was switched to pure CO₂, 15% v/v CO₂ in N₂ (total 50 ml·min⁻¹), or pure N₂. The temperature was kept constant for 30 min in order to measure the equilibrium capacity of the materials when exposed to the reactive gas. The resulting weight increase was interpreted as the adsorption capacity of the sorbents at the chosen temperature and for the given adsorbate. Note that, the exact value of the uptake at saturation was calculated both by using the “step horizontal” command of the TGA software and by further data processing through MS Office Excel. Afterwards, the temperature was increased up to 100 °C at a fixed heating rate (5 °C·min⁻¹) to see the effect of the temperature on the desorption capacity of the materials. Finally, the atmosphere was switched back

¹ The amount of sample used was the same as that used for ii

to N₂ and the temperature was increased to 120 °C to complete the desorption step.

The cyclic performance of the sorbents was also tested by repeating the post-combustion routine (“ii”) over 10 cycles. In this case, regeneration was accomplished in just a single step, which entailed heating the sample (heating rate of 5 °C·min⁻¹) up to 120 °C without changing the partial pressure of CO₂ (i.e. atmosphere was changed back to N₂ only once it had reached the final temperature for the start of the following cycle). This allowed simulation of a RTSA as a regeneration strategy.

Explanatory results related to TGA methods used are given in Chapters 4 and 6.

3.8.2 Calculation of heat of adsorption/desorption - DSC data

DSC data (i.e. heat flow) related to the post-combustion programme “ii” (ca. 53 °C, 15% v/v CO₂ in N₂ (total 50 ml·min⁻¹)) were used to calculate the heat of adsorption (ΔH_{ads}) and the heat of desorption (ΔH_{des}) according to the equation suggested by [116]. In particular, the heat flow raw data, expressed as mW, was integrated by using Origin Pro “Integrate” function over the relevant time span (0<t<30 min for adsorption or 30<t<40 min for desorption). Integral values were defined as Total enthalpy of adsorption/desorption and expressed as kJ after appropriate unit conversion. The latter was divided by the amount (expressed as moles) of gas (CO₂ or N₂) adsorbed onto/desorbed from the sample during the adsorption (0-30 min)/desorption (30-40 min) steps, which yielded the final value of heat of adsorption/desorption expressed as kJ·mol⁻¹.

4 Eco-friendly synthesis of selective CO₂ sorbents for post-combustion capture: the key role of basicity

4.1 Outline

This chapter is concerned with the preparation of activated carbons (ACs) starting from a traditional type of biomass, i.e. oak wood. The final ACs were then tested for CO₂ sorption.

As described in section 4.2, the raw feedstock was subjected to both to conventional pyrolysis and to hydrothermal carbonization (HTC). The repeatability of carbonization processes was evaluated in terms of char yield. As concerns hydrothermal synthesis, repeatability of water balance (see Chapter 3) was also evaluated.

In section 4.3, results related to the optimization of the CO₂ activation of oak wood chars are reported. In particular, the effect of activation temperature and holding time on the texture of the resulting carbons was studied. Chemical treatment using KOH was also applied. In this case, optimal conditions obtained for *Laminaria hyperborea* (see Chapter 5) were used. In addition, the effect of the washing procedure was studied. Also, repeatability of the activation process (i.e. activation yield) and textural properties of final carbons was evaluated.

Section 4.4 summarizes the textural properties of the optimally-activated carbons (only), comparing these with chars and raw material. This allowed highlighting of the change of porosity of the raw oak wood after each treatment applied (i.e. carbonization, activation). Insights concerning hysteresis phenomena are given for few representative samples. Textural characterization of a commercial carbon (GAC) was also included for comparison purposes. Moreover, CO₂ adsorption isotherms were measured for all selected samples to investigate narrower microporosity.

In section 4.5, attention is focused on how the abovementioned treatments affected the structure and the chemistry of the raw feedstock. Elemental and proximate analyses provided primary information about the chemical properties of the oak wood-derived materials. The morphology of the samples was examined through Scanning Electron Microscope (SEM) imaging. Energy-Dispersive X-ray (EDX) spectroscopy analyses corresponding to the SEM micrographs were also acquired in order to reveal the chemical nature of inorganic fractions found in the samples. Furthermore, X-Ray Diffraction (XRD) patterns were measured in an attempt to detect the presence of inorganic crystalline phases within the structure of oak wood-based samples.

A quantitative estimation of basic and acidic groups present on the surface of oak wood-based materials was obtained by Boehm titration. However, it is worth noting that, as this technique required a significant amount of sample, only some of the oak wood-derived samples were analysed. For instance, despite the largest texture development (see Table 4-9) exhibited by KOH-activated hydrochar (i.e. OW250CA), this material was discarded because of the extremely low activation yield (see Table 4-6). Furthermore, priority was given to samples exhibiting the most selective sorption under post-combustion conditions, as this was believed to be due to greater basicity. Based on these selection criteria, it was decided to focus on the comparison of pyrolyzed oak wood and its activated derivatives. Routines for the measurement of CO₂ sorption capacities are presented in section 4.6 for a representative sample. CO₂ uptakes were measured under two different sets of conditions. A first screening of the sorption potential for all the materials was carried out at higher partial pressure (100% by volume or 1 bar) and lower temperature (35 °C). In addition to this, the best performing samples were also tested for simulated post-combustion capture (0.15 bar, 53 °C). In particular, the samples selected were those that showed either the highest pure CO₂ uptakes (see Figure 4-28) or regeneration behaviour at higher temperatures that suggested chemisorption behaviour (see Figure 4-30).

Finally, in section 4.7, conclusions about the entire chapter are drawn.

4.2 Carbonization of oak wood

4.2.1 Repeatability of dry pyrolysis and HTC

The repeatability of carbonization processes was evaluated in terms of char yield. In addition, variability of water balance associated with hydrothermal process was also studied. Experimental runs were carried out in triplicate.

As concerns traditional pyrolysis, around 5 g of raw oak wood was carbonized in a ceramic furnace and all conditions (see Chapter 3) were kept the same in each run. Note that repeatability of liquid and gas fraction was not reported as no condensable were obtained during the runs. This was probably due to the low amount of raw material used and the high nitrogen flow rate, which apparently swept away all volatiles preventing their condensation in the bubbler.

With respect to HTC, ca. 24 g of raw feedstock were mixed with 220 g of distilled water and heated up at 250 °C for 1 h. Hydrothermal carbonization runs were also carried out in triplicates.

From results presented in Table 4-1, it is possible to see that the average yield obtained after dry carbonization of raw oak wood (21.50 wt%) was around

one third the analogue value recorded after hydrothermal carbonization (58.46 wt%). This result would suggest hydrothermal carbonization as more cost-effective route for the production of oak wood-based char. It is reasonable to attribute the lower pyrolysis yield to the far higher temperature condition held during traditional treatment. Yet, conventional carbonization caused a more intense devolatilization of the raw feedstock and a higher proportion of fixed carbon (FC) in the final product (see Table 4-11), thus leading to a more stable char.

Average pyrolysis yield was slightly lower than the figure reported by Sanchez *et al.* [160] (26 wt%), who carbonized *Quercus agrifolia* wood waste at 800 °C for 2 h. Moreover, Jindo *et al.* [179] pyrolyzed oak tree (*Quercus serrata*) at 800 °C for 10 h. This study reported a slightly lower char yield (ca. 19.1 wt%) compared to that measured in this work, probably due to the longer dwell time applied.

Traditional pyrolysis runs led to an excellent repeatability regarding the amount of final char obtained, as data showed very low standard deviation (0.3%). Furthermore, calculated standard deviation from the mean (1.45%) was well below the acceptable limit of 10% reported by literature [282], thus indicating an excellent reproducibility of the pyrolysis treatment. In addition to that, the average value of yield (21.50 wt%) was slightly lower than that measured after the pyrolysis (single run) of the same feedstock carried out in a stainless steel vertical furnace (ca. 24 wt%) under the same conditions of nitrogen flow rate and maximum temperature. However, note that pyrolysis rate depended upon the type of rig used, as it was not possible to set a specific heating rate (HR) by using furnace controllers. In particular, large scale-rig (stainless steel vertical furnace) entailed heating up the sample according to a slower heating ramp (ca. 10 °C·min⁻¹) than that observed for ceramic furnace (25 °C·min⁻¹). As suggested by Carpenter *et al.* [181], a slower heating ramp is expected to enhance char production and this may explain the higher yield in the latter case. In addition to that, it worth mentioning that a much larger amount of raw feedstock (ca. 240 g) was carbonized in the bigger rig. Nevertheless, as shown in Chapter 5, reactor loading did not seem to affect the pyrolysis yield after the carbonization of *Laminaria hyperborea* in the large-scale rig.

Average yield measured after hydrothermal carbonization (58.46 wt%) was found to be higher than the datum (43.6 wt%) reported in the work of Karagoz *et al.* [182]. These authors carried out hydrothermal synthesis of oak wood waste (sawdust) under the same conditions of temperature and holding time considered in this study. However, different amounts of raw material and distilled water were used, which might explain discrepancy between results. Additionally, a solid residue yield of 40 wt% was reported by Sevilla *et al.* [183] after hydrothermal carbonization of *Eucalyptus* sawdust. Even in this case, the feedstock/water phase ratio was different from that used in this work.

Furthermore, mixture was held at 250 °C for a longer dwell time (i.e. 2 h), which might have caused a lower char production.

Table 4-1 Repeatability of carbonization processes for raw oak wood

Carbonization				Water balance		
OW800 ²		OW250 ³				
Run	CY _{db} ⁴	Run	CY _{db}	m _{initial}	m _{recovered}	m _{lost}
-	wt%	-	wt%	mg	mg	mg
1	21.80	1	59.71	220.00	155.49	64.51
2	21.18	2	60.70	220.00	161.01	58.99
3	21.52	3	54.98	220.00	166.20	53.80
Mean	21.50	Mean	58.46	-	160.90	59.10
SD ⁵	0.31	SD	2.50	-	4.37	4.37
SD (% Mean)	1.45	SD (% Mean)	4.27	-	2.72	7.40

Table 4-1 also shows that HTC repeats exhibited a slightly higher variability compared to dry pyrolysis, with variation of up to 4.27%. High variability was found for the mass of water recovered after hydrothermal treatment, yielding to standard deviation of up to 4.37%. On the other hand, deviation from the mean reported was below 10% for all the parameters, which suggests an acceptable reproducibility of both carbonization processes [168].

4.3 Activation of oak wood-based chars

4.3.1 CO₂ activation of oak wood-based chars - Optimal conditions

The CO₂ activation of charred oak was carried out at constant flow (0.6 l·min⁻¹) and heating rate (10 °C·min⁻¹). Activation temperature and holding time were varied in order to evaluate their effect on the textural properties of the final carbons. Optimal conditions were those that maximized the surface areas of the resultant porous materials.

² Oak wood (OW) pyrolyzed at 800 °C

³ OW hydrothermally carbonized at 250 °C

⁴ Carbon yield (CY). Db stands for dry basis

⁵ Standard deviation

Note that textural parameters of the initial chars are reported in section 4.4 (see Table 4-9).

4.3.1.1 The effect of the temperature

4.3.1.1.1 Hydrothermally carbonized wood (OW250)

Hydrochar (OW250) was activated at 500, 600 and 700 °C. The final temperature was hold for 30 min in each case. As reported in Table 4-2, although the considerable burn-off (41 wt%), the initial temperature chosen (500 °C) was not sufficiently high to imply a significant increase of surface area of the starting char (see Table 4-9). This might be because when temperature was 500 °C the reaction between char and CO₂ was too slow. As seen in Table 4-2, 600 °C maximized the hydrothermally carbonized oak's surface area, and therefore it was deemed as optimal temperature. This condition corresponded to a burn-off of 46 wt%. It seems that the extra 7% burn-off opened up the (micro)porosity in the sample. Isotherm measured for this sample showed a significant micropore filling at the very beginning of the pressure range. In addition to that, the slope observed over mid pressure range can be attributed to multilayer adsorption process on the non-microporous surface (i.e. mesopores, macropores and external surface) [283].

Conversely, activation at the highest temperature tested (700 °C) was found to be too severe for the hydrochar, leading to higher material burn-off but lower porosity. This was probably because the sample had not experienced any previous high temperature treatment. As a result, a significant drop of pore volume was measured, likely caused by a collapse of the pore walls. This is shown by the lower volume of nitrogen adsorbed at the very low pressure and the milder slope in the mid-pressure range (see Figure 4-1). However, the isotherm shape of all activated carbons is closer to a type II [242], thus indicating a limited micropore percentage (up to 62.5% for OW250PA_600_0.5h). The latter can be calculated from values reported in Table 4-2 using (4.1)).

$$\left(\frac{V_{mi}}{V_{tot}}\right) \cdot 100 \quad (4.1)$$

The ineffectiveness of the lowest activation temperature (500 °C) was further backed by the non-local density functional theory (NLDFT) pore size distribution measured for OW250PA_500_0.5h, as no distinct peaks were observed. This confirmed that at 500 °C CO₂ oxidation of char was too slow to form any significant porosity. On the contrary, ACs obtained at 600 and 700 °C exhibited an intense sharp peak at ca. 0.3 nm, indicating development of ultramicroporosity (d<0.7 nm). However, peak shoulders extending up to ca. 1.2 nm were also observed, suggesting the presence of a supermicropore (d>0.7

nm) population. However, both ultra- and supermicropores decreased with increasing temperature from 600 to 700 °C. In addition to that, optimal sample (OW250PA_600_0.5h) exhibited an additional sharp peak centred at around 0.8 nm and very broad peaks for pore widths higher than 2 nm. The latter indicated a minor contribution of mesoporosity.

Table 4-2 Effect of CO₂ activation temperature (T) on burn-off and textural parameters of hydrothermally carbonized wood; t represents the activation dwell time.

Sample ID ⁶	T	t	BO ⁷	S _{BET} ⁸	V _{tot} ⁹	V _{mi} ¹⁰	V _{me} ¹¹	V _{ma} ¹²
	°C	h	wt%	m ² ·g ⁻¹	cm ³ ·g ⁻¹			
OW250PA_500_0.5h	500	0.5	41	39	0.071	0.020	0.023	0.028
OW250PA_600_0.5h	600	0.5	46	415	0.278	0.173	0.066	0.040
OW250PA_700_0.5h	700	0.5	53	257	0.163	0.102	0.023	0.039

⁶ PA stands for physically activated

⁷ Burn-off

⁸ Surface area calculated by applying Brunauer–Emmett–Teller (BET) method to N₂ adsorption data

⁹ Total pore volume calculated by applying Gurvitsch's rule at P/P₀=0.99

¹⁰ Micropore volume calculated by applying Dubinin-Radushkevich (DR) model to N₂ adsorption data

¹¹ Mesopore volume calculated by applying Barrett-Joyner-Halenda (BJH) model to N₂ adsorption data

¹² Macropore volume calculated by difference

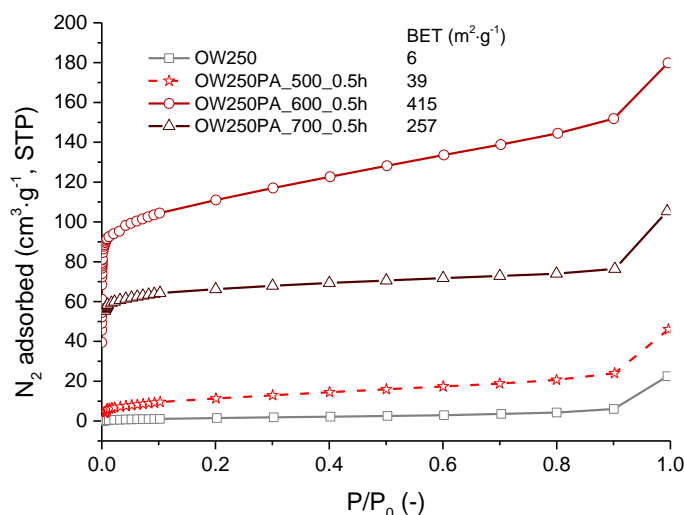


Figure 4-1 N₂ adsorption isotherms - Effect of temperature on CO₂ activation of hydrothermally carbonized oak wood

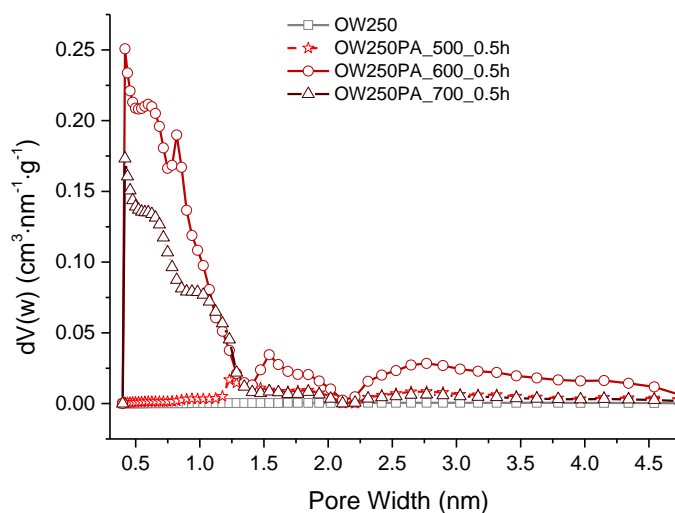


Figure 4-2 NLDFT pore size distributions - Effect of temperature on CO₂ activation of hydrothermally carbonized oak wood

4.3.1.1.2 Pyrolyzed wood (OW800)

Higher temperatures were chosen for the activation of the pyrolyzed oak wood, as this was already subjected to a more severe heat-treatment. In particular, runs were carried out at 750, 800 and 850 °C. In this case, sample was held to activation temperature for 1 h. Very similar textural properties and carbon burn-offs were obtained at 750 and 800 °C. However, the latter slightly prevailed over the former in terms of texture development. Isotherms measured for these samples may be considered as an intermediate between types I and II [264]. Although there was a pronounced upswing exhibited in the microporous pressure range, the mild slope in the mid pressure range indicated the presence of mesoporosity to some extent.

Table 4-3 Effect of CO₂ activation temperature on burn-off and textural parameters of pyrolyzed wood

Sample ID	T °C	t h	BO wt%	S _{BET} m ² ·g ⁻¹	V _{tot} cm ³ ·g ⁻¹	V _{mi} cm ³ ·g ⁻¹	V _{me} cm ³ ·g ⁻¹	V _{ma} cm ³ ·g ⁻¹
OW800PA_750_1h	750	1	32	505	0.257	0.193	0.037	0.026
OW800PA_800_1h	800	1	34	627	0.313	0.240	0.042	0.031
OW800PA_850_1h	850	1	89	0	0.000	0.000	0.000	0.000

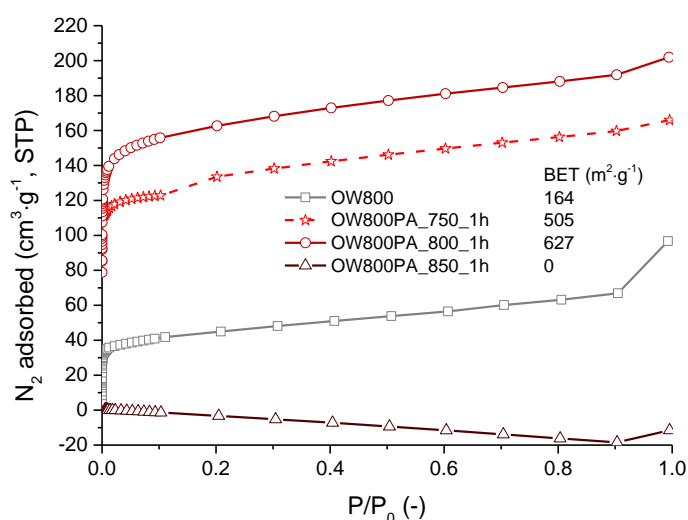


Figure 4-3 N₂ adsorption isotherms - Effect of temperature on CO₂ activation of pyrolyzed oak wood

In contrast, a further increase of activation temperature (up to 850 °C) of the initial char was detrimental, textural parameters being dramatically reduced down to effectively zero as given in Table 4-3. Accordingly, 800 °C resulted to be the optimal activation temperature for the pyrolysis-derived oak char. This result disagreed with the optimal condition reported by Sanchez *et al.* [160], who found increased surface area when increasing temperature from 800 to 840 °C. Yet, this might be ascribed to the lower burn-off (68.3 wt%) reported by these authors compared to that experienced by the oak wood char tested in this work under similar conditions (89 wt%).

An isotherm measured for OW800PA_850_1h showed evidence for the complete degradation of its texture (see Figure 4-3). A negative trend of the adsorbate volume with increasing pressure was observed. This clearly indicated a total destruction of the porous structure for this sample. It is likely that when temperature was 850 °C, activation went far beyond the limit of volatiles evolution, thereby leading to the damage of any porosity previously created.

As seen in Figure 4-4, a narrower distribution of pores was obtained when increasing activation temperature from 750 to 800 °C. In particular, it seemed that ultramicroporosity increased at the expense of supermicroporosity. As given in Table 4-3, this is consistent with the increase of surface area (from 505 up to 627 m²·g⁻¹) with increasing temperature.

In contrast, further increase of temperature up to 850 °C led to a collapse of the porosity created at 800 °C. This was shown by the flat NLDFT distribution exhibited OW800PA_850_1h.

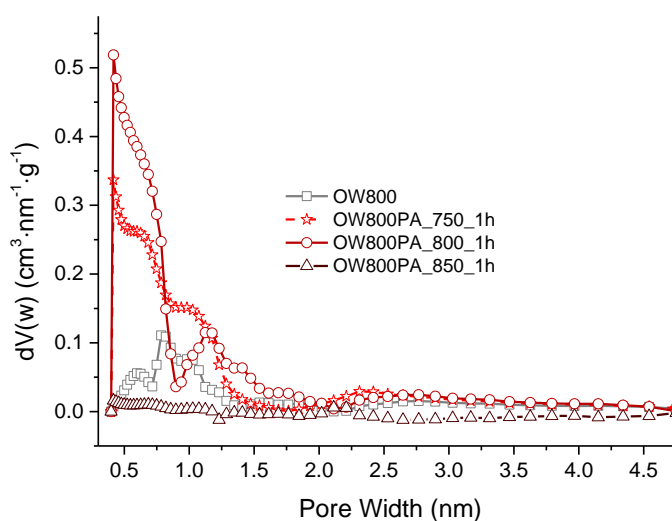


Figure 4-4 NLDFT pore size distributions - Effect of temperature on CO₂ activation of pyrolyzed oak wood

4.3.1.2 The effect of the dwell time

4.3.1.2.1 Hydrothermally carbonized wood (OW250)

Starting from the optimal condition of 600°C found in section 4.3.1.1.1, holding times other than initial value (0.5h) were examined in order to assess the influence of this factor on the texture change of the activated materials.

In particular, hydrochar (OW250) was held at the optimal temperature (600 °C) for no dwell time (0 h) or 1 h. Despite a small difference in burn-off, a substantial texture development was observed when increasing the dwell time from 0 to 30 min (see Table 4-4). The product obtained after activating the char for 0.5 h had the largest total pore volume, which was in agreement with the highest volume of nitrogen adsorbed by this sample (see Figure 4-5). In addition to that, the larger contribution of mesoporosity was in accordance with the steeper slope observed in the mid pressure range of the N₂ adsorption isotherm. Contrarily, longer holding time (i.e. 1 h) did not cause any further increase of the surface area. This might be because some of micro and mesopores were widened to form macropores when increasing dwell time from

30 min to 1 h. As shown in Figure 4-5, the larger volume of macropores was in line with the slightly steeper upswing of the isotherm near saturation. On the other hand, it worth noticing the drop in mesoporosity indicated by the less steep slope over the mid pressure range of the isotherm measured for OW250PA_600_1h. Based on these results, 0.5 h was deemed as optimal dwell for the activation of HTC-derived oak char.

Table 4-4 Effect of CO₂ activation dwell time on burn-off and textural parameters of hydrothermally carbonized wood

Sample ID	T °C	t h	BO wt%	S _{BET} m ² ·g ⁻¹	V _{tot} cm ³ ·g ⁻¹	V _{mi} cm ³ ·g ⁻¹	V _{me} cm ³ ·g ⁻¹	V _{ma} cm ³ ·g ⁻¹
OW250PA_600_0h	600	0	44	169	0.193	0.069	0.035	0.089
OW250PA_600_0.5h	600	0.5	46	415	0.278	0.173	0.066	0.040
OW250PA_600_1h	600	1	47	413	0.255	0.160	0.041	0.054

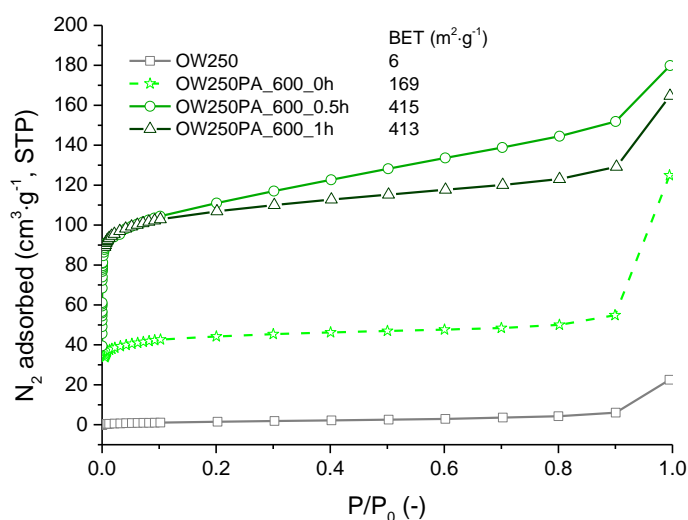


Figure 4-5 - N₂ adsorption isotherms - Effect of dwell time on CO₂ activation of hydrothermally carbonized oak wood

Surface area maximum attained by optimally activated hydrochar (OW250PA_600_0.5h) corresponded to a burn-out of ca. 46 wt%. This value was found to be higher than that measured after optimal activation of OW800 (i.e. OW800PA_800_1h, see Table 4-3). This was probably because hydrochar was poorly carbonized during hydrothermal treatment. Accordingly, a larger amount of volatile matter (VM) was released during the activation process (see Table 4-11).

As seen by the increased height of the peak centred over ca. 0.3 nm (see Figure 4-6), ultramicroporosity significantly increased when increasing holding time from 0 to 0.5 h. Apparently, when no dwell time was applied,

volatiles might have not been completely released. This did not allow for full exploitation of the activation treatment.

In line with nitrogen isotherms, porosity distribution did not significantly change when increasing dwell time from 0.5 to 1 h. After longest activation, ultramicroporosity population appeared to be entirely retained, whereas supermicroporosity slightly decreased (see missing peak at ca. 0.8 nm for OW250PA_600_1h). In addition to that, reduction of mesoporosity with increasing dwell time was indicated by pore distributions trend over the mesoporous range ($d > 2$ nm).

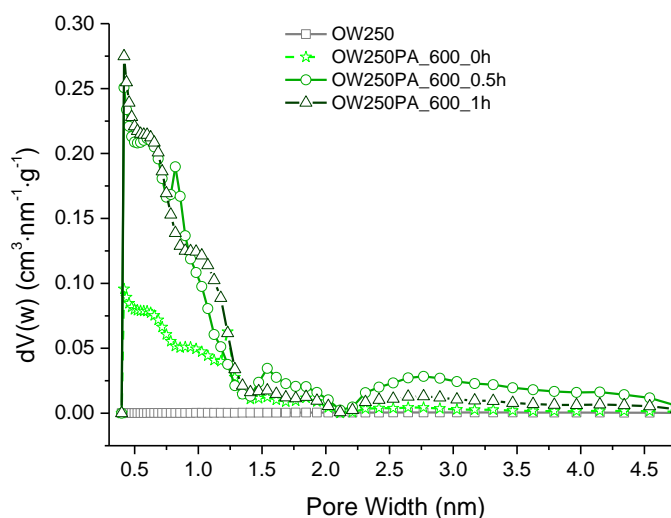


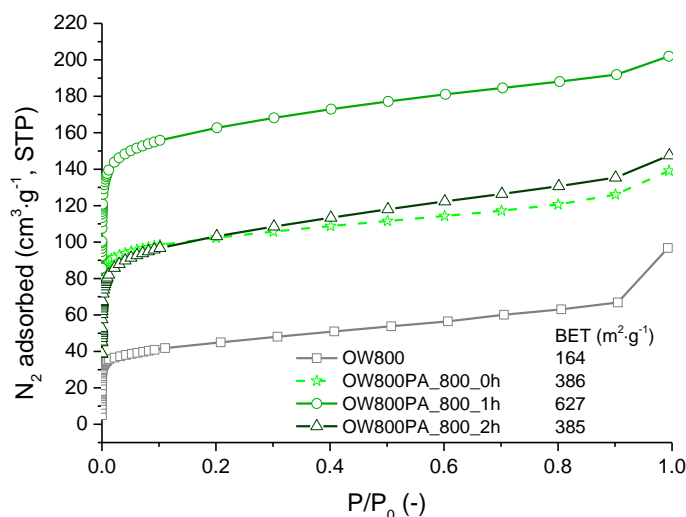
Figure 4-6 NLDFT pore size distributions - Effect of dwell time on CO₂ activation of hydrothermally carbonized oak wood

4.3.1.2.2 Pyrolyzed wood (OW800)

As reported in Table 4-5, the additional holding times examined for pyrolyzed oak wood (OW800) were 0 and 2 h. A significant difference in texture was measured when adjusting the activation dwell time. This was probably due to the larger time step considered in this case. However, findings did not appear to agree with the linear trend between dwell time and yield found by Sanchez *et al.* [160]. Also, the texture detriment when increasing dwell time from 1 to 2 h was not consistent with what reported by Zhang *et al.* [161]. Plausibly, discrepancies in optimal conditions might be ascribed either to different nature of the raw feedstock or to dissimilar pyrolysis conditions applied.

Table 4-5 Effect of CO₂ activation dwell time on burn-off and textural parameters of pyrolyzed wood

Sample ID	T °C	t h	BO wt%	S _{BET} m ² ·g ⁻¹	V _{tot} cm ³ ·g ⁻¹	V _{mi} cm ³ ·g ⁻¹	V _{me} cm ³ ·g ⁻¹	V _{ma} cm ³ ·g ⁻¹
OW800PA_800_0h	800	0	8	395	0.215	0.153	0.039	0.024
OW800PA_800_1h	800	1	34	627	0.313	0.240	0.042	0.031
OW800PA_800_2h	800	2	48	385	0.228	0.146	0.048	0.034

**Figure 4-7 - N₂ adsorption isotherms - Effect of dwell time on CO₂ activation of pyrolyzed oak wood**

As previously reported in section 4.3.1.2.1 for the hydrochar, when no holding time was applied activation treatment showed poor efficiency, as also indicated by the very low burn-off found for OW800PA_800_0h (see Table 4-5). This was likely owed to a low reaction rate between carbon dioxide and char. As illustrated by Figure 4-7, micropore filling significantly increased when increasing residence time from 0 to 1 h.

Isotherms measured for OW800PA_800_0h and OW800PA_800_1h seemed to follow the same path (but with more micropore filling for the latter) with increasing pressure. This was suggestive of unaltered meso and macroporosity, and in line with meso and macropore volumes given in Table 4-5.

Conversely, when holding the sample at the optimal temperature for too long (i.e. 2 h), surface areas and pore volumes significantly declined probably due to the collapse of the micropore walls. This is shown by the dramatic decrease in microporous volume (see Table 4-5). Moreover, it seemed that a minor proportion of micropores were widened to form meso and macropores. This agreed with the steeper slope of the isotherm measured for

OW800PA_800_2h over the mid pressure range. Furthermore, this finding was corroborated by the higher burn-out measured for this sample (48 wt%). These results coupled with those reported in section 4.3.1.1.2 would then imply that burn-offs higher than 34 wt% were detrimental for the porous structure of the activated-OW800. Therefore, a residence time of 1 h was found to be optimal for the activation of pyrolyzed oak.

Results shown in Figure 4-8 reflected aforementioned textural changes. In particular, ultramicropore population peaked at ca. 0.3 nm dramatically increased when increasing holding time from 0 to 1 h. On the contrary, prolonged activation (i.e. 2 h) caused a damage of the porous structure formed after the first hours of treatment.

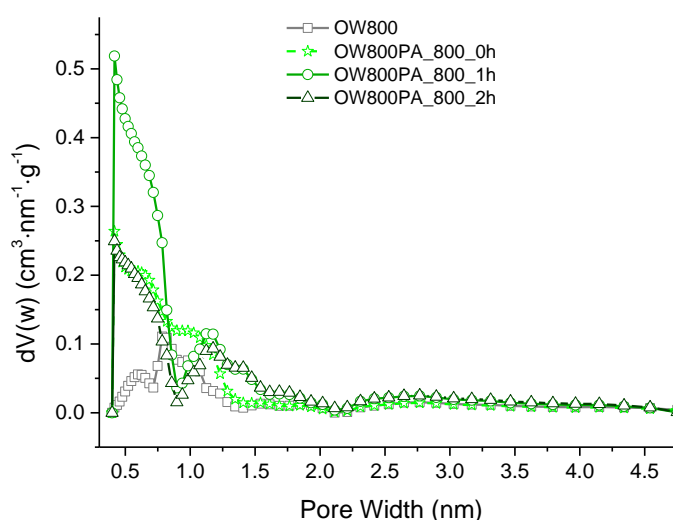


Figure 4-8 - NLDFT pore size distributions - Effect of dwell time on CO₂ activation of pyrolyzed oak wood

4.3.2 KOH activation of oak wood-based chars

Chemical activation of charred wood was carried out adopting the optimal conditions determined for *Laminaria hyperborea* (see Chapter 5).

As given in Table 4-6, KOH activation gave rise to a far more dramatic texture development of the final carbons compared to the CO₂-activated counterparts (see section 4.3.1). It is interesting to note that the largest surface area and pore volumes were attained after the chemical activation of the hydrochar. This could be attributed to the larger abundance of volatiles measured for the hydrothermally carbonized wood compared to those measured for OW800 (see Table 4-11). Despite the substantial texture development experienced by OW800CA, its surface area was found to be lower than that exhibited by a chemically-activated char derived from lignin prepared

by Fierro *et al.* [169]. These authors reported highest surface area of ca. 3000 $\text{m}^2\cdot\text{g}^{-1}$ when activation temperature was 700 °C and KOH:char ratio was 3:1.

Surface area attained by OW250CA was nearly as large as that reported by Sevilla *et al.* [93] after chemical activation of hydrothermally carbonized sawdust under similar conditions (800 °C, KOH:char ratio=4:1). On the other hand, the outstanding enhancement of porosity experienced by the hydrochar resulted in a very low activation yield (less than 3 wt%). As already mentioned in section 4.3.1, this was mostly because the hydrochar was poorly carbonized during the hydrothermal treatment, therefore experiencing much larger material loss during the activation process.

Gas adsorption isotherm and pore size distributions are reported for all samples in section 4.4.

Table 4-6 Yield and textural parameters of oak wood chars after KOH activation

	T	CR ¹³	AY _{db} ¹⁴	S _{BET}	V _{tot}	V _{mi}	V _{me}	V _{ma}
Sample ID	°C	-	wt%	$\text{m}^2\cdot\text{g}^{-1}$	$\text{cm}^3\cdot\text{g}^{-1}$	$\text{cm}^3\cdot\text{g}^{-1}$	$\text{cm}^3\cdot\text{g}^{-1}$	$\text{cm}^3\cdot\text{g}^{-1}$
OW250	-	-	-	6	0.035	0.001	0.012	0.022
OW250CA ¹⁵	750	4:1	2.44	2757	1.412	0.944	0.080	0.389
OW800	-	-	-	164	0.150	0.074	0.044	0.031
OW800CA	750	4:1	44.41	2061	1.008	0.773	0.067	0.168

4.3.2.1 The effect of the washing procedure

In this section, attention was focused on the importance of the washing procedure after KOH activation.

OW800CA was the selected sample. In particular, this carbon was obtained by mixing the pyrolyzed oak wood (OW800) and KOH according to a 1 to 4 ratio.

As illustrated in Figure 4-9, the porosity of the unwashed carbon was completely inaccessible. This might be ascribed to the presence of potassium-based compounds (e.g. potassium carbonate). These are believed to be formed

¹³ Chemical ratio (KOH:char)

¹⁴ Activation yield (AY). Db stands for dry basis.

¹⁵ CA stands for chemically activated

during heat-treatment (see Chapter 3) and deposited inside the carbon pores. The total lack of porosity found in this study for the unwashed sample was not consistent with results shown by Illingworth [168], who reported some degree of microporosity when no washing was applied. However, this might be owed to the lower KOH:char ratio (1:1) used by that author. Conversely, the larger amount of potassium hydroxide used (KOH:char ratio=4:1) in this work seemed to have led to a complete blockage of the sorption sites. This was in line with findings reported by Lozano-Costello *et al.* [167], who did not measure any porosity for an unwashed carbon obtained by using a 2:1 KOH:char ratio.

Apparently, the aqueous rinsing allowed releasing most of the chemical residue, thus revealing the greater part of the porous structure of the carbon. On the other hand, when acid was used as washing agent, an even more efficient unblocking of the pores was achieved. This led to a further increase of the microporous volume from ca. 0.52 to 0.77 cm³·g⁻¹, while surface area increased by 50%. These results disagreed with those reported by Illingworth [168], which showed no influence of the washing agent on the microporosity of the carbon. In addition to that, HCl washing revealed a significant increase of larger porosity, thereby indicating that a large proportion of meso and macroporosity were also created after KOH activation.

From Fourier Transform Infrared (FTIR) spectra recorded for the unwashed carbon (see Figure 4-10), absorbance bands (C-O stretch at ca. 1385 cm⁻¹, C-O out of plane at ca. 878 cm⁻¹ and C-O in plane at ca. 706 cm⁻¹) typical of inorganic carbonates [280] were observed.

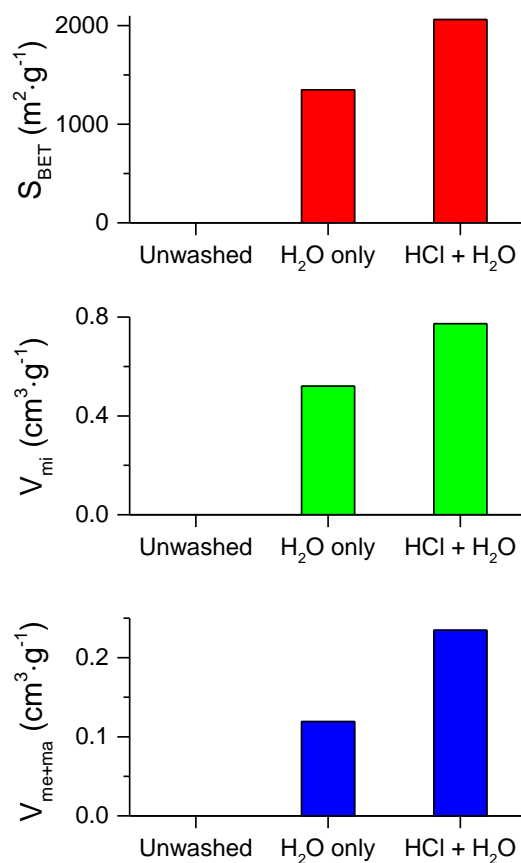


Figure 4-9 Influence of the washing procedure on textural parameters of pyrolyzed wood after KOH activation (OW800CA)

These absorption peaks could be reasonably assigned to the residual potassium carbonate, which was formed during chemical treatment. This was also confirmed by the very high concentration of potassium detected by EDX for the unwashed carbon (see Figure 4-11). The same bands were observed for the carbon washed with water only but the absorption peaks appeared to be much weaker, indicating that most of the potassium carbonate was removed by aqueous rinsing. This was also indicated by the negligible K content measured by EDX for the sample washed with distilled water only. In contrast, absorption bands disappeared in the spectrum recorded for the acid washed sample, thereby confirming the higher removal efficiency obtained through HCl rinsing. This agreed with EDX chemical compositions found for the acid washed carbon, where no K was detected (see Table 4-12). It is also worth noting that HCl washing left a lower concentration of impurities (see “Others” in Figure 4-11) compared to those retained by the chemically activated carbon after aqueous washing. Consequently, the purity of the carbon enriched relatively.

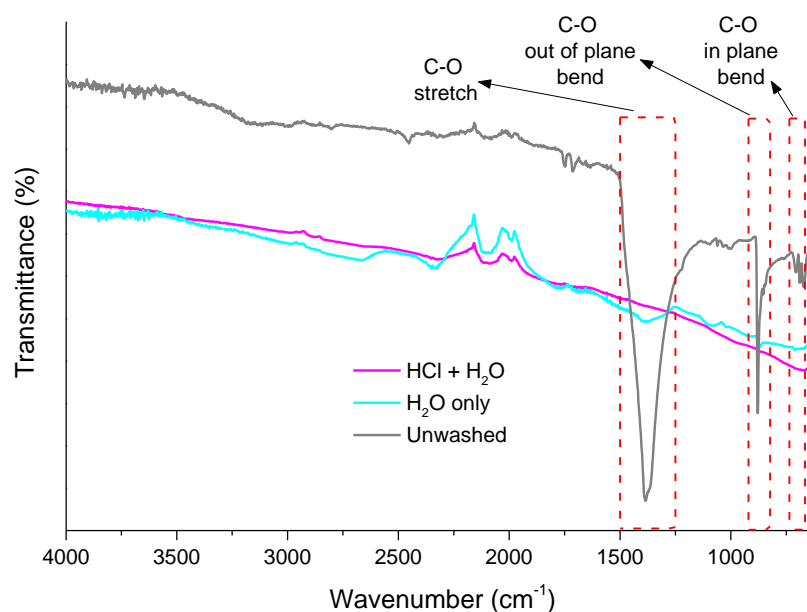


Figure 4-10 Influence of the washing procedure on FTIR spectra of OW800CA

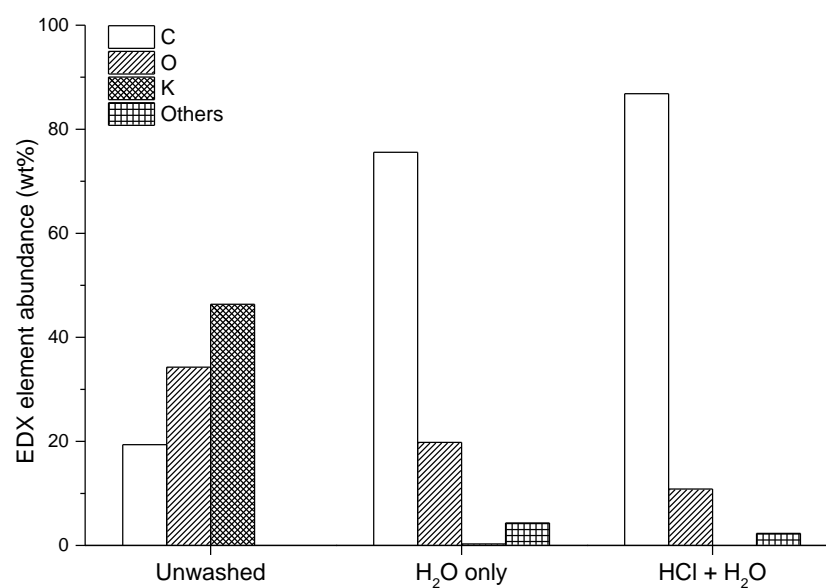


Figure 4-11 Influence of the washing procedure on EDX chemical compositions of OW800CA

4.3.2.2 Repeatability of the optimal run

The pyrolyzed oak wood activated by KOH (i.e. OW800CA) was chosen as sample to assess the repeatability of the chemical activation procedure with respect to yield and textural parameters. Although KOH activation implied two steps, i.e. heat-treatment and HCl washing, error related to the activation yield was relatively low with standard deviation below 3%.

On the other hand, textural parameters showed far higher variability with standard deviation from the mean of up to 12% for the total pore volume. This error would not be acceptable in terms of repeatability [282]. However, it is worth mentioning that textural parameters are significantly affected by the degree of activation (i.e. yield). In particular, as seen in Table 4-7, the higher the yield, the larger surface areas and pore volumes of the final carbon. Therefore, in order to perform a reliable repeatability test for textural properties, attention was focused on repeat textural property measurements on one of the activation runs previously considered (i.e. run 2).

Table 4-7 Repeatability of chemical activation of pyrolyzed oak wood (OW800CA) in terms of yield and textural parameters

Run	AY _{db} %	S _{BET} m ² ·g ⁻¹	V _{tot} cm ³ ·g ⁻¹	V _{mi} cm ³ ·g ⁻¹
1	44.41	2061	1.008	0.773
2	40.03	1768	0.788	0.674
3	38.34	1710	0.788	0.653
Mean	40.93	1846	0.86	0.70
SD	2.56	154	0.10	0.05
SD (% Mean)	6.2	8.3	12.0	7.5

Table 4-8 Repeatability of N₂ adsorption measurements for OW800CA (run 2)

Run	S _{BET} m ² ·g ⁻¹	V _{tot} cm ³ ·g ⁻¹	V _{mi} cm ³ ·g ⁻¹
2.1	1768	0.788	0.674
2.2	1882	0.865	0.721
2.3	1780	0.820	0.683
Mean	1810	0.824	0.693
SD	51	0.031	0.021
SD (% Mean)	2.8	3.8	3.0

As expected, in this case the error associated with textural parameters was far lower, as influence of activation yield was removed. As given in Table 4-8, standard deviation from the mean was found to be well below the limit of acceptance (10%) for all parameters. This indicated a good repeatability of the N₂ adsorption measurement for this sample.

4.4 Texture evolution of raw oak wood

4.4.1 N₂ adsorption isotherms

As seen in Figure 4-12, raw oak wood (OW) adsorbed a negligible volume of nitrogen. Interestingly, OW's surface area is slightly higher than that measured for its hydrothermally carbonized counterpart (OW250). This could be attributed to the enlargement of porosity (see increase of macropore volume in Table 4-9) observed after hydrothermal treatment. However, surface area of raw oak wood was lower than that reported by Zhang *et al.* [6] (95 m²·g⁻¹).

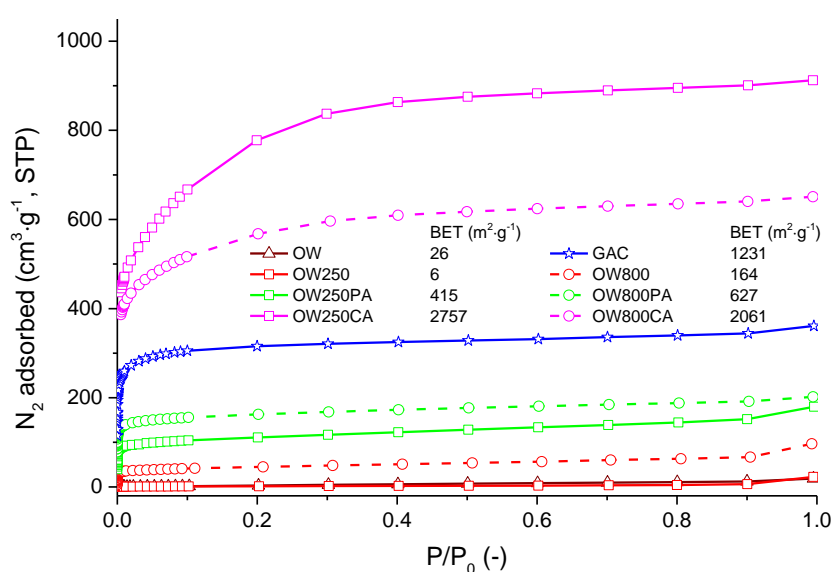


Figure 4-12 N₂ adsorption isotherms for key oak wood-based samples and commercial carbon

Unlike hydrothermal treatment, traditional pyrolysis of wood at 800 °C resulted in the creation of a more developed porous structure with surface areas increasing up to 164 m²·g⁻¹. This finding is in line with the more dramatic devolatilization caused by pyrolysis treatment (see Table 4-11). Nonetheless, OW800's surface area was lower than that measured by Jindo *et al.* [179] for pyrolyzed oak tree at 800 °C for 10 h. In that case, increased surface area might be ascribed to the prolonged pyrolysis process. In addition to that, as indicated by the NLDFT peaks at pore widths lower than 1 nm (see Figure 4-13), some extent of microporosity was created during heat-treatment at 800 °C.

Activation under CO₂ atmosphere led to a moderate increase of porosity for both chars. However, as concerns pyrolyzed char (OW800), physical treatment led to a maximum surface area lower than those reported by other works [160, 161]. In these studies, the authors reported highest textural development at burn-off far larger than the optimal figure found in the current work. In contrast, current experimentation showed a decrease in all textural

parameter when further increasing the severity (i.e. burn-off) of the treatment. On the other hand, OW800PA's surface area was comparable to values reported by Lopez *et al.* [180] for CO₂-activated carbons derived from pyrolyzed oak.

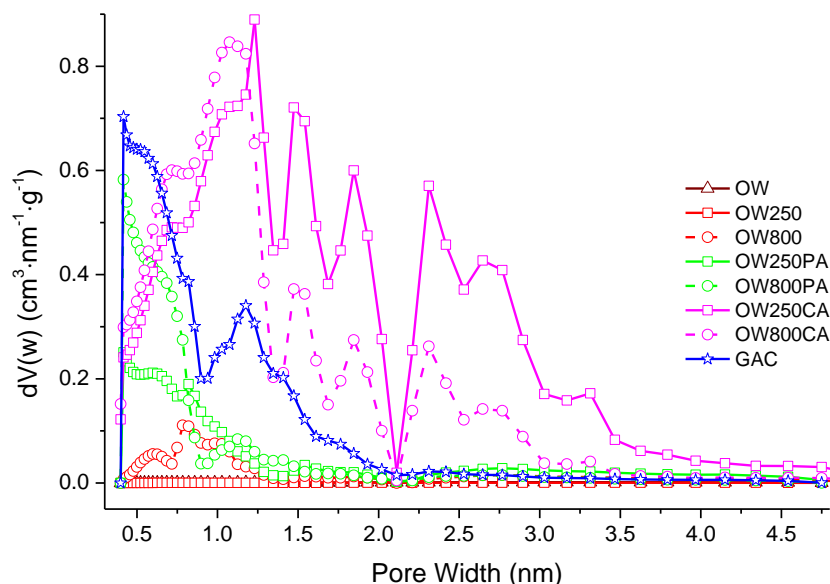


Figure 4-13 N₂ NLDFT pore size distributions for key oak wood-based samples and commercial carbon

Activated carbons produced N₂ adsorption isotherms which appeared to be closer to type I [242]. In particular, the relatively sharp knee at the very low pressure indicates a high micropore percentage (up to 77% for OW800PA), which was calculated as (4.1). This is further back by the narrow pore size distributions exhibited by physically activated carbons (see Figure 4-13). It is also worth noticing how NLDFT mode measured for OW800 was amplified and shifted toward lower pore diameter (from ca. 0.7 nm to ca. 0.4 nm) after CO₂ activation. This indicated the formation of ultramicropores ($d < 0.7$ nm) after activation under CO₂.

Although OW800PA features larger pore volume and surface area than those measured for OW250PA (see Table 4-9), the hydrochar exhibited a more dramatic texture enhancement after physical activation. In particular, OW250PA's surface area experienced a ca. 70-fold increase compared to the figure measured for the non-activated material. This finding might be explained by the poor carbonization that occurred during hydrothermal treatment. This was indicated by the lower values of carbon content and by the higher proportion of volatiles given in Table 4-11 for OW250. From this result, it could be inferred that a further devolatilization of the sample occurred throughout the activation treatment, resulting in larger development of porous structure. On the other hand, the limited texture enhancement observed for the pyrolysis-derived char might be attributed to its higher ash (A) content (Table 4-11). These were

not removed after physical treatment, thus deactivating some of the sorption sites.

In contrast, a far higher volume of nitrogen was adsorbed by commercial carbon (GAC), which is characterized by lower ash and higher carbon content (see Table 4-11). GAC's isotherm exhibited a more pronounced initial upswing at the lowest pressure values followed by a flat trend with increasing pressure. This is typical of type I-like isotherms, indicating a prevalent proportion of micropores (up to 85%) within the porous structure of this material. Additionally, GAC exhibited a bimodal pore size distribution. In particular, this sample showed a larger proportion of ultramicropores than that found for OW800PA (see the first peak centred at ca. 0.4 nm in Figure 4-13). In addition to this, the second broad peak extending from 1 to 2 nm indicated a great contribution of supermicropores, which were not significantly developed for the char-based carbon samples that were physically activated in this work.

Nevertheless, when activating chars with KOH, the final carbons exhibited much higher uptake of N₂ than all the other sorbents. Interestingly, the largest surface area was attained by OW250CA (up to 2757 m²·g⁻¹). As earlier mentioned for physical activation, this result might be essentially due to a higher degree of devolatilization experienced by the hydrochar during heat-treatment. However, it worth mentioning that KOH-activated samples presented a higher percentage of larger pores compared to that found for the corresponding CO₂-activated carbons. This was indicated by the different isotherm shape observed for chemically-activated wood in Figure 4-12. In fact, unlike physically activated and commercial carbons, KOH-activated samples exhibited a more open knee of the isotherm and, especially for OW250CA, the greater part of N₂ was adsorbed at higher pressure.

These findings matched with the multimodal NLDFT distributions exhibited by these samples, thereby indicating a more heterogeneous porous structure. However, it is worth noting that no peaks associated with ultramicropore widths ($d < 0.7$ nm) were measured for KOH-activated sorbents.

Although OW250CA exhibited a larger micropore volume than that measured for OW800CA (ca. 0.95 cm³·g⁻¹ vs ca. 0.77 cm³·g⁻¹ respectively), the latter featured a higher microporosity (77% vs 67%) as a fraction of total porosity. This was explained by the higher figure of macropore volume found for OW250CA (nearly 0.39 cm³·g⁻¹ vs ca. 0.17 cm³·g⁻¹ for OW800CA). As abovementioned, the different proportions of porosity types found for chemically treated carbons might be ascribed to the dissimilar degree of carbonization of the starting chars. Moreover, the more dramatic texture development experienced by KOH-activated chars might be because chemical treatment was more severe than CO₂ oxidation. Apparently, KOH attacked carbon structure more efficiently, thus creating a greater amount of porosity. Furthermore, acid washing step allowed for removal of most of the ash contained within the initial

chars, thereby unblocking further pores (see section 4.3.2.1). On the other hand, this treatment seemed to be less suitable for tailoring carbon with high degree of microporosity.

Table 4-9 Gas adsorption data for key oak wood-based samples and commercial carbon

Sample ID	N ₂ adsorption -196 °C					CO ₂ adsorption 0°C				
	S _{BET}	V _{tot}	V _{mi}	V _{me}	V _{ma}	V _{ads, 0 °C, 1bar} ¹⁶	V _{umi, NLDFT} ¹⁷	NLDFT mode	V _{umi, DR} ¹⁸	E _{0, DR} ¹⁹
	m ² ·g ⁻¹	cm ³ ·g ⁻¹	cm ³ ·g ⁻¹	cm ³ ·g ⁻¹	cm ³ ·g ⁻¹	cm ³ ·g ⁻¹	cm ³ ·g ⁻¹	cm ³ ·g ⁻¹	cm ³ ·g ⁻¹	kJ·mol ⁻¹
OW	26	0.029	0.002	0.014	0.013	0.4	0.001	0.007	0.001	-
OW250	6	0.035	0.001	0.012	0.022	1.5	0.003	0.028	0.005	-
OW800	164	0.150	0.074	0.044	0.031	11.8	0.028	0.251	0.087	-
OW250PA	415	0.278	0.173	0.066	0.040	9.9	0.024	0.247	0.095	-
OW800PA	627	0.313	0.240	0.042	0.031	15.0	0.040	0.356	0.064	30.3
OW250CA	2757	1.412	0.944	0.080	0.389	6.5	0.014	0.129	0.029	-
OW800CA	2061	1.008	0.773	0.067	0.168	11.3	0.026	0.233	0.078	25.2
GAC	1231	0.559	0.474	0.078	0.006	10.9	0.026	0.229	0.109	23.7

¹⁶ CO₂ adsorption at 0 °C and 1 bar

¹⁷ Ultramicropore volume calculated by applying NLDFT model to CO₂ adsorption data

¹⁸ Ultramicropore volume calculated by applying DR model to CO₂ adsorption data

¹⁹ Energy of adsorption calculated by applying DR model to CO₂ adsorption data

4.4.1.1 Study of isotherm hysteresis

As already mentioned in Chapter 3, adsorption leg was chosen for the calculation of mesopore volume. This decision was mostly dictated by the lack of consistency encountered when measuring N₂ desorption of materials analysed. Therefore, in this section few representative cases of isotherm hysteresis are shown (see Figure 4-14 and Figure 4-15). Moreover, estimation of mesoporous volume derived from the application of BJH model to desorption leg is reported for selected samples (see Table 4-10).

In particular, isotherms measured for some of the samples examined (see Figure 4-14) did not exhibit any closure of the hysteresis loop. As suggested by IUPAC recommendations [242], low-pressure hysteresis (LPH) phenomenon might be attributed to an inefficient degassing process that did not ensure the cleanness of the adsorbent surface prior to measuring N₂ adsorption. This might have occurred for the physically activated hydrochars that were degassed at a maximum temperature of 100 °C (see Table 4-10). This was because these samples kept releasing sticky volatiles when degassed at temperatures higher than 100 °C in agreement with the high proportion of volatile matter measured for OW250PA (see Table 4-11). Therefore, in order to prevent instrument contamination, more intense degassing process was avoided for these samples.

Results shown in this work agreed with those reported in the study of Silvestre-Albero *et al.* [284]. These authors showed that desorption leg did not re-join the adsorption branch at low-pressure region when degassing samples at low temperature (i.e. 150 °C). Contrarily, closure of hysteresis loop was observed when degassing materials at 250 °C. Apparently, after a poor degassing treatment, volatiles and other chemical compounds are retained within the porous structure of the adsorbent. These molecules tend to block narrow micropores, thus delaying or preventing nitrogen adsorption. Therefore, whenever possible, degassing of adsorbents at higher temperatures is highly recommended.

Moreover, Silvestre-Albero *et al.* [284] showed that hysteresis phenomena could be an artefact due to the lack of equilibrium during the measurement of N₂ isotherms. These authors reported that low-pressure hysteresis did not occur when using a longer elapsed time between consecutive pressure readings, as this ensured achieving a real equilibrium. In particular, they observed LPH when a low equilibration time (80 s) was considered, while no low-pressure hysteresis was observed when increasing equilibrium time to 300 s. In this study, an equilibration time of 180 s was used but the effect of this parameter on the LPH was not studied.

Nevertheless, as shown in Figure 4-14, hysteresis exhibited by isotherms was close to H3 type [242]. Desorption leg immediately deviated from

adsorption branch, thereby indicating condensation of adsorbate in mesoporous. Later on, desorption and adsorption legs run quasi-parallel with decreasing relative pressure, without re-joining because of low-pressure hysteresis phenomenon. As reported in Table 4-10, the choice of isotherm leg did not affect the estimation of the mesopore volume for OW250PA_700_0.5h. Yet, the application of the modified Kelvin equation to the isotherm desorption branch led to a slightly larger mesoporous volume for OW250PA_600_0.5h.

Isotherms reported in Figure 4-15 denoted a type H3 hysteresis [242], which is characteristic of aggregates of plate-like particles and implies a slit-shaped pore geometry. Note that a delayed opening of hysteresis loop that occurred for OW800PA at ca. $P/P_0=0.9$. This is typical of type H2 hysteresis [242], which indicated the probable presence of "ink-bottle" pores to some extent. These hindered the evaporation of adsorbate from the pores. It follows that this sample might present a partially disordered porous network.

Table 4-10 Hysteresis case studies - Mesoporous volume and degassing temperature

Sample ID	$V_{me, ads}^{20}$ cm ³ ·g ⁻¹	$V_{me, des}^{21}$ cm ³ ·g ⁻¹	$T_{max, degas}$ °C
OW250PA_600_0.5h	0.053	0.078	100
OW250PA_700_0.5h	0.023	0.022	100
OW800PA	0.042	0.080	200

²⁰ Mesopore volume calculated by applying BJH model to N₂ adsorption data

²¹ Mesopore volume calculated by applying BJH model to N₂ desorption data

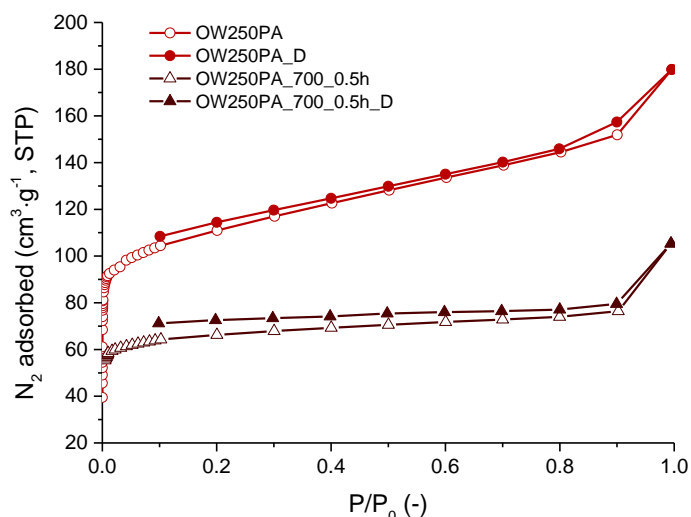


Figure 4-14 Isotherms hysteresis – case study 1 (“D” stands for desorption)

Nonetheless, unlike for samples discussed in case 1, isotherm desorption leg measured for OW800PA re-joined the adsorption branch at low pressure (see Figure 4-15). The closure of hysteresis loop at $P/P_0=0.4$ found for OW800PA is typical when using nitrogen as adsorptive [242]. Hysteresis loop reported in this study agreed fairly well with that shown by Zhang *et al.* [161] for a similar material (i.e. CO₂-activated oak wood at 800 °C for 1 h). According to IUPAC nomenclature [242], isotherm shown in Figure 4-15 should be defined as type IV rather than type II.

As reported in Table 4-10, in this case material was degassed at higher temperature (200 °C), as a limited release of gaseous compounds was observed during degassing. This confirmed the importance of a more efficient degassing at preventing LPH. Moreover, it is likely that the lower amount of volatiles found for this sample (see Table 4-11) might have facilitated the degassing process.

As given in Table 4-10, a larger mesopore volume was obtained when using desorption leg for BJH calculation. The increased mesopore volume was ascribed to the hysteresis area between lower branch (adsorption) and upper branch (desorption).

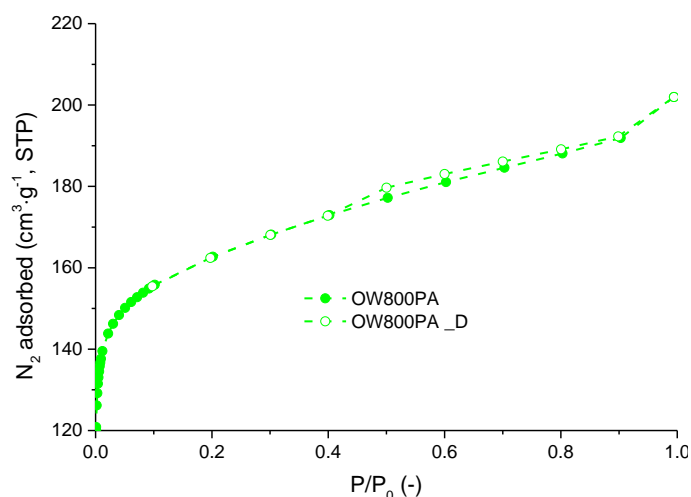


Figure 4-15 Isotherms hysteresis - case study 2 (“D” stands for desorption)

4.4.2 CO₂ adsorption isotherms

As depicted by Figure 4-16, all samples adsorbed a relatively small amount of CO₂ at 0 °C. As expected, negligible amounts of CO₂ were adsorbed by raw and hydrothermally carbonized wood. This agreed with the absence of porous structure already revealed by N₂ adsorption measurements for these samples.

Surprisingly, the pyrolyzed char (OW800) attained the second largest CO₂ uptakes among the set of samples tested. OW800’s performance outweighed sorption capacities exhibited by activated carbons featuring much larger surface areas, such as OW250PA, GAC and chemically-treated carbons. This finding suggested the formation of ultramicropores during the pyrolysis treatment. In addition to that, this emphasizes that KOH activation only led to the development of pores having larger widths ($d > 0.7$ nm). This also agreed with NLDFT distributions showed in Figure 4-17.

Conversely, a significant increase of ultramicropore volume was caused by physical activation, which appeared to be a more suitable treatment for developing sorbents with narrower pores. All samples exhibited a unimodal NLDFT distribution peaked in ultramicropores (pore width ca. 0.35 nm). Mode magnitude approximately followed the adsorbed volume of CO₂ at saturation, with the highest peak intensity found for OW800PA.

Based on the approximate linear correlation shown in Figure 4-18, the ultramicropore determined applying the NLDFT method to the CO₂ adsorption isotherms at 0 °C and 1 bar is proportional to the maximum volume of CO₂ adsorbed. Linear regression yielded a coefficient of determination $R^2 = 0.9895$. Results shown in this work agreed with findings reported by Presser *et al.* [285].

On the other hand, as seen in Figure 4-19, poor correlation was observed when plotting CO₂ uptakes versus ultramicropore volume determined by applying DR method to the CO₂ adsorption data. This was in contrast with what stated by Sevilla *et al.* [106]. Therefore, NLDFT method was believed to be a more reliable estimation of the narrow microporosity of the samples analysed in this study.

Nevertheless, DR model was applied to the CO₂ adsorption data to have a quantitative estimation of the interaction strength between the adsorbate (i.e. CO₂) and some of the adsorbents tested. In particular, the energy of adsorption E_0 followed the sequence OW800PA>OW800CA>GAC. It follows that the physically-activated carbon seemed to have a stronger affinity with CO₂ than the corresponding chemically activated sample and commercial carbon.

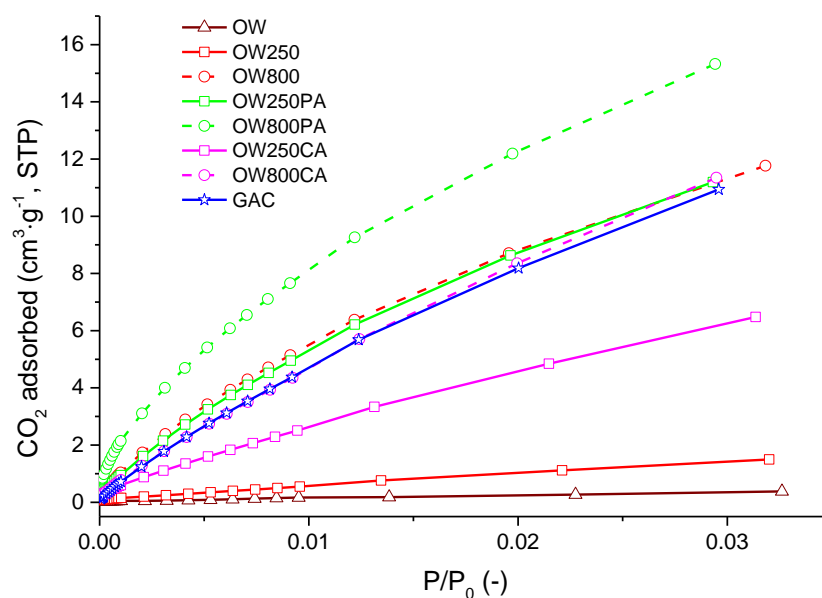


Figure 4-16 CO₂ adsorption isotherms for key oak wood-based samples and commercial carbon

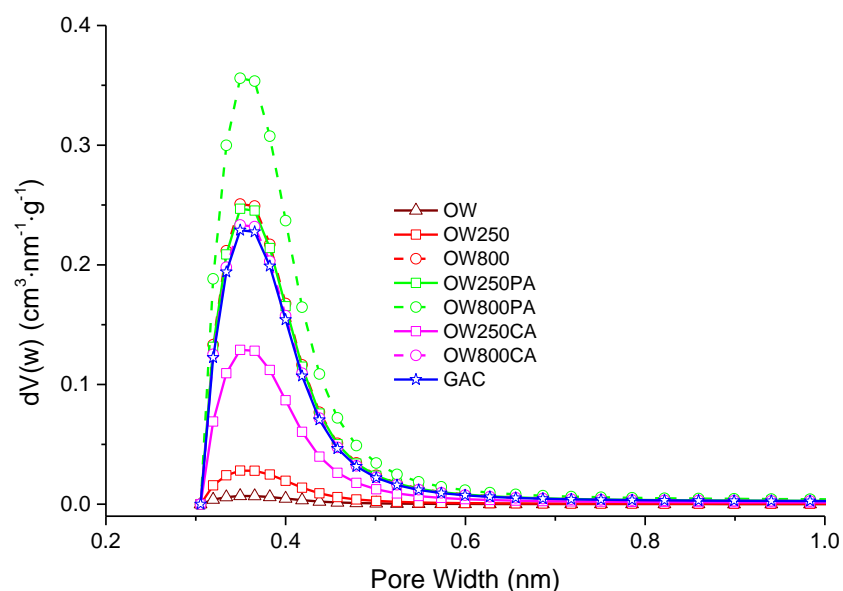


Figure 4-17 CO₂ NLDFT pore size distributions for key oak wood-based samples and commercial carbon

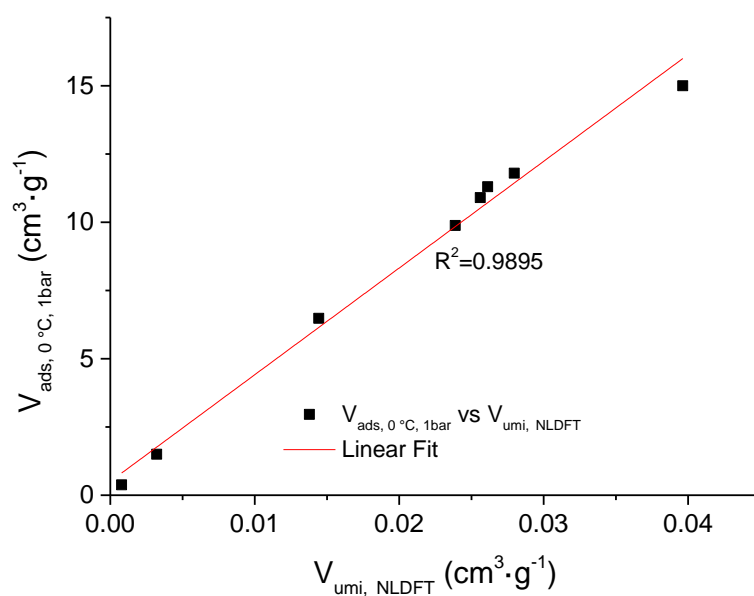


Figure 4-18 Correlation between CO₂ uptake at 273 K and 1 bar, and the narrow micropore volume ($d < 0.7$ nm) determined by applying the NLDFT method to the CO₂ adsorption isotherms measured for key oak wood-based samples and commercial carbon.

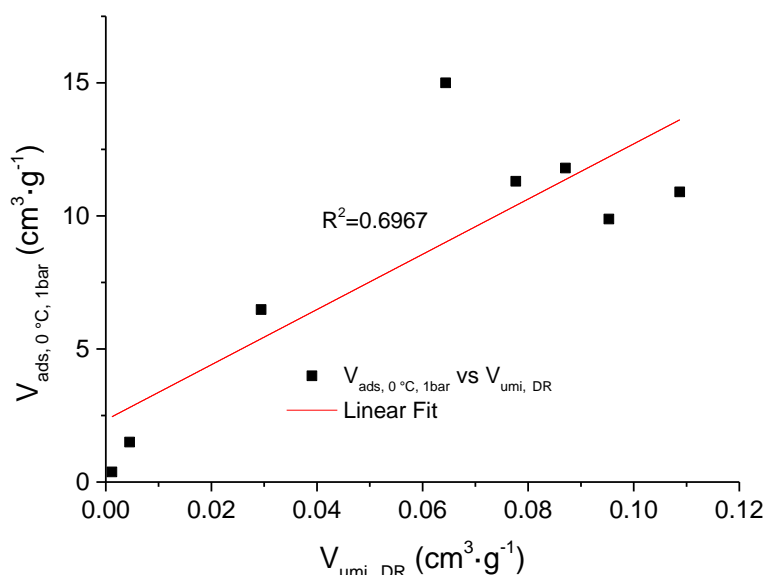


Figure 4-19 Correlation between CO₂ uptake at 273 K and 1 bar, and the narrow micropore volume ($d < 0.7$ nm) determined by applying the DR method to the CO₂ adsorption isotherms measured for key oak wood-based samples and commercial carbon.

4.5 Chemical and structural properties of raw oak wood and its derivatives

4.5.1 Elemental and proximate analyses

Elemental composition of raw oak wood mostly agreed with data previously reported in other works for similar feedstock [161, 180] and is typical of lignocellulosic materials. In addition to this, the high volatile content (up to ca. 86 wt%) was fairly consistent with the figure measured by Lopez *et al.* [286] for Pyrenean oak (80.6 wt%). Results revealed insignificant sulphur and low nitrogen contents for all samples (see Table 4-11). Hydrogen content below 1 wt% was measured for all materials, except for raw oak wood and HTC-derived products (OW250 and OW250PA). In particular, hydrochars normally have higher hydrogen content than that featured by pyrochars [287], as pyrolysis implies a more severe thermal conversion [288] in comparison to HTC. A decrease in H/C and O/C ratios after HTC of raw oak wood was observed, which was ascribed to dehydration reaction occurring during hydrothermal treatment [183].

Moreover, it is worth noting that the hydrochar (OW250) had a great proportion of volatiles, whose release during the activation process (OW250PA's VM is ca. 30 wt% lower than that of OW250) might have been responsible for the outstanding texture development (see Figure 4-12 and Table 4-9) experienced by this material. Apparently, as oak wood was poorly carbonized after HTC, the hydrochar was subjected to an additional

devolatilization during activation treatment, leading to an increase of the proportion of carbon from 61 to ca. 76 wt%. In addition to that, the high volatiles loss that occurred after the heat-treatment under CO₂ agreed with the larger reduction of H content, which decreased by ca. 60%. Also, fixed carbon enriched relatively (OW250PA's FC is ca. 30 wt% higher than that of OW250). Accordingly, it could be said that the liberation of volatile compounds accounted for most of the activation burn-off (ca. 45 wt% as given by Table 4-4) experienced by OW250. In contrast, volatiles content for OW800 was much lower as traditional pyrolysis, conducted at higher temperature than that held during HTC, had already removed most of the volatiles matter. This was also indicated by the lower carbon yield obtained after pyrolysis (ca. 21.5 wt%, see Table 4-1), which was less than half that of OW250 (nearly 56 wt%). As a result, a relatively lower burn-off (ca. 34 wt%, see Table 4-5) was measured after optimal activation of OW800.

Nonetheless, a higher proportion of fixed carbon (ca. 66 wt%) was found for OW800's compared to that featured by the OW250 hydrochar (nearly 33 wt%). This indicated the formation of a more stable carbon structure after pyrolysis. The higher degree of devolatilization, along with a slightly larger fraction of ash could explain why this sample did not experience a significant texture enhancement (see Figure 4-12) after physical activation.

Table 4-11 - Elemental and proximate analyses for key oak wood-based samples and commercial carbon

Sample ID	Ultimate, db					Proximate, db		
	N	C	H	S	O	VM	A	FC
OW	0.3	46.7	5.6	0.1	47.3	85.9	1.9	12.2
OW250	0.7	61.0	4.5	0.0	33.8	58.5	9.1	32.9
OW800	0.7	77.9	0.7	0.0	20.7	20.8	13.8	66.1
OW250PA	1.2	75.9	1.9	0.0	21.0	29.1	8.9	62.1
OW800PA	1.2	74.2	0.5	0.0	24.2	22.2	11.3	65.9
OW250CA	0.4	77.5	0.5	0.0	21.6	21.1	10.4	64.8
OW800CA	0.3	91.6	0.3	0.0	7.8	10.5	9.6	79.9
GAC	0.1	90.1	0.6	0.1	9.1	11.3	1.6	87.0

Heat-treatment under CO₂ did not cause any significant demineralization of the unactivated wood, as seen by the similar ash contents found for initial chars and physically activated counterparts. Indeed, these showed lower carbon purity than that observed for the commercial carbon (GAC). This was shown by GAC's extremely large fixed carbon content (87 wt%). In addition to

that, GAC's lower ash/volatile abundances were in line with its more developed texture (Figure 4-12 and Table 4-9) compared to that of physically activated oak wood.

On the other hand, chemical activation of OW800 followed by acid washing led to a material with comparable purity in carbon (overall C content up to 91.6 wt%) than that found for GAC (90.1 wt%). This was likely due to the washing treatment, which reduced the ash content from 13.8 wt% down to 9.6 wt%. In addition to this, release of oxygen as CO and CO₂ during KOH activation led to an increase in C/O ratio [289]. This was also in agreement with the lower concentration of volatiles measured for OW800CA (10.5 wt%) compared to that found for the physically activated carbon (22.2 wt%). In contrast, OW250CA exhibited lower carbon content (ca. 77 wt%) than that measured for OW800CA. The lower proportion of carbon found for OW250CA might be partly attributed to a poorer demineralization. This was suggested by the slightly higher fraction of ash measured by proximate analysis for this sample (ca. 10.4 wt%) compared to that featured by OW800CA (9.6 wt%). On the other hand, the lower purity of carbon matrix exhibited by OW250CA could be also explained by the higher amount of residual volatile matter (21.1 wt%) exhibited by this sample compared to that measured for OW800CA (10.5 wt%). Nevertheless, the hydrochar experienced a more dramatic reduction in volatiles (around 64% loss) than that occurred during KOH activation of pyrolyzed wood (ca. 50% loss). As previously stated, this might have caused the larger texture enhancement observed for OW250CA (see Table 4-9).

4.5.2 SEM and EDX analyses

SEM micrographs acquired at 5000 x magnification (Figure 4-20) depicts the morphology of all materials studied.

From Figure 4-20(a), the cellular appearance typical of a lignocellulosic biomass precursor [93, 183] could be observed. As seen in Figure 4-20(b) and (c), carbonization process did not significantly change the structure of the raw material. However, some small macropores can be observed for OW800, thus indicating that an elementary porous structure had started to develop during pyrolysis at 800 °C.

Although it was shown that heat-treatment under CO₂ led to the development of a more porous structure (see Table 4-9), this was not corroborated by SEM images as microporosity and mesoporosity are too small to be visible in SEM micrographs (see Figure 4-20(d) and (e)).

Nevertheless, SEM micrographs revealed the presence of particles dispersed onto the structure of chars and CO₂-activated carbons. As proved by EDX chemical compositions (see Figure 4-21) acquired on the micrographs shown in Figure 4-20, these particles were found to be inorganic. In particular,

Ca seemed to be the most abundant element both in raw oak wood and in synthesized derivatives (i.e. chars, activated carbons). Calcium concentration originally measured in the raw wood enriched relatively after carbonization and activation processes, whereas oxygen was found to decrease. This could be ascribed to the removal of O-based volatiles during heat-treatment of woody biomass.

SEM images taken for commercial carbon (GAC) showed an approximately regular macroporosity (see Figure 4-20(h)). By contrast, heterogeneously sized macropores were exhibited by KOH-activated samples, especially by OW800CA. The more evident development of porosity highlighted by SEM imaging agreed with the greater surface area noted for these samples in Table 4-9. Apparently, chemical treatment was more efficient at attacking the carbon matrix, thus creating a larger fraction of voids. Furthermore, unlike for oak wood chars and physically activated carbons, micrographs related to chemically activated wood and GAC showed lack of mineral matter. This was found to be consistent with what is highlighted in Figure 4-20, where a significantly lower inorganic content was measured for chemically activated samples. This was also in line with the lower ash abundances measured by proximate analysis (Table 4-11) for these materials.

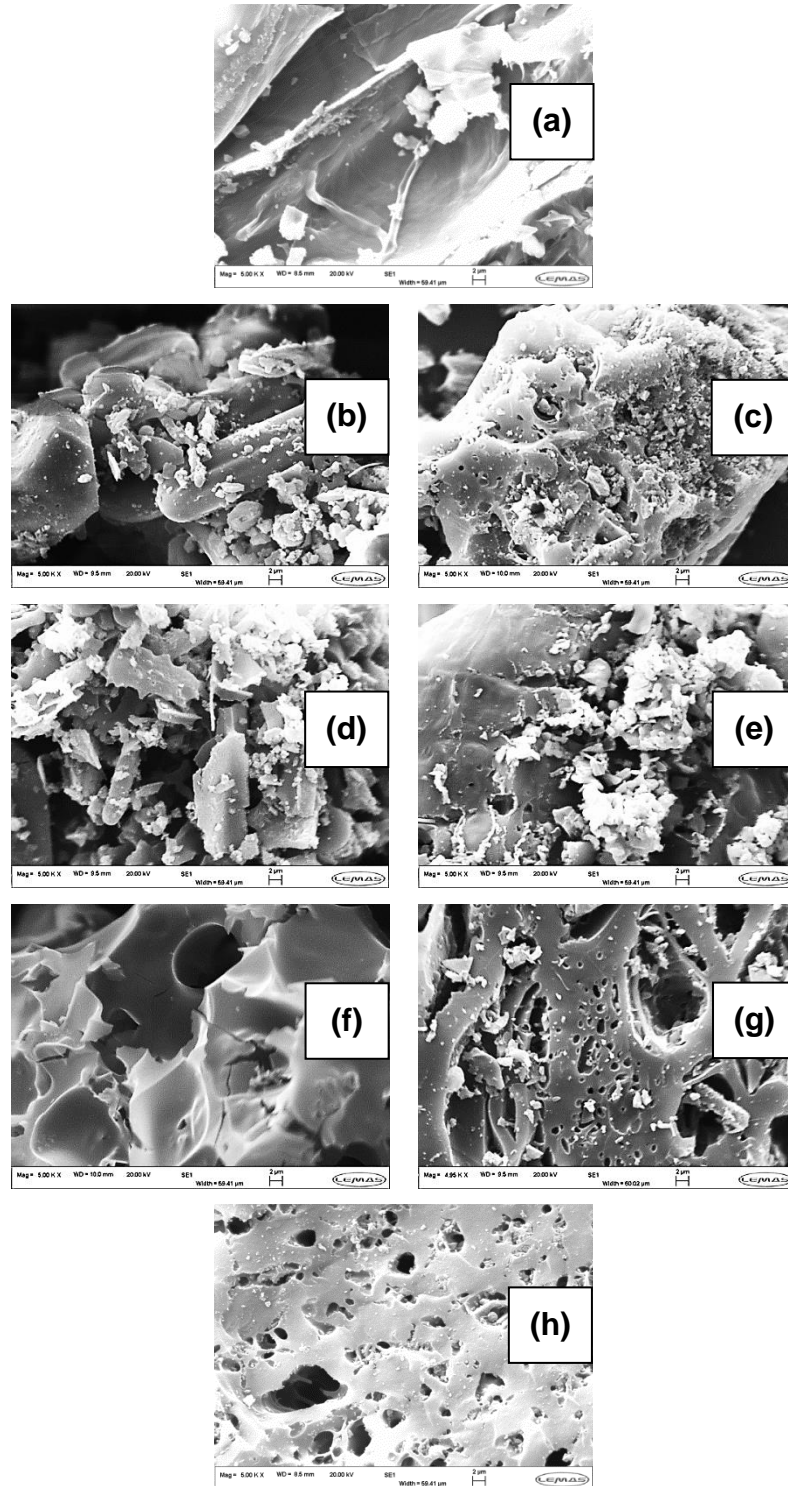


Figure 4-20 SEM images at 5000x magnification for (a) OW, (b) OW250, (c) OW800, (d) OW250PA, (e) OW800PA, (f) OW250CA, (g) OW800CA and (h) GAC.

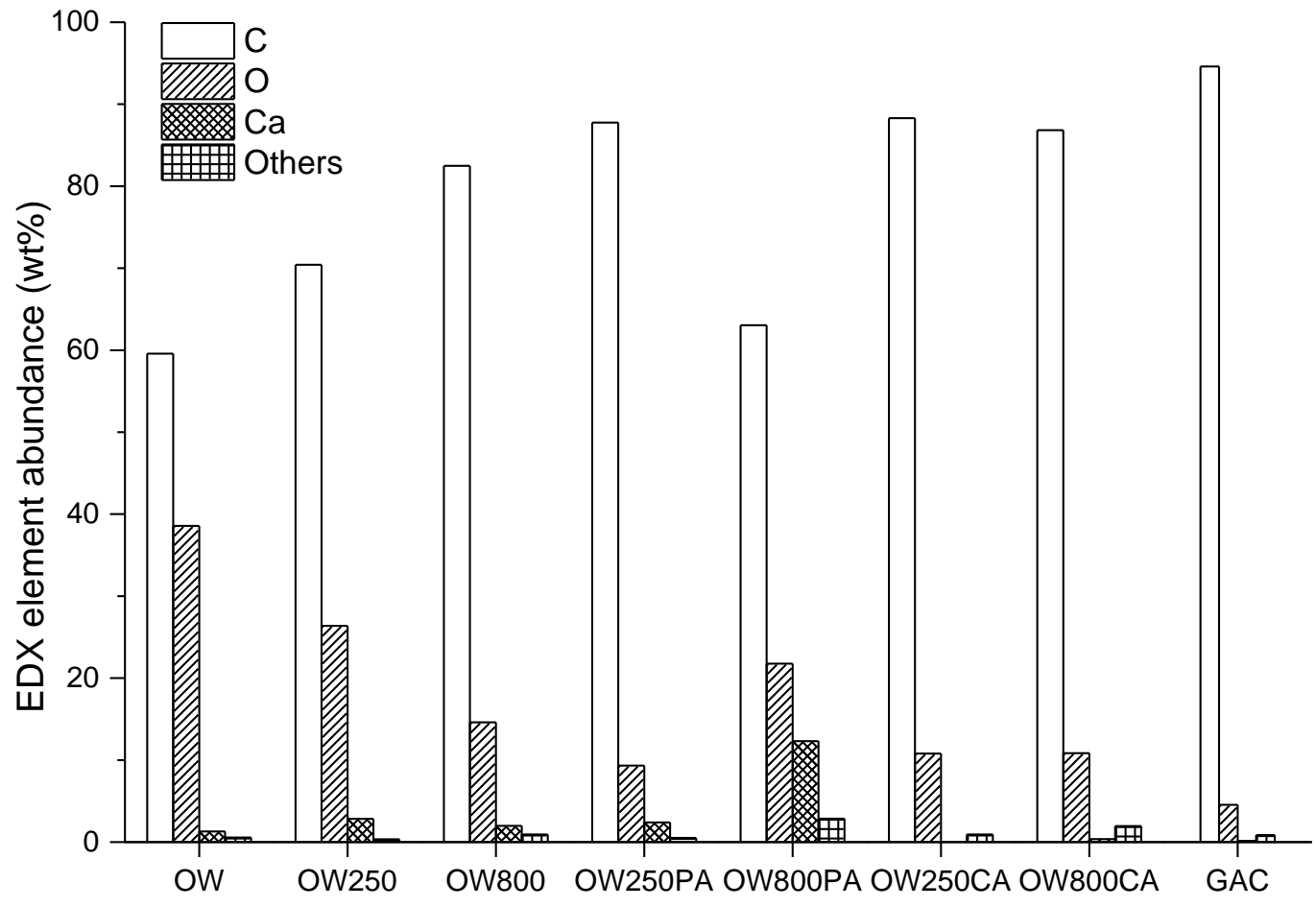


Figure 4-21 EDX chemical composition for key oak wood-based samples and commercial carbon

Table 4-12 - Details about inorganic elements (“Others” Figure 4-21) detected by EDX analyses for key oak wood-based samples and commercial carbon

OW		OW250		OW800		OW250PA		OW800PA		OW250CA		OW800CA		GAC	
Elem ²²	wt%	Elem	wt%	Elem	wt%	Elem	wt%	Elem	wt%	Elem	wt%	Elem	wt%	Elem	wt%
Al	0.10	Al	n.d.	Al	n.d.	Al	n.d.	Al	n.d.	Al	0.51	Al	0.47	Al	n.d.
Cl	n.d.	Cl	n.d.	Cl	0.42	Cl	n.d.	Cl	1.14	Cl	0.28	Cl	0.37	Cl	n.d.
Cu	n.d.	Cu	0.35	Cu	0.24	Cu	0.33	Cu	0.77	Cu	0.13	Cu	0.95	Cu	0.12
Fe	n.d.	Fe	n.d.	Fe	n.d.	Fe	0.09	Fe	n.d.	Fe	n.d.	Fe	n.d.	Fe	n.d.
K	0.38	K	n.d.	K	0.15	K	0.10	K	0.35	K	n.d.	K	n.d.	K	0.11
Mg	0.09	Mg	n.d.	Mg	0.12	Mg	n.d.	Mg	0.33	Mg	n.d.	Mg	n.d.	Mg	n.d.
Mn	n.d.	Mn	n.d.	Mn	n.d.	Mn	n.d.	Mn	0.28	Mn	n.d.	Mn	n.d.	Mn	n.d.
Mo	n.d.	Mo	n.d.	Mo	n.d.	Mo	n.d.	Mo	n.d.	Mo	n.d.	Mo	n.d.	Mo	0.60

²² Elem stands for Element.

4.5.3 XRD patterns

As depicted by Figure 4-22(a), XRD pattern of raw oak wood showed a broad scattering between 20 and 25° 2 θ . This might be ascribed to the 002 reflection, associated with disordered structure of non-graphitising carbon [79]. This peak is normally observed over the reported 2 θ range for carbon solids with a long-chain structural order [290]. Signal appeared to be broader and with a lower intensity after thermal treatment of wood (see Figure 4-22(b-d)). In addition to that, the reflection seemed to be shifted toward higher angles. This could have occurred because of the reduction of the interlayer distance between 002 graphitic planes [272]. The decrease of interlayer spacing with increasing temperature treatment has already been reported by Zhang *et al.* [82] for non-graphitising carbons.

However, slightly sharp peaks were also measured for pristine oak wood and best fitted by the standard pattern of a Ca-based crystalline phase (i.e. calcium oxalate hydrate, 00-016-0379). The three most intense peaks were recorded at ca. 15.1, 24.5 and 30.3° 2 θ . The same compound was identified after hydrothermal carbonization of wood, as all characteristic peaks were also measured for OW250 (see Figure 4-22(b)). However, peaks increased in sharpness, therefore indicating an increase of the crystallinity after the heat-treatment at 250 °C. Nonetheless, some impurities (see asterisks in Figure 4-22(a) and (b)) were present within both the raw material and within hydrochar. Moreover, according to the Sherrer equation [291] (see also Chapter 3), the increase of sharpness was caused by the growth of the crystallites size after heat-treatment. Indeed, the average crystal size of calcium oxalate hydrate was found to increase from 48.7 to 54.2 nm.

In contrast, sharp peaks measured for pyrolyzed char (i.e. OW800) matched with the standard pattern of calcium hydroxide (00-004-0733). Main peaks were measured at ca. 18.1, 34.1 and 47.1° 2 θ . The presence of calcium hydroxide might be explained by the conversion of calcium oxalate hydrate during pyrolysis. Calcium carbonate was identified on the structure of Holm and Pyrenean oak after pyrolysis at 600 °C by Lopez *et al.* [180]. However, as concerns OW800, it might be that at 800 °C calcium carbonate might have calcined to some extent [292], thus leading to the formation of calcium hydroxide.

As seen in Figure 4-22(c), XRD patterns of physically activated chars revealed the presence of calcium carbonate. In particular, a very sharp peak was measured at ca. 29.4° 2 θ , matching with the most intense peak of the standard pattern (01-080-9776). Additionally, a good matching was found for the remaining peaks having lower intensity. The most intense were measured at ca. 36.0, 39.5, 43.2, 47.5 and 48.5° 2 θ . Apparently, under CO₂ atmosphere, Ca-based compounds initially present within the chars (i.e. calcium oxalate hydrate and calcium hydroxide respectively) were converted into calcium carbonate

through carbonation reaction. XRD results were consistent with EDX findings, revealing a major presence of Ca-based particles onto the oak wood-based samples (see Figure 4-21).

As concerns KOH-activated chars, XRD analyses showed few sharp peaks but having low intensity (see Figure 4-22(d)). This suggested that most of the Ca-based crystalline phases were removed after acid washing. This was in agreement with the lower ash content found for these samples by proximate analyses as given in Table 4-11. Additionally, a lower concentration of inorganic species was detected by EDX for chemically-activated carbons. Nonetheless, peaks measured for OW800CA were fitted by calcium carbonate pattern, thus indicating a residual presence of this compound onto the structure of the chemically-activated wood. This might suggest that demineralization was not fully efficient and agreed with EDX results, showing a residual abundance of calcium for OW800CA (see Figure 4-21).

In contrast, aluminium oxide was identified as best match of peaks measured for OW250CA. This finding was once again consistent with EDX chemical composition measured for this sample, giving Al as the most abundant among inorganic species detected, followed by Cl and Cu. Al-based impurities might have not been detected for other samples because of the presence of more dominant phases. However, aluminium detected for OW250CA might have come from the alumina crucible used during the heat-treatment, as the ceramic vessel was acid washed in order to facilitate the recovery of the carbon product when KOH activation was performed.

However, results showed that KOH-activated carbons were characterized by a more amorphous structure typical of activated carbons. This agreed with the higher purity of the carbon matrix exhibited by these samples, especially by OW800CA (see Table 4-11). Finally, as depicted by Figure 4-22(e), a very amorphous structure was revealed for commercial carbon (GAC), only showing very broad peaks.

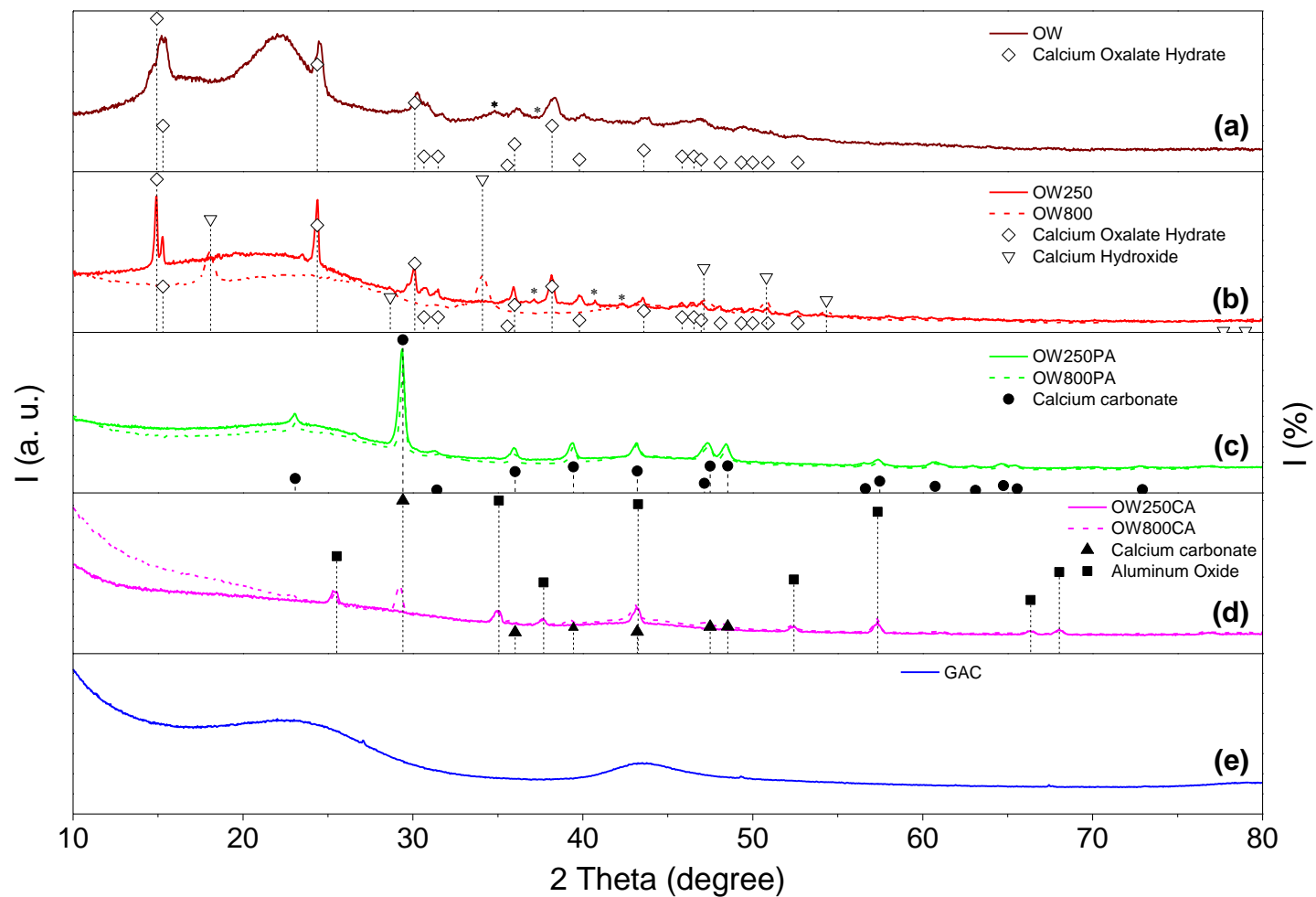


Figure 4-22 XRD patterns and standard stick patterns for raw oak wood (a), oak wood-derived chars (b), physically-activated chars (c), chemically-activated chars (d) and commercial carbon (e).

4.5.4 Boehm titration for selected samples

Figure 4-23 gave quantitative information about the surface chemistry of some of the samples analysed. It is interesting to note that the number of basic functionalities measured for the physically activated oak wood (OW800PA) exceptionally prevailed over those measured for OW800CA and GAC. In accordance with EDX and XRD results, it is reasonable to relate the more pronounced basic character of this sample to the presence of Ca-based compounds within its carbon matrix.

On the other hand, a low amount of acidic groups was measured for all samples. In particular, OW800CA had the largest number of acidic functionalities, probably due to the acid washing treatment following chemical activation.

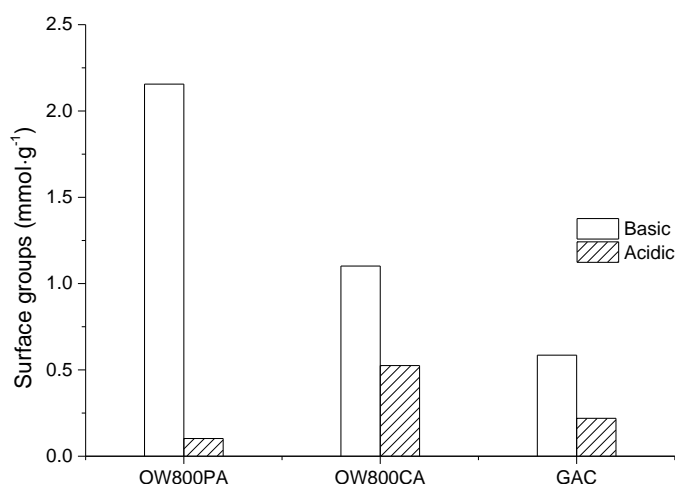


Figure 4-23 Boehm titration for selected samples

4.6 Assessment of CO₂ sorption performance

4.6.1 CO₂ uptake programmes

The present section aims to describe how the CO₂ sorption capacity of the sorbents was interpreted starting from Thermogravimetric Analysis (TGA) measurements carried out at atmospheric pressure and controlled gas atmosphere. In particular, OW800PA was chosen as representative sample for the illustration of the results. As already mentioned in Chapter 3, a preliminary method was created with the purpose of screening the best-performing sorbents. This was done at relatively low temperature (35 °C) and high partial pressure of CO₂ (100% by volume at 1 bar). In addition to this, another routine was made in an attempt to simulate a post-combustion condition, entailing

higher temperature (ca. 53 °C) and lower partial pressure of CO₂ (15% by volume or 0.15 bar).

4.6.1.1 35 °C, 100% CO₂

Figure 4-24 showed temperature programme and sample weight change related to the routine used for an initial test of the sorption capacity of the carbons. In particular, Figure 4-24(a) illustrates results obtained from the first version of the programme. This had to be amended for different reasons. First, the duration of degassing step at 120 °C was reduced from 60 to 30 min as limited weight losses were recorded in the last 30 min. Furthermore, for the same reason, the duration of the last isothermal step under N₂ at 120 °C was decreased from 30 to 15 min.

However, the major change concerned the cooling step prior to switching gas atmosphere from N₂ to CO₂ (S1). In fact, as seen in Figure 4-24(a), the switch to CO₂, dictating the beginning of the adsorption step, started when temperature was still decreasing. This occurred as a nominal cooling rate (HR=10 °C·min⁻¹) was initially considered, corresponding to a ca. 9 min time span. However, as clearly shown by Figure 4-24(a), TGA furnace took much longer (ca. 24 min overall) to cool down to the desired temperature, as the actual cooling rate was slower than the theoretical one. Therefore, in order to estimate the sorption capacity at constant temperature, an isothermal step under N₂ as long as the difference between actual (24 min) and theoretical duration (9 min) of cooling stage was added in the amended programme immediately after the 30 min degassing step. Consequently, as illustrated in Figure 4-24(b), this amendment allowed switching to CO₂ (i.e. starting the adsorption step) when both sample weight and temperature attained a plateau (see S1 at t=54 min). As a result, the increase in weight occurring at constant temperature (ca. 35 °C) when sample was exposed to CO₂ was interpreted as the CO₂ adsorption capability of the sample only, i.e. thereby eliminating weight changes due to buoyancy effects caused by cooling.

Adsorption kinetics were measured at constant temperature for 30 min, i.e. from t=54 min to t=84 min. However, note that later on a time scale 0-30 min was used for the visual representation of the sorption kinetics alone (see for instance Figure 4-28). Sample was regenerated at 100 °C at a heating rate of 5 °C·min⁻¹ (i.e. between t=84 min and t=97 min) and the residual amount of CO₂ was plotted against the temperature (see Figure 4-30) in order to evaluate the desorption behaviour of the material. Regeneration of the sorbent was then completed by switching back to nitrogen (S2) and bringing the temperature up to 120 °C. Final temperature was then held for further 15 min.

Sample run shown in Figure 4-24(b) was corrected for buoyancy effects by running the same programme for an empty pan (blank), which was shown in

Figure 4-25. The initial buoyancy was due to the decrease of temperature during the cooling stage. According to ideal gas law, nitrogen has higher density at lower temperature, thus involving a lower apparent weight of the pan. However, at ca. 50 °C (t=ca. 40 min), weight started to increase. This was ascribed to the sorption of the purging gas onto the alumina pan surface. A more significant buoyancy effect was observed when gas atmosphere was switched from nitrogen to carbon dioxide (at ca. 54 min). As the latter has a higher molecular weight and thus higher density than that of nitrogen, exposing the sample to CO₂ will result in a lower apparent weight of the pan. Vice versa, for the aforementioned reasons, weight increase occurred both when increasing the temperature (at ca. 84 min) and when switching back gas atmosphere to nitrogen (ca. 97 min).

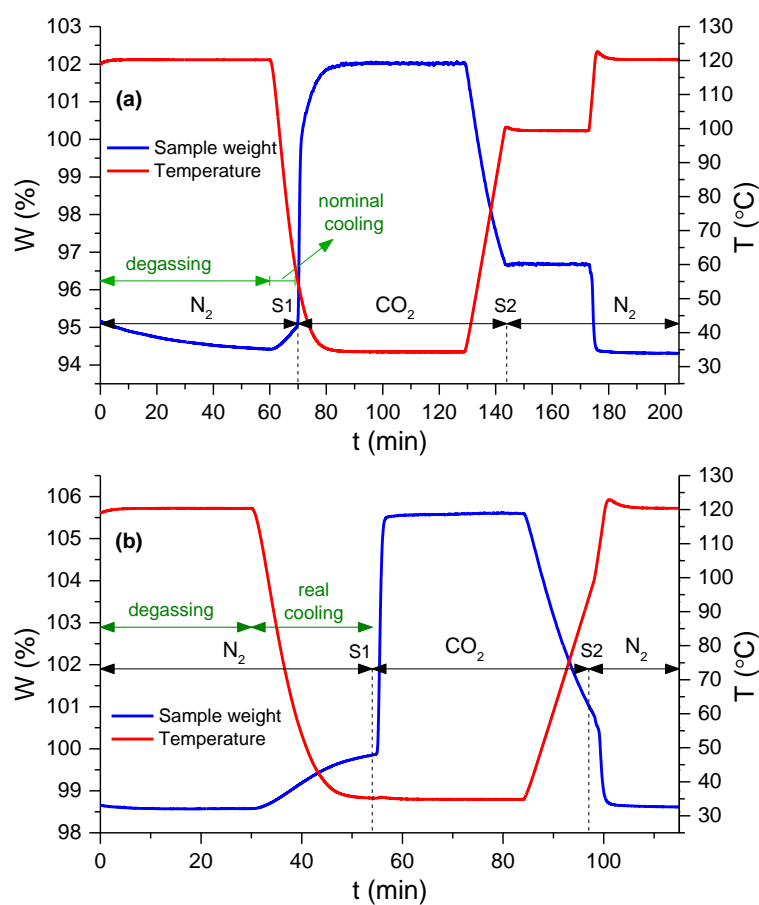


Figure 4-24 CO₂ uptakes programme (100% CO₂, 35 °C) for representative sample (OW800PA): (a) before amendment and (b) after amendment

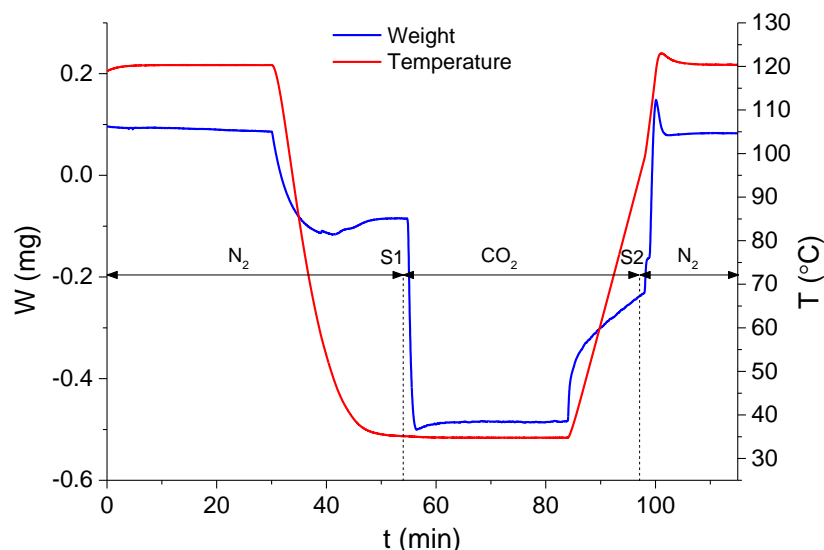


Figure 4-25 CO₂ uptakes programme (100% CO₂, 35 °C) - Blank run

4.6.1.2 53 °C, 15% CO₂

As previously described in Chapter 3, starting from the amended routine reported in section 4.6.1.1, a slightly different programme was created with the end of simulating post-combustion capture (15% CO₂ in N₂, 53 °C). As seen in Figure 4-26, all the main steps are maintained. On the other hand, cooling stage is slightly shorter (from t=30 min to t=52 min) as sample was cooled down to ca. 53 °C rather than to 35 °C. Accordingly, adsorption kinetic was measured for 30 min but from t=52 min to 82 min, while duration of desorption was reduced (from t=82 min to t=92 min) owed to the shorter temperature swing. As aforementioned, post combustion kinetics were generally shown over a time scale ranging from 0 to 30 min (see for instance Figure 4-31).

Once again, buoyancy correction was performed by blank subtraction (see Figure 4-27). Blank run is roughly similar to that measured in Figure 4-25. Nonetheless, it is worth noticing that a far lower drop in weight was recorded immediately after the first switch (see S1 in Figure 4-25 and Figure 4-27). Presumably, this was because in this case gas atmosphere was switched from N₂ to 15% CO₂ diluted in N₂ rather than pure CO₂, thus implying a less dramatic change in density.

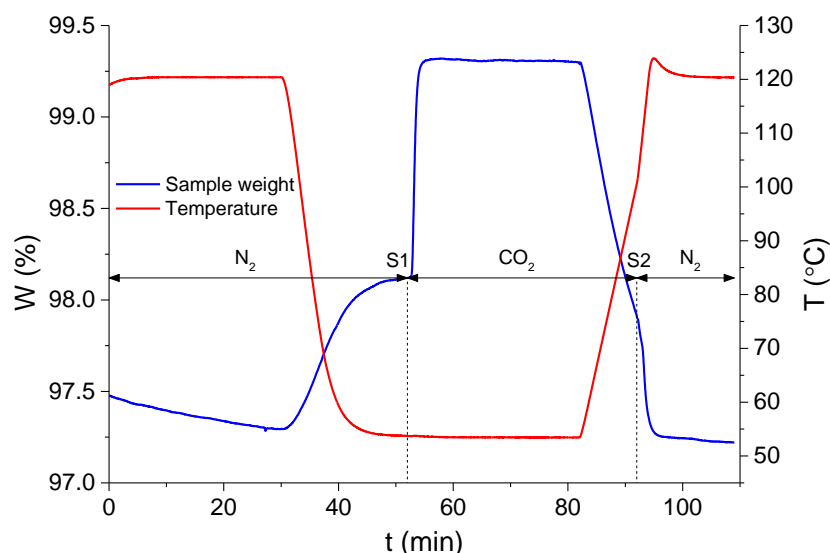


Figure 4-26 CO₂ uptakes programme (15% CO₂, 53 °C) for representative sample (OW800PA)

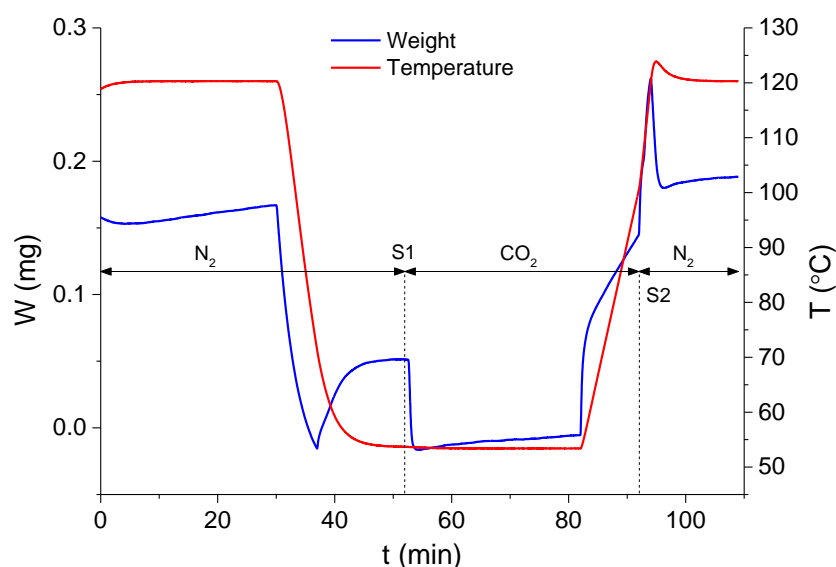


Figure 4-27 CO₂ uptakes programme (15% CO₂, 53 °C) - Blank run

4.6.2 First screening

As seen in Figure 4-28, except hydrothermally carbonized wood (OW250), all samples exhibited fast pure CO₂ sorption kinetics and relatively high uptakes at 35 °C. All materials reached their maximum capacity (saturation of sorption sites) within ca. 3 min. Interestingly, pyrolyzed oak wood (OW800) achieved a CO₂ uptake as large as that attained by the physically activated hydrochar (OW250PA). Despite the latter exhibited a larger surface area (see Table 4-9), this result might be explained by the comparable narrow microporosity measured by these samples (see Figure 4-16).

As reported in Table 4-13, the highest CO₂ capacity at 35 °C was recorded for the OW800CA, which adsorbed 71.6 mg CO₂·g⁻¹ (ca. 1.62 mmol CO₂·g⁻¹). This datum is comparable or even higher than values reported in other studies, where CO₂ uptakes were achieved under similar conditions [221, 293]. Nevertheless, sorption capacity fall short those of the best performance ever reported for ACs at room temperature and under pure CO₂ by Sevilla *et al.* [93]. These authors prepared CO₂ sorbents through KOH activation of hydrothermally carbonized chars derived from biomass, achieving up to ca. 212 mg CO₂·g⁻¹. The lower CO₂ capacities of the sorbents tested in this study might be partly attributed to the higher sorption temperature considered (35 °C as opposed to room temperature), but also to the carbon's smaller ultramicropore volumes (highest value of ca. 0.040 cm³·g⁻¹ for OW800PA vs 0.52 cm³·g⁻¹ [93]). In fact, this feature, in line with what reported in other works [294, 295], seems to be chiefly responsible for adsorbing carbon dioxide at high partial pressure (i.e. 1 bar).

Nevertheless, OW800CA outweighed the sorption performances of a commercial carbon included for comparison purposes. This can be ascribed to the more developed porous structure obtained after chemical activation of pyrolyzed wood (see Table 4-13). On the other hand, despite larger surface area and micropore volume than OW800CA, OW250CA attained a CO₂ uptake of only 45 mg CO₂·g⁻¹. This could be attributed to the lower narrow microporosity featured by this sample (0.014 cm³·g⁻¹) compared to that measured for OW800CA (0.026 cm³·g⁻¹). Furthermore, it is worth noting that the adsorption capability achieved at 35 °C by the physically activated oak wood (OW800PA) was very close to that of commercial carbon, although the latter has significantly higher textural properties (GAC's surface area is twice that of OW800PA), which should have implied far higher CO₂ uptake.

It follows that both ultramicropore volume and larger porosity (i.e. surface area) seem to be affecting CO₂ sorption at 35 °C and 1 bar. This was proved by correlations reported in Appendix A. In particular, for a selected set of samples, uptakes at 35 °C and 1 bar were plotted vs either BET surface area or a textural factor determined as BET surface area times the ultramicropore volume calculated by applying NLDFT model to the CO₂ adsorption isotherms measured at 0 °C. In particular, poor correlation was found between CO₂ uptakes and the surface area only ($R^2=0.5103$). In contrast, coefficient of determination increased up to 0.9024 when considering correlation between CO₂ uptakes and textural factor.

Nonetheless, some other parameters might have played a key role in the CO₂ uptake process. This was indicated by Figure 4-29, where CO₂ uptakes were normalized by surface area to remove the effect of texture. The higher figure of normalized uptakes measured for physically activated oak wood (see Table 4-13), coupled with the higher amount of basic functionalities (see Figure 4-23) found for this sample, suggested that, if texture is disregarded, CO₂-

activated oak wood has a greater CO₂ sorption potential than that of the corresponding chemically-activated carbon (OW800CA) and GAC. The greater affinity between CO₂ and OW800PA could be due to the stronger basic character exhibited by the CO₂-activated wood (see Figure 4-23). Basicity of OW800PA could be attributed to some Ca-based groups, as calcium was the most abundant element for all oak wood-derivatives (see Figure 4-21). In particular, alkalinity might have arisen from the amorphous fractions of calcium oxide and/or hydroxide (not detected by XRD pattern in Figure 4-22(c)) intrinsically present within the structure of the material. Crystalline form of Ca(OH)₂ had already been identified for OW800 (see Figure 4-22(b)) and it may have not been totally converted into calcium carbonate after CO₂ activation. On the other hand, it may be that some of the calcium carbonate decomposed at 800 °C [292], thus giving rise to amorphous calcium oxide/hydroxide. This would explain a probable chemisorption of CO₂ occurring onto the oak wood-derived carbons (carbonation reaction).

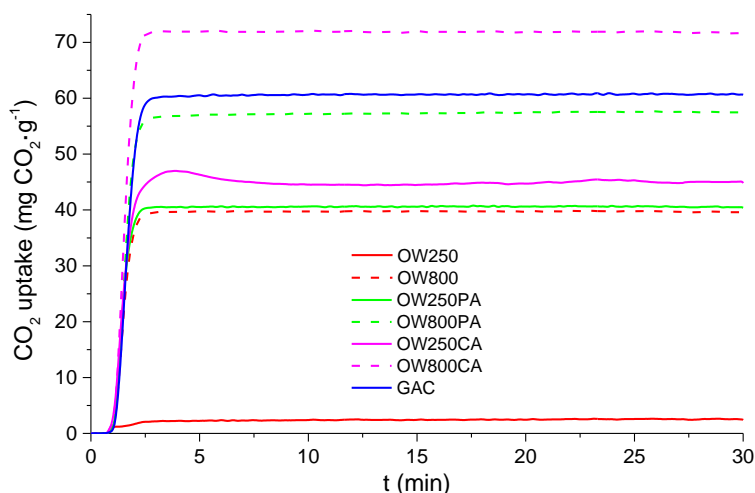


Figure 4-28 CO₂ kinetics measured at 35 °C and 1 bar (total pressure of 1 bar) for all samples

Moreover, as illustrated in Figure 4-30, the CO₂ uptakes decreasing trend with increasing temperature was less steep for OW800PA, in particular between 35 °C and 60 °C. This was also indicated by the lowest weight loss recorded for this sample (see Table 4-13) over this temperature range. Indeed, as clearly visible from Figure 4-30, OW800PA's curve crosses over GAC's and OW800CA's at ca. 55 °C and 70 °C respectively. Chemically-activated wood exhibited the most dramatic decrease of CO₂ capacity with increasing temperature, thus indicating a weak interaction between this sample and carbon dioxide molecule. This could be attributed to the lower amount of basic functionalities (see Figure 4-23) found for this material. This was in line with the scarcity of ash and the lower inorganic content measured after chemical activation of pyrolyzed char (see Table 4-11 and Table 4-12 respectively) as a

result of acid washing. The stronger bond between OW800PA and carbon dioxide was also suggested by the higher energy of adsorption calculated for this sample by applying DR model to the CO₂ adsorption isotherms measured at 0 °C (see Table 4-9).

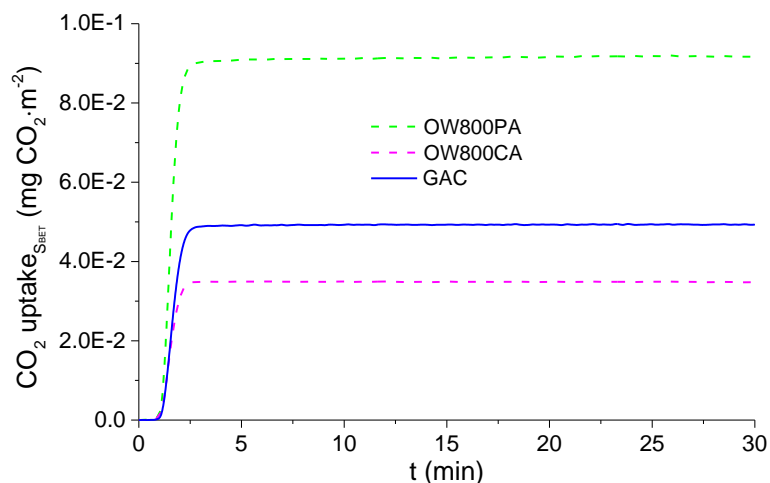


Figure 4-29 CO₂ kinetics measured at 35 °C and 1 bar (total pressure of 1 bar) and normalized by surface area for best performing samples

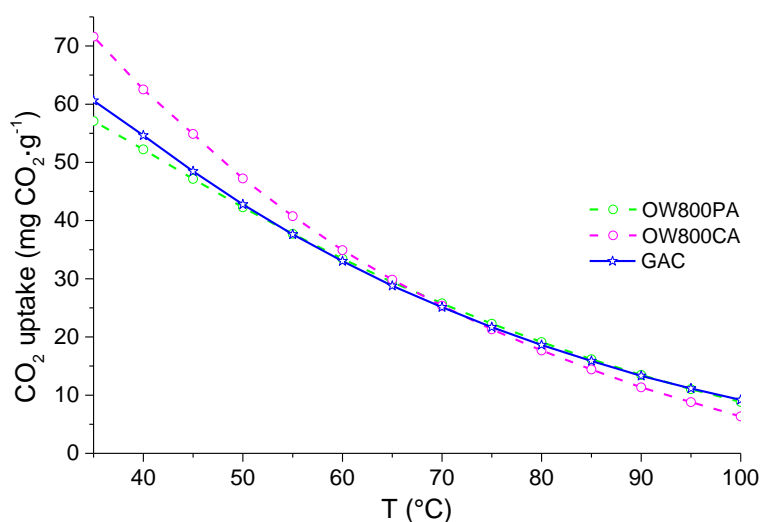


Figure 4-30 Regeneration (single rapid temperature swing adsorption (RTSA) cycle, 35-100 °C) for best performing samples

Table 4-13 CO₂ uptakes measured at a total pressure of 1 bar for oak wood derivatives (chars and activated carbons) and commercial carbon (GAC)

Sample ID	1 bar (100% CO ₂)				0.15 bar (15% CO ₂)		
	35 °C	35 °C , Norm ²³	60 °C	W _{loss, 35-60 °C} ²⁴	100 °C	W _{loss, 60-100 °C} ²⁵	53 °C
	mg CO ₂ ·g ⁻¹	mg CO ₂ ·m ⁻²	mg CO ₂ ·g ⁻¹	%	mg CO ₂ ·g ⁻¹	%	mg CO ₂ ·g ⁻¹
OW250	2.6	-	-	-	-	-	NM ²⁶
OW800	39.6	-	-	-	-	-	NM
OW250PA	40.6	-	-	-	-	-	7.2
OW800PA	57.1	9.1E-02	33.4	41	8.8	74	11.8
OW250CA	45.0	-	-	-	-	-	5.1
OW800CA	71.6	3.5E-02	34.9	51	6.3	82	8.4
GAC	60.6	4.9E-02	33.0	45	9.2	72	9.0

²³ CO₂ uptakes normalized by BET surface area

²⁴ Calculated as difference between the sorption capacity at 35 and 60 °C, and expressed as a % of the sorption capacity at 35 °C.

²⁵ Calculated as difference between the sorption capacity at 60 and 100 °C, and expressed as a % of the sorption capacity at 60 °C.

²⁶ Not measured

4.6.3 Simulated post-combustion performance

As depicted by Figure 4-31, under simulated post-combustion conditions (ca. 53 °C, 15% CO₂) all selected materials attained fast CO₂ sorption kinetics. However, the highest sorption capacity measured for the thus synthesized virgin carbons (ca. 12 mg CO₂·g⁻¹ or 0.27 mmol CO₂·g⁻¹ for OW800PA) is slightly lower than the best performance (0.50 mmol CO₂·g⁻¹) reported in the literature for ACs under similar conditions (ca. 40 °C, 0.15 bar) [58].

Nevertheless, it is interesting to observe that OW800PA attained larger CO₂ uptakes than those measured for OW800CA (8.4 mg CO₂·g⁻¹) and GAC (9 mg CO₂·g⁻¹) at the equilibrium. As already stated in section 4.6.2, it seems reasonable to associate such behaviour with the more favoured surface chemistry of OW800PA. Apparently, basic surface of the oak wood carbon ensured stronger interactions with the carbon dioxide molecule at higher temperatures and lower gas concentration, thus implying a higher (CO₂/N₂) selectivity of the sorbent. In contrast, the performance of the other two sorbents (GAC and OW800CA), only relying on texture, was significantly affected by the increase of temperature, when physisorption becomes less effective. Indeed, chemically activated wood appeared to release some CO₂ over equilibration time. As observed in Figure 4-31, decreasing trend led to the cross over between sorption curves measured for OW800CA and GAC occurring at ca. 15 min.

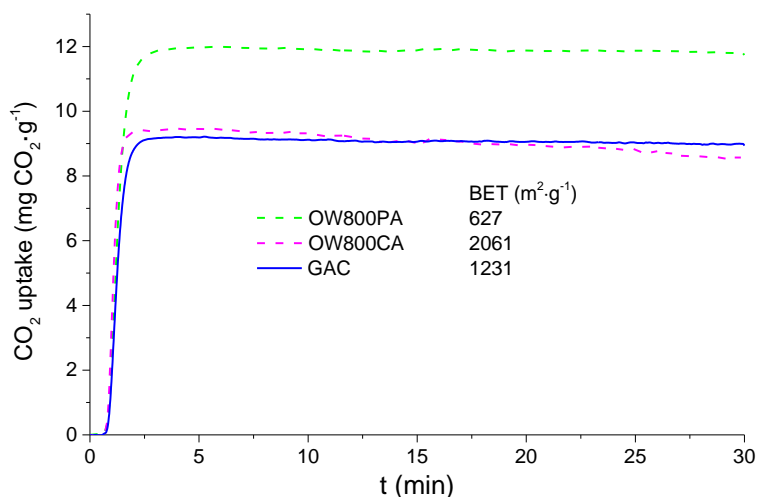


Figure 4-31 15% CO₂ adsorption kinetics at 53 °C and 0.15 bar (total pressure of 1 bar) measured for best performing samples

Figure 4-32 showed the regeneration of the materials after one single RTSA cycle at 100 °C. CO₂ was fully desorbed from all sorbents at ca. 90 °C. In particular, OW800PA exhibited a similar or even easier desorption than that observed for OW800CA and GAC, respectively. The regeneration capacity of the best performing sample (i.e. OW800PA) was then tested over multiple

RTSA cycles. In this case, material regeneration was accomplished at 120 °C. Note that, despite Figure 4-32 suggested 100 °C as suitable condition for regeneration of OW800PA, other sorbents (see Chapter 5 and 6) were not fully regenerated at this temperature.

Therefore, in order to compare the regeneration capability of materials under identical conditions, 120 °C was chosen as regeneration temperature for cyclic experiments. In particular, Figure 4-33(a) illustrates the recyclability of the physically-activated carbon (OW800PA). Note that the apparent decrease of the plateau observed in Figure 4-33(a) is due to a continuous baseline drift downwards. Nonetheless, as clearly seen by Figure 4-34, where only the first 2 adsorption/desorption cycles are shown, the sorbent regeneration was rapidly (ca. 14 min) completed when swinging the temperature up to 120 °C. Interestingly, Figure 4-34 also showed that during the first adsorption step OW800PA exhibited a slower CO₂ sorption kinetic in comparison to that observed over the second adsorption stage. In addition to this, as represented in Figure 4-33(b), the CO₂ uptake attained by OW800PA after the first adsorption step was higher than those attained during the following cycles. These observations seem to suggest that (Ca-based) chemical functionalities present within OW800PA were removed after the first temperature swing at 120 °C. Consequently, as depicted by Figure 4-33(b), the CO₂-activated wood only attained ca. the 75% of the initial sorption capacity at the end of the second adsorption step. In spite of this, Figure 4-33(b) also showed that from the second cycle onward OW800PA's sorption capability appeared to be steady, thus indicating a good durability of the sorbent.

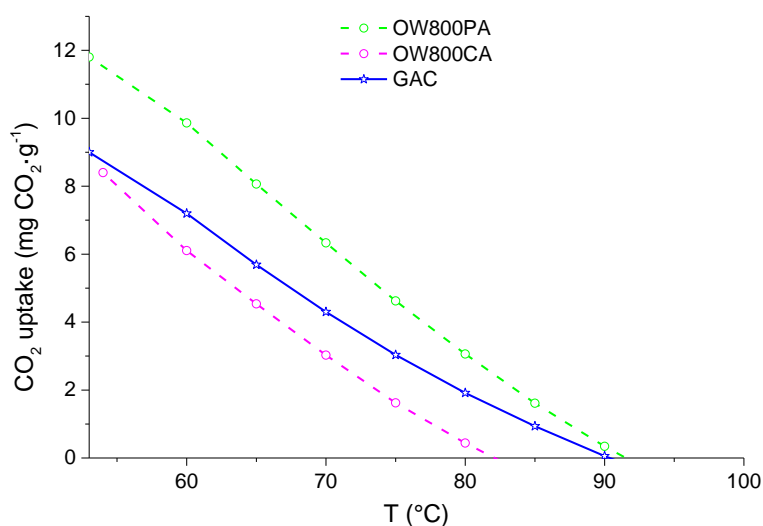


Figure 4-32 Regeneration (single RTSA, 53-100 °C) for best performing samples

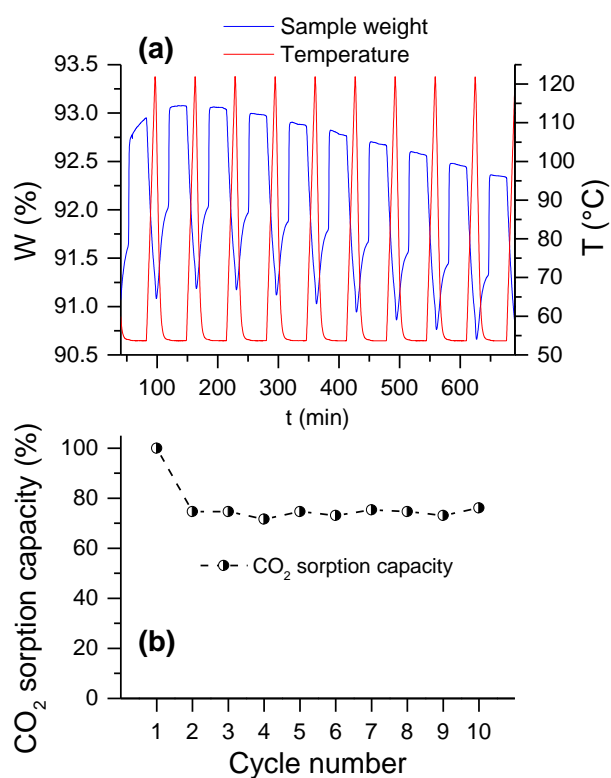


Figure 4-33 (a) Regeneration performance and (b) CO_2 sorption capacity over ten RTSA cycles for the physically-activated wood (OW800PA)

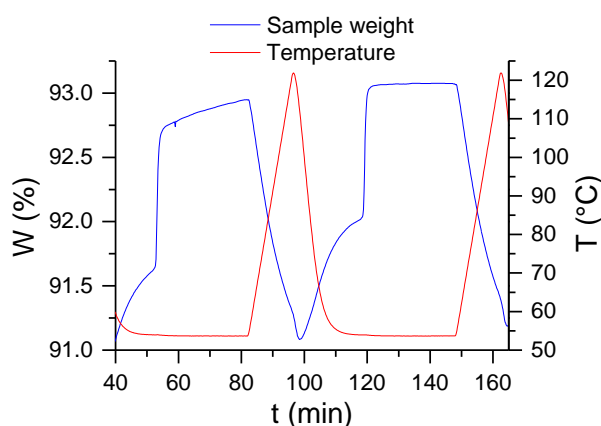


Figure 4-34 Zoom of the first 2 RTSA cycle for the physically-activated wood (OW800PA)

4.7 Chapter Conclusions

Raw oak wood (OW) was successfully converted into activated carbons through a two steps process, i.e. carbonization and activation.

Pyrolysis of wood conducted at high temperature (i.e. 800 °C) resulted in a higher extent of carbonization compared to that obtained by hydrothermal treatment. In fact, fixed carbon found for pyrolyzed wood (OW800) was twice as

large (66 wt% vs 33 wt%) that measured for hydrochar (OW250). In contrast, raw material was not completely devolatilized after hydrothermal treatment. Consequently, hydrothermally carbonized wood did not show any well-defined porous structure, whereas some degree of microporosity was already formed after pyrolysis. Both carbonization processes were found to be repeatable in terms of char yield. Additionally, pyrolysis of wood was not affected by the type of rig used. On the other hand, mass balance carried out for HTC process water showed a slightly higher variability. Nevertheless, relatively low errors were obtained for all parameters, thus indicating acceptable repeatability of the carbonization processes.

Synthesized chars were then activated by pursuing two different routes. Physical activation of biochars was optimized by maximizing surface area as a function of activation temperature and dwell time. Results revealed a stronger influence of the former parameter on the texture development of activated hydrochar. However, a remarkable effect of the activation holding time on the textural parameters of pyrolyzed wood was observed. In particular, surface area dramatically increased when increasing the dwell time from 0 to 1 h, whereas significantly decreased when prolonging the holding time from 1 to 2 h. Optimal conditions were found to be 600 °C for 30 min and 800 °C for 1 h for hydrochar and pyrolyzed wood respectively. After optimal heat-treatment, hydrochar (OW250) was subjected to a higher carbon burn-off (46 wt%) than that measured for OW800 (34 wt%). This was likely because of a further devolatilization experienced by the hydrothermally carbonized wood during activation. Yet, limited values of surface areas were obtained for physically-activated carbons, i.e. 415 m²·g⁻¹ for OW250PA and 627 m²·g⁻¹ for OW800PA.

Conversely, KOH activation followed by acid washing led to far more dramatic texture enhancement than that achieved through physical (CO₂) activation. In particular, the highest surface area (2757 m²·g⁻¹) was achieved after chemical activation of hydrochar (OW250CA). In addition, a washing step was found to be essential in order to exploit the porosity created by KOH carbonation. Particularly, porosity of unwashed sample was completely inaccessible. This was ascribed to potassium carbonate residues blocking the pores. The presence of residual potassium carbonate was proved by combining FTIR and EDX results. In addition, after acid washing of OW800CA, surface area increased by 50% compared to the value obtained after washing the sample with water only. This was due to a more efficient removal of potassium-based compounds deposited within the carbon pores after heat treatment. Furthermore, especially for OW800CA, chemical treatment resulted in a higher purity of the carbon matrix, as most of the inorganic impurities were dissolved by acid. On the other hand, chemical activation involved some drawbacks. First, especially after KOH activation of hydrochar, a very low yield was obtained (less than 3 wt%). Therefore, the production of this material on a larger scale would be uneconomical. In contrast, larger activation yield were obtained for

OW800CA (ca. 44 wt%). Yet, it is worth mentioning that a very light powder with low mechanical strength was obtained as final product. This could represent an issue if an adsorption column was to be packed with this material, as mechanically strong particles would be preferred in industrial applications.

Interestingly, activation treatments of hydrothermally synthesized wood led to much more dramatic texture development than that experienced by pyrolysis-derived char. As aforementioned, this was mostly due to the additional devolatilization that occurred when submitting hydrochars to the activation process. Based on observation reported, it could be inferred that physical activation of hydrochar might be a more energetically convenient route for the preparation of porous sorbents, especially when starting from wet feedstock containing low amount of ash.

According to CO₂ adsorption isotherms measured at 0 °C, activation methods gave rise to carbons having a very low proportion of narrow microporosity. NLDFT model was believed to give a more reliable estimation of the ultramicropore volume as a stronger correlation with the volume of CO₂ adsorbed at 0 °C and 1 bar was found.

SEM imaging coupled with EDX analysis allowed for detection of Ca-containing particles attached to the carbon structure of oak wood derivatives. XRD patterns confirmed the presence of Ca-based crystalline phases for all samples except KOH-activated hydrochar (OW250CA), as inorganic fractions were mostly removed after HCl washing. In particular, hydrated forms of calcium-containing compounds (calcium oxalate and calcium hydroxide) were identified within the structure of raw and carbonized wood, while physically activated chars exhibited calcium carbonate as main crystalline phase. This might have arisen after carbonation reaction occurring throughout CO₂ activation. On the other hand, amorphous fractions of calcium hydroxide (not detected) may have formed following to a slow rate decomposition of calcium carbonate at 800 °C. However, larger proportion of alkali metal-containing species were believed to be responsible for the higher basic character possessed by OW800PA. Indeed, as shown by Boehm titration, this sample exhibited a far larger number of basic functionalities compared to that measured for its chemically-activated analogue (OW800CA) and for a commercial carbon (GAC) included for comparison purposes.

All carbons exhibited fast CO₂ sorption kinetics at 35 °C and 1 bar, reaching saturation within less than 5 min. OW800CA attained the largest sorption capacity (around 70 mg CO₂·g⁻¹). This figure was higher than that exhibited by the commercial carbon (GAC), but far lower than highest values reported by literature. Lower CO₂ uptakes measured in this study were mostly attributed to the undeveloped ultramicroporosity of the materials tested. This confirms the importance of narrower microporosity in the CO₂ uptake process at high partial pressure. Nevertheless, correlations reported in this work seemed to

suggest that CO₂ sorption at 35 °C and 1 bar might be governed by a combination of surface area (i.e. larger porosity) and narrow microporosity.

Unexpectedly, under simulated post-combustion conditions (53 °C, 0.15 bar) the physically activated carbon (OW800PA) was more selective at capturing CO₂ than other sorbents with well more developed texture (i.e. OW800CA and GAC). This finding was ascribed to the larger basicity measured for OW800PA, which in its turn was related to Ca-containing species intrinsically present within the structure of the CO₂-activated wood. It seemed that alkali metal-based inorganic matter ensured a stronger interaction between CO₂ and the physically-activated carbon. This agreed with the higher energy of adsorption measured between the sorbent and CO₂ at 0 °C. Inorganic species were mostly removed after chemical treatment, by acid washing, and were not present within the commercial carbon. Since OW800CA and GAC were not as selective as OW800PA under post-combustion conditions, the findings clearly indicated that texture is no longer the predominant parameter at higher temperature and lower partial pressure (i.e. post-combustion condition). In contrast, basicity appeared to be the key factor to be considered when designing selective sorbents for post combustion capture.

Along with increased selectivity, OW800PA also exhibited a more facile desorption step and was fully regenerated at 100 °C. This suggested that a very low temperature could be applied for the regeneration of the material over multiple RTSA cycles. Accordingly, heat required for the sorbent regeneration would be reduced, thus optimizing energy costs. Furthermore, excepting an initial loss after the first adsorption-desorption cycle, the sorbent capacity seemed to attain a plateau over the remaining 8 cycles, thereby indicating good durability over the time.

In conclusion, traditional pyrolysis followed by chemical activation seemed to be the most suitable route to produce cost-effective CO₂ (physi)sorbents at higher partial pressure of CO₂ and lower temperature. In addition to this, raw oak wood revealed to be an advantageous precursor for an eco-friendly synthesis of selective CO₂ sorbents under post-combustion conditions. In particular, alkali metal (Ca)-containing compounds intrinsically incorporated within the raw material allowed producing highly basic sorbents without applying any chemical modifications. Physical activation is preferred to chemical treatment for preparation of CO₂ sorbents at low partial pressure, as it does not remove basic inorganic functionalities, which are evidently vital under post-combustion conditions. Additionally, physical treatment is less contaminant than KOH activation.

5 Sustainable and regenerable alkali metal-containing carbons derived from seaweed for post-combustion capture of CO₂

5.1 Outline

This chapter focuses on the use of a widely available feedstock, seaweed, for a sustainable preparation of alkali metal-containing activated carbons (ACs). In particular, attention was directed toward a type of brown macroalgae (i.e. *Laminaria hyperborea*), which was selected as precursor for ACs fabrication.

The raw material processing was similar to that pursued for the oak wood (see Chapter 4). A first step entailed obtaining chars either by dry pyrolysis or by hydrothermal carbonization (HTC). Results related to the repeatability of the carbonization of *Laminaria hyperborea* are reported in section 5.2.

Following this, pyrolyzed and hydrothermally carbonized *Laminaria hyperborea* were activated by pursuing two different routes, i.e. either physical (CO₂) or chemical (KOH) activation. In section 5.3, the optimal conditions are systematically determined for both activation procedures. In particular, the Brunauer-Emmett-Teller (BET) surface area of the carbons is maximized as a function of chosen parameters. As concerns the CO₂ activation, in line with experiments already done for the oak wood in Chapter 4, the influences of activation temperature and dwell time on the textural properties of the carbons were assessed. With respect to the chemical treatment, the effects of activation temperature and KOH to char ratio were examined.

In section 5.4, the textural parameters of the raw macroalgae and all its derivatives (i.e. chars and optimally-activated carbons) are compared. In addition, the CO₂ adsorption at 0 °C was also measured in an attempt to quantify the narrow microporosity of the samples.

The alteration of the chemical properties of the raw *Laminaria hyperborea* induced by carbonization and activation processes is discussed in section 5.5. However, some of the characterizations (i.e. X-Ray Diffraction (XRD) and Boehm titrations) were conducted only for some of the macroalgae-derived materials (see section 5.5.3). This choice was mostly dictated both by the large amount of material required by these techniques and by the scarcity of the raw feedstock. In addition to this, in accordance with the strategy already described in Chapter 4, the samples of interest were selected according to their CO₂ capture performance (see section 5.6). In particular, a first test carried out at lower temperature (35 °C) and higher partial pressure of CO₂ (1 bar) was used to identify samples showing the most interesting behaviour in terms of CO₂

uptake and sorption kinetics. Based on results observed, additional characterizations and a post-combustion test were carried out only for pyrolyzed *Laminaria hyperborea* (LH_S800) and its activated counterparts (LH_S800PA and LH_S800CA).

Finally, a summary of the chapter is given in section 5.7.

5.2 Carbonization of *Laminaria hyperborea*

5.2.1 Repeatability of dry pyrolysis and HTC

As already done for the oak wood in Chapter 4, the carbonization of *Laminaria hyperborea* was carried out in triplicate in order to assess its repeatability. In particular, the variation of the carbonization yield was determined for both dry pyrolysis and for hydrothermal carbonization. Furthermore, for each HTC run, the errors related to the water balance (see Chapter 3) were also calculated.

Around 5 g of raw *Laminaria hyperborea* were pyrolyzed in a ceramic furnace, and each run was performed under the same conditions (see Chapter 3). As already mentioned in Chapter 4, it was not possible to estimate the repeatability of liquid and gas fractions, as the limited amount of volatiles produced was dragged away to the exhaust by the purge gas before it could condense in the trap.

Standard amounts of raw material (24 g) and water (220 g) were used for the hydrothermal treatment repeats. The mixture was then heated up at 250 °C and held at this temperature for 1 h.

As seen in Table 5-1, the pyrolysis treatment led to higher yield variability than that measured for the HTC repeats. This was indicated by the higher value of standard deviation from the mean (up to 7.33%) calculated for the LH_S800's yield compared to that obtained for LH_S250 (3.56%). Yet, the repeatability of both carbonization processes was within the maximum tolerable value (i.e. 10% [282]).

The average pyrolysis yield (ca. 27 wt%) was higher than that recorded for the pyrolyzed wood (21.50 wt%, see Chapter 4). This might be due to the catalytic effect of the higher inorganic fractions (especially K) contained by *Laminaria hyperborea* (see Table 5-11 and Table 5-12), which are expected to increase the char production [134, 181, 200, 201]. On the other hand, proximate analyses revealed that the proportion of fixed carbon (FC) measured for pyrolyzed *Laminaria hyperborea* (27.5 wt%) was much lower than that measured for OW800 (66.1 wt%). This was probably because of the larger amount of ash (A)-free organic matter contained within the raw oak wood, which

was converted to ash-free carbon [296]. This might suggest oak wood as a better candidate for activated carbon production.

Pyrolysis of *Laminaria hyperborea* was also conducted in a larger scale (stainless steel) rig under the same conditions held when using the ceramic furnace, but loading larger amounts of raw feedstock. The large-scale pyrolysis was carried out in duplicate, yet a different mass of raw material was used for each run (ca. 65 or ca. 140 g). Interestingly, the carbonization runs led to very similar yields (ca. 30.36 wt% and 30.79 wt% respectively), thus showing that the mass of raw feedstock did not affect the final char yield. In addition to that, it is notable that the pyrolysis process conducted in the large-scale rig resulted in a slightly higher char formation compared to the carbonization carried out in the small-scale rig (i.e. ceramic furnace). Accordingly, if the influence of the reactor loading was to be excluded, this finding might be ascribed to a slower pyrolysis (lower heating rate (HR)) occurred in the large-scale rig, which might have facilitated char production [181]. This result was also in line with that found by Ross *et al.* [134], reporting a larger char formation for slow ramp rate pyrolysis than for flash pyrolysis.

According to the author's best knowledge, no data related to the carbonization of *Laminaria hyperborea* under similar conditions used in this study were found in the literature. However, few studies about the pyrolysis of different types of *Laminaria* have been reported. For instance, Bae *et al.* [138] pyrolyzed *Laminaria japonica* at 600 °C for 1h, measuring a product yield of ca. 40 wt%. This was higher than that measured in this study likely because of the lower pyrolysis temperature applied. In addition, Ferrera-Lorenzo *et al.* [203] pyrolyzed a macroalgae solid waste under similar conditions to those used in this work (i.e. 750 °C for 1 h). A carbonization yield of ca. 30 wt% was reported by these authors, which agrees with that found in the present study, especially when pyrolyzing *Laminaria hyperborea* in the large scale reactor. Also, Stratford *et al.* [202] reported a lower char formation (i.e. 17 wt%) after pyrolysis of *Laminaria digitata* (oarweed) at 800 °C. However, in this case the product yield was determined considering the solid residue following pyrolysis and acid washing.

The hydrothermal treatment of *Laminaria hyperborea* yielded a slightly larger amount of solid residue (ca. 34 wt%) than that measured after pyrolysis. This was in accordance with results already found for oak wood (see Chapter 4), as the hydrothermal synthesis of biomass was carried out at much lower temperature compared to that used for the pyrolytic treatment.

Previous studies on the hydrothermal treatment of macroalgae are also limited. A solid residue of ca. 25 wt% was reported by Anastasakis and Ross [206] who performed HTC of *Laminaria hyperborea* at 250 °C for 15 min. Furthermore, another type of macroalgae (i.e. *Enteromorpha prolifera*) was hydrothermally carbonized by Xu *et al.* [208] at 250 °C for 60 min, obtaining a

solid yield of 15 wt%. HTC of *Enteromorpha prolifera* was also carried out by Zhou *et al.* [205], who reported hydrochar yields below 20 wt% when conducting hydrothermal treatment at temperatures of 240 and 260 °C held for 30 min. It is worth noting that the higher yield obtained for *Laminaria hyperborea* in this work might indicate this feedstock as a more convenient precursor in terms of hydrochar production.

Table 5-1 Repeatability of carbonization processes of *Laminaria hyperborea*. SD is the standard deviation of the three measurements.

Carbonization				Water balance		
LH_S800 ²⁷		LH_S250 ²⁸				
Run	CY _{db} ²⁹	Run	CY _{db}	m _{initial}	m _{recovered}	m _{lost}
-	wt%	-	wt%	mg	mg	mg
1	24.63	1	34.05	220.00	166.58	53.42
2	28.16	2	35.26	220.00	162.88	57.12
3	27.93	3	32.84	220.00	163.79	56.21
Mean	26.91	Mean	34.05	-	164.42	55.58
SD	1.97	SD	1.21	-	1.57	1.57
SD (% Mean)	7.33	SD (% Mean)	3.56	-	0.96	2.83

Nonetheless, in contrast to results found for traditional pyrolysis, the average yield measured for hydrothermal carbonization of *Laminaria hyperborea* (ca. 34 wt%) was substantially lower than that obtained for the hydrothermally carbonized wood (ca. 58.5 wt%). This finding might signify that the catalytic effect of inorganic matter during hydrothermal treatment was not as important as that during pyrolysis. In fact, some inorganics might have been released into the HTC process water. On the other hand, wood-derived biomass normally features higher levels of lignin, which is believed to favour char production [134, 181, 200, 201].

A very low variability of the water balance was achieved when repeating HTC of *Laminaria hyperborea*, with standard deviation below 1%. The average amount of process water recovered after hydrothermal carbonization of

²⁷ *Laminaria hyperborea* summer (LH_S) pyrolyzed at 800 °C

²⁸ LH_S hydrothermally carbonized at 250 °C

²⁹ Carbon yield (CY). Db stands for dry basis

Laminaria hyperborea (164.42 mg) was comparable to that found for oak wood-derived hydrochar (160.90 mg), which seems to suggest that the type of feedstock did not significantly affect the amount of water lost during the hydrothermal process.

5.3 Activation of macroalgae-based chars - Optimal conditions

5.3.1 CO₂ activation

The physical activation of carbonized *Laminaria* was conducted under the same conditions of CO₂ flowrate (0.6 l·min⁻¹) and heating rate (10 °C·min⁻¹) already used for oak wood (see Chapter 4). These were maintained constant for each run. Once again, the influence of activation temperature and holding time on the development of the textural parameters of the activation products was studied. Initially, a first attempt value of dwell time was used, whereas the activation temperature was varied. Following this, the optimal activation temperature was maintained unaltered while the holding time was varied.

In order to avoid repetition, the textural properties related to the chars are only reported in Table 5-10.

5.3.1.1 The effect of the temperature

5.3.1.1.1 Hydrothermally carbonized *Laminaria hyperborea* (LH_S250)

Laminaria hyperborea-derived hydrochar was activated at 550, 600 and 650 °C. At this stage, the activation temperature was held for 30 min.

As suggested by Figure 5-1, OW250 experienced a dramatic improvement of texture after activation at 550 °C. Indeed, hydrochar's surface area increased from 6 to 248 m²·g⁻¹. Interestingly, a slightly milder condition (500 °C for 30 min) applied for physical activation of hydrothermally carbonized wood in Chapter 4 led to limited textural enhancement. These results appear to indicate 550 °C as the onset temperature for an efficient reaction between carbon dioxide and HTC-derived chars.

A further increase of porosity was obtained when increasing temperature from 550 to 600 °C. In particular, the isotherm measured for LH_S250PA_600_0.5h (see Figure 5-1) displayed an increase of micropore filling at low pressure, which was consistent with the increase in microporous volume reported in Table 5-2. In contrast, a slight decrease in total pore volume occurred. This suggested that the higher temperature condition might have caused the collapse of meso and macropore walls, which is in line with the less steep upswing measured at saturation for LH_S250PA_600_0.5h. Nonetheless,

the isotherms shape (type II [242]) was not noticeably affected by the temperature of the treatment.

Conversely, a reduction of porosity occurred when the temperature was further increased from 600 to 650 °C. In particular, the detriment of porosity mostly affected micropores, whose volume was reduced by ca. 50%. The isotherm measured for LH_S250PA_650_0.5h did not change in shape but appeared to be shifted down.

Table 5-2 Effect of CO₂ activation temperature on burn off and textural parameters of hydrothermally carbonized *Laminaria hyperborea*

Sample ID ³⁶	T	t	BO ³⁰	S _{BET} ³¹	V _{tot} ³²	V _{mi} ³³	V _{me} ³⁴	V _{ma} ³⁵
	°C	h	wt%	m ² ·g ⁻¹	cm ³ ·g ⁻¹			
LH_S250PA_550_0.5h	550	0.5	44	248	0.331	0.103	0.069	0.158
LH_S250PA_600_0.5h	600	0.5	48	301	0.288	0.121	0.057	0.109
LH_S250PA_650_0.5h	650	0.5	51	160	0.228	0.062	0.053	0.112

³⁰ Burn-off

³¹ Surface area calculated by applying BET method to N₂ adsorption data

³² Total pore volume calculated by applying Gurvitsch's rule at P/P₀=0.99

³³ Micropore volume calculated by applying DR model to N₂ adsorption data

³⁴ Mesopore volume calculated by applying Barrett-Joyner-Halenda (BJH) model to N₂ adsorption data

³⁵ Macropore volume calculated by difference

³⁶ PA stands for physically activated

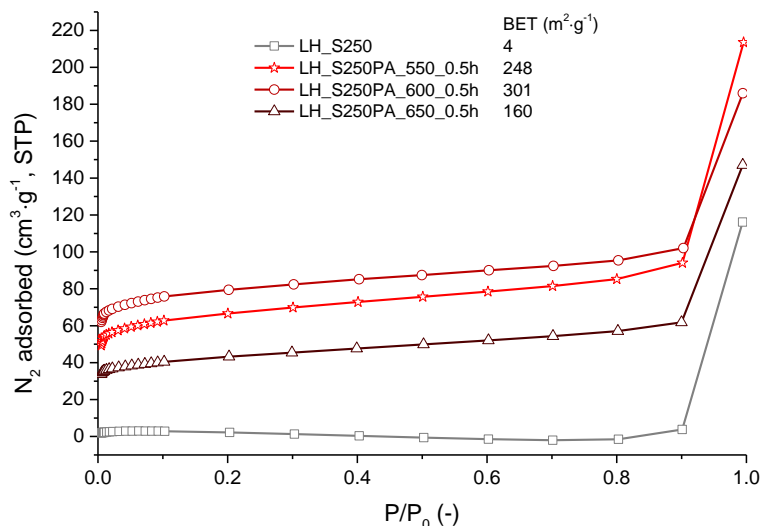


Figure 5-1 N₂ adsorption isotherms - Effect of temperature on CO₂ activation of hydrothermally carbonized *Laminaria hyperborea*

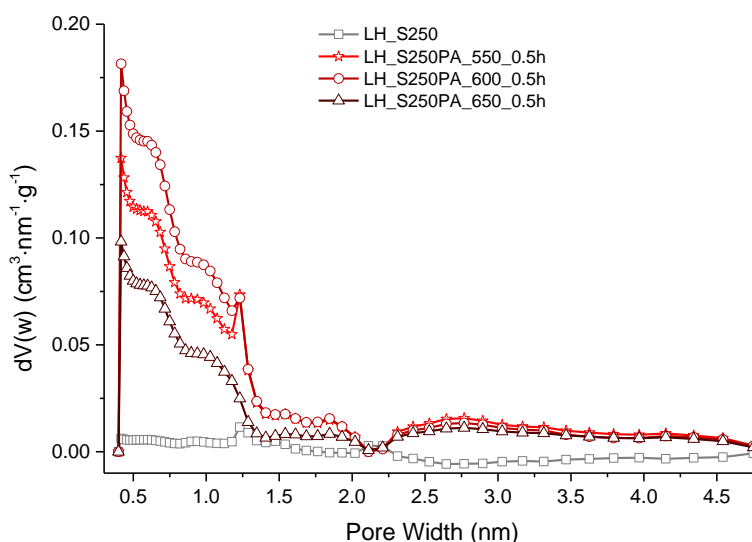


Figure 5-2 Non-local density functional theory (NLDFT) pore size distributions by volume - Effect of temperature on CO₂ activation of hydrothermally carbonized *Laminaria hyperborea*

As illustrated in Figure 5-2, regardless of the temperature, the activation treatment led to a significant development of ultramicroporosity. Particularly, the peak centred at ca. 0.3 nm hit a maximum at 600 °C, which is in agreement with the highest value of micropore volume exhibited by LH_S250PA_600_0.5h. Interestingly, ACs obtained at 550 and 600 °C exhibited a second peak centred at around 1.2 nm, thus indicating the presence of supermicropores. When increasing temperature from 600 to 650 °C, the supermicropores population mostly disappeared, while ultramicroporosity was significantly reduced. This seems to indicate damage of the microporous structure previously created between 550 and 600 °C. The optimum temperature for CO₂ activation of

hydrothermally carbonized *Laminaria hyperborea* was therefore deemed to be 600°C.

5.3.1.1.2 Pyrolyzed *Laminaria hyperborea* (LH_S800)

As depicted by Figure 5-3, irrespective of the activation temperature, pyrolyzed *Laminaria hyperborea* exhibited a limited improvement of texture after heat-treatment under CO₂.

Unlike the hydrothermal treatment, pyrolysis generally implies the creation of a more stable char as the raw material undergoes a more intense devolatilization. Therefore, it was decided to apply a more severe heat-treatment for the activation of LH_S800. However, LH_S800 exhibited much higher burn out (50 wt% at 750 °C for 0.5 h) than that showed by the oak wood analogue (32 wt%, see Chapter 4) under similar conditions (750 °C for 1 h). The high material loss caused the destruction of the micropore walls. Indeed, as given in Table 5-3, the micropore volume was found to decrease by ca. 87% when increasing temperature from 700 to 750 °C. 700 °C was found to be the optimal activation temperature, with surface area increasing up to 189 m²·g⁻¹. However, it is worth noticing that LH_S800PA_650_0.5h featured a higher proportional microporosity³⁷ (ca. 73%) than that of LH_S800PA_700_0.5h (ca. 55%). This agreed with the different shapes of the isotherms measured for these samples. In particular, the isotherm knee widened when increasing temperature from 650 to 700 °C. Moreover, the isotherm measured for the sample activated at 700 °C showed a noticeable slope with increasing pressure, suggesting the formation of mesoporosity. According to the IUPAC classification [242], this is typical of type II isotherms and agreed with the increased volume of mesopores reported in Table 5-3 for this material. By contrast, LH_S800PA_650_0.5h exhibited a near type I isotherm, with a narrower knee followed by a flat trend over the mid pressure range, which indicated negligible mesoporosity.

As observed in Figure 5-4, the larger micropore percentage of LH_S800PA_650_0.5h was confirmed by the narrower pore size distribution (PSD) shown for this sample in comparison to LH_S800PA_700_0.5h and LH_S800PA_750_0.5h. In addition, LH_S800PA_650_0.5h attained the highest abundance of the peak centred in ultramicropores. In contrast, when increasing temperature from 650 to 700 °C, populations of supermicropores were formed, with pore diameter ranging from 1 to 2 nm. Furthermore, broad peaks at pore widths larger than 2 nm corroborated the presence of mesopores within LH_S800PA_700_0.5h. Peaks observed over the microporous width range

³⁷ Calculated as $(V_{mi}/V_{tot}) \cdot 100$.

disappeared for LH_S800PA_750_0.5h, thus reiterating the significant reduction of microporosity that occurred when increasing temperature from 700 to 750 °C.

Table 5-3 Effect of CO₂ activation temperature on burn off and textural parameters of pyrolyzed *Laminaria hyperborea*

Sample ID	T °C	t h	BO wt%	S _{BET} m ² ·g ⁻¹	V _{tot} cm ³ ·g ⁻¹	V _{mi} cm ³ ·g ⁻¹	V _{me} cm ³ ·g ⁻¹	V _{ma} cm ³ ·g ⁻¹
LH_S800PA_650_0.5h	650	0.5	7	140	0.078	0.057	0.009	0.013
LH_S800PA_700_0.5h	700	0.5	13	189	0.126	0.069	0.030	0.028
LH_S800PA_750_0.5h	750	0.5	50	83	0.066	0.009	0.034	0.023

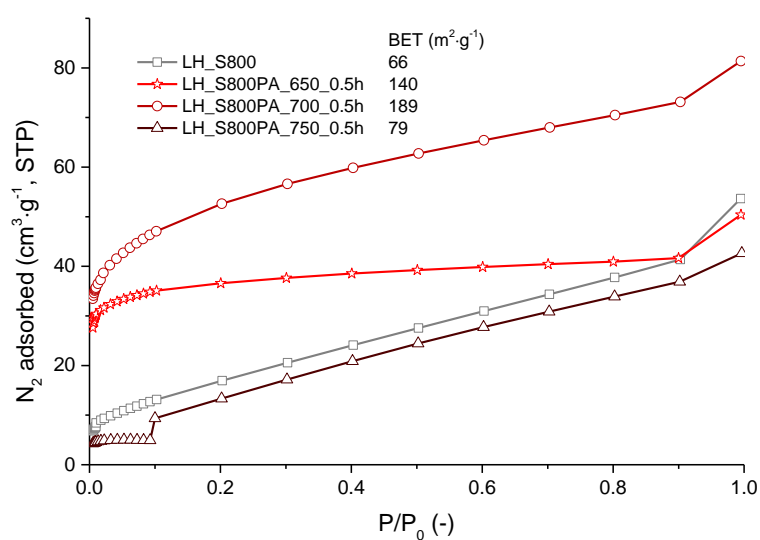


Figure 5-3 N₂ adsorption isotherms - Effect of temperature on CO₂ activation of pyrolyzed *Laminaria hyperborea*

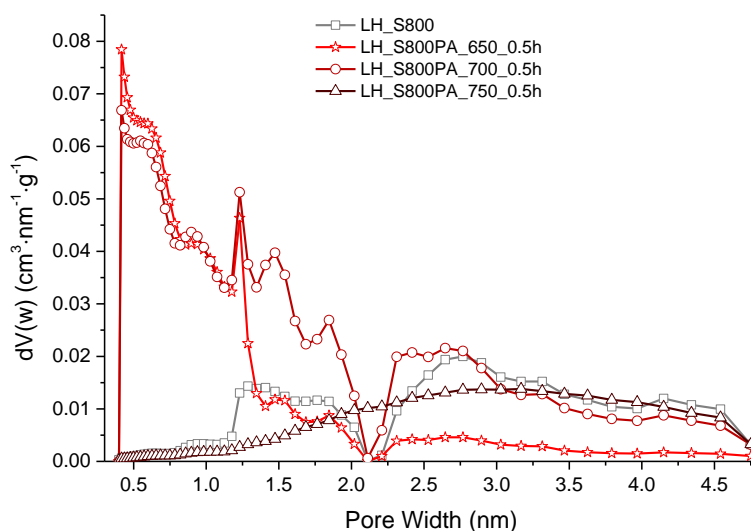


Figure 5-4 NLDFT Pore size distributions by volume - Effect of temperature on CO₂ activation of pyrolyzed *Laminaria hyperborea*

5.3.1.2 The effect of the dwell time

5.3.1.2.1 Hydrothermally carbonized *Laminaria hyperborea* (LH_S250)

The optimal activation temperature of 600°C, determined in section 5.3.1.1.1 for a dwell time of 30 min, was also held for no residence time (i.e. 0 h) or 1 h. In particular, when the char was not held at temperature, the efficiency of CO₂ oxidation was lower, probably due to a slow reaction rate. In contrast, a longer holding time of 1h led to a detriment of the porosity created at 600 °C for 0.5 h.

Table 5-4 Effect of CO₂ activation dwell time on burn off and textural parameters of hydrothermally carbonized *Laminaria hyperborea*

	T	t	BO	S _{BET}	V _{tot}	V _{mi}	V _{me}	V _{ma}
Sample ID	°C	h	wt%	m ² ·g ⁻¹	cm ³ ·g ⁻¹			
LH_S250PA_600_0h	600	0	46	118	0.210	0.046	0.063	0.101
LH_S250PA_600_0.5h	600	0.5	48	301	0.288	0.121	0.057	0.109
LH_S250PA_600_1h	600	1	49	180	0.224	0.076	0.044	0.104

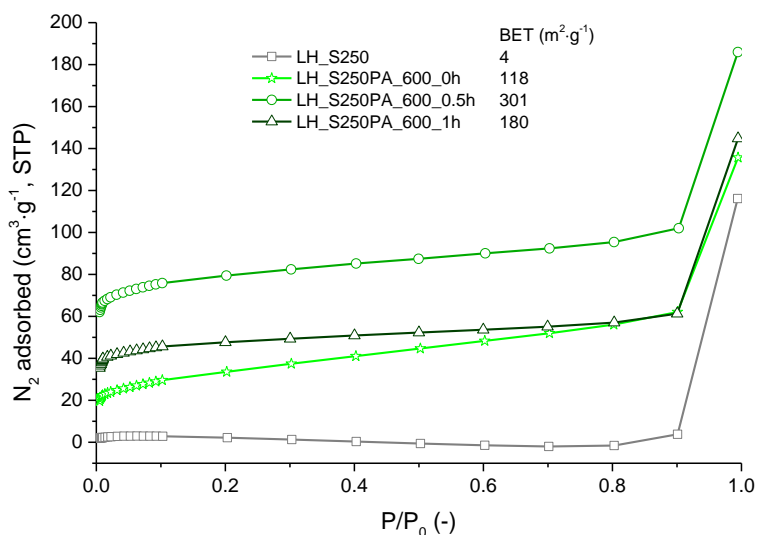


Figure 5-5 N₂ adsorption isotherms - Effect of dwell time on CO₂ activation of hydrothermally carbonized *Laminaria hyperborea*

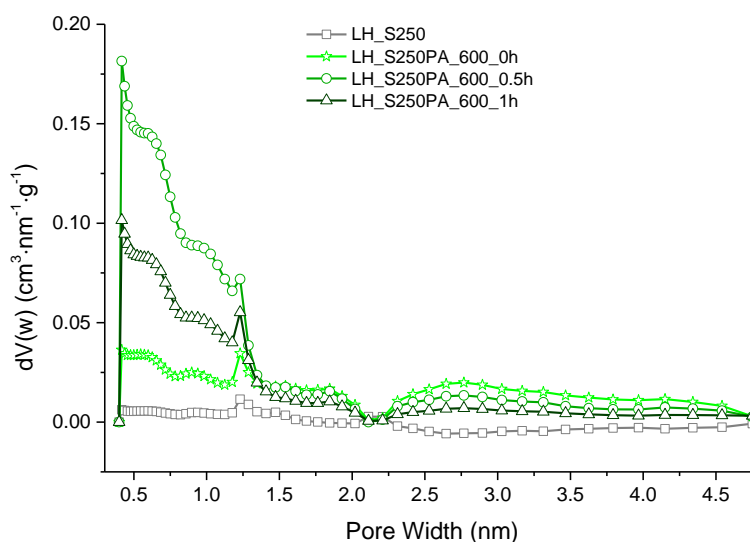


Figure 5-6 NLDFT Pore size distributions by volume - Effect of dwell time on CO₂ activation of hydrothermally carbonized *Laminaria hyperborea*

Therefore, 600 °C for 0.5 h was found to be optimal for the CO₂ activation of *Laminaria*-derived hydrochar. Identical optimal conditions were found for the wood-based hydrochar (see Chapter 4), corresponding to a carbon burn out (46 wt%), nearly as large as that experienced by LH_S250PA_600_0.5h (48 wt%, see Table 5-4). However, the hydrothermally carbonized wood attained a noticeably higher surface area (415 m²·g⁻¹) than that of macroalgae-derived hydrochar.

The dwell time seemed not to affect the shape of the pore distributions of the materials. Indeed, regardless of the residence time, samples exhibited a

bimodal pore size distribution with peaks at ca. 0.5 and ca. 1.2 nm respectively. NLDFT modes reflected the isotherms' results.

5.3.1.2.2 Pyrolyzed *Laminaria hyperborea* (LH_S800)

The effect of the dwell time on the textural properties of LH_S800 was evaluated by considering the same time steps used for hydrothermally carbonized *Laminaria hyperborea*. This entailed holding the optimal temperature (i.e. 700 °C, see section 4.3.1.1.2) for 0 or 1 h. Compared to the pyrolyzed oak wood (see Chapter 4), a lower time span was chosen in an attempt to gradually refine the material burn out.

Nevertheless, the variation of the residence time did not lead to any improvement of the texture. Indeed, a dwell time of 30 min was found to be optimal for the CO₂ activation of *Laminaria*-derived pyrolysis char because resulted in the highest surface area. In particular, as seen by Table 5-5, when no dwell time was applied the porosity development of the final carbon was very similar to that experienced by the sample held at the same temperature for 30 min. This was in accordance with the comparable burn-offs measured for these samples. On the other hand, increasing activation duration from 0 to 30 min led to a further development of meso and macropores, while no additional microporosity was formed. In fact, although micropore filling at the very low pressure was not affected by the increase of the dwell time, the isotherm measured for LH_S800PA_700_0.5h exhibited a more open knee, leading to a higher adsorption of nitrogen with increasing pressure. This was consistent with the slightly larger meso and macropore volumes found for this sample (see Table 5-5). In contrast, when the activation was further prolonged up to 1 h, a significant increase of burn off was measured (from 13 to 38 wt%), which appeared to damage the micropore walls (micropore volume decreased by 45%).

Table 5-5 Effect of CO₂ activation dwell time on burn off and textural parameters of pyrolyzed *Laminaria hyperborea*

Sample ID	T °C	t h	BO wt%	S _{BET} m ² ·g ⁻¹	V _{tot} cm ³ ·g ⁻¹	V _{mi} cm ³ ·g ⁻¹	V _{me} cm ³ ·g ⁻¹	V _{ma} cm ³ ·g ⁻¹
LH_S800PA_700_0h	700	0	6	171	0.110	0.068	0.026	0.016
LH_S800PA_700_0.5h	700	0.5	13	189	0.126	0.069	0.030	0.028
LH_S800PA_700_1h	700	1	38	93	0.069	0.032	0.020	0.016

Interestingly, as seen in Figure 5-8, it seemed that ultramicroporosity decreased when increasing dwell time from 0 to 30 min, while new

supermicropore populations appeared for LH_S800PA_700_0.5h. Apparently, when prolonging the activation process some of the ultramicropores were widened to form supermicropores. Conversely, both ultramicroporosity and supermicroporosity decreased when the activation dwell time was increased from 30 to 60 min.

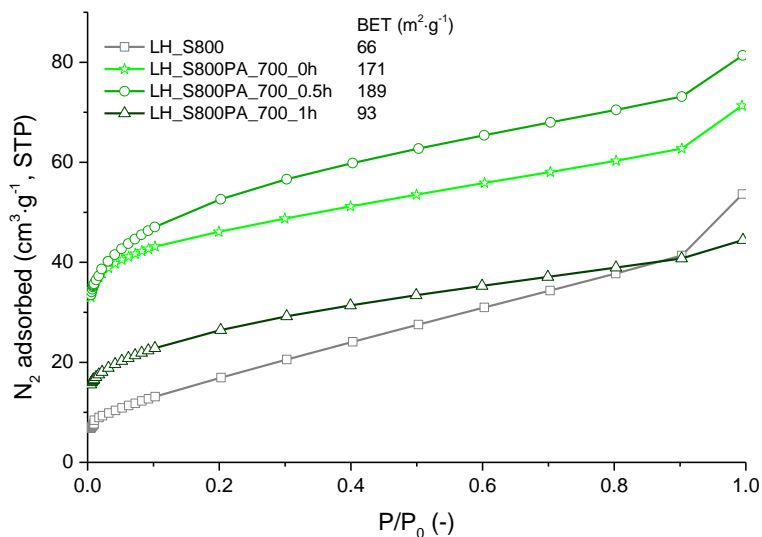


Figure 5-7 N₂ adsorption isotherms - Effect of dwell time on CO₂ activation of pyrolyzed *Laminaria hyperborea*

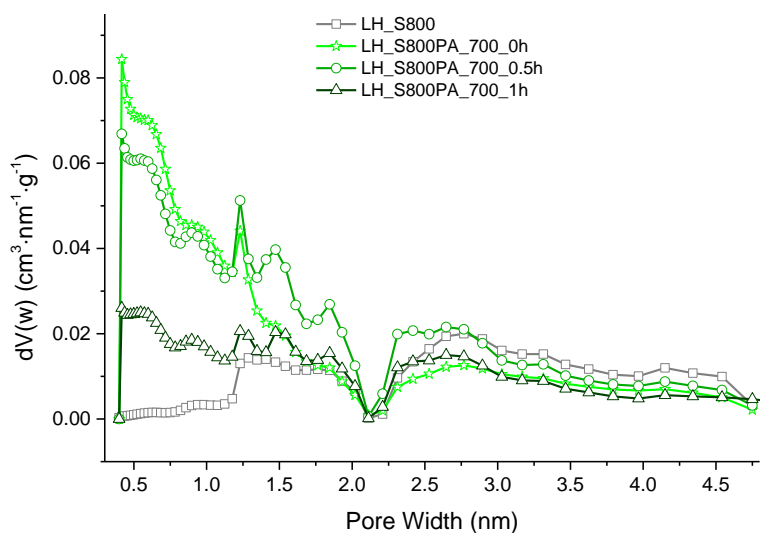


Figure 5-8 NLDFIT Pore size distributions by volume - Effect of dwell time on CO₂ activation of pyrolyzed *Laminaria hyperborea*

5.3.2 KOH activation

For all chemical activation runs the heat-treatment step was conducted under identical conditions of N₂ flowrate (100 ml·min⁻¹), heating rate (5 °C·min⁻¹) and dwell time (1 h). However, different values of activation temperature and

chemical ratio were examined. Initially, KOH:char ratio was maintained at 4:1, while activation temperature was varied (i.e. 550, 650 or 750 °C). Afterwards, the optimal activation temperature was kept unaltered, while chemical ratios other than the initial one (1:1 or 2:1) were applied.

5.3.2.1 The effect of the temperature

5.3.2.1.1 Hydrothermally carbonized *Laminaria hyperborea* (LH_S250)

As seen in Figure 5-9, all KOH activation runs caused a dramatic enhancement of the texture of the hydrochar. However, as given in Table 5-6, the activated chars obtained after heat-treatment at 550 °C presented a much larger proportional microporosity (ca. 80%) than those of products obtained at 650 (71%) or 750 °C (60%). The high micropore percentage of LH_S250CA_550_4:1 agreed with the near type I isotherm measured for this sample. This could be ascribed to the slow rate of the carbonation reaction at 550 °C, which prevented micropores from widening.

A significant increase of porosity occurred when increasing activation temperature from 550 to 650 °C. This was consistent with findings shown by Illingworth [168], who KOH-activated some pyrolyzed flax fibre. That author reported a major porosity development occurring between 450 (onset of activation) and 650 °C. Formation of pores was predominantly attributed to the removal of volatile/disorganized material from the char. However, when temperature was raised from 550 to 650 °C, a transition from type I isotherm to type I-II was observed. In particular, the isotherm knee appeared to be distinctly shifted upward but also widened. Micropore volume and surface area experienced a near 3-fold increase. A moderate further increase of porosity was measured when increasing temperature up to 750 °C. However, mostly meso and especially macropores were formed at this stage, while the micropore volume did not substantially change. Once again, this result was found to be in agreement with observations reported by Illingworth [168]. In particular, that author related pore widening to the increased speed of the gasification reactions between fixed carbon (i.e. micropore walls) and steam/CO₂ produced during the activation process at a temperature higher than 700 °C. The enlargement of the average pore width with increasing activation temperature was also reported by Sevilla *et al.* [106], who KOH-activated an HTC-derived product consisting of a mixture of microalgae (*Spirulina platensis*) and glucose.

Table 5-6 Effect of activation temperature on activation yield and textural parameters of hydrothermally carbonized *Laminaria hyperborea*

Sample ID ⁴⁰	T °C	CR ³⁸ -	AY _{db} ³⁹ wt%	S _{BET} m ² ·g ⁻¹	V _{tot} cm ³ ·g ⁻¹	V _{mi} cm ³ ·g ⁻¹	V _{me} cm ³ ·g ⁻¹	V _{ma} cm ³ ·g ⁻¹
LH_S250CA_550_4:1	550	4:1	19	980	0.481	0.382	0.022	0.077
LH_S250CA_650_4:1	650	4:1	8	2659	1.344	0.959	0.100	0.285
LH_S250CA_750_4:1	750	4:1	3	2771	1.558	0.942	0.169	0.447

³⁸ Chemical ratio (KOH:char)

³⁹ Activation yield (AY). Db stands for dry basis

⁴⁰ CA stands for chemically activated

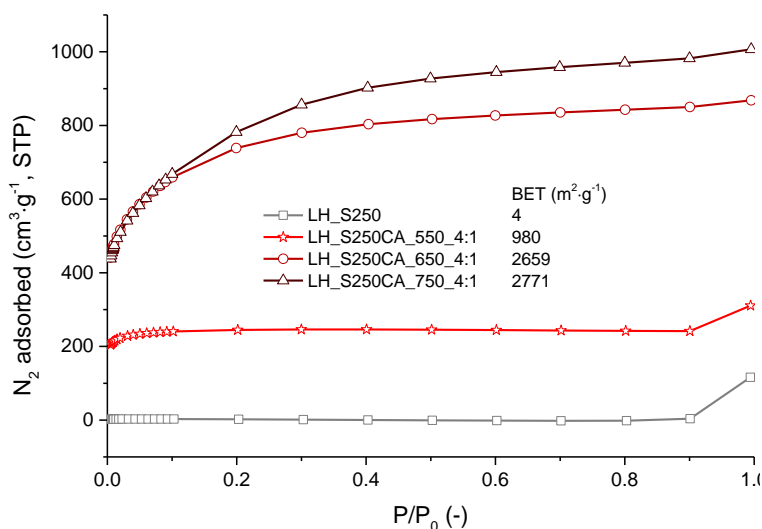


Figure 5-9 N₂ adsorption isotherms - Effect of temperature on chemical activation of hydrothermally carbonized *Laminaria hyperborea*

Apparently, KOH carbonation was very fast at 750°C, such that the speed of micropore widening was higher than that of micropore formation. As illustrated by Figure 5-9, isotherms measured for LH_S250CA_650_4:1 and LH_S250CA_750_4:1 seem to follow the same path up to P/P_0 ca. 0.1. Yet, with increasing pressure, sample activated at 750 °C adsorbed larger amount of nitrogen onto the additional meso and macropores formed within its structure. As given in Table 5-6, the pore widening was accompanied by a decline in the activation yield, thus suggesting that the formation of larger pores was caused by the removal of material from the char.

As suggested by data reported in Table 5-6, porosity progressively increased with decreasing product yield. However, in terms of surface area maximization, an activation temperature of 750 °C was optimal for the KOH activation of hydrothermally carbonized *Laminaria*.

As depicted by Figure 5-10, the narrower pore size distribution exhibited by LH_S250CA_550_4:1 corroborated the higher microporosity exhibited by this sample. In particular, the NLDFT mode appeared at ca. 0.3 nm, but this peak's shoulder, extending up to 2 nm indicated a pore population featuring both ultra and supermicropores. Conversely, with increasing temperature supermicropores were developed at the expense of ultramicropores by the latter's widening. In addition, a multimodal distribution was observed for carbons obtained at 650 and 750 °C, thus indicating the formation of different groups of pores with diameter ranging from 1.2 to 2 nm. Furthermore, the development of a mesopore population was observed, which was consistent with the isotherms' shape discussed earlier.

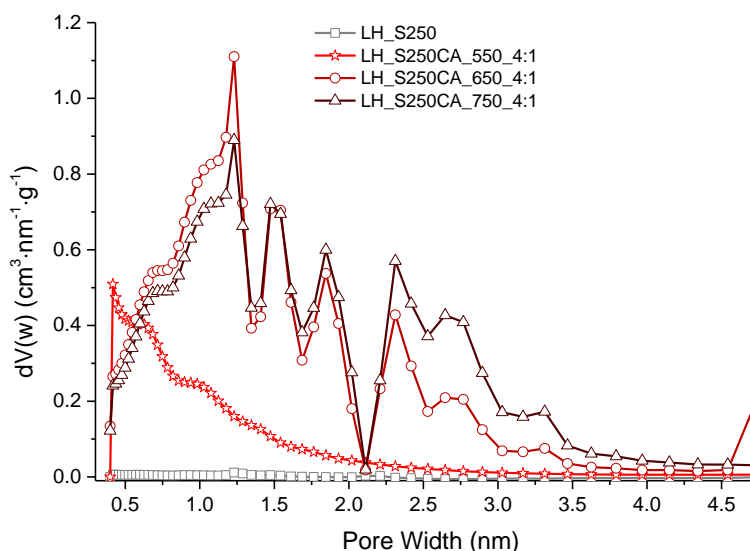


Figure 5-10 NLDFT Pore size distributions by volume - Effect of temperature on chemical activation of hydrothermally carbonized *Laminaria hyperborea*

5.3.2.1.2 Pyrolyzed *Laminaria hyperborea* (LH_S800)

The pyrolyzed macroalgae exhibited a more gradual increase of porosity with increasing temperature compared to LH_S250. Once again, at the lowest temperature (i.e. 550 °C), the porous structure of the carbon was mostly composed of micropores, as highlighted by the near type I isotherm observed for LH_S800CA_550_4:1 in Figure 1-11. It is worth noting that, under the same conditions of temperature and chemical ratio, the KOH activation of pyrolyzed *Laminaria hyperborea* led to a far larger activation yield (ca. 53 wt%) than that obtained after chemical treatment of the corresponding hydrochar (19 wt%). This was likely due to the higher degree of devolatilization experienced by the hydrothermally carbonized *Laminaria hyperborea* during the activation process. The isotherm's knee progressively increased and widened with increasing temperature, leading to a maximum surface area of 2266 m²·g⁻¹ and a total pore volume of 1.384 cm³·g⁻¹. Thus, of the temperatures studied, 750°C was deemed to be to optimum activation temperature.

PSD by volume shown in Figure 5-12 reflected results already discussed for the chemical activation of the hydrochar in section 5.3.2.1.1. In particular, PSD comparisons revealed the pore widening of the samples activated at higher temperature (>550 °C) for the same KOH:char ratio (4:1). This can be seen from the broadening of the distributions observed for LH_S800CA_650_4:1 and LH_S800CA_750_4:1. Essentially, narrow ultramicropores formed at 550 °C were enlarged to form supermicropores when applying more severe temperature conditions (650 and 750 °C). A similar correlation between porosity and temperature has already been reported in

other studies [150, 175, 297]. These reported a predominant formation of narrow micropores between 400 and 700 °C, whereas ultramicroporosity began to decline in favour of larger micropores and mesopores for temperatures higher than 600 °C. Pore enlargement was also found by Ferrera-Lorenzo *et al.* [142] after increasing activation temperature from 750 to 900 °C (KOH:char ratio of 1). In particular, these authors chemically-activated a char derived from the pyrolysis of an algal meal at 750 °C. However, the same study showed an increase of ultramicroporosity with increasing temperature when KOH:char ratio was 0.5. This was probably due to the lower intensity of activation (see also section 5.3.2.2).

Table 5-7 Effect of activation temperature on activation yield and textural parameters of pyrolyzed *Laminaria hyperborea*

Sample ID	T °C	CR -	AY _{db} wt%	S _{BET} m ² ·g ⁻¹	V _{tot} cm ³ ·g ⁻¹	V _{mi} cm ³ ·g ⁻¹	V _{me} cm ³ ·g ⁻¹	V _{ma} cm ³ ·g ⁻¹
LH_S800CA_550_4:1	550	4:1	53	768	0.406	0.260	0.037	0.109
LH_S800CA_650_4:1	650	4:1	19	1454	0.805	0.545	0.104	0.157
LH_S800CA_750_4:1	750	4:1	13	2266	1.384	0.822	0.197	0.365

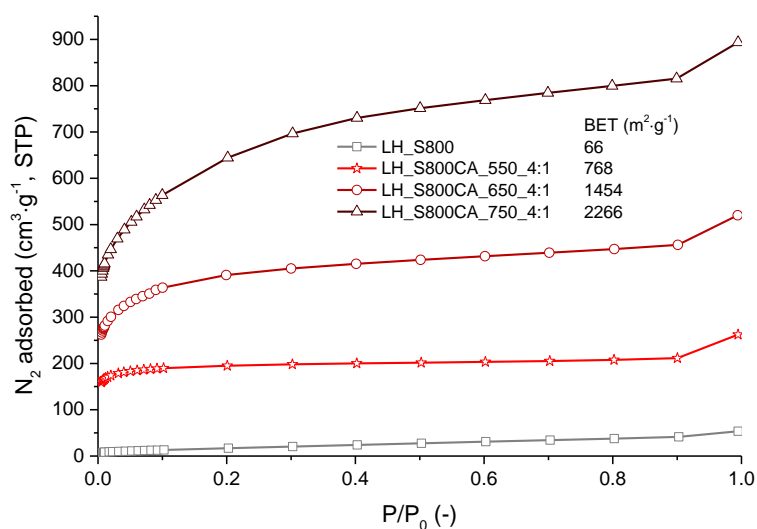


Figure 5-11 N₂ adsorption isotherms - Effect of temperature on chemical activation of pyrolyzed *Laminaria hyperborea*

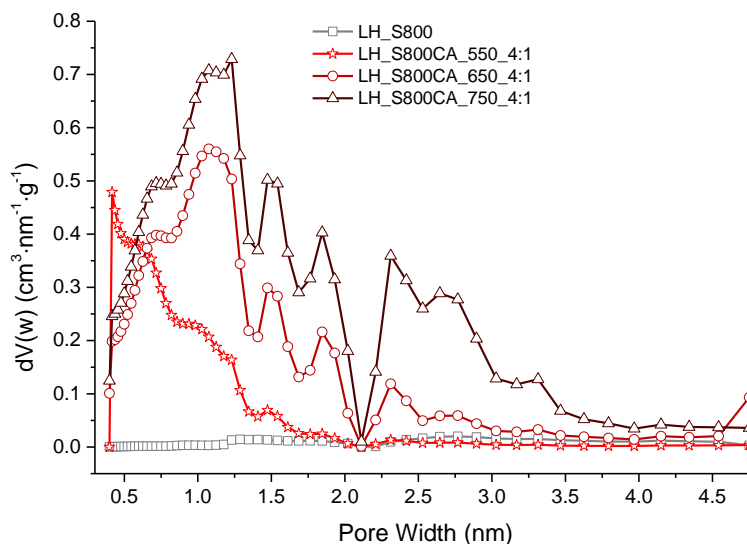


Figure 5-12 NLDFT Pore size distributions by volume - Effect of temperature on chemical activation of pyrolyzed *Laminaria hyperborea*

It is worth mentioning that pore abundances observed in the pore size distributions of the carbons derived from pyrolyzed *Laminaria hyperborea* were lower than those measured for the chemically activated hydrochar. This agreed with the higher surface areas obtained after KOH activation of LH_S250. The lower texture development experienced by pyrolyzed *Laminaria hyperborea* was likely due to the higher amount of ash found in LH_S800 (see Table 5-11). These might have hindered the interaction between KOH and the carbon skeleton of the char.

5.3.2.2 The effect of the KOH/char ratio

5.3.2.2.1 Hydrothermally carbonized *Laminaria hyperborea* (LH_S250)

As depicted by Figure 5-13, changing the chemical ratio had a less dramatic influence on the textural parameters of the hydrochar-derived carbons compared to that caused by varying the activation temperature (see section 5.3.2.1.1). In particular, as reported in Table 5-8, comparable product yields and textural properties were found for carbons obtained using KOH:char ratios of 1:1 and 2:1. By contrast, when the chemical ratio was increased from 2 to 4, the isotherm knee became lower and broader. Indeed, as seen in Figure 5-13, the isotherm measured for LH_S250CA_750_4:1 appeared to cross over the isotherms exhibited by LH_S250CA_750_1:1 and LH_S250CA_750_2:1 at P/P_0 ca. 0.1. The lower contribution of microporosity reflected the decrease of micropore volume found when the chemical ratio was 4, whereas total (i.e. mesoporous and macroporous) volume increased (see Table 5-8). From these observations, it was inferred that, with increasing severity of activation (i.e. amount of KOH used), the carbonation reaction rate between KOH and the

carbon structure was faster. Accordingly, during the activation process most of smaller pores were widened immediately after being formed, giving rise to meso and macroporosity. Similar results were reported in previous works concerning KOH activation of biomass-derived chars [78, 178]. Nonetheless, a chemical ratio of 4 was optimal for the KOH activation of LH_S250 as LH_S250CA_750_4:1 had the highest surface area.

Table 5-8 Effect of KOH:char ratio on activation yield and textural parameters of hydrothermally carbonized *Laminaria hyperborea*

Sample ID	T	CR	AY _{db}	S _{BET}	V _{tot}	V _{mi}	V _{me}	V _{ma}
	°C	-	wt%	m ² ·g ⁻¹	cm ³ ·g ⁻¹			
LH_S250CA_750_1:1	750	1:1	15	2702	1.374	0.974	0.093	0.307
LH_S250CA_750_2:1	750	2:1	16	2651	1.224	0.999	0.059	0.165
LH_S250CA_750_4:1	750	4:1	3	2771	1.558	0.942	0.169	0.447

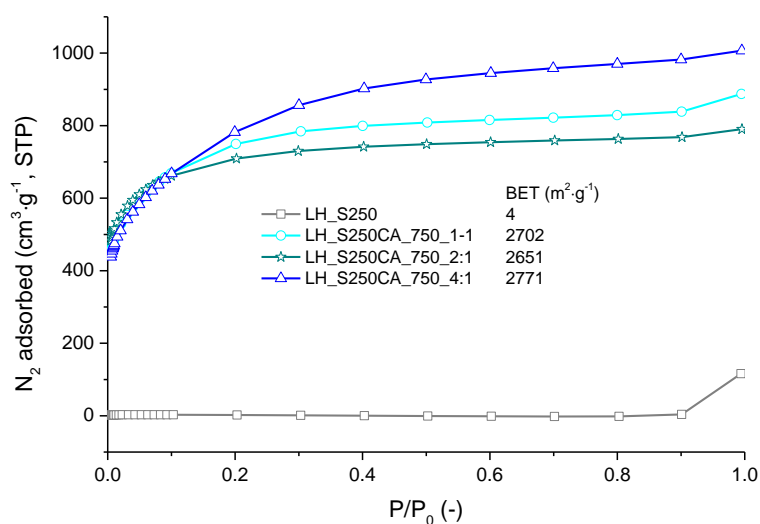


Figure 5-13 N₂ adsorption isotherms - Effect of KOH:char ratio on chemical activation of hydrothermally carbonized *Laminaria hyperborea*

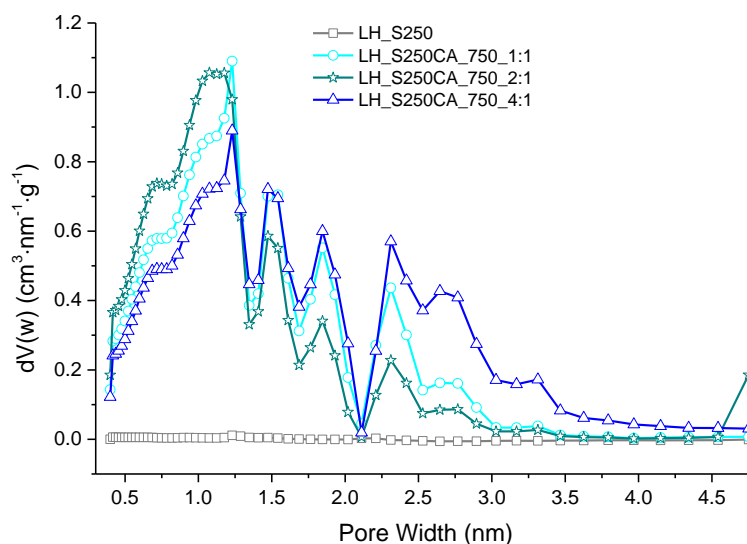


Figure 5-14 NLDFT Pore size distributions by volume - Effect of KOH:char ratio on chemical activation of hydrothermally carbonized *Laminaria hyperborea*

According to results in Figure 5-14, the KOH:char ratio did not significantly affect the micropore width distribution of the activated carbons. All chemically-activated samples presented a very broad PSD, thus signifying the presence of a heterogeneous porosity. However, it is worth mentioning that for all samples no distinct contribution in the ultramicroporous domain ($d < 0.7$ nm) was observed. This was probably due to the high intensity of activation. Moreover, when using the highest chemical ratio (KOH:char=4), smaller supermicropores (between 0.7 and 1.2 nm) were enlarged to form larger supermicroporosity (between 1.2 and 2 nm) and mesoporosity ($d > 2$ nm).

5.3.2.2.2 Pyrolyzed *Laminaria hyperborea* (LH_S800)

Compared to results shown for LH_S250 in Figure 5-13, variation of the KOH:char ratio had more distinct effects on the texture of the carbons derived from pyrolyzed *Laminaria hyperborea* (see Figure 5-15). In fact, a clear increase of LH_S800's porosity was observed with increasing KOH:char ratio. A gradual broadening of the isotherms' knee was observed, which reflected a progressive increase of total pore volume and surface area. Based on this, a KOH:char ratio of 4 was deemed to be optimal for the chemical activation of *Laminaria*-derived pyrolysis char. Nonetheless, when increasing the amount of KOH used, the contribution from larger pores increased. In particular, when the chemical ratio was increased from 1 to 2, the relative increase of meso (ca. 41%) and macropores (ca. 56%) was higher than that of micropores (ca. 20%). As discussed earlier, this suggested that microporosity enlargement prevailed over formation of micropores. Additionally, the increase of KOH:char from 2 to 4

caused a further slowing of micropores formation (now ca. 16%), while mesopore volume appeared to be constant. In addition to this, extra macropores were created at the expense of micro and mesopores.

The same effect was already observed when increasing activation temperature (see section 5.3.2.1). In this case, a higher abundance of KOH might have increased opportunities for reaction with the carbon matrix.

Table 5-9 Effect of KOH:char ratio on activation yield and textural parameters of pyrolyzed *Laminaria hyperborea*

Sample ID	T °C	CR -	AY _{db} wt%	S _{BET} m ² ·g ⁻¹	V _{tot} cm ³ ·g ⁻¹	V _{mi} cm ³ ·g ⁻¹	V _{me} cm ³ ·g ⁻¹	V _{ma} cm ³ ·g ⁻¹
LH_S800CA_750_1:1	750	1:1	34	1527	0.899	0.584	0.142	0.172
LH_S800CA_750_2:1	750	2:1	27	1871	1.172	0.703	0.201	0.268
LH_S800CA_750_4:1	750	4:1	13	2266	1.384	0.822	0.197	0.365

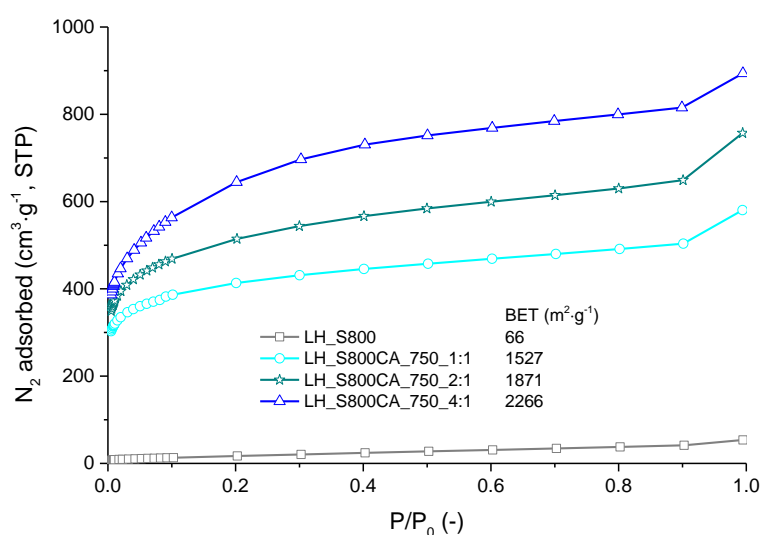


Figure 5-15 N₂ adsorption isotherms - Effect of KOH:char ratio on chemical activation of pyrolyzed *Laminaria hyperborea*

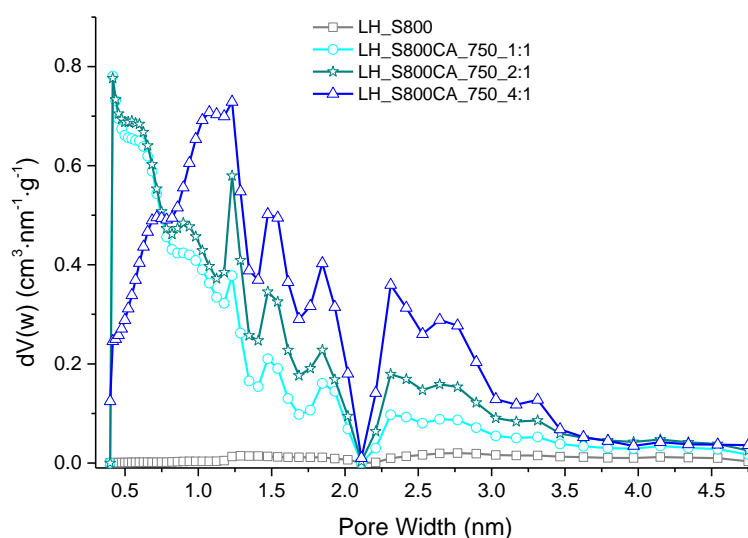


Figure 5-16 NLDFT Pore size distributions by volume - Effect of KOH:char ratio on chemical activation of pyrolyzed *Laminaria hyperborea*

Interestingly, as highlighted by Figure 5-16, ultramicroporosity was only observed for KOH:char=1:1 and 2:1. In contrast, when using a KOH:char ratio of 4:1, the PSD mode was shifted toward larger pore widths (i.e. from ca. 0.3 to 1.2 nm), thereby indicating widening of ultramicropores to form supermicroporosity. This confirmed that using higher KOH:char ratios caused a broadening of the PSD within the microporous domain, thus signifying a more heterogenous micropore size distribution. However, for pore diameters larger than 1.2 nm, PSD plots were found to have a similar shape for all carbons, wherein the abundance associated with each pore size increased with increasing KOH:char ratio.

5.4 Texture development of raw *Laminaria hyperborea*

5.4.1 N₂ adsorption isotherms

Figure 5-17 shows an absence of porous structure for raw *Laminaria hyperborea*. A negligible surface area (<1 m²·g⁻¹) has already been reported for raw macroalgae waste (algal meal) by Ferrera-Lorenzo *et al.* [142]. The same authors found a very low surface area (ca. 4 m²·g⁻¹) after pyrolysis of macroalgae at 750 °C, which was lower than that measured for *Laminaria hyperborea* after pyrolysis at 800 °C in this study (ca. 66 m²·g⁻¹). This could be attributed to the slightly higher temperature applied during the pyrolytic treatment performed in this work, which seemed to have caused the development of a rudimentary porous structure. It is worth mentioning that the pyrolysis of *Laminaria* led to a char having lower porosity than that found for the pyrolyzed oak wood (see Chapter 4). This was ascribed to the higher amount of

ash found by proximate analysis of the raw macroalgae (see Table 5-11) compared to that found for the pristine oak wood (see Chapter 4). A very low surface area was measured for the hydrothermally carbonized *Laminaria hyperborea*. On the other hand, this sample had a larger pore volume than that measured for its pyrolyzed analogue. Nonetheless, the hydrochar porosity was predominantly composed of macropores, thus explaining the limited surface area of LH_S250. The porosity of *Laminaria hyperborea* derived-hydrochar was found to be very similar to that of the hydrothermally carbonized oak wood, thereby confirming that HTC generally give rise to macroporous materials. On the other hand, slightly larger surface areas (up to ca. $32 \text{ m}^2 \cdot \text{g}^{-1}$) were reported after hydrothermal carbonization of other macroalgae (i.e. *Sargassum horneri*) [207].

A very limited texture enhancement was achieved after CO_2 activation of *Laminaria hyperborea* macroalgae-based chars. This was attributed to the high amount of mineral matter contained within seaweed (see Table 5-11). The mild oxidation under CO_2 does not allow for removal of ash. Therefore, the inorganic fractions remained within the carbon structure hindered the creation of new cavities. However, it is worth noting that the macroalgae-derived hydrochar experienced a larger increase of porosity than that observed for pyrolyzed *Laminaria hyperborea*, reaching surface areas up to $300 \text{ m}^2 \cdot \text{g}^{-1}$. As already elucidated when comparing oak wood-derived chars in Chapter 4, this could be reasonably attributed to the lower degree of carbonization involved by the HTC treatment. Consequently, a more intense devolatilization occurred when further heat-treating the hydrochar at higher temperature ($600 \text{ }^\circ\text{C}$) under CO_2 atmosphere (see Table 5-11). Overall, isotherms exhibited by physically-activated *Laminaria hyperborea* could be identified as type II [242].

In contrast, the corresponding chemically-activated carbons presented outstanding textural properties. Isotherms displayed by both of the KOH-activated chars could be defined as intermediate between types I and II [264]. As seen by the significant upswing that occurred at very low pressure, chemically-activated materials exhibited a more pronounced micropore filling. Nonetheless, the isotherms' knees were very broad and the nitrogen volume adsorbed increased with increasing pressure. This is typical of a hierarchical porous system combining micropores and mesopores [107]. In addition to that, as explained by Zhang *et al.* [107], inorganic fractions contained within macroalgae-based chars might have contributed to the porosity development. Indeed, during heat-treatment under N_2 , ash is believed to function as an in situ template for the creation of porous sites. After this, the removal of inorganic species by acid washing is necessary to reveal the voids within the carbon matrix.

The KOH activation of pyrolyzed *Laminaria hyperborea* led to a maximum surface area of $2266 \text{ m}^2 \cdot \text{g}^{-1}$ and total pore volume of ca. $1.384 \text{ cm}^3 \cdot \text{g}^{-1}$. These were found to be larger than the highest values ($1727 \text{ m}^2 \cdot \text{g}^{-1}$ and 0.774

cm³·g⁻¹ respectively) reported by Ferrera-Lorenzo *et al.* [142], who chemically-activated macroalgae waste after pyrolysis at 750 °C. These authors obtained the largest texture development at 900 °C using a KOH:char ratio of 1.

KOH-activated carbons derived from hydrothermally carbonized *Laminaria hyperborea* exhibited far larger surface area (2771 m²·g⁻¹) and pore volume (1.558 cm³·g⁻¹) than those reported by Zhang *et al.* [107] (418 m²·g⁻¹ and 0.37 cm³·g⁻¹ respectively) after chemical activation of *Enteromorpha prolifera*-based hydrochar. However, in the study of Zhang *et al.* [107], a wet impregnation was carried out prior to heat-treating KOH-impregnated hydrochar at 600 °C. Therefore, the limited texture enhancement might have been due either to a previous carbonation of KOH during the drying step or to the mild nature of the heat-treatment. In addition to that, the optimal conditions for maximizing the surface area of LH_S250 were very similar to those reported by Sevilla *et al.* (700 °C, KOH:char ratio of 4), who chemically-activated a microalgae-derived hydrochar. However, the chemically-activated carbon obtained in this work showed higher surface area compared to that reported in the study of Sevilla (2390 m²·g⁻¹). Therefore, in comparison with results reported in the literature for other types of macroalgae, *Laminaria hyperborea* seems to be a more promising precursor for preparing highly porous carbons.

Pore size distributions by volume plotted in Figure 5-18 emphasize the near absence of micro and mesoporosity within raw and carbonized *Laminaria hyperborea*. Furthermore, the PSDs clearly highlight a substantially different distribution of porosity exhibited by CO₂- and KOH-ACs. In particular, physically-activated carbons exhibited narrower distributions, showing populations only within the microporous size range. By contrast, very broad multimodal distributions were observed for KOH-activated carbons, indicating that these materials were characterized by a heterogeneous porous structure.

Table 5-10 Gas adsorption data for key *Laminaria hyperborea*-based samples and magnesium oxide. NM stands for not measured

Sample ID	N ₂ adsorption -196 °C					CO ₂ adsorption 0 °C ⁴¹				
	S _{BET}	V _{tot}	V _{mi}	V _{me}	V _{ma}	V _{ads, 0 °C, 1bar}	V _{umi, NLDFT}	NLDFT mode	V _{umi, DR}	E _{0, DR}
	m ² ·g ⁻¹	cm ³ ·g ⁻¹	cm ³ ·g ⁻¹	cm ³ ·g ⁻¹	cm ³ ·g ⁻¹	cm ³ ·g ⁻¹	cm ³ ·g ⁻¹	cm ³ ·nm ⁻¹ ·g ⁻¹	cm ³ ·g ⁻¹	kJ·mol ⁻¹
LH_S	0	0.015	0.000	0.006	0.009	0.0	0.000	0.000	0.000	-
LH_S250	4	0.180	0.006	0.048	0.126	0.0	0.000	0.000	0.000	-
LH_S800	66	0.083	0.021	0.039	0.024	0.4	0.000	0.002	0.001	44.14
LH_S250PA	301	0.288	0.121	0.057	0.109	11.8	0.030	0.269	0.084	-
LH_S800PA	189	0.126	0.069	0.030	0.028	5.6	0.015	0.014	0.044	27.01
LH_S250CA	2771	1.558	0.942	0.169	0.447	8.8	0.020	0.018	0.100	-
LH_S800CA	2266	1.384	0.822	0.197	0.365	6.6	0.015	0.013	0.500	22.08
MgO	72	0.129	0.037	0.071	0.021	NM	NM	NM	NM	NM

⁴¹ See Table 4-9 for parameters description

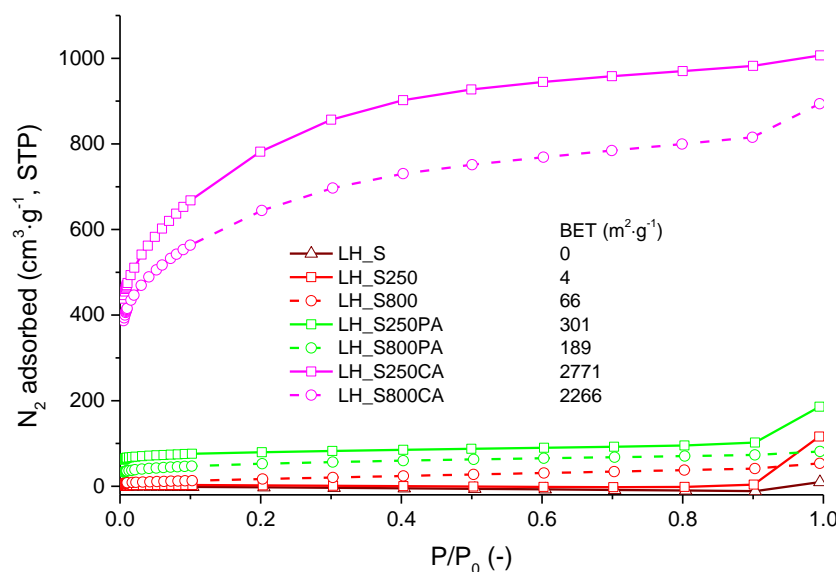


Figure 5-17 N₂ adsorption isotherms for key *Laminaria hyperborea*-based samples.

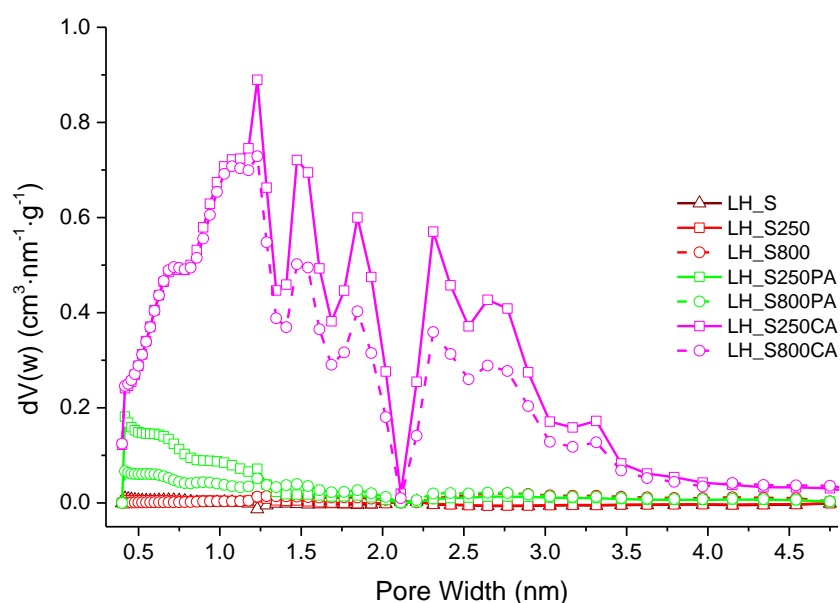


Figure 5-18 NLDFT pore size distribution for key *Laminaria hyperborea*-based samples.

5.4.2 CO₂ adsorption isotherms

As expected, no CO₂ was adsorbed at 0 °C onto raw and hydrothermally carbonized *Laminaria hyperborea*. This was in line with N₂ adsorption data reported in section 5.4.1. A very low amount of CO₂ was adsorbed at saturation by pyrolyzed *Laminaria hyperborea* (ca. 0.4 cm³·g⁻¹), thus confirming the lack of narrow microporosity within this sample. Nevertheless, it is interesting to notice the high energy of adsorption (ca. 44 kJ·mol⁻¹) calculated for LH_S800,

signifying a strong interaction between CO₂ and seaweed char. This value was far higher than that obtained for LH_S800's activated counterparts, thereby indicating a lower affinity between carbon dioxide and these adsorbents.

Figure 5-19 also shows that physically-activated hydrochar adsorbed a higher volume of CO₂ compared to KOH-activated carbons, thus indicating a larger proportion of ultramicropores. Results were consistent with those reported in Figure 5-20, wherein it was possible to observe that LH_S250PA attained the highest CO₂ NLDFT mode centred at ca. 0.35 nm. Nonetheless, these observations are in contrast with findings reported in Figure 5-18, where KOH-activated samples appear to exhibit a higher ultramicroporosity. However, this inconsistency might have been due to nitrogen diffusional limitations through the pore network of physically-activated carbons, thus leading to an underestimation of the PSD abundance in the ultramicroporous domain for these samples.

It is also worth noting that LH_S800PA seems to adsorb more CO₂ than the corresponding KOH-activated carbons at the very low pressure ($P/P_0 < 0.0175$). After this, the uptake per unit pressure exhibited by the physically activated sample was found to decline with increasing pressure. The different isotherm shape shown by LH_S800PA in comparison to KOH-activated carbons might be attributed to increased affinity between the adsorptive and the material at very low partial pressure of CO₂ ($P < 0.34$ bar).

In line with results presented in Chapter 4, the correlation between CO₂ uptakes measured at 0 °C and 1 bar and ultramicropore volumes was higher when applying the NLDFT model for calculation of narrow microporosity ($R^2 = 0.9901$, see Figure 5-21) compared to that obtained when applying the Dubinin-Radushkevich (DR) method. In contrast, the application of the DR model gave rise to an overestimation of ultramicroporosity (up to 0.5 cm³·g⁻¹ for LH_S800CA, see Table 5-10) and a lower coefficient of determination ($R^2 = 0.8426$, see Figure 5-22). Nevertheless, an increase of correlation was observed compared to that found for oak wood-derived samples. However, based on the more reliable predictions given by the NLDFT model, the maximum ultramicropore volume attained by macroalgae-derived carbons (0.03 cm³·g⁻¹, see Table 5-10) was well smaller than the highest figure reported in the literature (0.52 cm³·g⁻¹ [93]).

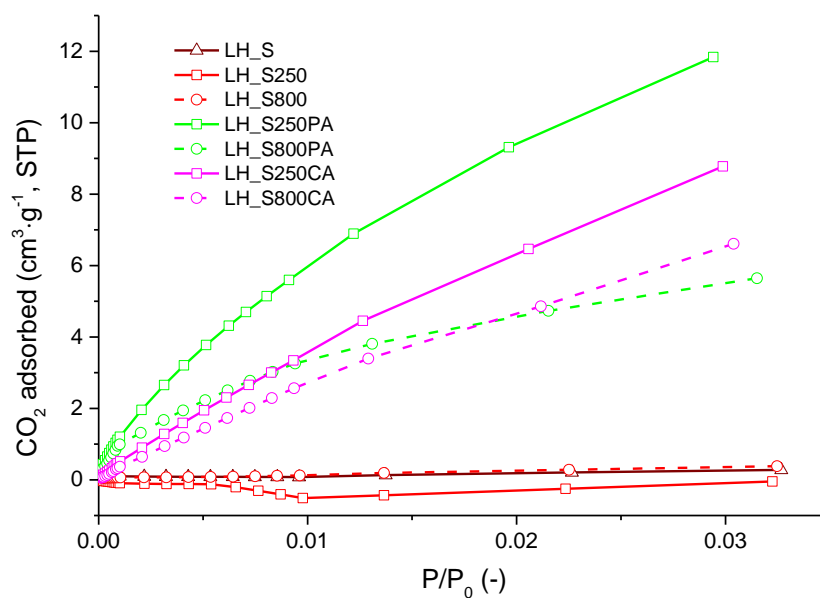


Figure 5-19 CO₂ adsorption isotherms for key *Laminaria hyperborea*-based samples

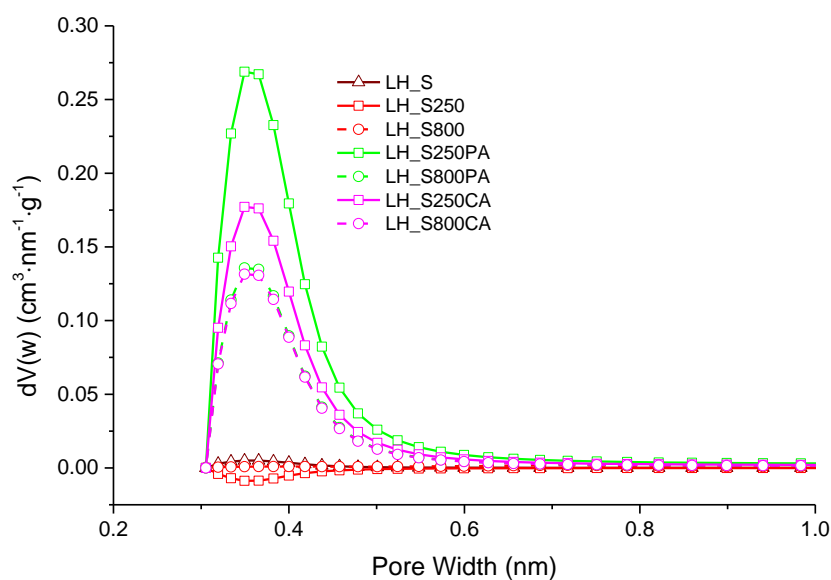


Figure 5-20 NLDFT pore size distribution for key *Laminaria hyperborea*-based samples

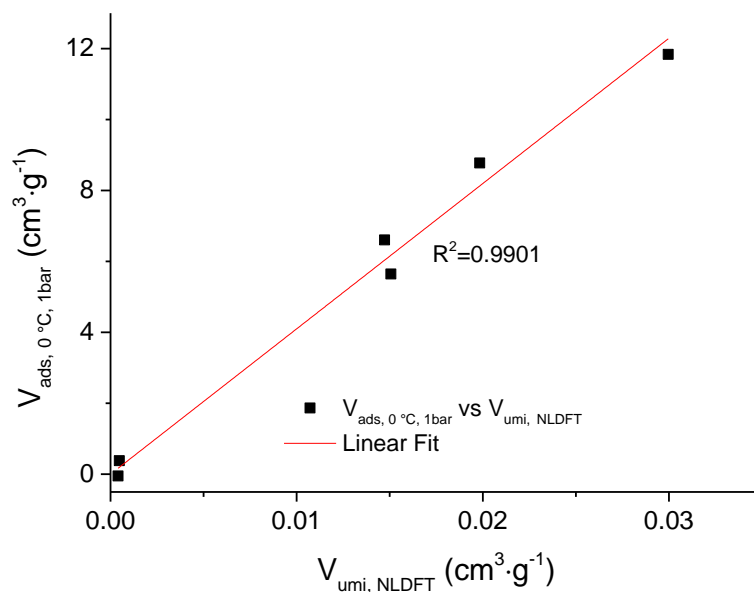


Figure 5-21 Linear correlation between CO₂ uptake at 273 K and 1 bar, and the narrow micropore volume ($d < 0.7$ nm) determined by applying the NLDFT method to the CO₂ adsorption isotherms for key *Laminaria hyperborea*-based samples.

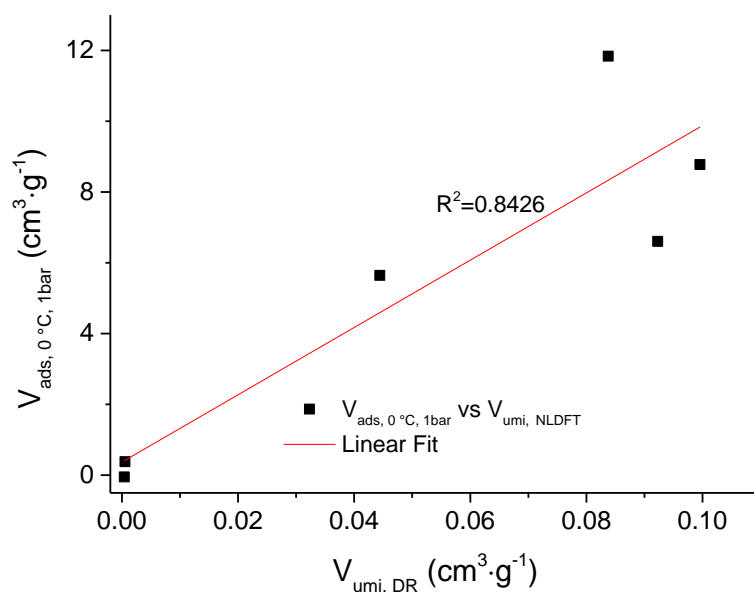


Figure 5-22 Correlation between CO₂ uptake at 273 K and 1 bar, and the narrow micropore volume ($d < 0.7$ nm) determined by applying the DR method to the CO₂ adsorption isotherms for key *Laminaria hyperborea*-based samples.

5.5 Chemical and structural characterization of raw *Laminaria hyperborea* and its derived products

5.5.1 Elemental and proximate analyses

Results obtained from the elemental analysis of *Laminaria hyperborea* showed a certain similarity to those reported by Ross *et al.* [134]. In that study, the proximate analyses of the raw feedstock were measured using Thermogravimetric Analysis (TGA). Data were quite consistent with those reported in this work, indicating a high proportion of volatile matter (VM) within the seaweed sample.

As seen in Table 5-11, a relative increase of N content was observed after hydrochar formation, thus suggesting that most of N functionalities are retained within the solid fraction after hydrothermal carbonization. By contrast, the level of N remained unaltered after pyrolysis of the raw feedstock. This result was in agreement with that reported by Haykiri-Acma *et al.* [200], who pyrolyzed brown seaweed (*Phaeophyta*) at 900 °C. On the other hand, N functionalities are partly removed after activation, in particular after the chemical treatment (i.e. KOH activation followed by HCl washing).

Haykiri-Acma *et al.* [200] also reported an increase of the sulphur content after pyrolysis at high temperature, which also agreed with results reported in this work for LH_S800. This is due to the presence of carbohydrates and proteins, although the biochemical composition of macroalgae is different to that in terrestrial biomass as reported in the literature for this type of feedstock [134, 203].

A high level of H was retained within the hydrothermally-carbonized *Laminaria hyperborea*. In contrast, a dramatic reduction in the hydrogen content occurred after pyrolysis, thus indicating a more severe thermal conversion [288]. A moderate drop in H content was measured after CO₂ activation of the hydrochar. On the other hand, H was removed for the greater part after the chemical treatment.

The O concentration initially exhibited by the raw material decreased after the carbonization step as this entailed heat-treating materials under near O-free atmosphere. Accordingly, a reduction of the O-based functionalities might have occurred. As expected, the O abundance of the chars increased after oxidization under CO₂ atmosphere, especially for LH_S800. Conversely, chemical activation caused a dramatic reduction of the O content, as chars were heat-treated under pure nitrogen. Indeed, the release of oxidized forms of C as volatiles is expected to occur during KOH activation [289]. In addition to this, as O fraction was determined on a dry basis, oxygen content includes metal oxides (i.e. ash). These were removed by acid washing after KOH activation, thus contributing to the dramatic reduction of the O abundance for the chemically-treated samples.

Apparently, the hydrothermal synthesis of *Laminaria hyperborea* yielded a more highly carboniferous product (64.7 wt%) compared to that obtained after the pyrolysis treatment (46.9 wt%). However, only half of the overall carbon content was actually bound to the structure of the hydrochar (see fixed carbon of 33.5 wt%). This was in line with the higher proportion of volatile compounds measured for the hydrothermally carbonized *Laminaria hyperborea* (57.1 wt%) compared to those found in LH_S800 (13.2 wt%). Most of the volatile matter contained in the raw *Laminaria hyperborea* was retained within the hydrochar after the milder carbonization achieved by HTC. However, despite the more dramatic devolatilization that occurred after the pyrolysis of macroalgae, the LH_S800's carbon fraction was found to increase only from ca. 40 wt% to ca. 47 wt%. The limited increase in the carbon content could be attributed to loss of carbon via the volatiles and to the high levels of ash from the raw seaweed. Consequently, a substantial enrichment in ash content occurred after pyrolysis. Nonetheless, it is worth noting that the hydrochar had a noticeably higher fixed carbon (33.5 wt%) than that measured for LH_S800 (27.5 wt%). This result, along with the decrease in ash found after HTC treatment, may be explained by the dissolution of inorganic species within the aqueous HTC process.

The carbon content of the pyrolyzed char was found to decrease after activation under CO₂. This could be partly attributed to the creation of porosity to some extent (i.e. carbon burn off). Once again, the low levels of carbon found for LH_S800PA was mostly because physical treatment does not remove the inorganic fractions present within pyrolyzed macroalgae. On the other hand, after CO₂ activation of pyrolyzed *Laminaria hyperborea* ash content slightly decreased from 59.3 wt% to 48.7 wt%. This might be explained by recombination of the O contained within ash to form oxygen-containing functional groups. Conversely, the activation of the hydrochar caused an additional evaporation of volatiles (see drop by more than 40 wt% as given in Table 5-11) from the poorly carbonized sample. As a result, LH_S250's enriched in fixed carbon relatively. These findings agreed fairly well with those reported for physically-activated oak wood (see Chapter 4).

Nevertheless, much higher carbon content was exhibited by KOH-activated carbons, which is probably due to the removal of the inorganic fraction by acid-washing of the KOH-activated carbons. This was consistent with the lower levels of ash found for LH_S250CA and LH_S800CA compared to those found in the physically activated analogues. This chemical activation of pyrolyzed *Laminaria hyperborea* gave rise to a slightly higher carbon content (89.1 wt%) than that measured for LH_S250CA (83 wt%). This result was consistent with EDX elemental compositions (see Figure 5-26), and was ascribed to the larger amount of residual volatiles left within LH_S250CA. On the other hand, the hydrochar exhibited a dramatic decrease of the volatile fraction (ca. 64% loss) after chemical activation. The high degree of devolatilization experienced by LH_S250CA might explain the larger texture

development exhibited by LH_S250CA compared to that of LH_S800CA (see Table 5-10).

According to data reported in Table 5-11, the volatiles content of pyrolyzed seaweed slightly increased after KOH activation (from 13.2 to 16.4 wt%). However, it is worth noting that the VM figure reported in Table 5-11 for seaweed char (LH_S800) was carried out by using the British Standards Institution (BSI) method, while the volatile content reported for the chemically-activated counterpart (LH_S800CA) was obtained by TGA. In contrast, the char's volatile content measured by TGA (ca. 18 wt%, see Figure 5-23) was found to be slightly higher than that measured for LH_S800CA.

LH_S250CA appeared to contain a larger abundance of carbon bound to its structure (79.4 wt%) than that found in LH_S800CA (72.5 wt%). This was attributed to the lower amount of residual ash (0.3 wt%) from the KOH-activated hydrochar compared to that left by its pyrolyzed counterpart (11.1 wt%). Apparently, the washing treatment applied for LH_S250CA was more efficient than that carried out for LH_S800CA as a higher percentage of ash was removed for the former (96.8% loss vs 81.3% loss, respectively). This agreed with the lower activation yield measured for LH_S250CA (see Table 5-6), and might have been a contributory factor in its more remarkable texture enhancement (see Table 5-10).

Table 5-11 Elemental and proximate analyses for isotherms for key *Laminaria hyperborea*-based samples

Sample ID	Ultimate, db					Proximate, db		
	N	C	H	S	O	VM	A	FC
LH_S	1.7	40.1	5.3	0.3	52.6	77.7	18.1	4.2
LH_S250	3.1	64.7	4.9	0.3	27.0	57.1	9.4	33.5
LH_S800	1.7	46.9	0.9	2.3	48.3	13.2	59.3	27.5
LH_S250PA	2.9	67.4	2.1	0.0	27.7	14.4	13.4	72.2
LH_S800PA	1.4	28.5	0.7	0.0	69.3	21.1	48.7	30.2
LH_S250CA	1.4	82.9	0.7	0.5	14.5	20.3	0.3	79.4
LH_S800CA	0.9	89.1	0.4	1.1	8.5	16.4	11.1	72.5

5.5.1.1 Insight regarding TGA as a method for proximate analyses

As already mentioned in Chapter 3, proximate analysis was carried out using TGA for the seaweed-derived ACs. For comparison purposes, the thermogravimetric method was also applied for the proximate analysis of the pyrolyzed seaweed (LH_S800).

Figure 5-23 displays the weight losses experienced by the sample during TGA. The first weight loss was ascribed to the evaporation of moisture (around 9 wt%). After this, sample was pyrolyzed under N₂ up to 900 °C in order to release its volatile matter. The amount of volatiles (ca. 18 wt% db) observed was slightly higher than that measured by BSI method (13.2 wt% db as seen in Table 5-11). The fixed carbon measured by the TGA (ca. 41 wt% db) was considerably higher than that found using the standard method (27.5 wt% db). Consequently, this led to estimate a lower abundance of ash compared to that measured by the BSI methodology (ca. 40.9 wt% and 59.3 wt% db respectively).

In theory, the fixed carbon obtained from the thermogravimetric analysis should be considered more reliable as it represents a direct estimation of the parameter. Conversely, when referring to standards (i.e. BSI method), fixed carbon is calculated by difference. The other way around applies to determination of ash content.

However, the lower proportion of fixed carbon might have been due to an incomplete combustion of the carbon fraction when heat-treating the devolatilized sample inside the furnace (standard method), thus leading to an overestimation of the residual ashes. On the other hand, it might also be that the thermogravimetric programme used was not suitable for determining proximate analysis for this type of char.

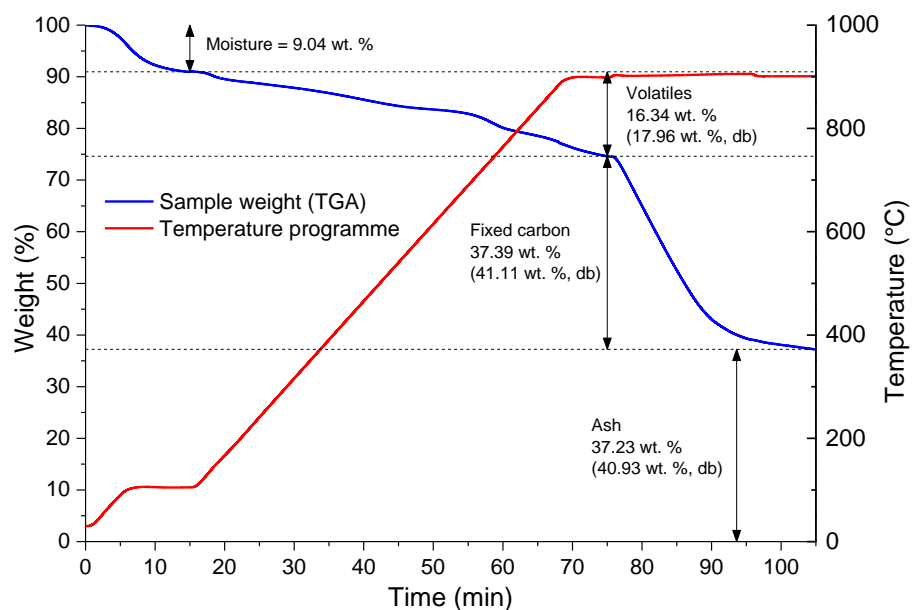


Figure 5-23 Proximate analyses determined by TGA for pyrolyzed *Laminaria hyperborea* (LH_S800)

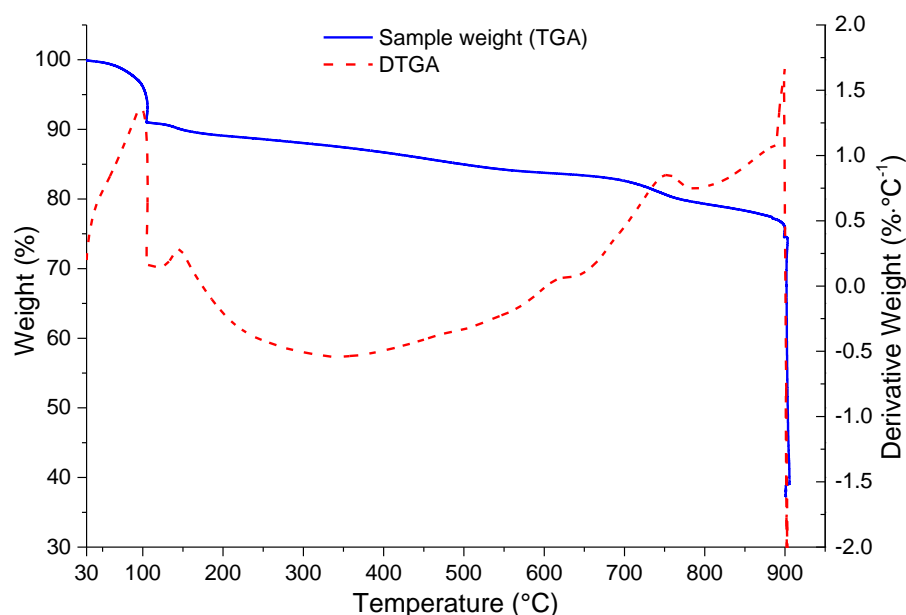


Figure 5-24 Comparison between TGA and DTGA curves for pyrolyzed *Laminaria hyperborea* (LH_S800)

From the Differential Thermogravimetric Analysis (DTGA) curve shown in Figure 5-24, it was possible to identify the temperature values at which maximum weight losses occurred. All peaks shown are upwards, which, according to the convention used in calculating DTGA, are associated with an endothermic process. The first endothermic reaction was attributed to the evaporation of moisture, reaching a maximum at ca. 100 °C. Afterwards the sample released its volatile compounds, with the highest weight loss achieved

at ca. 750 °C. The last peak, observed at 900 °C, was ascribed to the carbon burn off occurring after changing gas atmosphere from nitrogen to air.

5.5.2 Scanning Electron Microscope (SEM) and Energy-Dispersive X-ray (EDX) analyses

Figure 5-25(a) depicts the morphology of raw *Laminaria hyperborea*. This was typical of a plant tissue structure [141].

Carbonization and physical activation processes did not significantly change the initial morphology of macroalgae (see Figure 5-25(b, c, d, e)). This might explain the limited increase of porosity measured after CO₂ activation of the chars (see section 5.3.1). In addition, coarse particles were clearly shown for chars and physically-activated counterparts. These were found to be inorganic as revealed by EDX chemical compositions (see Table 5-12) acquired on the same area shown by the micrographs.

Unlike abovementioned treatments, the KOH activation and subsequent acid-washing stripped the seaweed-based chars of inorganic particles. This led to an outstanding development of porosity as described in section 5.3.2. Nonetheless, only macropores could be observed from Figure 5-25(f, g) as the resolution did not allow the identification of smaller pores. No particles were clearly identified for chemically-activated carbons, which agreed with the scarcity of inorganic fractions detected by EDX analysis for these samples (see Figure 5-26).

Carbon contents measured by EDX agreed fairly well with those found by elemental analysis (see Table 5-11). In fact, data shown in Figure 5-26 confirmed that traditional pyrolysis of seaweed gave rise to a char lower in carbon in comparison to hydrochars. HTC led to a larger increase of the overall carbon content and to a lower inorganic fraction. This was in agreement with the lower ash content measured by proximate analysis for the hydrochar (see Table 5-11). The lower level of inorganic matter exhibited by the hydrochar (see Figure 5-26) might suggest aqueous leaching of inorganics to some extent during hydrothermal carbonization.

CO₂ activation affected the chars in different ways. In spite of the higher activation burn-off recorded for LH_S250 in Table 5-2, this sample exhibited an increase of the carbon content (see Table 5-11). As already described in section 4.5.1, this was likely due to the additional devolatilization of the hydrochar occurred during the activation step. Consequently, the carbon fraction enriched relatively. By contrast, Figure 5-26 showed that, after oxidation with CO₂, LH_S800's carbon content decreased, whereas its oxygen abundance increased. These results were in line with elemental analysis (Table 5-11). Accordingly, a more significant rise of the overall abundance of inorganic

elements was measured for this sample. Nevertheless, this finding disagrees with the ash reduction measured by proximate analysis for the LH_S800PA.

In addition to this, Figure 5-26 also illustrates how chemical treatment caused a reduction of the inorganic fraction of the unactivated materials (i.e. chars). This was likely due to the HCl washing carried out after the heat-treatment. As a result, an increase of the carbon abundance was measured for both KOH-activated carbons.

Further details about the nature of the inorganic fractions detected by EDX analyses were given in Table 5-12 for all the samples. A broad range of elements was detected in the raw and pyrolyzed macroalgae, whose inorganic fraction was mostly composed of alkali metals and chlorine.

Alkali metals and chlorine were largely retained after CO₂ activation of pyrolyzed *Laminaria hyperborea*. In contrast, the KOH activation and subsequent acid-washing led to the removal of most of inorganic elements originally present within raw and carbonized macroalgae. This was consistent with proximate results (see Table 5-11).

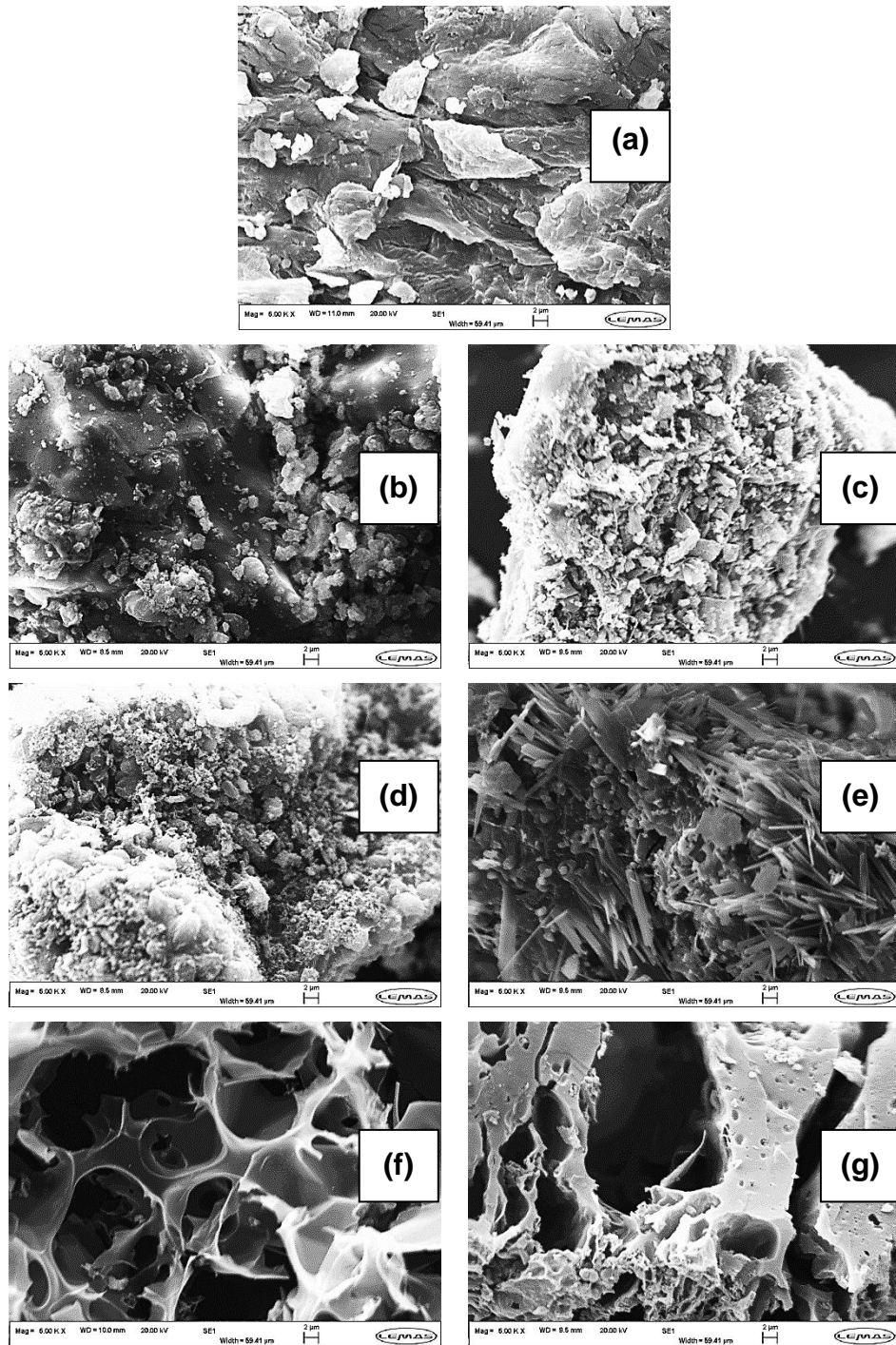


Figure 5-25 SEM images at 5000x magnification for (a) LH_S, (b) LH_S250, (c) LH_S800, (d) LH_S250PA, (e) LH_S800PA, (f) LH_S250CA and (g) LH_S800CA

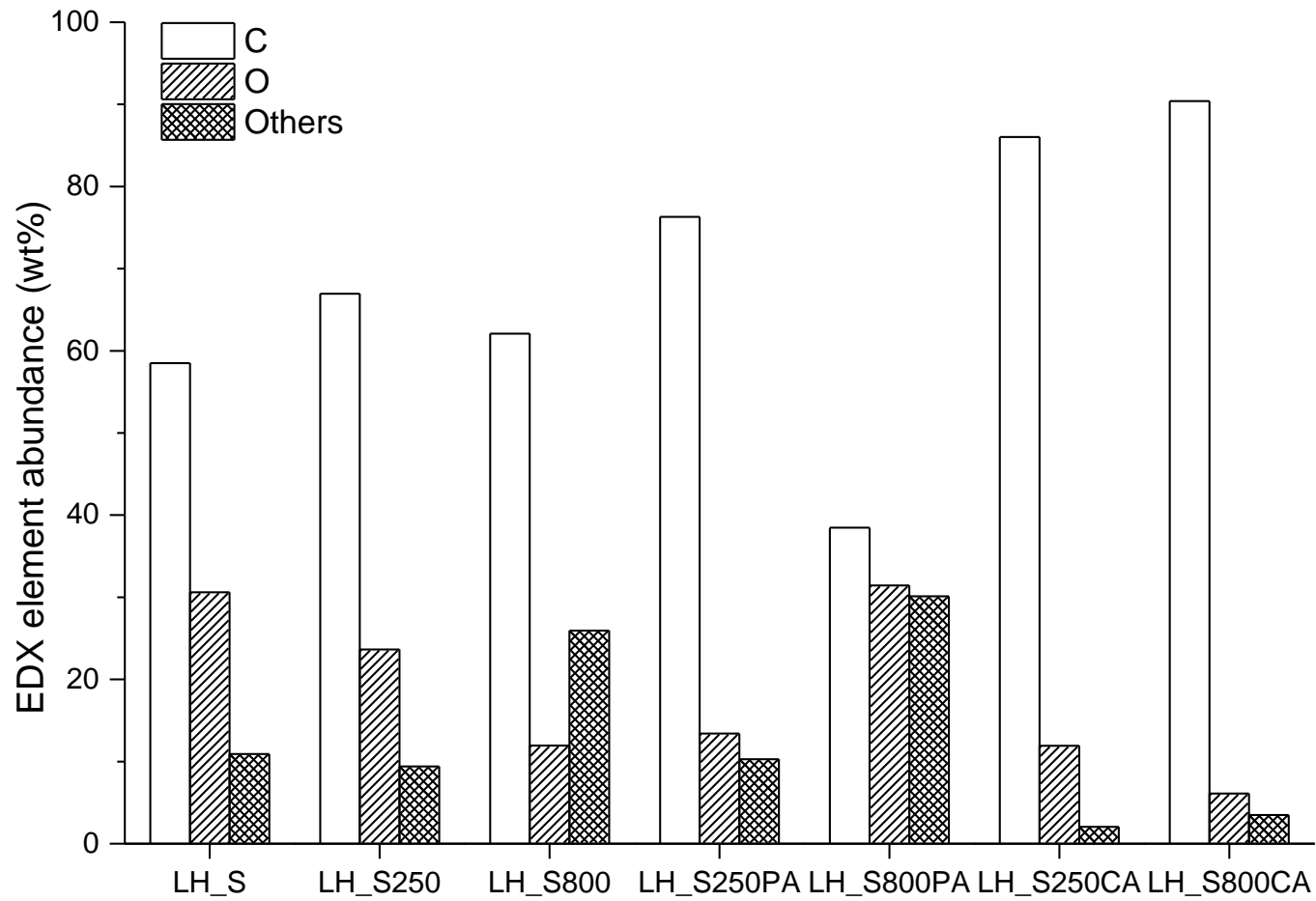


Figure 5-26 EDX chemical compositions acquired on the micrographs shown in Figure 5-25 for for key *Laminaria hyperborea*-based samples

Table 5-12 Details about inorganic elements (see “Others” Figure 5-26) detected by EDX analyses for for key *Laminaria hyperborea*-based samples

LH_S		LH_S250		LH_S800		LH_S250PA		LH_S800PA		LH_S250CA		LH_S800CA	
Element	wt%	Element	wt%	Element	wt%	Element	wt%	Element	wt%	Element	wt%	Element	wt%
Al	2.98	Al	ND ⁴²	Al	0.09	Al	ND	Al	ND	Al	1.02	Al	2.48
Ca	2.59	Ca	1.42	Ca	1.21	Ca	5.33	Ca	0.71	Ca	ND	Ca	ND
Cl	1.89	Cl	1.55	Cl	8.07	Cl	0.08	Cl	1.79	Cl	ND	Cl	0.46
Cu	1.26	Cu	0.24	Cu	0.49	Cu	0.33	Cu	ND	Cu	ND	Cu	ND
Fe	ND	Fe	ND	Fe	ND	Fe	0.33	Fe	ND	Fe	ND	Fe	ND
I	0.73	I	ND	I	0.55	I	ND	I	ND	I	ND	I	ND
K	0.60	K	2.45	K	9.03	K	0.11	K	1.05	K	ND	K	ND
Mg	0.33	Mg	0.51	Mg	0.58	Mg	0.87	Mg	6.03	Mg	0.62	Mg	ND
Na	0.27	Na	1.04	Na	3.90	Na	ND	Na	12.50	Na	ND	Na	ND
P	0.20	P	0.29	P	0.33	P	2.84	P	4.97	P	ND	P	ND
S	0.06	S	1.91	S	1.69	S	0.40	S	3.06	S	0.4	S	0.56

⁴² Not detected

5.5.3 Further characterization for selected samples

5.5.3.1 XRD patterns

As depicted by Figure 5-27(a) and (b), XRD patterns measured for raw macroalgae (LH_S) and its pyrolyzed counterpart (LH_S800) displayed the presence of a series of sharp and intense peaks. The untreated macroalgae also exhibited a very broad peak measured between 20 and 25° 2 θ . A similar broad peak was already shown by XRD pattern measured for raw oak wood in Chapter 4, and can be ascribed to a non-graphitizing form of carbon [79]. Following heat treatment under N₂ atmosphere (i.e. pyrolysis at 800 °C and chemical activation) the distance between the (002) graphitic planes decreased [82]. Accordingly, as seen in Figure 5-27(b) and (c), the location of the Bragg [272] diffraction angle of the broad peak was slightly shifted to the right for pyrolyzed *Laminaria hyperborea* and its activated derivatives.

Most of the sharp peaks found for virgin *Laminaria hyperborea* matched the standard pattern of potassium chloride (00-004-0587), which can be considered as the main crystalline phase for this sample. All peaks related to this phase were also detected in the XRD pattern of pyrolyzed *Laminaria hyperborea*. This was in line with the high content of K and Cl found by EDX (Table 5-12) for raw and pyrolyzed *Laminaria hyperborea*. Most of the remaining peaks identified for LH_S were associated with sodium chloride (01-080-3939). All these peaks were also found in the pattern of pyrolyzed *Laminaria hyperborea*, yet a slight shift toward lower angles was noticed. This might have been due to a distortion of the lattice parameter of the crystals.

Crystalline phases detected in this study for virgin and carbonized seaweed agreed with results previously reported in the literature. In particular, Wang *et al.* [298] identified the presence of alkaline chlorides within seaweed-based ashes. In addition to that, sylvite (KCl) was detected on seaweed ashes by Yaman *et al.* [200], while halite (NaCl) matched the pattern of oarweed-based chars obtained after pyrolysis at 500 °C [202]. Furthermore, reflections corresponding to halite were also found for raw seaweed (i.e. *Undaria pinnatifida*) by Song *et al.* [133]. The same phase was retained after pyrolysis at 1000 °C.

By comparing Figure 5-27(a) and Figure 5-27(b), it was possible to observe that the most intense peaks related to potassium and sodium chloride became sharper after pyrolysis. This suggested the growth of the crystals after heat-treatment [291]. The average crystal sizes of sylvite and halite were calculated by applying the Scherrer equation (see Chapter 3) to XRD data as also reported in the study of Salari *et al.* [274]. For each phase, the full-widths at half-maximum (FHMWs) of the three most intense peaks were averaged. The latter were measured at ca. 28.5, 40.6 and 50.3° 2 θ for sylvite, whereas those related to halite were observed at ca. 31.8, 45.6 and 56.6° 2 θ . The average size

of sylvite crystals was found to increase from 35.8 to 38.3 nm, while halite crystallites increased from 38.5 to 45.0 nm.

Interestingly, as observed in Figure 5-27(b), additional signals were measured for pyrolyzed seaweed. This suggested the formation of new phases after pyrolysis treatment. In particular, reflections observed at ca. 43.0, 62.4 and 78.7° 2 θ were assigned to magnesium oxide (04-014-7436). This compound was also identified by Song *et al.* [133] after pyrolysis of seaweed (i.e. *Undaria pinnatifida*) at 1000 °C. According to the authors, magnesium ions (normally incorporated within alginates present in raw macroalgae) may react with oxygen-containing species such as H₂O to form MgO during pyrolysis at high temperature. In addition to this, as suggested by Ross *et al.* [134], most of the inorganic fractions contained in raw seaweed tend to decompose to their oxides when pyrolyzed at 750-800 °C. Accordingly, it might be that crystalline MgO arose from the pyrolytic breakdown of amorphous Mg alginates present within the raw brown algae [299]. Some residual peaks with low intensity measured at ca. 20.8 and 34.4° 2 θ were ascribed to unknown impurities (see asterisks in Figure 5-27(b)). These reflections might be attributed to trace alkali metals or alkali metal-based alginates whose detection was prevented by overlapping with phases that are more dominant.

Figure 5-27(b) also showed that all peaks identified within pyrolyzed *Laminaria hyperborea* were observed for its CO₂-activated counterpart. This result seems to suggest that inorganic phases were largely retained after physical treatment. In addition, the intensity of the XRD pattern measured for LH_S800PA appeared to be shifted down. This might be attributed to the formation of pores following to the CO₂ activation of seaweed char (see Table 5-10 and Figure 5-17). Nevertheless, peak widths corresponding to potassium chloride seemed to shrink after physical treatment. This agreed with a further increase of size (from 38.3 to 46.4 nm) found for sylvite crystallites. By contrast, the lattice spacing of halite crystals dramatically decreased from 45.0 to 17.9 nm. This was consistent with the significant reduction of intensity observed for peaks assigned to halite, and seemed to indicate the decomposition of sodium chloride during activation treatment. A moderate decrease of MgO crystallite (from 40.3 to 38.3 nm) was also found, thus indicating that magnesium oxide was mostly retained within the physically-activated carbon.

As seen by Figure 5-27(c), no peaks associated with alkali chlorides and magnesium oxides were found for LH_S800CA. This might be due to the dissolution of crystallites after acid (HCl) washing, which agreed with the dramatic decrease of ash content measured by proximate analysis (from ca. 59 wt% to ca. 11 wt%, see Table 5-11). Furthermore, as given in Table 5-12, EDX analysis did not detect any of the elements present within the aforementioned compounds, except for a low concentration of Cl. Nonetheless, the latter presence might be due to the washing treatment of the sample by hydrochloric acid.

However, a series of low intensity peaks were measured for LH_S800CA. Most of these were best fitted by the standard pattern of aluminium oxide (04-013-1687) and aluminium hydroxide (04-014-1754). The presence of Al-based impurities was in accordance with EDX chemical composition measured for LH_S800CA (see Table 5-12), wherein Al is the most abundant inorganic element detected. Interestingly, aluminium oxide is also identified for the chemically-activated wood (OW250CA) in Chapter 4. It seems that acid etching removed most of the inorganic species but oxidized forms of Al appeared to be the only inorganic phases that were not fully dissolved by acid washing. Al-containing impurities might have not been detected within raw and pyrolyzed seaweed because of the higher background swamping their XRD patterns. In addition to this, aluminium compounds might have underlain other predominant crystalline phases (e.g. alkaline chlorides). However, it may also be that crystalline Al-based compounds might have arisen from the heat-treatment of amorphous aluminium originally contained within macroalgae (see Table 5-12). Weak peaks related to other unknown impurities (see asterisks in Figure 5-27(c)) were observed at ca. 29.3 and 42.6° 2 θ . These might be ascribed to trace alkali metals. Nevertheless, LH_S800CA's pattern also showed two broad peaks at around 25 (002) and 43° 2 θ (100). These highlighted a more amorphous structure of the sample, typical of activated carbon [77].

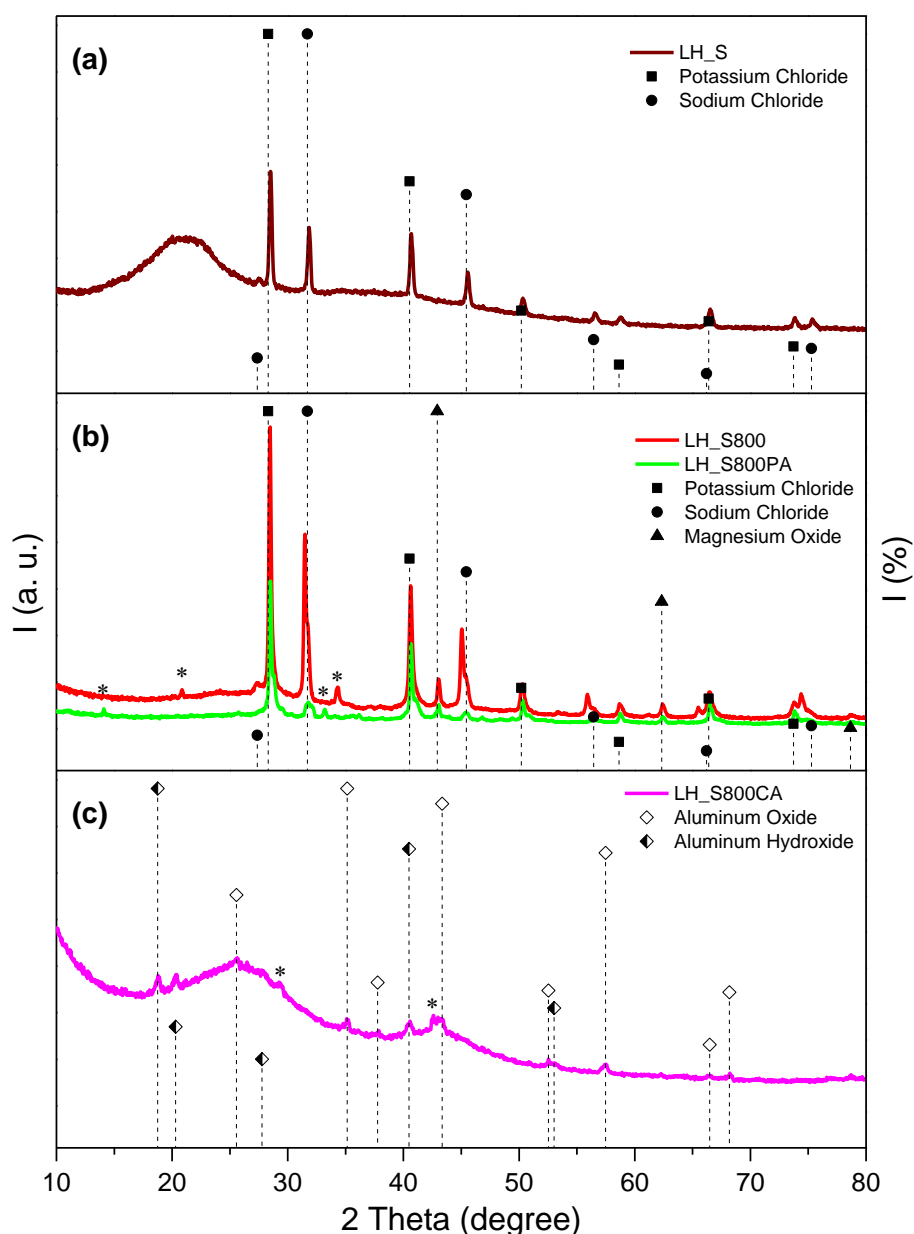


Figure 5-27 XRD Patterns for (a) raw macroalgae (LH_S), (b) pyrolyzed macroalgae (LH_S800) and physically-activated counterpart (LH_S800PA), and (c) chemically-activated counterpart (LH_S800CA)

5.5.3.2 Boehm titration

As observed from Figure 5-28, a large number of basic groups (up to ca. $2.2 \text{ mmol}\cdot\text{g}^{-1}$) was measured for pyrolyzed seaweed. The significant concentration of basic functionalities could be attributed to the high level of alkaline species previously identified by EDX analyses (see Table 5-12). Basic functionalities appeared to be entirely retained after CO_2 activation. Conversely, a far lower basicity was found for the chemically activated char (LH_S800CA). This might be associated with the demineralization that occurred after HCl washing of KOH-activated carbon. This was in agreement with proximate

findings, revealing a dramatic decrease of ash after chemical treatment as a result of acid washing. In addition to this, EDX results also showed a drop in the overall content of inorganic material (see others in Figure 5-26) from 25.9 to 3.5 wt%.

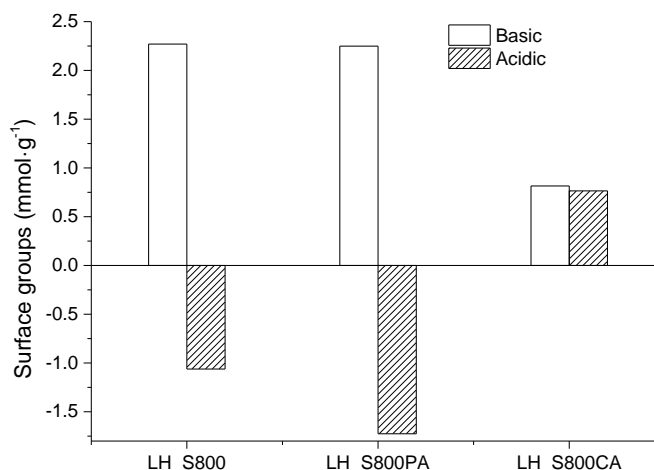


Figure 5-28 Basic and acidic functionalities measured by Boehm's titration for pyrolyzed macroalgae (LH_S800), physically-activated counterpart (LH_S800PA), and chemically-activated counterpart (LH_S800CA)

Figure 5-28 also displayed a negative amount of acidic groups for LH_S800 and LH_S800. This indicated not only the total absence of acidic functionalities within the sample but also the presence of weakly bonded basic functionalities that might have been leached from the char. When mixing materials with the alkaline standard solution (0.05 M NaOH) used to neutralize acidic groups, some basic functionalities might have migrated into the liquid phase (supernatant). As a result, the supernatant basicity might have been increased. Accordingly, as the number of acidic groups was determined by difference between the amount of alkaline species in the supernatant before and after exposure to the material, this yielded a negative value. In contrast, the higher number of acid groups found for LH_S800CA could be attributed to some residual washing acid (HCl) that was not completely washed off the material.

5.6 CO₂ uptake measurements

5.6.1 First screening

Figure 5-29 showed that, at 35 °C and 1 bar, seaweed chars exhibited slower kinetics and lower uptakes than those achieved by their activated counterparts. In particular, the hydrochar (i.e. LH_S250) showed a negligible

CO₂ uptake, probably because of its poor textural properties (see Table 5-10). Nevertheless, although of rather low surface area (see Table 5-10), the pyrolyzed char (i.e. LH_S800) and its physically-activated derivative (LH_S800PA) showed a higher sorption potential in comparison to the other samples. The sorption curve of observed for these materials did not reach a plateau after 30 min, indicating that higher uptakes could have been achieved if the adsorption step were to be prolonged.

Despite the limited texture development, CO₂ activation of hydrochar led to a substantial increase of the CO₂ uptake capability and to a rapid sorption kinetic. This might be predominantly attributed to its relatively high ultramicropore volume as given in Table 5-10. This result confirmed the importance of the narrower porosity for adsorbing CO₂ at high partial pressure [295]. Conversely, physical activation of LH_S800 did not significantly change the sorption behaviour of the pyrolyzed char. However, a moderate increase of the sorption speed was observed for the LH_S800PA. Although physical activation caused only limited development of texture (see Table 5-10), the creation of this new porosity might have facilitated the access of CO₂ to the sorption sites.

Nevertheless, as it was possible to observe from Figure 5-29, sorption curves of pyrolyzed char and its physically-activated derivative exhibited a similar trend and converged after 30 min. The comparable CO₂ sorption kinetic was ascribed to the similar inorganic composition found for these materials. In particular, as suggested by EDX results (see Table 5-12), the presence of alkali (K and Na) and alkali earth (Ca, Mg) metals were detected within both the char and its physically-activated counterpart. In addition, XRD patterns obtained for LH_S800 and LH_S800PA (see Figure 5-27(b)) revealed the presence of magnesium oxide within the structure of these samples. These results might suggest that carbonation reaction between magnesium oxide and CO₂ might have occurred to some extent. Indeed, it was previously reported that MgO can absorb CO₂ at low temperature (50-100 °C) and in presence of moisture [300], which might have been retained within the carbon structure. On the other hand, absorption of CO₂ onto MgO particles was also reported under dry conditions and at temperatures ranging from 25 to 75 °C [131]. In addition, chemisorption of CO₂ onto magnesium oxide at low temperature (ca. 53 °C) was demonstrated in this work by the measurement of CO₂ sorption kinetics under post-combustion conditions for pure MgO (see Figure 5-31).

In contrast, chemically-activated macroalgae exhibited higher CO₂ uptakes and faster sorption kinetics, thus showing a behaviour typical of physisorbents. This agreed with the much higher surface areas measured for these samples. The different sorption performance displayed by KOH-ACs was also attributed due to the removal of alkali metal-based compounds (with specific regard to magnesium oxide) after chemical treatment due to acid washing. In particular, as revealed by EDX (see Table 5-12), none of alkali

metals was detected after KOH activation of pyrolyzed seaweed. This was probably due to the acid washing step.

Interestingly, LH_S250CA reached the highest value of CO₂ uptake but significant fluctuations were recorded during the adsorption stage, thus suggesting a weak interaction between CO₂ and the sorption sites. However, it is worth noting that this KOH-activated carbon had lower narrow micropore volume than its CO₂-activated analogue (see Table 5-10). Results would thus imply that CO₂ uptakes at 35 °C and 1 bar might be governed by a combination of narrow micropores and larger pores (i.e. surface area). This was also corroborated by correlations reported in Appendix 1 (see also Chapter 4).

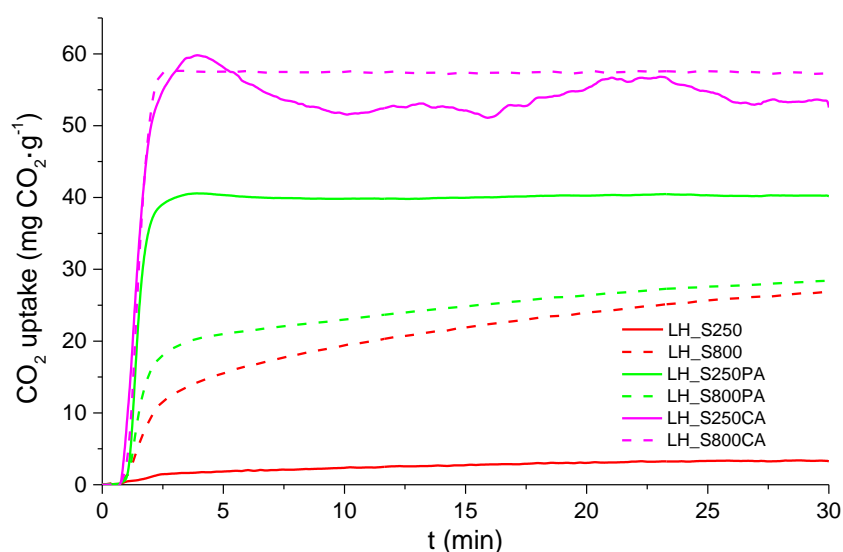


Figure 5-29 CO₂ adsorption kinetic at 35 °C and 1 bar for key *Laminaria hyperborea*-based samples

Table 5-13 CO₂ uptakes measurement at a total pressure of 1 bar for key *Laminaria hyperborea*-based samples

Sample ID	1 bar (100% CO ₂)			0.15 bar (15% CO ₂)		
	35 °C	60 °C	$W_{\text{loss, 35-60 °C}}^{43}$	100 °C	$W_{\text{loss, 60-100 °C}}^{44}$	53 °C
	mg CO ₂ ·g ⁻¹	mg CO ₂ ·g ⁻¹	%	mg CO ₂ ·g ⁻¹	%	mg CO ₂ ·g ⁻¹
LH_S250	3.3	0.3	90	0.0	100	NM ⁴⁵
LH_S800	26.5	20.1	24	3.3	84	10.4
LH_S250PA	40.2	22.67	44	2.3	90	NM
LH_S800PA	28.4	21.13	26	4.9	77	10.7
LH_S250CA	54.1	27.45	49	10.2	63	NM
LH_S800CA	57.2	26.95	53	3.5	87	6.3
MgO	NM	NM	NM	NM	NM	4.6

⁴³ Calculated as difference between the sorption capacity at 35 and 60 °C, and expressed as a percentage of the sorption capacity at 35 °C.

⁴⁴ Calculated as difference between the sorption capacity at 60 and 100 °C, and expressed as a percentage of the sorption capacity at 60 °C.

⁴⁵ Not measured

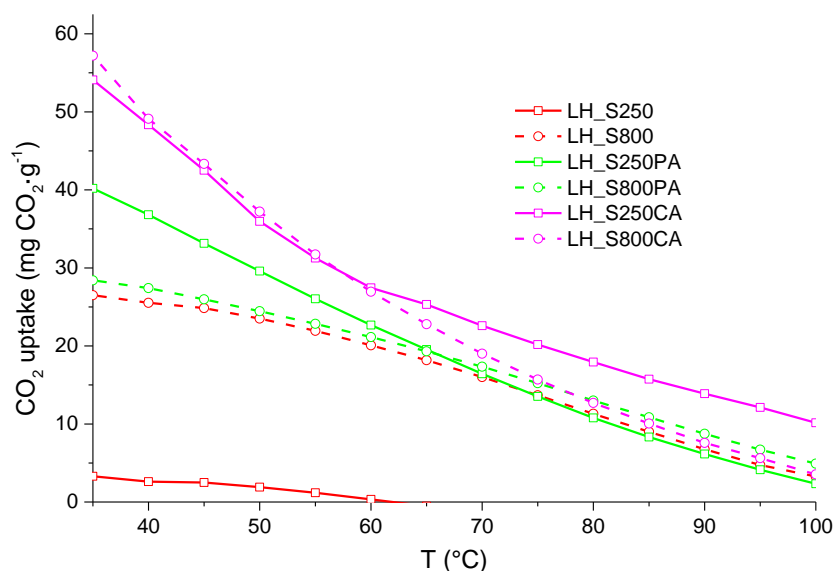


Figure 5-30 Regeneration (rapid temperature swing adsorption (RTSA), 35-100 °C) for key *Laminaria hyperborea*-based samples

As shown in Figure 5-30, except for LH_S250, which adsorbed a very low amount of CO₂, all samples failed to fully regenerate at 100 °C. This suggested that a higher temperature should be used when RTSA cycles were to be performed. At lower temperature (e.g. below 60 °C), KOH-activated carbons exhibited the fastest desorption rate, losing up to 53% of the CO₂ adsorbed (see Table 5-13). However, It is worth noticing that, at temperature higher than 60 °C, LH_S250CA desorption curve was less steep. This result reflected the lowest weight loss exhibited between 60 and 100 °C (see Table 5-13). Apparently, an outer layer of weakly adsorbed CO₂ might have been released as temperature was increased initially. This is in line with the unsteady CO₂ uptake profile previously shown in Figure 5-29 for LH_S250CA. On the other hand, some of the CO₂ molecules might have been strongly attached to the sample structure, thus implying a difficult regeneration of the material at higher temperatures.

By contrast, both LH_S800 and LH_S800PA showed a very slow CO₂ removal rate at lower temperature as can be seen from the near flat shape of the desorption curve. Indeed, as given in Table 5-13, a very low percentage of CO₂ was released from these samples between 35 and 60 °C. This might have been caused by a stronger bond (i.e. chemisorption) established between the CO₂ molecule and inorganic species (e.g. MgO) present within these samples (see Figure 5-27).

5.6.2 Simulated post-combustion performance

In this section, the simulated post-combustion capture performance of pyrolyzed *Laminaria hyperborea* and its activated derivatives was compared. Furthermore, pure magnesium oxide (MgO) was included for comparison purposes.

As seen in Figure 5-31, when measuring the sorption kinetic at lower partial pressure (0.15 bar) of CO₂ and higher temperature (53 °C), the sorption capacity of the chemically-activated seaweed dramatically decreased. LH_S800CA exhibited the fastest sorption kinetic, reaching saturation in less than 2 min. On other hand, although having significantly higher surface area, this KOH-AC had a lower maximum sorption capability than those measured for its parent char and its physically-activated counterpart. In addition, the CO₂ sorption capacity recorded for LH_S800CA was not steady, but appeared to decrease over the equilibration time. Although the temperature was constant throughout the adsorption stage, it seems that some of the (weakly bonded) CO₂ captured by LH_S800CA at the early stage of the adsorption process might have been subsequently desorbed. This behaviour could be attributed to the prolonged exposure of the material at a relatively high temperature (53 °C), which may have favoured desorption of carbon dioxide. This would then suggest a pure physisorption process for LH_S800CA, which becomes less effective at higher temperature.

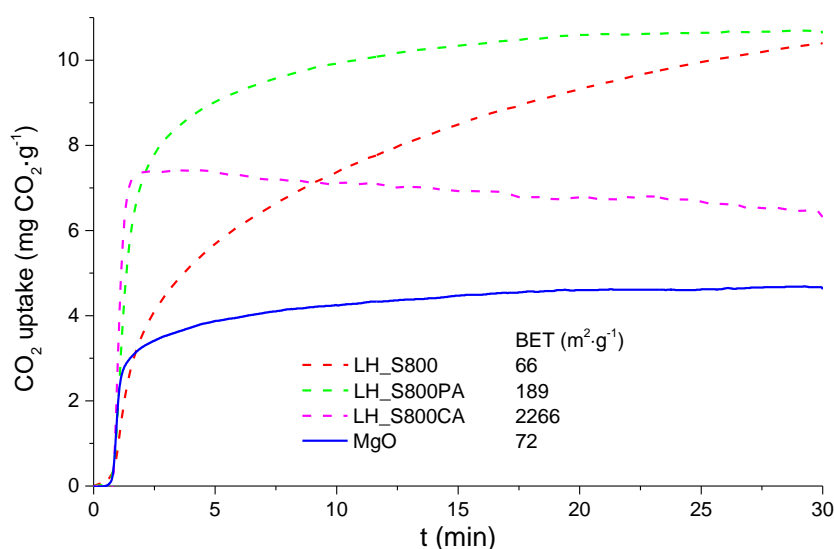


Figure 5-31 CO₂ adsorption kinetic at 53 °C and 0.15 bar (total pressure of 1 bar) measured for pyrolyzed macroalgae (LH_S800), physically-activated counterpart (LH_S800PA), chemically-activated counterpart (LH_S800CA), and magnesium oxide (MgO).

By contrast, despite the very low surface area available, LH_S800 and LH_S800PA significantly outweighed the sorption performance of the KOH-activated *Laminaria hyperborea*, capturing nearly twice as much CO₂ than that adsorbed by LH_S800CA after 30 min. The remarkable difference in surface area between the samples (see Table 5-10) seems to suggest that the sorption potential exhibited by macroalgae char and its CO₂-activated derivative was independent of textural properties. Unlike for LH_S800CA, which was demineralized (i.e. by HCl washing), a relatively high concentration of alkali metals were found for LH_S800, which was largely retained after physical activation (see Table 5-12). The inherent alkalinity of seaweed-char and its physically activated derivative agreed with the higher number of basic groups measured for these samples (see Figure 5-28). Therefore, it appears that the effect of inorganics on the sorption potential of LH_S800 and LH_S800PA becomes more influential at lower partial pressure, when a higher selectivity is vital. In particular, magnesium oxide, which was identified by XRD analyses on the structure of pyrolyzed and CO₂-activated macroalgae (see Figure 5-27), may have been responsible for a more selective (chemi)sorption of CO₂ under post-combustion conditions.

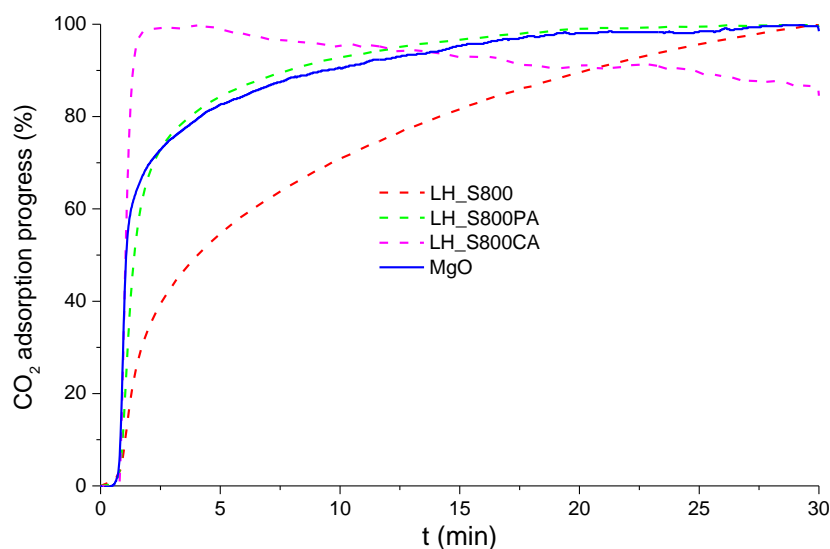


Figure 5-32 CO₂ adsorption progress at 53 °C and 0.15 bar (total pressure of 1 bar) measured for pyrolyzed macroalgae (LH_S800), physically-activated counterpart (LH_S800PA), and magnesium oxide (MgO).

As indicated by Figure 5-31 and Figure 5-32, this assumption was corroborated by the CO₂ sorption kinetic measured for magnesium oxide under simulated post-combustion conditions, which appeared to mirror those observed for physically activated *Laminaria* (LH_S800PA). Figure 5-31 showed that MgO exhibited the lowest CO₂ uptake (4.6 mg CO₂·g⁻¹, i.e. ca. 0.105 mmol CO₂·g⁻¹), which was lower than figures reported in the literature at higher temperature [301]. The small sorption potential found in the present study at 53 °C might be

due to the poor reactivity of the MgO at lower temperature, which might imply a limited CO₂ conversion (into MgCO₃).

As seen in Figure 5-31, LH_S800PA displayed far higher uptakes than those observed for MgO. On the other hand, as highlighted by Figure 5-32, when the CO₂ adsorption kinetics of the materials are normalized by the maximum CO₂ uptakes (see equation (5.1)), the sorption rate (i.e. CO₂ adsorption progress) observed for magnesium oxide closely follows that found for LH_S800PA. This seems to suggest that the chemisorption contribution observed for LH_S800PA may be similar to the mechanism typical of pure MgO [302].

$$CO_{2, ads pro} (t) = \frac{CO_{2, ads}(t)}{CO_{2, ads max}} \cdot 100 \quad (5.1)$$

where, for each sample, CO_{2, ads pro} (t), defined as CO₂ adsorption progress, is the percentage fraction of the overall CO₂ adsorption capacity (CO_{2, ads max}) at a given time t, and CO_{2, ads} (t) is the CO₂ adsorption at a given time t.

The CO₂ (chemi)sorption kinetic observed in this study for magnesium oxide was consistent with that measured by Song *et al.* [303] under similar conditions (50 °C, 0.15 bar). These authors synthesized porous MgO and described its sorption behaviour as a two-stage process. In particular, the faster CO₂ uptake occurring at the early stage of the adsorption step is believed to be governed by diffusion through the gas film surrounding the MgO particles, whereas intraparticle diffusion resistance becomes more dominant during the second step, resulting in a slower sorption process.

Nonetheless, the higher CO₂ sorption potential exhibited by the physically-activated *Laminaria* might be ascribed to the larger surface area measured for this sample (see also Table 5-10). LH_S800PA's capture potential seems to be the result of a synergetic effect of physisorption and chemisorption contributions. Presumably, the more developed porous network not only ensured a higher physisorption effect, but might have also facilitated the access of CO₂ to the chemisorption sites (i.e. MgO crystals).

By contrast, although the macroalgae-based char (LH_S800) attained nearly as large CO₂ uptakes as that achieved by LH_S800PA, LH_S800 exhibited a much slower uptake rate. This may be attributed to the undeveloped porous network found for this sample (see Table 5-10). This may cause reduced mobility of CO₂ through the pore channels of the material, and therefore a delay in accessing both the carbon pores (i.e. physisorption sites) and the MgO particles (i.e. chemisorption sites) present within the porous network of the material.

The highest sorption capacity exhibited by MgO-containing materials synthesized in this work (10.7 mg CO₂·g⁻¹ for LH_S800PA, see Table 5-13) was

lower than the capture capability ($63 \text{ mg CO}_2\cdot\text{g}^{-1}$) achieved by a MgO-containing mesoporous carbon under similar conditions ($T_{\text{ads}}=50 \text{ }^\circ\text{C}$, $P_{\text{CO}_2}=0.15 \text{ bar}$ [131]). However, the synthesis of alkali metal-containing sorbents presented in this study was more sustainable and easier compared to that reported in the work of Bhagiyalakshmi *et al.* [131], as seaweed treatment did not involve any chemical addition (i.e. impregnation of alkali-containing compounds), and a widely available feedstock was used.

In addition to this, *Laminaria hyperborea*-based sorbents were fully regenerated at $100 \text{ }^\circ\text{C}$ (see Figure 5-33), which is lower than the temperature applied by [131] ($200 \text{ }^\circ\text{C}$) for the regeneration of Mg-containing carbons. Therefore, the use of the sorbents examined in this study would potentially imply a lower cost associated with RTSA cyclic operations. The easier regeneration (at ca. $80 \text{ }^\circ\text{C}$) exhibited by LH_S800CA in Figure 5-33 seems to indicate a weak (physi)sorption of CO_2 onto this sample, which is in accordance with the sorption trend shown in Figure 5-29. Importantly, the regeneration of physically activated *Laminaria hyperborea* appeared to be fully accomplished at $100 \text{ }^\circ\text{C}$. In contrast, LH_S800 and pure magnesium oxide appeared to be less easy to regenerate, as indicated by the slower release of CO_2 with increasing time and the residual CO_2 retained within these samples at the end of the desorption step.

The evolution profile of the residual CO_2 on the sample with increasing time (during desorption) was also normalized in a similar manner to the CO_2 adsorption kinetic by using equation (5.2).

$$CO_{2, \text{ des pro}} (t) = \frac{CO_{2, \text{ ads}}(t)}{CO_{2, \text{ ads max}}} \cdot 100 \quad (5.2)$$

where, for each sample, $CO_{2, \text{ des pro}} (t)$, defined as CO_2 desorption progress, is the percentage reduction of $CO_{2, \text{ ads max}}$ at a given time t during the desorption step, and $CO_{2, \text{ ads}} (t)$ is the residual CO_2 remaining adsorbed onto the sample at a given time t .

Interestingly, when comparing the CO_2 desorption progress of the materials (see Figure 5-34), it was noticed that the desorption behaviour observed for pure MgO was closer to that found for *Laminaria hyperborea*-derived char (LH_S800). This might suggest a different CO_2 chemidesorption mechanism in comparison to that occurring from LH_S800PA. In particular, it might be that the CO_2 activation of the macroalgae-based char led to the formation of potassium and/or sodium carbonate. As reported by [58, 126, 304], Na and K-based carbonates can absorb CO_2 under moist conditions, giving rise to alkali metal bicarbonates. These are less stable than the corresponding carbonates and can be easily regenerated at low temperature ($100\text{-}200 \text{ }^\circ\text{C}$). Assuming that some water molecules remained trapped within the structure of physically-activated carbon after initial degassing at $120 \text{ }^\circ\text{C}$ for 30 min, this

would explain the more facile regeneration exhibited by LH_S800PA. Nonetheless, at 100 °C LH_S800 and pure MgO also released most of the CO₂ captured (nearly 80%), thus indicating a relatively weak interaction with CO₂ molecule, which favored desorption.

The regeneration temperature of carbonated magnesium oxide and MgO-containing carbon materials fabricated in this work was far lower than that usually reported for MgO (450-500 °C [131, 305]). However, MgCO₃ reconversion (into MgO) at relatively low temperature (200 °C) has already been reported by Bhagiyalakshmi *et al.* [131], who synthesized a magnesium oxide-containing carbon. These authors explained this behaviour through the weaker interaction between CO₂ and the MgO particles not embedded within the framework of the carbon-based sorbent. On this premise, the CO₂ sorption capacity of the macroalgae-based sorbents may be mostly attributed to magnesium oxide particles not bound to the carbon structure (i.e. MgO present on the external surface of the solid material).

Nevertheless, based on results presented earlier, a cyclic test under post-combustion conditions was performed both for pyrolyzed *Laminaria hyperborea* (LH_S800) and for its physically activated counterpart (LH_S800PA), as these were the most promising samples in terms of sorption potential and selectivity. In addition, in order to ensure full regeneration of both sorbents, it was decided to extend the temperature swing up to 120 °C when performing RTSA cycling as the regeneration strategy (see Figure 5-35(a)).

As seen in Figure 5-35(a), pyrolyzed *Laminaria hyperborea* exhibited very slow sorption kinetics without reaching a plateau within 30 min. This agrees with sorption kinetics previously shown in Figure 5-31. As already mentioned, it is presumed that the delayed kinetics were due to the lack of porous channels, which did not allow for efficient transport of CO₂ onto (chemi)sorption sites (i.e. MgO crystalline particles). However, the char clearly showed a great sorption potential which could be fully exploited if adsorption was to be prolonged, potentially leading to even higher uptakes. On the other hand, as depicted by Figure 5-36, the sample was successfully regenerated at 100 °C after each cycle. It is worth noting that, in Figure 5-36 the peak sample weight does not coincide with the start of the heating stage. This seems to confirm the presence of a stronger interaction between CO₂ and pyrolyzed *Laminaria*, whose regeneration appears to be less sensitive to the increase of temperature in comparison to a physisorbent. In addition, as highlighted in Figure 5-35(b), the sorption capability remained stable over 9 adsorption-desorption cycles. Nonetheless, a relatively higher capacity loss (ca. 20%) was observed after the last adsorption-desorption cycle. This might indicate poisoning of some inorganics functionalities, thus leading to a reduced chemisorption contribution.

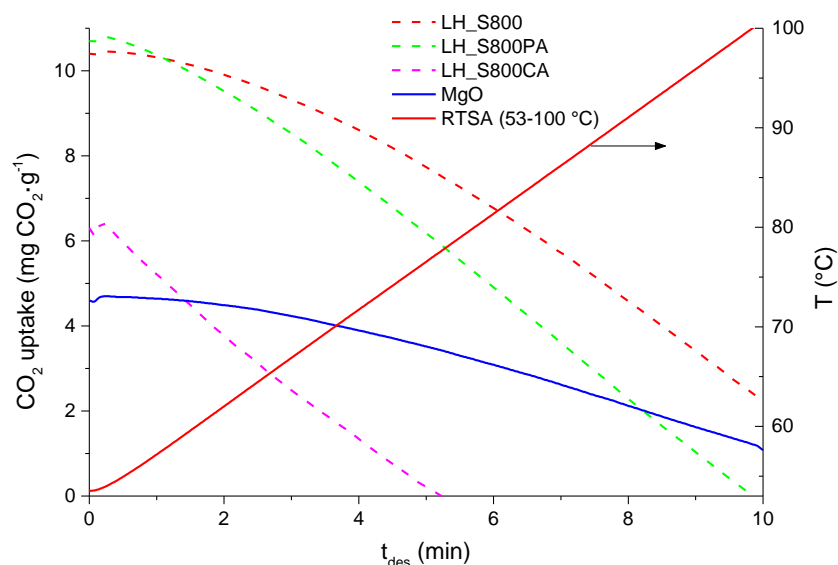


Figure 5-33 Regeneration (RTSA, 53-100 °C) for pyrolyzed macroalgae (LH_S800), physically-activated counterpart (LH_S800PA), chemically-activated counterpart (LH_S800CA), and magnesium oxide (MgO)

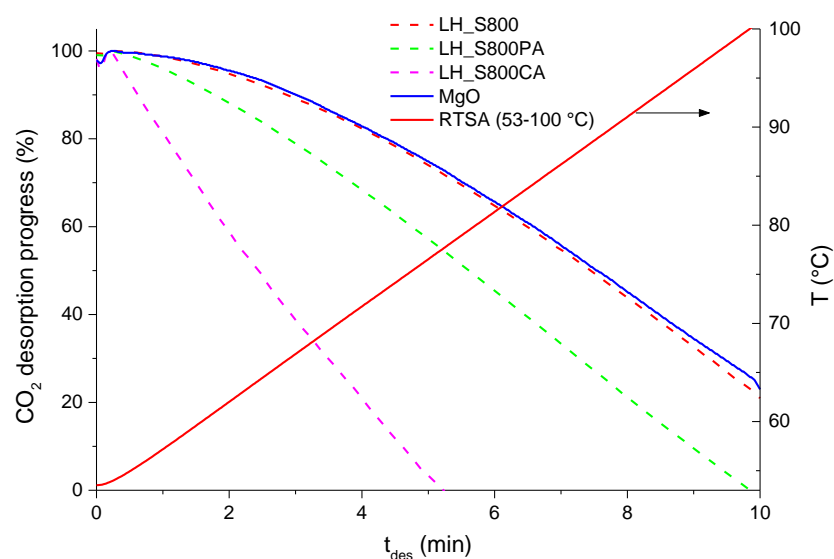


Figure 5-34 CO₂ desorption progress (RTSA, 53-100 °C) for pyrolyzed macroalgae (LH_S800), physically-activated counterpart (LH_S800PA), and magnesium oxide (MgO).

As depicted by Figure 5-37(a) and Figure 5-38, a faster CO₂ uptake rate was observed for LH_S800PA, which was also consistent with the sorption behaviour displayed by this sample in Figure 5-31. Nonetheless, this sorbent still appeared not to reach its maximum capacity at the end of the equilibration time, thereby indicating the potential of attaining even higher sorption capability over a longer adsorption stage. Desorption of CO₂ was efficiently accomplished after swinging the temperature up to 120 °C. Nevertheless, as illustrated by

Figure 5-33 and Figure 5-38, this material can be fully regenerated at temperature even lower than 120 °C (100 °C), thus potentially implying a lower cost of the regeneration step.

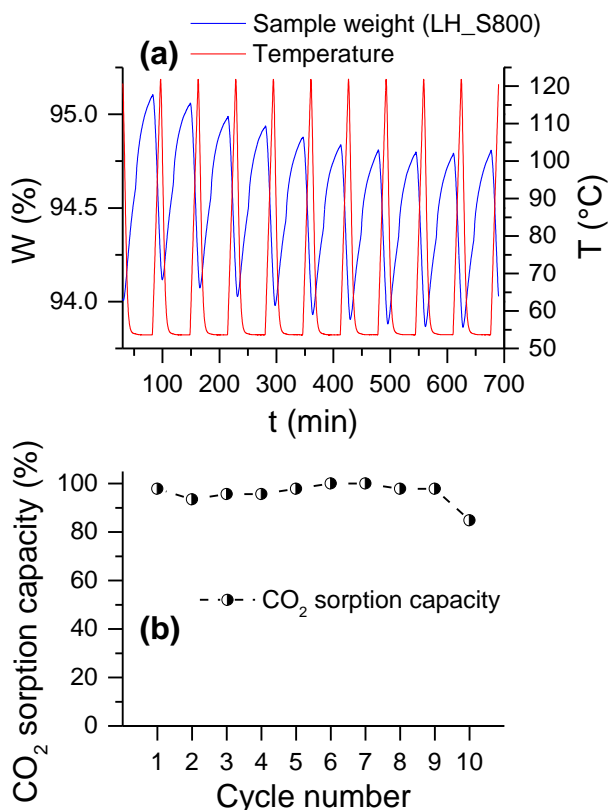


Figure 5-35 (a) Recyclability and (b) sorption capacity over ten RTSA cycles for pyrolyzed *Laminaria* (LH_S800)

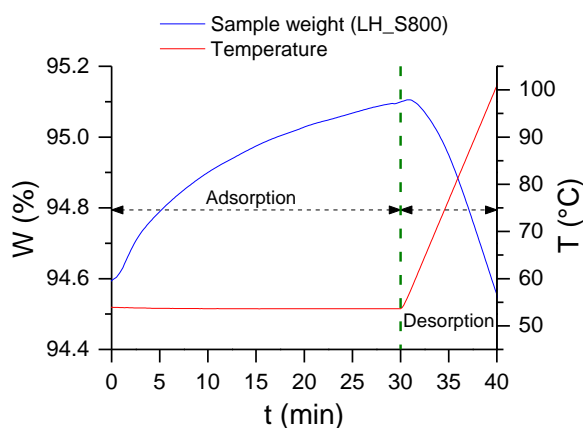


Figure 5-36 1st RTSA cycle for pyrolyzed *Laminaria* (LH_S800)

Furthermore, as shown in Figure 5-37(b), a noticeable capacity loss (ca. 20%) was observed between the first and subsequent capture/regeneration cycles. Interestingly, the same drop in sorption capacity after the first cycle is displayed for the physically-activated wood (OW800PA) in Chapter 4. This

might suggest that the decline of sorption capability was due to the removal of chemical functionalities weakly bonded to the carbon's structure, which apparently were released from the material when heated up to 120 °C for the first time. However, this may also be attributed to the incomplete reconversion of magnesium carbonate into MgO (i.e. formation of intermediates such as $\text{Mg}(\text{OH})_2$), thus leading to a decrease of chemisorption potential. Nevertheless, it is worth noting that the sorbent's capacity stabilized after the first cycle, thus indicating good durability over time.

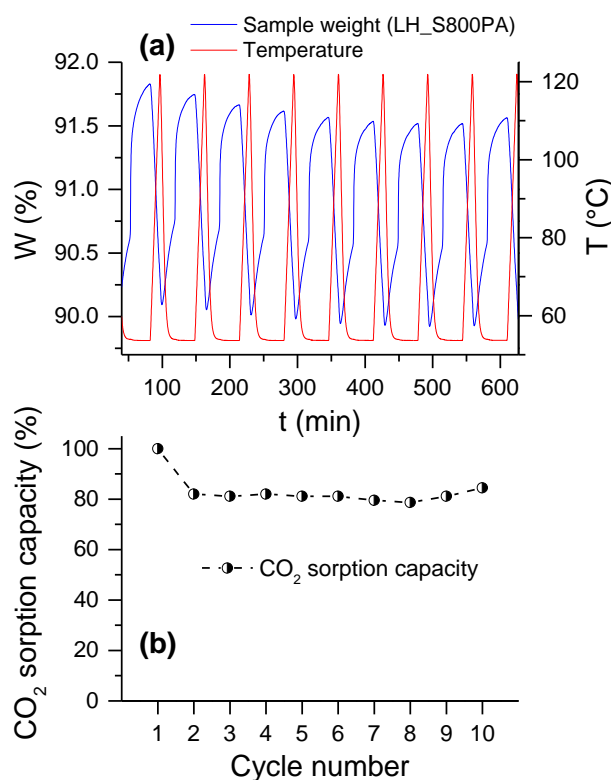


Figure 5-37 (a) Recyclability and (b) sorption capacity over ten RTSA cycles for physically-activated *Laminaria* (LH_S800PA)

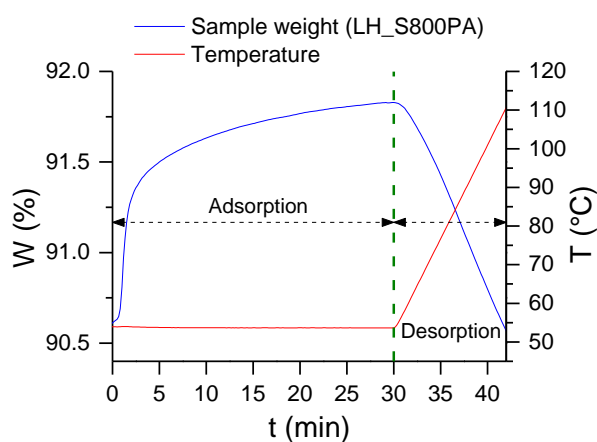


Figure 5-38 1st RTSA cycle for physically-activated *Laminaria* (LH_S800PA)

5.7 Chapter Conclusions

Laminaria hyperborea was found to be a versatile precursor for sustainable synthesis of activated carbons intended for various applications. HTC of this macroalgae resulted in a slightly larger carbonization yield than that obtained after pyrolysis. Both processes showed good repeatability in terms of char production. The type of reactor was found not to significantly affect the product yield upon pyrolysis. Low errors related to HTC water balance measurements were obtained. The structure of *Laminaria hyperborea*-derived hydrochar (LH_S250) was essentially non-porous (except for a small amount of macroporosity), probably because the raw material was not completely devolatilized after the hydrothermal synthesis. Some porosity was measured for the pyrolyzed char (LH_S800) and this contained a far lower amount of volatile compounds. This was likely due to the higher degree of carbonization achieved at higher temperature (800 °C). On the other hand, like oak wood (see Chapter 4), *Laminaria hyperborea*, when poorly carbonized by HTC, exhibited a more dramatic development of texture following activation treatments.

CO₂ activation of *Laminaria hyperborea*-based chars caused a moderate texture development. Final surface areas and total pore volumes were even lower than those obtained after physical activation of the carbonized wood (see Chapter 4). In addition, under optimal conditions, the surface area per unit of burn off obtained for *Laminaria hyperborea*-derived carbons was lower than that obtained after activation of wood-based chars. These results were attributed to the lower carbon purity found in carbonized *Laminaria hyperborea*. This was particularly true when comparing pyrolysis-derived products. Indeed, an extremely high ash content (ca. 60 wt%) was measured for the pyrolyzed macroalgae. After activation with CO₂ inorganic species were mostly retained within the carbon matrix. Accordingly, a more limited development of porosity was obtained in comparison to that caused by the chemical activation.

The optimal temperatures for physical activation were 600 °C and 700 °C for hydrothermally carbonized and pyrolyzed macroalgae, respectively. A dwell time of 30 min was found to be optimal in both cases. However, as already found for the activation of oak wood-based chars, the holding time had a less dramatic influence on the textural parameters of the final carbons compared to the effect of the activation temperature. Overall, the porosity of physically-activated carbons was low, with a predominant contribution from micropores. However, a relatively high proportion of meso and macropores were also present. Interestingly, CO₂ activation led to narrower pore size distribution, with a significant contribution from ultramicropores, especially for the activated hydrochar.

Conversely, KOH activation led to a far more dramatic increase of textural parameters. 750 °C was found to be the optimal KOH-activation temperature for both chars. In addition, the higher the KOH:char ratio, the larger the surface area of the final carbons. However, optimal conditions in terms of surface area maximization corresponded to minimum values of the product yield. It is interesting to note that a lower intensity of activation ($T=550$ °C, KOH:char ratio=1) led to highly microporous materials, featuring mostly narrower micropores. These showed a type I-like isotherm. Conversely, when more severe conditions ($T>550$ °C, KOH:char ratio >1) were applied, pore widening became a significant feature of the process. Consequently, the final carbons displayed a type I/II isotherm, which is usually found for porous materials featuring both micro and mesopores. HCl washing was an essential step for increasing the purity and the porosity of the chemically-ACs, as it removed not only residual potassium compounds, but also other inorganic species (ashes).

Owing to their outstanding texture development, the chemically-activated carbons exhibited fast sorption kinetics and high CO₂ uptakes (up to nearly 60 mg CO₂·g⁻¹) at 35 °C and 1 bar. These results seem to suggest that carbons derived from the KOH activation of *Laminaria hyperborea*-based chars might be promising candidates for pre-combustion capture of CO₂. This was in line with results shown in Chapter 4, leading to the inference that the texture governs CO₂ adsorption at higher partial pressure. However, correlations reported in Appendix 1 suggest that narrow microporosity and surface area might be both contributing to capturing CO₂. Although causing limited enhancement of surface area (from 4 to ca. 300 m²·g⁻¹), physical activation of hydrochar caused a dramatic improvement of the sorption capacity of the unactivated material (from ca. 3 to 40 mg CO₂·g⁻¹). This was mostly attributed to the significant increase of ultramicropore volume. Conversely, *Laminaria hyperborea*-based char (LH_S800) and its physically-activated counterpart (LH_S800PA) exhibited lower uptakes and much slower kinetics, thereby indicating a different sorption behaviour. Their sorption potential appeared to be more dominated by the chemical nature of the materials.

Under post-combustion conditions, the CO₂ sorption capacity of the KOH-activated carbon dramatically decreased. Interestingly, in spite of their undeveloped porous structure, pyrolyzed *Laminaria hyperborea* (LH_S800) and its physically activated counterpart (LH_S800PA) exhibited a far greater sorption potential than that measured for the chemically-activated macroalgae (LH_S800CA). This result was ascribed to the chemisorption contribution afforded by alkali metal-based functionalities. Indeed, alkali metals were detected by EDX within the structure of the char and its CO₂-AC counterpart. In addition to this, crystalline forms of alkali metal-containing compounds (with particular regard to magnesium oxide) were identified by XRD. The alkaline nature of the *Laminaria hyperborea*-derived char and its physically-activated

counterpart was corroborated by the higher number of basic surface functionalities measured through Boehm titrations for these materials compared to those found on LH_S800CA's surface. In contrast, the chemical activation and subsequent acid-washing resulted in removal of inorganic species as was highlighted by proximate, EDX and XRD results. These observations seem to confirm that the higher selectivity at low partial pressure of CO₂ showed by LH_S800 and LH_S800PA was less dependent on textural properties, and more due to the favourable chemistry of these sorbents. In particular, MgO crystals appeared to have played a key role in the selective sorption of CO₂ at lower partial pressure and higher temperature. This speculation is supported by the very similar sorption behaviour observed for pure magnesium oxide and *Laminaria hyperborea*-based sorbents during the post-combustion test. Additionally, a stronger interaction between CO₂ and seaweed-derived sorbents was revealed by the calculated energy of adsorption at 0 °C, following the sequence LH_S800>LH_S800PA>LH_S800CA.

6 Chemical modification of activated carbons: Optimized wet impregnation of amines

6.1 Outline

The present chapter focuses on the chemical modification of activated carbons (ACs). In particular, the wet impregnation of polyethyleneimine (PEI) onto a commercial carbon (AR) was optimized. The optimization entailed assessing the effect of a series of parameters on the CO₂ sorption capacity of the impregnated carbons measured under simulated post-combustion conditions. For each parameter, the optimal value was determined for maximum uptake of CO₂.

Initially, the amount of polymer loaded onto the carbon support was varied between 29 and 50 wt%, while a stirring time of 30 min and methanol as solvent were set as fixed conditions (see section 6.2.1). After this, the optimal loading identified with methanol as solvent were kept as constant conditions in order to determine the optimal value of the stirring time of the PEI/methanol/carbon mixture (see section 6.2.2.1). The duration of the agitation was varied from 0.5 to 8 h. Moreover, the effect of this parameter was also evaluated for loadings other than the optimal value (see section 6.2.2.2). Following this, the optimal values of PEI loading and stirring time were kept unaltered in an attempt to determine the effect of the type of solvent (i.e. methanol or water) used to dissolve the polymer (section 6.2.3). CO₂ uptakes were measured both at 53 °C and at 77 °C in order to determine the effect of the temperature on the sorption behaviour of the PEI-impregnated materials. Results specifically related to the optimization of the aqueous impregnation (i.e. water as solvent) are reported in sections 6.2.3.1 (53 °C) and 6.2.3.2 (77 °C).

Afterwards, starting from the optimal conditions found at 53 °C, the effect of additional factors on the CO₂ sorption capacity of the impregnated carbons was investigated. In particular, the influence of an alternative carbon support (see section 6.2.4) and the effect of a different impregnating agent (see section 6.2.5) were studied. Furthermore, the effect of the addition of hydroxyl group-containing compound (i.e. glycerol) was evaluated (see section 6.2.6).

The carbon prepared under optimized conditions (defined as AR-PEI) was then subjected to a variety of characterizations in order to detect the presence of PEI on its structure (see section 6.3).

Experimental sorption kinetics measured for virgin (AR) and optimally PEI-impregnated carbon (AR-PEI) were fitted to models in section 6.4.

Section 6.5 is concerned with the CO₂ capture performance of the optimal sorbent. First, the optimally PEI-modified sample was compared with the parent carbon and a benchmark sorbent (i.e. zeolite Z-13X (Z13X)), included for comparison purposes (see section 6.5.1). In line with experiments carried out for in-house ACs (see Chapter 4 and 5), materials were first tested at low temperature (35 °C) and high CO₂ partial pressure (1 bar) (see section 6.5.1.1). After this, attention was focused on the simulation of the post-combustion capture behaviour, which is presented in section 6.5.1.2. In addition to this, the cyclic regeneration capacity of the optimally PEI-impregnated carbon under simulated post-combustion conditions is illustrated in section 6.5.2.

Conclusions related to the present chapter are then set out in section 6.6.

6.2 Optimization of the PEI impregnation procedure

6.2.1 Effect of PEI loading (methanol, 53 °C)

Results reported in Table 6-1 refer to the optimization of (i) PEI nominal loading (NL) (29-50 wt%, 0.5 h, methanol), (ii) stirring time (0.5-8 h, optimal nominal PEI loading, methanol) and (iii) solvent type (methanol or water, optimal nominal PEI loading and stirring time) at 53 °C.

For each impregnated sample, the amount of PEI actually loaded onto the carbon was calculated gravimetrically and noted in Table 6-1. The percentage ratio of actual loading to the nominal loading was defined as impregnation efficiency. It is worth noting that the highest efficiency was achieved when using water as solvent. This might indicate that water is a better carrier of the polymer within the pore channels.

Elemental analysis confirmed a distinct increase of the nitrogen content with increasing polymer loading for all impregnated samples. On the other hand, as revealed by the textural parameters of the impregnated samples given in Table 6-2, PEI impregnation caused a dramatic pore blockage. As seen in Figure 6-1(a) and (b), and Figure 6-2(a), the reduction of accessible pore volume is more pronounced at higher loading. It is interesting to note that most of the pore volume reduction is accounted for by micropore blocking. Nevertheless, it is difficult to say whether the polymer actually fills the micropores rather than just blocking them off [116]. However, Figure 6-2(a) also shows that increasing the amount of polymer loaded onto the carbon led to a rise of the N content of the impregnated samples.

Table 6-1 Primary optimization - Impregnation efficiency and Nitrogen content

Sample ID	AL ⁴⁶	Impregnation efficiency ⁴⁷	N ⁴⁸	N, SE ⁴⁹
	wt%	%	wt%	wt%
AR	-	-	0.4	-
AR_PEI_29%_Me_0.5h	19.8	68.1	4.2	0.2
AR_PEI_38%_Me_0.5h	25.6	67.4	4.6	0.2
AR_PEI_44%_Me_0.5h	29.6	67.2	5.5	0.5
AR_PEI_50%_Me_0.5h	32.7	65.4	7.1	0.2
AR_PEI_44%_Me_2h	30.3	68.8	7.1	0.1
AR_PEI_44%_Me_4h	28.5	64.9	6.6	0.2
AR_PEI_44%_Me_6h	30.9	70.1	7.4	0.3
AR_PEI_44%_Me_8h	31.0	70.5	7.7	0.1
AR_PEI_44%_W_8h	34.3	78	8.2	0.1
Z13X	-	-	0	-

As suggested by Figure 6-2(b), the optimal loading (nominal loading of 44 wt%, corresponding to an actual loading of ca. 29.6 wt% as given in Table 6-1) in terms of maximized CO₂ uptake (see also Table 6-3) seems to be due to an ideal compromise between the N functionalities incorporated and the pore volume reduction. This optimal loading was determined based on a stirring time of 0.5 h with methanol as solvent. Loadings lower than the optimal value gave a lower sorption capacity, probably due to the lower concentration of basic N-containing groups. Conversely, the drop in the CO₂ uptakes associated with higher loadings might be due to the limited diffusion of carbon dioxide through the PEI film [120]. This agrees with the slower kinetic exhibited by AR_PEI_50%_Me_0.5h (see Figure 6-3).

⁴⁶ Actual loading calculated by mass balance

⁴⁷ Expressed as percentage of actual loading divided by nominal loading

⁴⁸ Measured by CHNS elemental analysis in triplicate; data represent average values.

⁴⁹ Standard error (n=3)

Table 6-2 Primary optimization - Textural parameters

Sample ID	S_{BET}^{50}	V_{tot}^{51}	V_{mi}^{52}	$V_{\text{me+ma}}^{53}$
	$\text{m}^2 \cdot \text{g}^{-1}$	$\text{cm}^3 \cdot \text{g}^{-1}$	$\text{cm}^3 \cdot \text{g}^{-1}$	$\text{cm}^3 \cdot \text{g}^{-1}$
AR	1531	0.691	0.569	0.122
AR_PEI_29%_Me_0.5h	1336	0.614	0.49	0.124
AR_PEI_38%_Me_0.5h	1040	0.475	0.389	0.086
AR_PEI_44%_Me_0.5h	966	0.456	0.359	0.097
AR_PEI_50%_Me_0.5h	793	0.392	0.293	0.099
AR_PEI_44%_Me_2h	783	0.364	0.295	0.07
AR_PEI_44%_Me_4h	729	0.352	0.275	0.077
AR_PEI_44%_Me_6h	677	0.289	0.261	0.028
AR_PEI_44%_Me_8h	610	0.273	0.234	0.039
AR_PEI_44%_W_8h	355	0.179	0.136	0.043
Z13X	521	0.398	0.207	0.191

⁵⁰ Surface area calculated by applying Brunauer–Emmett–Teller (BET) method to N₂ adsorption data

⁵¹ Total pore volume calculated by applying Gurvitsch's rule at $P/P_0=0.99$

⁵² Microporous volume calculated by applying Dubinin-Radushkevich (DR) model to N₂ adsorption data

⁵³ *Sum of mesoporous and macroporous volume, calculated by difference ($V_{\text{tot}} - V_{\text{mi}}$)*

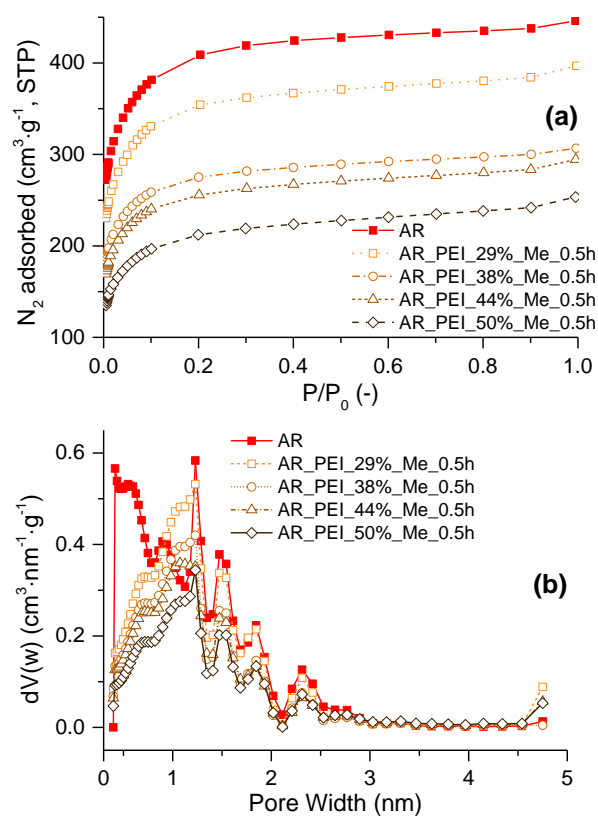


Figure 6-1 Effect of PEI loading: (a) N_2 Adsorption Isotherms and (b) non-local density functional theory (NLDFT) Pore size distributions (PSDs) by volume. A stirring time of 0.5 h and methanol solvent were used to impregnate these samples

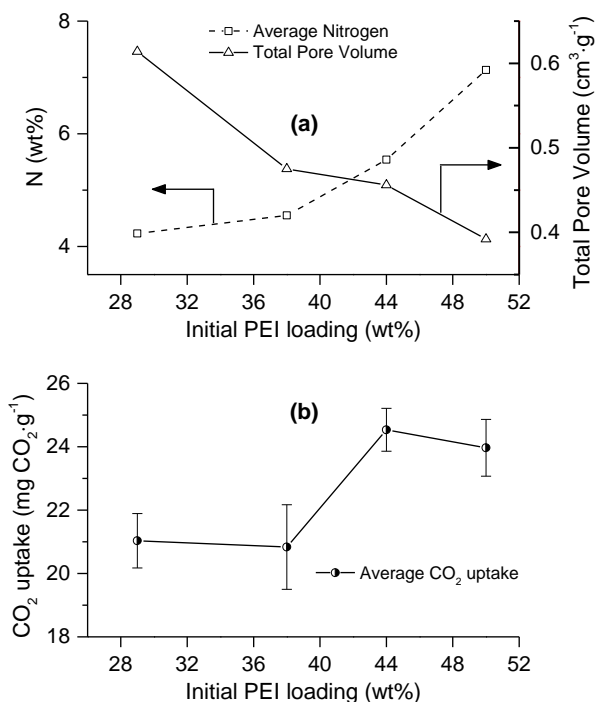


Figure 6-2 Effect of PEI loading: (a) N content and pore volume reduction, and (b) CO₂ uptakes at 53 °C and 0.15 bar (total pressure of 1 bar). A stirring time of 0.5 h and methanol solvent were used to impregnate these samples. Error bars represent standard error (n=3).

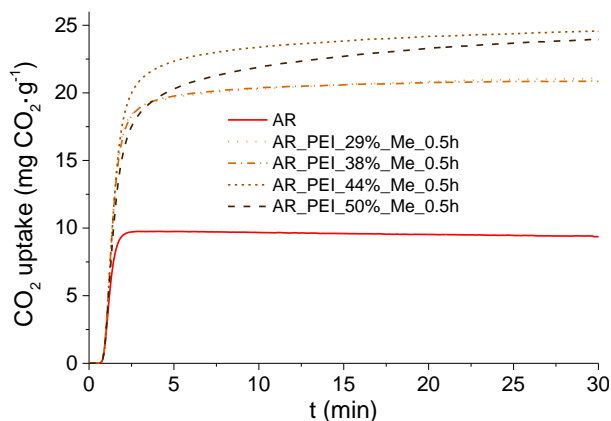


Figure 6-3 Effect of PEI loading: CO₂ adsorption kinetics at 53 °C and 0.15 bar (total pressure of 1 bar). A stirring time of 0.5 h and methanol solvent were used to impregnate these samples.

Table 6-3 Primary optimization - CO₂ uptakes at 53 or 77 °C and 0.15 bar (total pressure of 1 bar)

Sample ID	CO ₂ uptakes ⁵⁴			Capacity loss ⁵⁵
	53 °C	53 °C, SE ⁵⁶	77 °C	%
AR	9.4	0.8	6.8	18
AR_PEI_29%_Me_0.5h	21.0	0.9	-	-
AR_PEI_38%_Me_0.5h	20.8	1.3	-	-
AR_PEI_44%_Me_0.5h	24.5	0.7	-	-
AR_PEI_50%_Me_0.5h	24.0	0.9	-	-
AR_PEI_44%_Me_2h	23.9	1.0	-	-
AR_PEI_44%_Me_4h	25.0	1.1	-	-
AR_PEI_44%_Me_6h	29.2	2.0	-	-
AR_PEI_44%_Me_8h	33.4	0.4	21.8	35
AR_PEI_44%_W_8h	23.8	-	21.8	8
Z13X	22.7	0.6	-	-

6.2.2 Effect of stirring time (methanol, 53 °C)

6.2.2.1 Optimal PEI loading

The effect of the stirring time of the PEI/solvent/carbon blend on product characteristics was assessed based upon the optimal value of 44 wt% (on nominal basis) PEI loading (from methanol solution) found in section 6.2.1.

As plotted in Figure 6-4(a), when increasing the agitation time from 0.5 h to 2 h, a slight increase of the nitrogen content of the PEI-impregnated carbon was measured. This coincides with the significant reduction of the total pore volume observed between stirring time values of 0.5 and 2 h, and might suggest that the lowest duration (30 min) was not sufficient for an efficient polymer loading. In contrast, as indicated by Figure 6-4(a) and Table 6-1, for stirring durations longer than 2 h and for the same (optimal) NL, the amount of polymer

⁵⁴ Uptakes measured as mg of CO₂ per g of sorbent in triplicate. Data represent average values.

⁵⁵ Calculated as difference between the sorption capacity at 77 and 53 °C, and expressed as a percentage of the sorption capacity at 53 °C

⁵⁶ Standard error (n=3)

loaded onto the carbon support did not significantly change. On other hand, although the available porosity of the carbon continuously declined with increasing agitation duration (see Figure 6-4(a)), the CO₂ capacity of the sorbent increased (Figure 6-4(b)). This could be explained by the fact that longer stirring time might have improved the dispersion of PEI through the porous network of the support, thus enhancing the diffusion of CO₂ and the access to the amino groups.

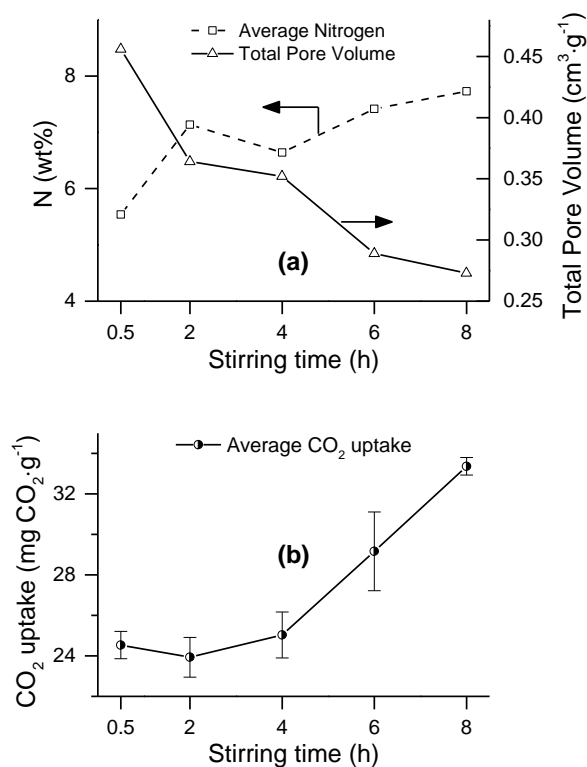


Figure 6-4 Effect of stirring time: (a) N content and pore volume reduction, and (b) CO₂ uptakes at 53 °C and 0.15 bar (total pressure of 1 bar). Optimal nominal PEI loading (44 wt%) and methanol solvent were used to impregnate these samples. Error bars represent standard error (n=3).

Accordingly, a longer agitation of the slurry seems to suggest enhanced PEI penetration into the carbon porosity. In turn, this optimized utilization of the pores led to an increase of CO₂ uptakes as seen in Figure 6-4(b). In particular, although a slight drop in CO₂ uptake between stirring time values of 0.5 and 2 h occurred, the carbon dioxide capacity progressively increased for stirring times longer than 2 h. The initial decrease of CO₂ uptake capability might be attributed to a higher amount of polymer loaded when increasing stirring time from 0.5 to 2 h (see increase of N in Figure 6-4(a)). However, it is possible that, for lower stirring time (e.g. 2 h), the polymer might have been deposited in localized spots on the solid support, thereby limiting the diffusion of CO₂ throughout the porous matrix but without compensating factor of well-distributed PEI to enhance CO₂ uptake. This agrees with the more pronounced pore

blocking experienced by AR_PEI_44%_Me_2h (see Figure 6-4(a)). In addition to this, as depicted in Figure 6-5, AR_PEI_44%_Me_2h exhibited a slower sorption rate than that of AR_PEI_44%_Me_0.5h, thus corroborating the decrease of CO₂ diffusivity when increasing stirring time from 0.5 to 2 h. Conversely, for higher stirring times (>2 h), it is speculated that a more efficient distribution of PEI through the porous network, with consequently more amino groups accessible to CO₂, might outweigh the pore blocking and diffusional limitations.

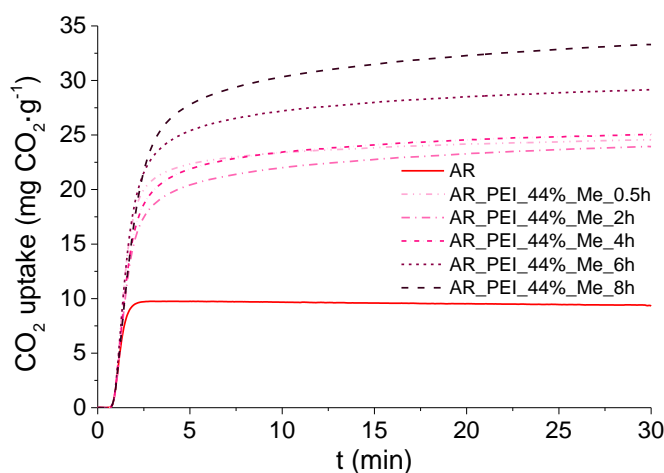


Figure 6-5 Effect of stirring time: CO₂ adsorption kinetics at 53 °C and 0.15 bar (total pressure of 1 bar). Optimal nominal PEI loading (44 wt%) and methanol solvent samples were used to prepare these samples.

6.2.2.2 Non-optimal PEI loadings

Results presented in this section further evidence the beneficial effect of a longer agitation on the CO₂ sorption capacity of the PEI-impregnated samples. Uptake of CO₂ increased with increasing stirring time even when considering polymer loadings other than the optimal one. In particular, for a nominal loading of 38 wt%, a dramatic increase of CO₂ sorption capacity was measured when agitation time was increased from 0.5 h to 2 h (see Figure 6-6(b)). A more moderate rise of the CO₂ uptake was recorded between 2 and 4 h, whereas sorption capability decreased when agitation was carried out for 6 h. This was probably due to the higher amount of polymer actually loaded when stirring time was 6 h (also see higher values of actual loading and N content for AR_PEI_50%_Me_6h as given in Table 6-4), which might have blocked the mobility of CO₂ through the porous support. N and actual loading data correlated with the dramatic reduction of pore volume when increasing stirring time from 4 to 6 h (see Figure 6-6(a) and Table 6-4). However, note that nitrogen content and PEI actual loading figures do not always follow the same trend likely because of errors in the experimental measurements. Nonetheless, the CO₂ sorption capacity appeared to increase again when increasing stirring time from 6 to 8 h. This was likely due to a better dispersion achieved at the

longest stirring time studied, which partly outweighed the pore blockage and therefore the diffusional limitations.

An improvement of the CO₂ sorption capacity with increasing stirring time was also observed for the largest nominal loading studied (i.e. 50 wt%). In particular, a steep rise of the sorbent's CO₂ uptake occurred when increasing the stirring time from 2 h, reaching a maximum when the PEI/methanol/carbon mixture was stirred for 4 h (see Figure 6-7(b)). However, unlike for NLs of 38 and 44 wt%, where CO₂ uptake maximum was achieved for a stirring time of 8 h, when using a higher NL (50 wt%) the CO₂ capacity peak was shifted to a shorter agitation duration (e.g. 4 h). This was attributed to the slightly larger amount of polymer actually loaded onto the carbon when using a NL of 50 wt% (see Table 6-4) in comparison to those recorded for lower NLs and for stirring times longer than 4 h (see Table 6-4 and Table 6-1). Accordingly, the extra loading of polymer appeared to be responsible for a higher extent of pore blockage and lower CO₂ uptakes (see Table 6-5 and Figure 6-7(a)). Nevertheless, even in this case, diffusional limitations seem to be partly compensated by a better distribution of the polymer when further increasing agitation duration from 6 to 8 h.

As seen by the CO₂ sorption kinetics presented in Figure 6-8, samples impregnated for longer times (darker curves) generally prevailed over those prepared through shorter agitations (lighter curves). In addition to this, as indicated by results given in Table 6-3 and Table 6-6, when using a nominal PEI loading of 50 wt% and stirring times longer than 0.5 h, higher CO₂ uptakes were achieved in comparison to those measured for a nominal PEI loading of 38 wt%. On the other hand, for the same stirring times, CO₂ sorption kinetics recorded for samples impregnated with a nominal loading of 50 wt% were generally slower than those measured for materials obtained using a PEI nominal loading of 38 wt%. The lower sorption speed could be attributed to the larger amount of PEI introduced within the porous structure of the sorbents (see actual loading of 35 wt% for AR_PEI_50%_Me_6h vs 26.4 wt% for AR_PEI_38%_Me_6h, as noted in Table 6-4). This was consistent with the more remarkable pore blocking observed when using a nominal loading of 50 wt% (see comparison between Figure 6-6(a) and Figure 6-7(a)).

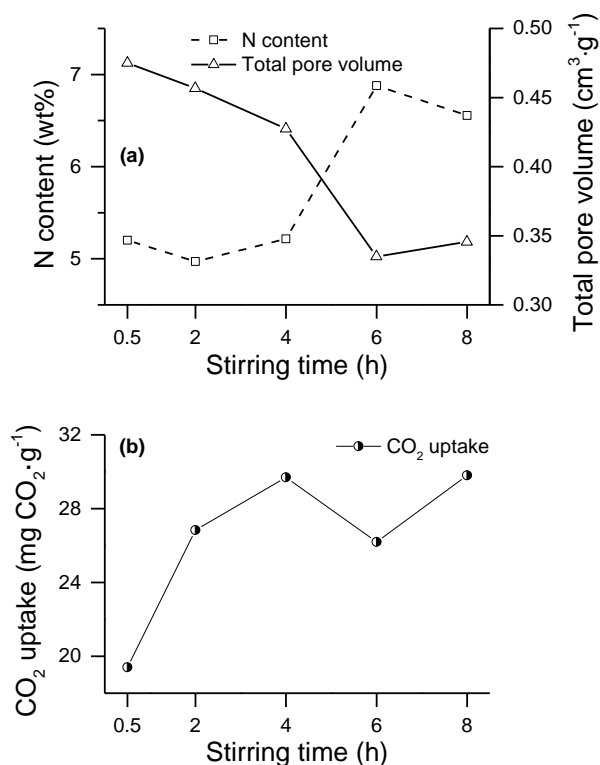


Figure 6-6 Effect of stirring time: (a) N content and pore volume reduction, and (b) CO₂ uptakes at 53 °C and 0.15 bar (total pressure of 1 bar). Nominal PEI loading of 38 wt% and methanol solvent were used to impregnate these samples.

Table 6-4 Effect of stirring time for non-optimal PEI loadings - Impregnation efficiency and Nitrogen content

Sample ID	AL	Impregnation efficiency	N
	wt%	%	wt%
AR_PEI_38%_Me_2h	23.9	62.9	5.0
AR_PEI_38%_Me_4h	23.3	61.4	5.2
AR_PEI_38%_Me_6h	26.4	69.4	6.9
AR_PEI_38%_Me_8h	26.3	69.1	6.6
AR_PEI_50%_Me_2h	32.6	65.2	7.1
AR_PEI_50%_Me_4h	31.6	64.0	7.1
AR_PEI_50%_Me_6h	35.0	70.0	7.3
AR_PEI_50%_Me_8h	32.6	65.2	6.9

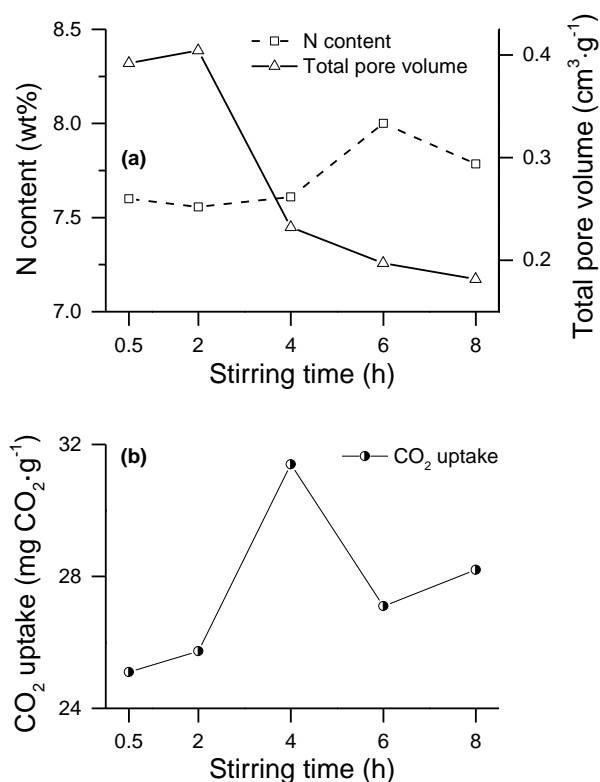


Figure 6-7 Effect of stirring time: (a) N content and pore volume reduction, and (b) CO₂ uptakes at 53 °C and 0.15 bar (total pressure of 1 bar). Nominal PEI loading of 50 wt% and methanol solvent were used to impregnate these samples.

Table 6-5 Effect of stirring time for non-optimal PEI loadings - Textural parameters

Sample ID	S _{BET}	V _{tot}	V _{mi}	V _{me+ma}
	m ² ·g ⁻¹	cm ³ ·g ⁻¹	cm ³ ·g ⁻¹	cm ³ ·g ⁻¹
AR_PEI_38%_Me_2h	983	0.457	0.369	0.088
AR_PEI_38%_Me_4h	876	0.427	0.322	0.105
AR_PEI_38%_Me_6h	720	0.335	0.270	0.065
AR_PEI_38%_Me_8h	684	0.346	0.254	0.092
AR_PEI_50%_Me_2h	879	0.404	0.329	0.075
AR_PEI_50%_Me_4h	492	0.232	0.184	0.048
AR_PEI_50%_Me_6h	411	0.197	0.159	0.038
AR_PEI_50%_Me_8h	412	0.182	0.159	0.023

Table 6-6 Effect of stirring time for non-optimal loadings - CO₂ uptakes at 0.15 bar (total pressure of 1 bar) and 53 °C

Sample ID	CO ₂ uptakes	
	53 °C	77 °C
AR_PEI_38%_Me_2h	26.8	-
AR_PEI_38%_Me_4h	29.7	-
AR_PEI_38%_Me_6h	26.2	-
AR_PEI_38%_Me_8h	29.8	-
AR_PEI_50%_Me_2h	25.7	-
AR_PEI_50%_Me_4h	31.4	22.5
AR_PEI_50%_Me_6h	27.1	-
AR_PEI_50%_Me_8h	28.2	-

Overall, for both non-optimal nominal values of PEI loading investigated, stirring times longer than 30 min led to higher CO₂ uptakes. This seemed to indicate that an extended duration of impregnation allowed a more efficient distribution of the polymer onto the carbon support, which outweighed the negative effect of pore blockage and slow gas diffusion, thereby maximizing the final CO₂ sorption capacity of the PEI-loaded carbons (see also Table 6-6). However, in accordance with results showed in section 6.2.1, it seems that the CO₂ uptake maximum is reached for an optimal compromise between utilized porosity and amount of N incorporated.

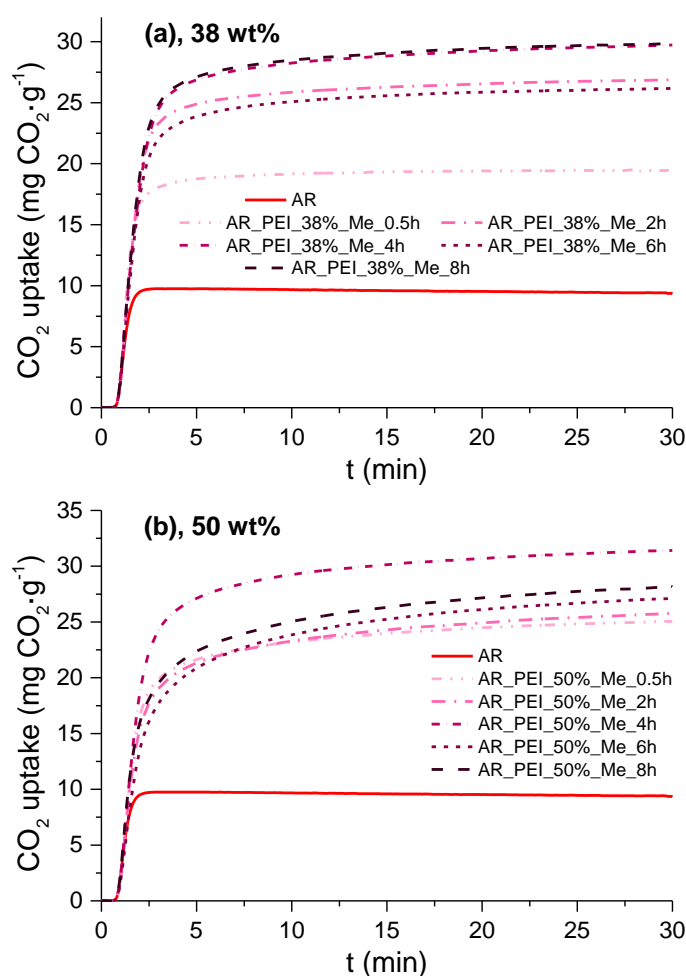


Figure 6-8 Effect of stirring time: CO₂ adsorption kinetics at 53 °C and 0.15 bar (total pressure of 1 bar). Nominal PEI loading of (a) 38 wt% or (b) 50 wt% and methanol solvent were used to prepare these samples

6.2.3 Effect of solvent type and sorption temperature

Figure 6-9 shows the influence of the kind of solvent employed to dissolve the polymer during the impregnation. Values of nominal PEI loading and stirring time of the polymer/solvent/carbon blend were chosen according to the optimal values for maximized CO₂ uptake (i.e. 44 wt% and 8h) determined above. The CO₂ sorption kinetics were measured at two different temperatures.

At the lower temperature (dashed lines) in particular, the PEI-loaded carbon impregnated using methanol (AR_PEI_44%_Me_8h_53 °C) achieved much larger uptakes than when using water (AR_PEI_44%_W_8h_53 °C). The latter sample showed somewhat slower kinetics, which might be due diffusional limitations of the carbon dioxide molecule through the PEI gel [120, 123]. The delayed CO₂ sorption agreed with the larger values of actual loading and N contents found for AR_PEI_44%_W_8h (see Table 6-1). This was further corroborated by the higher extent of pore blockage experienced by this sample as given in Table 6-2. Interestingly, CO₂ uptakes almost as large as those

achieved by AR_PEI_44%_Me_8h were attained by using water as solvent but with lower polymer loading and shorter stirring time (see AR_PEI_38%_W_2h in Table 6-9).

As expected, when measuring the CO₂ uptakes at higher temperature (i.e. 77 °C), kinetics became faster for both samples (solid lines). In addition to this, it is remarkable to observe that the CO₂ sorption curves tend to converge at saturation. It is worth mentioning that, if adsorption stage was to be extended over long duration, sorption curves measured at lower temperature (53 °C) might be also converge. Moreover, as shown by Figure 6-9, a more dramatic drop in capacity (ca. 35%, see Table 6-3) was experienced by AR_PEI_44%_Me_8h, compared to AR_PEI_44%_W_8h. This suggested that the CO₂ uptake process onto AR_PEI_44%_Me_8h was thermodynamically-controlled [214]. Conversely, the PEI-modified carbon impregnated using water (i.e. AR_PEI_44%_W_8h) exhibited a lower reduction of sorption capacity at higher temperature. This seemed to indicate a kinetic, diffusion controlled process [123] for the uptake of CO₂ onto this sample. It appears that the larger number of amino groups loaded onto the carbon when using water was not fully accessible at lower temperature (53 °C) because of resistance to diffusion of CO₂ through the PEI gel, which was attenuated at higher temperature (77 °C). However, CO₂ sorption capability of PEI-impregnated carbons generally decreased at higher temperature. This might suggest a predominant role is played by thermodynamic (sorption) effects, which, unlike diffusion, become unfavourable with increasing temperature. This result was in contrast with those reported by previous works, in which 75 °C was found to be optimal in terms of maximization of CO₂ uptakes [120, 223-225]. However, as suggested by Wang *et al.* [226], at temperatures higher than 75 °C desorption of CO₂ may be occurring, thus counteracting the uptake process and resulting in a net decrease of sorption capacity.

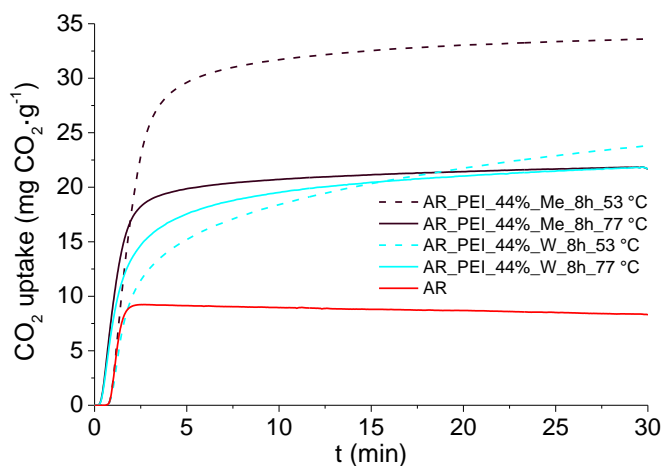


Figure 6-9 Effect of solvent type and sorption temperature: CO₂ adsorption kinetics at 0.15 bar (total pressure of 1 bar) for 53 °C and 77 °C; samples were prepared using optimal values of nominal PEI loading (44 wt%) and stirring time (8 h)

Following these results, optimization of aqueous impregnation was studied and is presented below both at 53 °C (see section 6.2.3.1) and at 77 °C (see section 6.2.3.2).

6.2.3.1 Optimization of aqueous impregnation at 53 °C

6.2.3.1.1 Effect of PEI loading (water, 53 °C)

For a common value of stirring time (i.e. the optimal value of 8h determined for methanol solvent in section 6.2.2.1), Figure 6-10(a) shows that the N content of the PEI-impregnated carbons increased with increasing amount of polymer loaded onto the porous support. Consequently, this led to a progressive decrease of porosity due to pore blocking.

Interestingly, as given in Table 6-7, higher impregnation efficiency (up to 81% for AR_PEI_38%_W_8h) was achieved when water was used as solvent. This seems to suggest the more environmentally sound aqueous impregnation as being a more efficient technique for loading the polymer onto the carbon support. Consequently, as seen in Figure 6-10(b), the optimal nominal loading value (i.e. 38 wt%) was lower than that ascertained when using methanol (i.e. 44 wt%, see Figure 6-2(b)).

Table 6-7 Optimization of aqueous impregnation - Impregnation efficiency and Nitrogen content

Sample ID	AL	Impregnation efficiency	N
	wt%	%	wt%
AR_PEI_38%_W_0.5h	29.1	76.4	5.5
AR_PEI_44%_W_0.5h	34.5	78.4	6.8
AR_PEI_50%_W_0.5h	38.0	76.0	7.5
AR_PEI_38%_W_2h	28.6	75.2	6.7
AR_PEI_38%_W_4h	29.6	77.8	6.9
AR_PEI_38%_W_6h	32.0	84.3	7.9
AR_PEI_38%_W_8h	30.8	81.1	7.3
AR_PEI_50%_W_2h	40.5	80.9	8.1
AR_PEI_50%_W_4h	38.8	77.7	7.9
AR_PEI_50%_W_6h	39.9	79.7	8.1
AR_PEI_50%_W_8h	38.1	76.2	7.7

As shown in Figure 6-10(b), the minimum CO₂ uptake was attained for a nominal PEI addition of 44 wt%. Moreover, a further increase of nominal PEI loading (up to 50 wt%) led to a delayed sorption kinetic (see AR_PEI_50%_W_8h's sorption curve in Figure 6-11). This was ascribed to increased diffusional limitations of CO₂ through the polymer bulk due to the more pronounced pore blockage experienced by AR_PEI_50%_W_8h (see Figure 6-10(b) and Table 6-8). On the other hand, in spite of the lower uptake rate at the beginning of adsorption step, this sample attained a slightly larger uptake at saturation than that measured for AR_PEI_44%_W_8h (see cross over at ca. 7 min in Figure 6-11). This was probably due to the higher amount of effective N functionalities incorporated onto AR_PEI_50%_W_8h's structure, which balanced the lack of CO₂ diffusion within pore channels.

Table 6-8 Optimization of aqueous impregnation - Textural parameters

Sample ID	S_{BET}	V_{tot}	V_{mi}	$V_{\text{me+ma}}$
	$\text{m}^2\cdot\text{g}^{-1}$	$\text{cm}^3\cdot\text{g}^{-1}$	$\text{cm}^3\cdot\text{g}^{-1}$	$\text{cm}^3\cdot\text{g}^{-1}$
AR_PEI_38%_W_0.5h	886	0.438	0.330	0.108
AR_PEI_44%_W_0.5h	859	0.404	0.322	0.082
AR_PEI_50%_W_0.5h	722	0.396	0.256	0.140
AR_PEI_38%_W_2h	734	0.381	0.277	0.104
AR_PEI_38%_W_4h	640	0.303	0.236	0.067
AR_PEI_38%_W_6h	460	0.224	0.173	0.051
AR_PEI_38%_W_8h	628	0.306	0.237	0.069
AR_PEI_50%_W_2h	292	0.159	0.111	0.048
AR_PEI_50%_W_4h	366	0.221	0.137	0.084
AR_PEI_50%_W_6h	279	0.131	0.110	0.021
AR_PEI_50%_W_8h	183	0.110	0.071	0.039

Table 6-9 Optimization of aqueous impregnation - CO₂ uptakes at 53 or 77 °C and 0.15 bar (total pressure of 1 bar)

Sample ID	CO ₂ uptakes		Capacity loss
	53 °C	77 °C	%
AR_PEI_38%_W_0.5h	31.5	-	-
AR_PEI_44%_W_0.5h	28.5	-	-
AR_PEI_50%_W_0.5h	30.2	18.3	39
AR_PEI_38%_W_2h	32.1	-	-
AR_PEI_38%_W_4h	21.4	-	-
AR_PEI_38%_W_6h	27.0	-	-
AR_PEI_38%_W_8h	28.3	17.2	39
AR_PEI_50%_W_2h	-	27.1	-
AR_PEI_50%_W_4h	25.8	27.3	-6
AR_PEI_50%_W_6h	-	20.8	-
AR_PEI_50%_W_8h	25.9	22.0	15

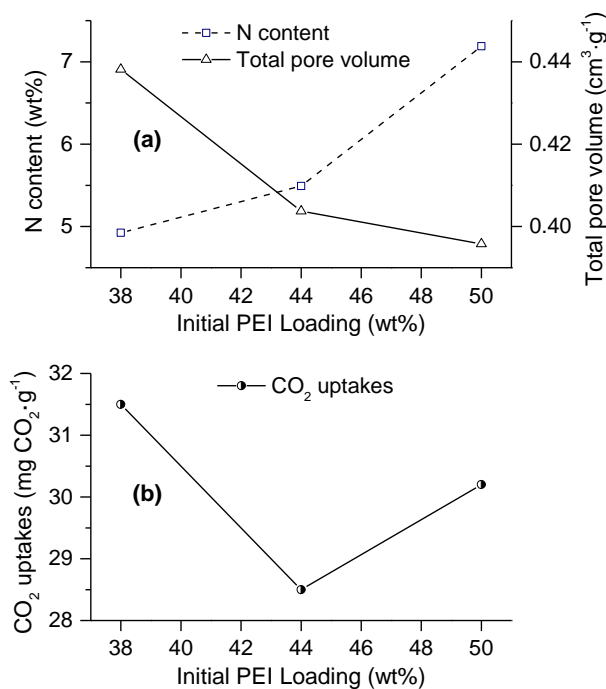


Figure 6-10 Effect of PEI loading: (a) N content and pore volume reduction, and (b) CO₂ uptakes at 53 °C and 0.15 bar (total pressure of 1 bar). A stirring time of 0.5 h and water solvent were used to impregnate these samples.

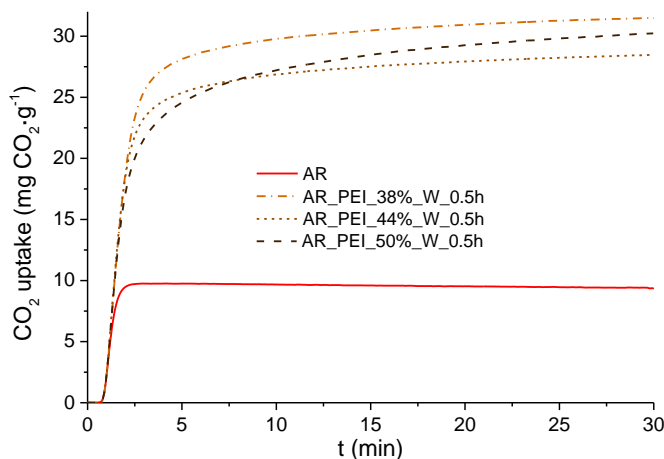


Figure 6-11 Effect of PEI loading: CO₂ adsorption kinetics at 53 °C and 0.15 bar (total pressure of 1 bar). A stirring time of 0.5 h and water solvent were used to impregnate these samples.

6.2.3.1.2 Effect of stirring time (water, 53 °C)

As observed in Figure 6-12(a), for the same nominal loading of PEI (optimal value determined in section 6.2.3.1.1 (i.e. 38 wt%)), a longer stirring time (up to 6h) loaded a slightly larger amount of polymer onto the porous support. In particular, the highest amount of PEI was loaded onto

AR_PEI_38%_W_6h (up to 32 wt%, see Table 6-7). This resulted in the lowest pore volume attained by this sample (see Table 6-8 and Figure 6-12(b)).

It seemed that lower stirring times (e.g. 0.5 h) might have been not sufficient to disperse the polymer through the pores, which might thus have been retained in the solvent to a higher extent. This has already been observed when studying the effect of the stirring time on the N content of samples impregnated using methanol as solvent (see Figure 6-4, Figure 6-6, and Figure 6-7).

On the other hand, excessive loadings of polymer appear to hinder the diffusion of CO₂ through the pore channels when measuring sorption at 53 °C. This is shown by the slower kinetics (see Figure 6-13) exhibited by samples impregnated for durations longer than 2 h. Indeed, as shown in Figure 6-12(b), the highest CO₂ uptake was achieved when agitation was stopped after 2 h. In contrast, the sorption capacity significantly decreased when increasing stirring time from 2 to 4 h, where a minimum was attained. Nevertheless, CO₂ uptakes then exhibited an increasing trend for stirring times between 4-8 h. Apparently, prolonged agitation might have caused a more efficient dispersion of the larger amount of polymer loaded, thus outweighing the adverse impact of pore blockage. This was further corroborated by the larger reduction of pore volume exhibited for a stirring time of 6h (see Figure 6-12(a) and Table 6-8).

It is worth pointing out that the optimization of aqueous impregnation conducted at 53 °C gave rise to CO₂ uptakes (32.1 mg CO₂·g⁻¹, see Table 6-9) nearly as large as the optimal value (33.6 mg CO₂·g⁻¹ see Table 6-3) achieved when solvent was methanol. On the other hand, this was accomplished using lower polymer loading (38 wt%) and shorter stirring time (2 h) with a “greener” solvent. Hence, this would represent a more environmentally friendly option, as it would entail using no methanol and a lower amount of amines. In addition to that, this solution would allow faster preparation of the CO₂ sorbents.

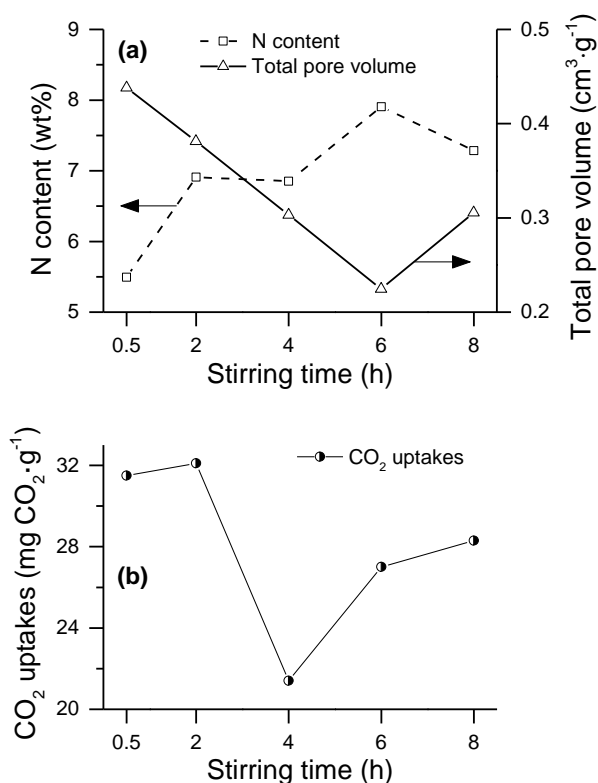


Figure 6-12 Effect of stirring time: (a) N content and pore volume reduction, and (b) CO_2 uptakes at 53 °C and 0.15 bar (total pressure of 1 bar). Optimal nominal PEI loading (38 wt%) and water as solvent were used to prepare the samples.

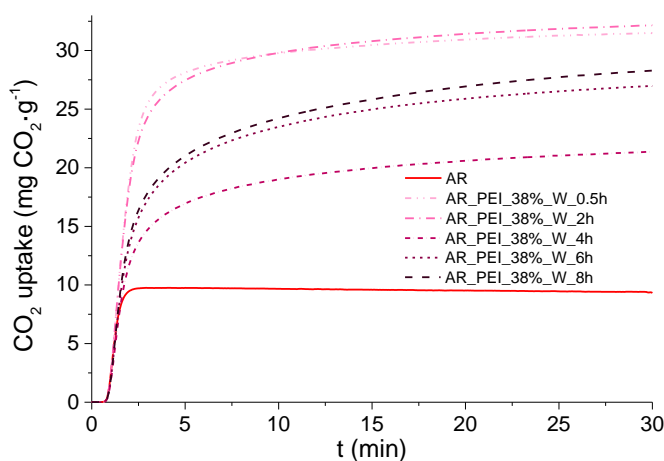


Figure 6-13 Effect of stirring time: CO_2 adsorption kinetics at 53 °C and 0.15 bar (total pressure of 1 bar); samples were prepared using an optimal value of nominal PEI loading (38 wt%) and water as solvent.

6.2.3.2 Optimization of aqueous impregnation at 77 °C

In section 6.2.3, regardless of the solvent, the CO₂ sorption capacity of PEI-impregnated carbons declined as the sorption temperature was raised from 53 to 77 °C. Nonetheless, it is also evident that, at 77 °C and for the same conditions of PEI loading and stirring time, the aqueous impregnation results in as large CO₂ uptakes as those achieved by using methanol (see Figure 6-9). Therefore, this section aims to investigate whether the more environmentally friendly aqueous impregnation could be further optimized in terms of CO₂ sorption capacity measured at increased temperature (i.e. 77 °C).

6.2.3.2.1 Effect of PEI loading (water, 77 °C)

As shown by Figure 6-14(a), the nitrogen content of the PEI-coated carbons increased with increasing amount of polymer loaded onto the porous substrate. By contrast, the pore volume decreased with increasing PEI loading. This was in line with results previously shown (see Figure 6-2(a) and Figure 6-10(a)).

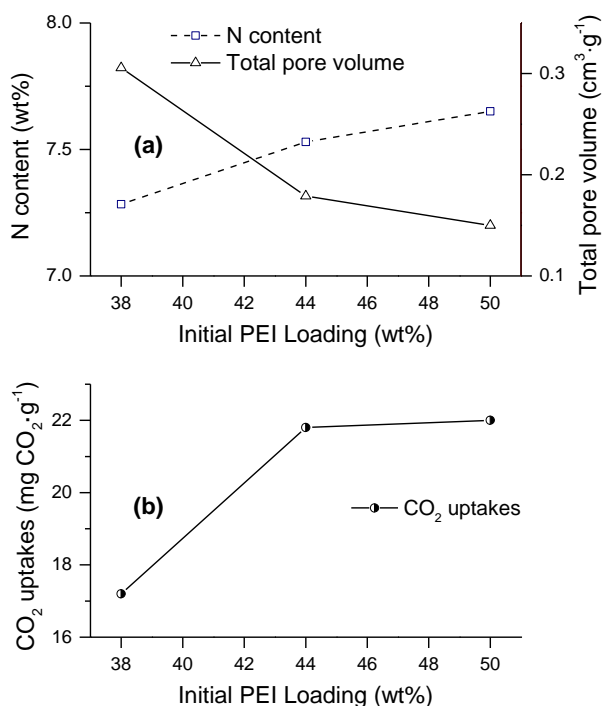


Figure 6-14 Effect of PEI loading: (a) N content and pore volume reduction, and (b) CO₂ uptakes at 77 °C and 0.15 bar (total pressure of 1 bar). A stirring time of 8 h and water as solvent were used to impregnate these samples.

Figure 6-14(b) shows that the highest CO₂ uptake measured at 77 °C was achieved when the nominal PEI loading was 50 wt%. Interestingly, the optimal value of nominal PEI loading determined at 77 °C was larger than that

found at 53 °C when using water (i.e. 38 wt%, see section 6.2.3.1.1) or methanol (i.e. 44 wt%, see section 6.2.1) as solvent. This suggests a mutual relation between PEI loading and sorption temperature, and is consistent with observations reported by Wang *et al.* [222]. This behaviour was attributed to the effect of a higher temperature condition, which apparently facilitated the diffusion of CO₂ through the polymer film. Consequently, more amines become available for CO₂ sorption, thereby resulting in increasing CO₂ uptakes with increasing amount of polymer loaded onto the carbon.

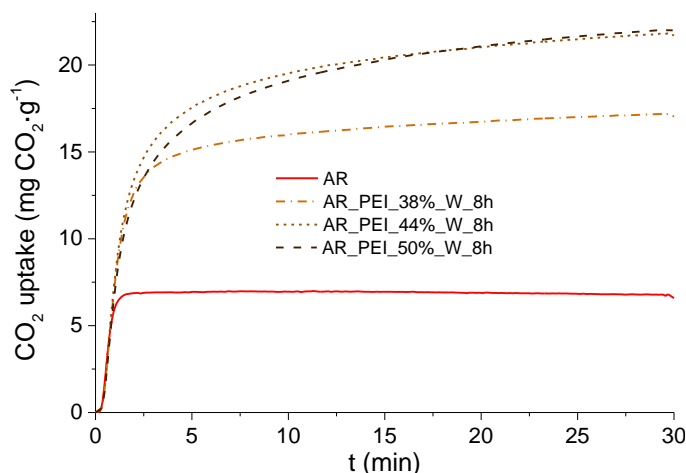


Figure 6-15 Effect of PEI loading: CO₂ adsorption kinetics at 77 °C and 0.15 bar (total pressure of 1 bar). A stirring time of 8 h and water solvent were used to impregnate these samples.

On the other hand, Figure 6-15 showed very slow sorption kinetics for AR_PEI_50%_W_8h. This was evidently due to the larger amount of polymer loaded onto this sample (see values of actual PEI loading in Table 6-7) compared to that coated onto the porous structure of AR_PEI_38%_W_8h and AR_PEI_44%_W_8h (see values of actual PEI loading in Table 6-1 and Table 6-7). The sorption behaviour of highly loaded materials is typical of a kinetically-diffusion controlled process, wherein access of CO₂ to the amino groups of the polymer is delayed [120].

6.2.3.2.2 Effect of stirring time (water, 77 °C)

As illustrated by Figure 6-16(a), for the same value of nominal PEI loading (optimal value of 50 wt% as determined in section 6.2.3.2.1), a noticeably higher amount of N was incorporated onto the carbon substrate when carrying out agitation for stirring time values between 2 and 6 h. This trend generally reflected the actual loading data noted in Table 6-7. On the other hand, total porosity exhibited a general decreasing trend with increasing stirring time.

A significant improvement of CO₂ sorption capacity was observed when increasing the stirring time from 0.5 to 2 h (see Figure 6-16(b)). This could be ascribed to the beneficial effect of a longer mixing step, which not only allowed the loading of more N groups but might have also ensured a more efficient utilization of the porosity of the carbon support. CO₂ uptakes exhibited a slight increase when impregnation duration was further prolonged from 2 to 4 h, where a maximum was attained. On the other hand, a drop in CO₂ uptakes was measured for stirring times longer than 4 h. Although at 77 °C CO₂ is supposed to diffuse more easily through the PEI film, an excess of polymer might have prevented some of the gas from reaching amino groups. In fact, when using water as solvent a higher amount of polymer was actually loaded onto the carbon (32.6 wt% for AR_PEI_50%_Me_8h vs 38.1 wt% for AR_PEI_50%_W_8h, see Table 6-4 and Table 6-7 respectively). Accordingly, the pore blockage of the solid support was more pronounced (0.182 cm³·g⁻¹ for AR_PEI_50%_Me_8h vs 0.110 cm³·g⁻¹ for AR_PEI_50%_W_8h, see Table 6-5 and Table 6-8 respectively). This result was corroborated by the slower CO₂ sorption kinetics measured for samples stirred for longer time (see Figure 6-17). In contrast, AR_PEI_50%_W_0.5h exhibited the fastest sorption kinetic but the lowest uptake at saturation.

Moreover, note that, under identical optimal conditions in terms of nominal PEI loading (50 wt%) and stirring time (4 h), a more sustainable (i.e. aqueous) impregnation led to higher uptakes (27.3 mg CO₂·g⁻¹ see Table 6-9 and Figure 6-16(b)) than those achieved when solvent was methanol (22.5 mg CO₂·g⁻¹ see Table 6-6). In addition, the CO₂ sorption capacity measured for AR_PEI_50%_W_4h increased at 77 °C (see Table 6-9). This suggests that, for larger polymer loading and at higher temperature, the benefit of having a greater number of N-based functional groups outweighs the polymer-induced pore blocking. In fact, in contrast to sorption (thermodynamic effect), diffusion is favoured by the higher temperature (i.e. 77 °C in this case), which maximized CO₂ uptake. This finding seems to agree with results previously reported by literature for amines/silica blends [120, 223-225].

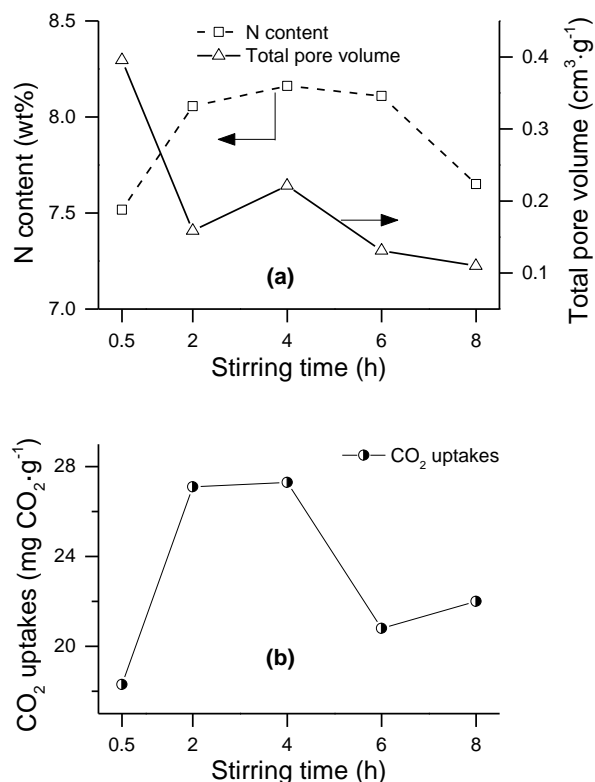


Figure 6-16 Effect of stirring time: (a) N content and pore volume reduction, and (b) CO₂ uptakes at 77 °C and 0.15 bar (total pressure of 1 bar). An optimal value of nominal PEI loading (50 wt%) and water as solvent were used to prepare these samples.

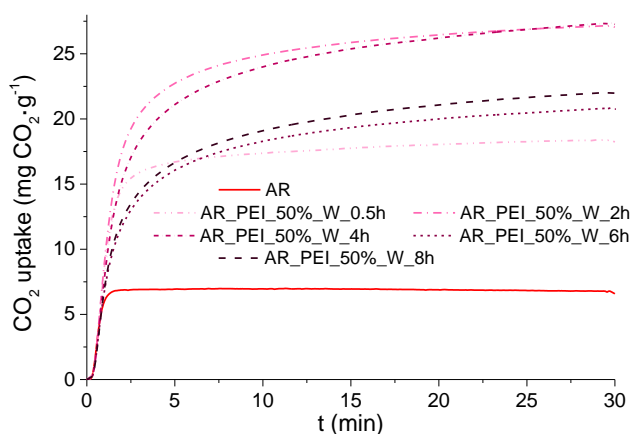


Figure 6-17 Effect of stirring time: CO₂ adsorption kinetics at 77 °C and 0.15 bar (total pressure of 1 bar); samples were prepared using an optimal value of nominal PEI loading (50 wt%) and water solvent.

Table 6-10 Main optimal conditions as identified by maximization of the CO₂ sorption capacity of PEI-impregnated carbons - Optimal values of PEI loading and stirring time are reported for each sorption temperature and solvent type used

		53 °C		77 °C	
		Water	Methanol	Water	Methanol
Opt. NL ⁵⁷	wt%	38	44	50	50
Opt. AL ⁵⁸	wt%	28.6	31.0	38.8	31.6
Opt. Stirring time ⁵⁹	h	2	8	4	4
Max CO ₂ uptake	mg CO ₂ ·g ⁻¹	32.1	33.6	27.3	22.5

6.2.4 Influence of the carbon support

As given in Table 6-11, OW800CA exhibited a far larger porosity than that of AR. Accordingly, larger values of actual loading and N content were measured after PEI impregnation of the wood-derived substrate (see Table 6-11). Note that impregnation conditions used for coating PEI onto OW800CA were the optimal parameters identified when measuring CO₂ sorption at 53 °C and reported in Table 6-10 (i.e. methanol as solvent, a NL of 44 wt%, and a stirring time of 8 h).

Table 6-11 Effect of the carbon support - Textural parameters, actual loading and N content

Sample ID	S _{BET} m ² ·g ⁻¹	V _{tot} cm ³ ·g ⁻¹	V _{mi} cm ³ ·g ⁻¹	V _{me+ma} cm ³ ·g ⁻¹	AL wt%	N wt%
AR	1531	0.691	0.569	0.122	-	0.4
AR_PEI	610	0.273	0.234	0.039	31.0	6.9
OW800CA	2061	1.008	0.773	0.235	-	0.3
OW800CA_PEI	0	0.000	0.000	0.000	41.7	9.5

The increased actual loading measured for OW800CA was reflected by more dramatic pore blockage depicted by isotherms (see Figure 6-18) and

⁵⁷ Optimal nominal loading determined for a common value of stirring time

⁵⁸ Optimal actual loading corresponding to the optimal nominal loading

⁵⁹ Determined for a common (optimal) value of PEI loading

PSDs by volume (see Figure 6-19) for this sample. Indeed, as reported in Table 6-11, the porosity of OW800CA was entirely used up after PEI impregnation.

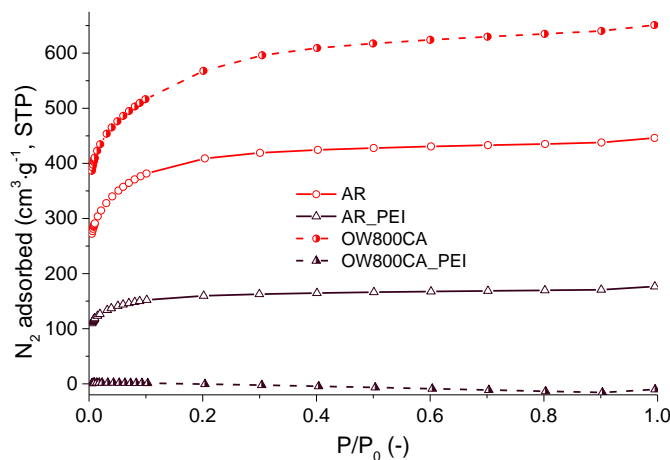


Figure 6-18 Effect of the carbon support - N₂ adsorption isotherms

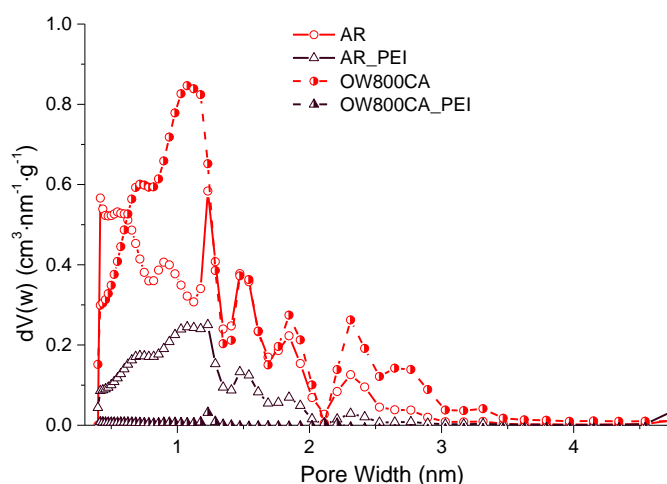


Figure 6-19 Effect of the carbon support - NLDFT PSDs by volume

Figure 6-20 revealed that OW800CA had a far more functionalized surface than that featured by AR. In particular, oak wood-derived carbon exhibited more acidic groups compared to those present within AR's structure. These might have resulted in a stronger affinity between the oak wood-based support and the polymer, thus facilitating the PEI coating onto the solid support. On the other hand, the OW800CA's acidic functionalities might have neutralized part of the basic groups contained within the polymer. Accordingly, the net amount of amines available for CO₂ uptake might have been much lower. This would explain the less significant improvement of the CO₂ sorption capacity shown in Figure 6-21.

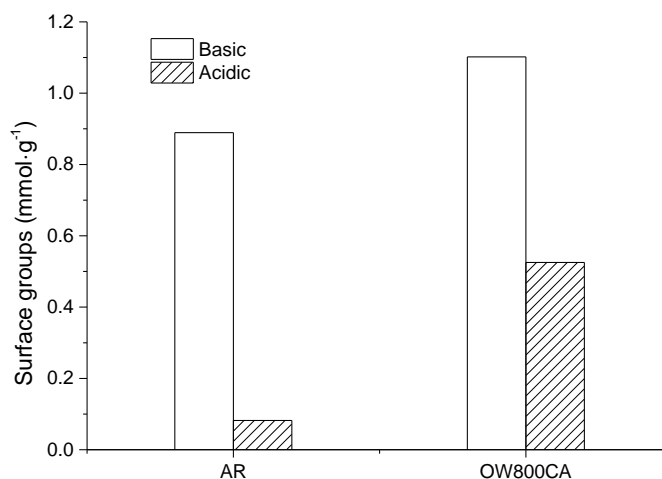


Figure 6-20 Effect of the carbon support – Basic and acidic functionalities measured by Boehm titrations

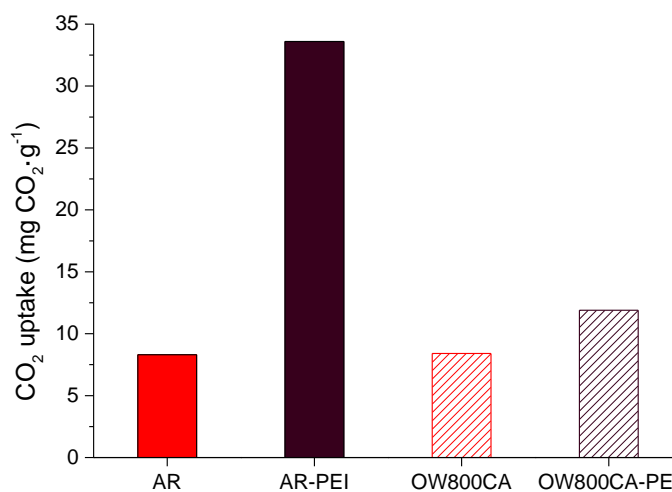


Figure 6-21 Effect of the carbon support - CO₂ uptakes at 53 °C and 0.15 bar (total pressure of 1 bar)

As seen in Figure 6-22, the unmodified supports exhibited fast sorption kinetics typical of physisorbents, while PEI-impregnated derivatives showed slower kinetics evidently due to a reduced diffusivity of CO₂ through the polymer bulk.

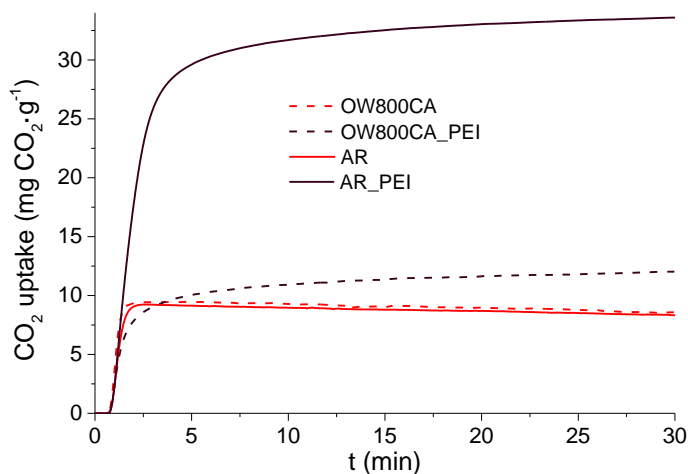


Figure 6-22 Effect of the carbon support - CO₂ adsorption kinetics at 53 °C and 0.15 bar (total pressure of 1 bar)

6.2.5 Influence of the impregnating agent

Various types of N-containing additives were impregnated onto commercial carbon (AR). Impregnation conditions (PEI NL, stirring time and solvent type) were the same as those used in section 6.2.4. As seen in Table 6-12, a lower weight of polymer was actually loaded onto the carbon support after monoethanolamine (MEA) impregnation. This result was in line with the less dramatic pore blockage exhibited by AR-MEA (see Table 6-12 and Figure 6-23). It is worth pointing out that, as seen in Figure 6-24, AR-MEA exhibited a different pore size distribution in comparison to those observed for AR-PEI and AR-tetraethylenepentamine (TEPA). In particular, despite, or perhaps because of, the MEA molecule being smaller than TEPA and PEI, MEA impregnation appeared to cause a lower reduction of microporosity than that experienced by AR-TEPA and AR-PEI. This observation seems to suggest that part of the amount of TEPA and PEI (larger molecules than MEA) loaded onto the carbon support might have not entered micropores. Indeed, as also suggested by Gibson *et al.* [116], TEPA and PEI might have simply blocked micropores for nitrogen adsorption.

Although MEA is a primary amine, thus implying a higher basicity than that featured by secondary amines, the impregnation of this compound did not bring any significant improvement to the CO₂ sorption capacity of the pristine carbon (see in Figure 6-25). This was attributed to the lower number of amino groups available for CO₂ chemisorption contained by the MEA molecule, which agreed with the lower nitrogen content measured for AR-MEA.

Table 6-12 Effect of the impregnating agent - Textural parameters, actual loading and N content

Sample ID	S_{BET} $\text{m}^2\cdot\text{g}^{-1}$	V_{tot} $\text{cm}^3\cdot\text{g}^{-1}$	V_{mi} $\text{cm}^3\cdot\text{g}^{-1}$	$V_{\text{me+ma}}$ $\text{cm}^3\cdot\text{g}^{-1}$	AL (wt%)	N (wt%)
AR	1531	0.691	0.569	0.122	-	0.4
AR_PEI	610	0.273	0.234	0.039	31	6.9
AR_MEA	898	0.406	0.342	0.064	16.6	3
AR_TEPA	593	0.307	0.215	0.092	34.1	5.2

In contrast, as observed in Figure 6-25, a more dramatic enhancement of the CO₂ sorption performance of the virgin carbon occurred after impregnation with PEI or TEPA. This could be ascribed to the higher density of amino groups of these molecules. However, this finding might also suggest that secondary amines, present within both TEPA and PEI, are mostly responsible for an increased affinity with CO₂. This is in agreement with what previously found in other works [306-308]. Therefore, the enhancement of CO₂ capture capacity might be due to a combination of N groups' density and type (i.e. amines).

It is worth mentioning that chemical modification with TEPA resulted in a slightly higher increase of the CO₂ capacity of the parent carbon compared to that achieved after PEI impregnation. This is consistent with results reported in other studies [121, 122, 224, 237, 238], and probably due to favoured physical properties (lower viscosity and density, see Chapter 3) of TEPA in comparison to those typical of PEI, which might have facilitated the tetraethylenepentamine distribution through the pore channels of the carbon support and the CO₂ diffusion through the TEPA bulk. This agrees with what reported by Sanz-Pérez *et al.* [121]. In addition to this, as suggested by Wang *et al.* [237], this result may also be ascribed to the higher density of amino groups present within TEPA molecule. Furthermore, because of steric reasons (the PEI molecule is a lot larger than TEPA), polyethyleneimine has a higher number of amino groups that cannot be easily accessed by CO₂, thus leading to a lower CO₂ uptake compared to that of TEPA [116].

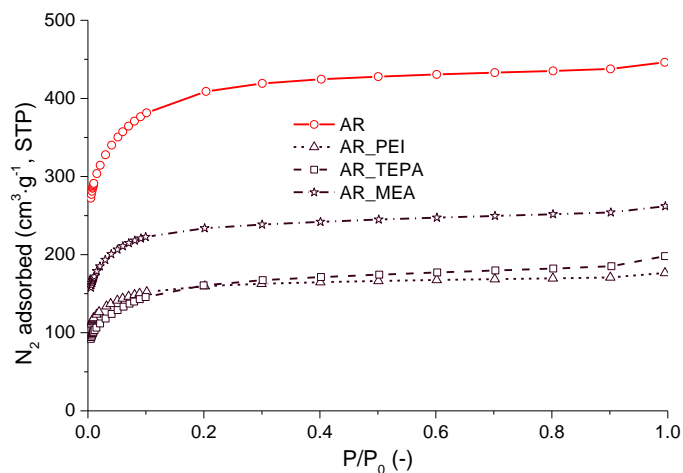


Figure 6-23 Effect of impregnating agent - N₂ adsorption isotherms

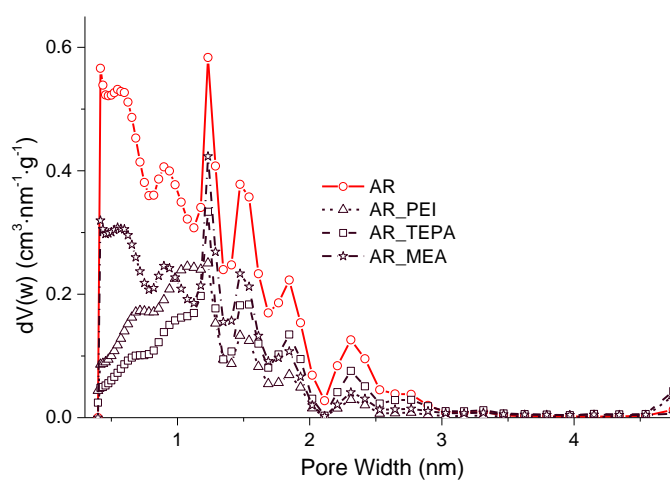


Figure 6-24 Effect of impregnating agent - NLDFT PSDs by volume

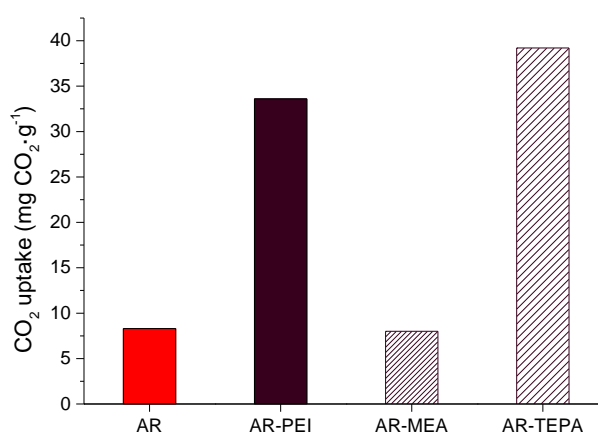


Figure 6-25 Effect of impregnating agent - CO₂ uptakes at 53 °C and 0.15 bar (total pressure of 1 bar)

As observed in Figure 6-26, both AR-PEI and AR-TEPA exhibited more slowly equilibrating CO₂ sorption kinetics compared to that found for the parent carbon. On the other hand, impregnated samples attained a significantly higher plateau than AR, with AR-TEPA prevailing over AR-PEI.

Figure 6-27 showed that AR-MEA exhibited a lower regeneration rate (i.e. decrease of CO₂ uptake·°C⁻¹) than those observed for AR-TEPA and AR-PEI, probably due to stronger bond between primary amine and carbon dioxide. However, as MEA-impregnated carbon captured a negligible amount of CO₂, its regeneration was accomplished at 100 °C. By contrast, both AR-TEPA and AR-PEI displayed an easier removal of carbon dioxide with increasing temperature but larger amount of residual CO₂ at 100 °C. This suggested the choice of a higher temperature in an attempt to ensure the full regeneration of these chemisorbents.

Although TEPA-impregnated carbon slightly outperformed PEI-impregnated support, it was decided to use PEI for following experiments, as this compound has a much higher molecular weight than TEPA (see Chapter 3), thereby implying a higher thermal stability [237]. This was considered a crucial factor when opting for rapid temperature swing adsorption (RTSA) as the regeneration strategy. This decision was also supported by a few studies reporting a more intense TEPA leaching from solid supports compared to that exhibited by PEI when performing cycling tests [29, 116, 121, 122, 224, 237, 238].

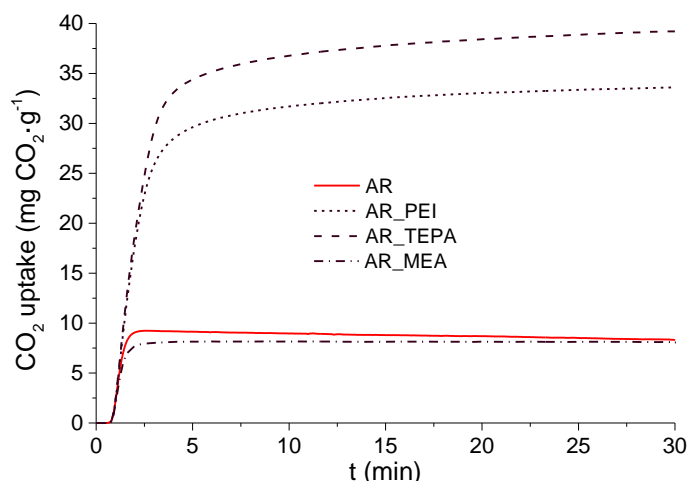


Figure 6-26 Effect of impregnating agent - CO₂ adsorption kinetics at 53 °C and 0.15 bar (total pressure of 1 bar)

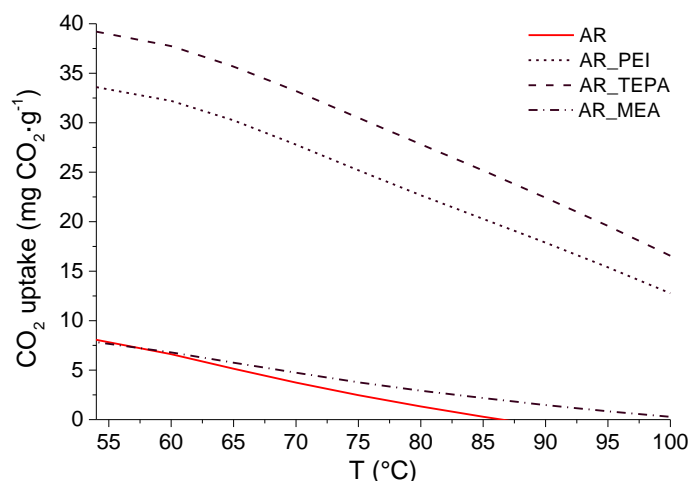


Figure 6-27 Effect of impregnating agent - Regeneration (RTSA, 53-100 °C)

6.2.6 Influence of OH group-containing additive

The successful incorporation of glycerol onto the carbon support was corroborated by elemental analysis (see Table 6-13). In particular, H increased with increasing amount of glycerol loaded during impregnation. Accordingly, the proportion of N relatively decreased for all glycerol-containing samples.

Table 6-13 Effect of glycerol addition - Actual loading and elemental analysis; the actual loading measured for the glycerol-containing samples refers to the PEI/glycerol mixture. Gly stands for Glycerol.

Sample ID	AL	N	C	H	S
	(wt%)	(wt%)	(wt%)	(wt%)	(wt%)
AR_PEI	31.0	6.9	74.7	2.8	0.0
AR_PEI_Gly_4:1	35.6	6.3	77.8	3.0	0.0
AR_PEI_Gly_2:1	38.2	6.3	75.7	3.2	0.0
AR_PEI_Gly_1:1	43.4	6.1	74.1	3.3	0.0

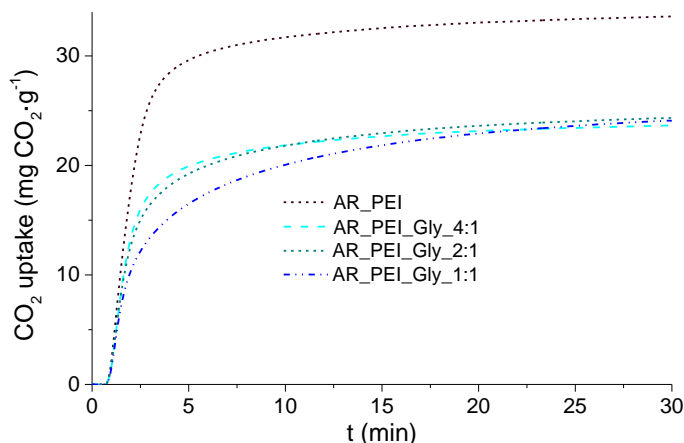


Figure 6-28 Effect of glycerol addition - CO₂ adsorption kinetics at 53 °C and 0.15 bar (total pressure of 1 bar).

Table 6-14 Effect of glycerol addition - CO₂ uptakes (CO_{2, ads max}) at 53 °C and 0.15 bar (total pressure of 1 bar), and amine efficiency. N* represents the amount of nitrogen actually incorporated after impregnation of PEI or PEI/glycerol blend onto the carbon support, and is calculated by subtracting the N content of AR (see Table 6-1) from the N levels measured for impregnated samples (see Table 6-13). The CO_{2, ads max} /N* molar ratio is then calculated as (CO_{2, ads max}/N*)·(MW_(N)/MW_(CO₂)), where CO_{2, ads max} is expressed as wt%.

Sample ID	CO _{2, ads max}		N*	CO _{2, ads max} ·N* molar ratio
	mg CO ₂ ·g ⁻¹	wt%		
AR_PEI	33.6	3.36	6.54	0.164
AR_PEI_Gly_4-1	23.7	2.37	5.90	0.128
AR_PEI_Gly_2-1	24.3	2.43	5.93	0.130
AR_PEI_Gly_1-1	24.1	2.41	5.71	0.134

However, as clearly depicted by Figure 6-28, the addition of glycerol to the PEI/solvent/carbon mixture did not improve the CO₂ uptake capability of the PEI-impregnated carbon (AR-PEI) under simulated post-combustion conditions. This is in contrast with findings reported by previous works for PEI or TEPA-impregnated silica [214, 216, 233]. Nonetheless, the decrease of the CO₂ adsorption capacity observed in this work when adding glycerol is consistent with the lower ratio of moles of CO₂ adsorbed per mole of N incorporated after impregnation (see values reported in Table 6-14) exhibited by glycerol-doped materials compared to that calculated for the glycerol-free sample (AR-PEI).

The lower CO₂ capacity and CO₂ captured:N molar ratio (usually defined as amine efficiency) exhibited by glycerol-containing samples might be

attributed to the additional pore blockage (see Figure 6-29 and Table 6-15) caused by the insertion of the glycerol within the porous structure of the carbon support. In fact, as given in Table 6-15, increasing amount of glycerol (i.e. decreasing PEI:Glycerol ratio) caused a progressive reduction of porosity. This might have impeded the access of CO₂ to some of the amino groups incorporated through PEI impregnation. Diffusional limitations might have outweighed the beneficial effect imparted by the presence of OH moieties (i.e. increase of theoretical amine efficiency from 0.5 to 1) [115, 216, 232]. The porosity reduction trend reflected the larger overall loading observed with increasing amount of glycerol (i.e. decreasing PEI:Glycerol ratio) as given in Table 6-13.

Nonetheless, when comparing glycerol-modified samples only, the CO₂:N ratio in Table 6-14 appears to slightly increase with increasing amount of glycerol added (i.e. decreasing PEI:Glycerol ratio). This seems to indicate that the amine efficiency is favoured by a higher amount of hydroxyl groups, which might have interacted with amino groups to a low extent in order to enhance the CO₂ chemisorption mechanism [115, 216, 232]. This observation is consistent with the fact that the reduction of the maximum CO₂ uptake capacity appears to be independent of the PEI:Glycerol ratio (and therefore from the pore volume reduction). It follows that, with increasing amount of glycerol loaded onto the carbon support, the higher amine efficiency might have counteracted the adverse effect of pore blockage (i.e. lower gas diffusivity).

It is also worth mentioning that the CO₂:N molar ratio calculated for AR-PEI (0.164, see Table 6-14) is lower than the maximum theoretical value under dry conditions reported in the literature (i.e. 0.5 [116, 216-218]). This was partly due to some of the N functionalities contained within PEI, with particular regard to tertiary amines, which are not effectively contributing to the CO₂ conversion process, as these are not able to form carbamate under dry conditions (i.e. their theoretical amine efficiency is 0) [232]. Indeed, the actual maximum amine efficiency for PEI-modified solid sorbents under anhydrous conditions was reported to be 0.39 [215], assuming a primary:secondary:tertiary amine ratio of 44:33:23 within low molecular weight (800 g·mol⁻¹) PEI [309]. In addition to this, some of the primary and secondary amines might have not been accessible to carbon dioxide because of diffusion resistance through the PEI film. Nevertheless, the amine efficiency exhibited by AR-PEI is as high as [215, 237] or slightly lower [231] than other values reported in the literature for PEI-supported sorbents in absence of water.

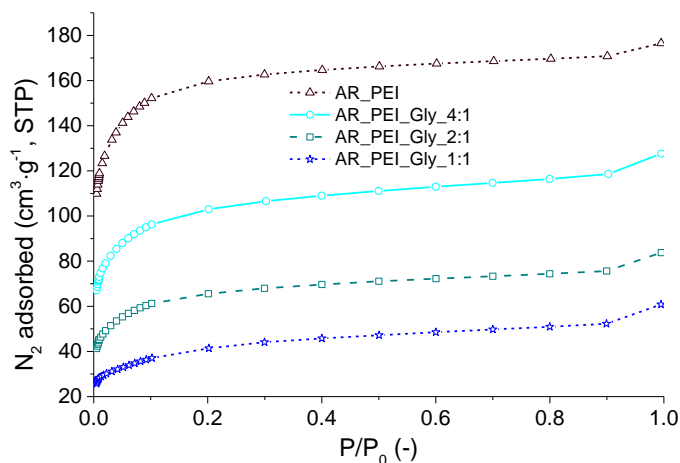


Figure 6-29 Effect of glycerol addition - N_2 adsorption isotherms. 4:1, 2:1 and 1:1 are the PEI:Glycerol ratios examined.

Table 6-15 Effect of glycerol addition - Textural parameters

Sample ID	S_{BET}	V_{tot}	V_{mi}	V_{me+ma}
	$m^2 \cdot g^{-1}$	$cm^3 \cdot g^{-1}$	$cm^3 \cdot g^{-1}$	$cm^3 \cdot g^{-1}$
AR_PEI	610	0.273	0.234	0.039
AR_PEI_Gly_4:1	386	0.198	0.148	0.050
AR_PEI_Gly_2:1	247	0.130	0.093	0.037
AR_PEI_Gly_1:1	148	0.094	0.055	0.039

In order to appreciate the effect of the glycerol addition on the variation of the CO_2 adsorption rate, the CO_2 sorption kinetics measured for glycerol-free and glycerol-containing samples were normalized by their relative maximum uptake (see equation related to the CO_2 adsorption progress used in Chapter 5). In fact, when comparing the CO_2 adsorption progress in Figure 6-30, it is possible to observe that, at the very beginning of the adsorption stage (i.e. $t < 3$ min), AR_PEI_Gly_4:1 shows a slightly faster CO_2 uptake rate than that measured for AR-PEI. Previous studies reported an acceleration of the CO_2 adsorption rate when adding PEG to PEI-impregnated sorbents [123, 217]. Moreover, Labreche *et al.* [214] postulated that the addition of glycerol might hasten the adsorption process as the rigid PEI chain is plasticized, thus favouring the diffusion of CO_2 through the polymer gel. In spite of this, these authors did not show the effect of the glycerol on the CO_2 adsorption kinetics. However, the CO_2 adsorption progress of all glycerol-containing samples decreased with increasing time. In addition, the greater the pore reduction (see Figure 6-29), the slower sorption rate is, following the sequence AR_PEI_Gly_1:1 < AR_PEI_Gly_2:1 < AR_PEI_Gly_4:1. This seems to suggest that the slower kinetics in the late stage of the adsorption process exhibited by

glycerol-doped sorbents might be ascribed to pore blockage and consequent diffusional limitations.

Furthermore, in an attempt to highlight the influence of the additive (i.e. glycerol) on the CO₂ desorption rate, the same normalization was also applied to the CO₂ desorption kinetics of all the samples. In particular, as illustrated in Figure 6-31(b), when the CO₂ desorption progress is considered, all glycerol-plasticized samples exhibited a noticeably faster release of CO₂, especially at higher temperature. As suggested by Yue *et al.* [216], more facile regeneration of the chemisorbent may occur because, when hydroxyl groups are present, a less thermally stable carbamate type zwitterion is formed.

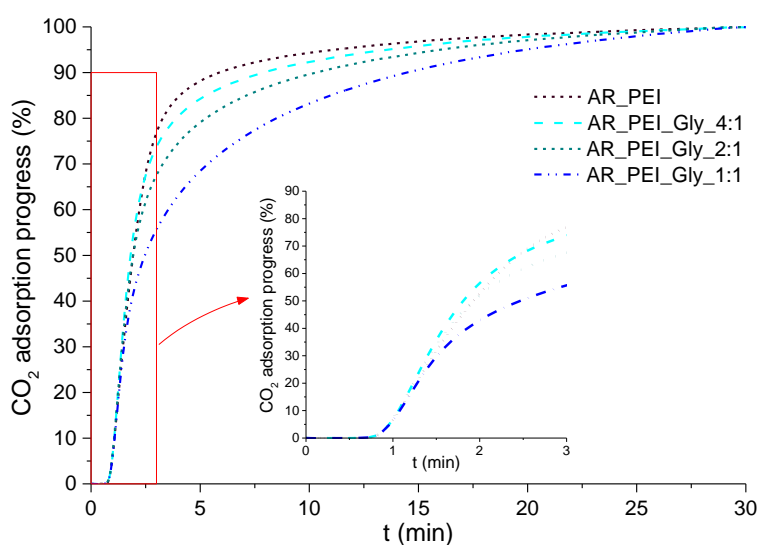


Figure 6-30 Effect of glycerol addition - CO₂ adsorption progress at 53 °C and 0.15 bar (total pressure of 1 bar). Inset shows the first 3 min of the CO₂ adsorption step.

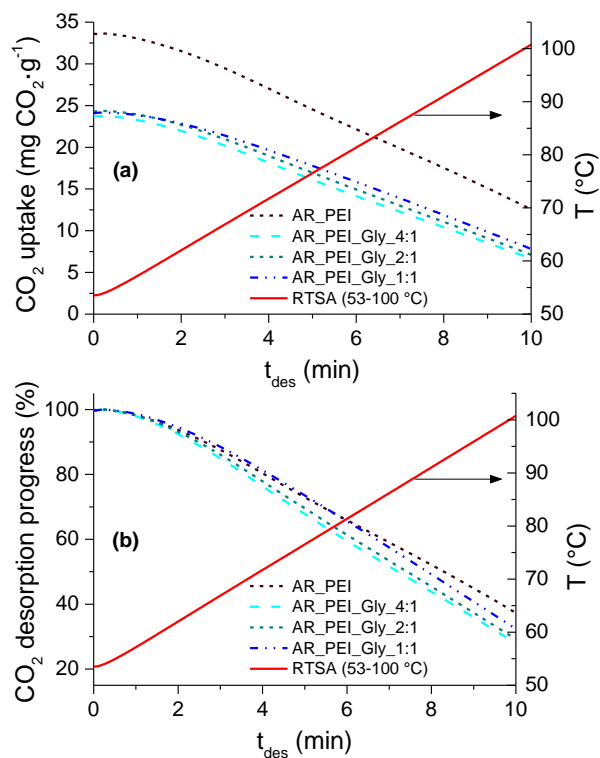


Figure 6-31 Effect of the glycerol addition: (a) CO₂ desorption kinetics and (b) CO₂ desorption progress at 53-100 °C and 0.15 bar (total pressure of 1 bar).

6.3 Detection of PEI on the optimally PEI-impregnated carbon

The presence of PEI inside the carbon pores is confirmed by the dramatic reduction of the N₂ volume that can be adsorbed after PEI impregnation (Figure 6-32 (a)). However, as shown by Figure 6-32(b), the PEI-loaded carbon exhibited a larger CO₂ adsorption capacity at 0 °C than that of the virgin carbon. Figure 6-32(b) also highlights how the CO₂ isotherm shapes for the two samples are somewhat different, as shown by the initial steeper plot exhibited by the PEI-modified carbon at low-pressure values. This behaviour is explained by the increased affinity of the PEI-loaded carbon for carbon dioxide due to the presence of the N-based functionalities contained in the polymer.

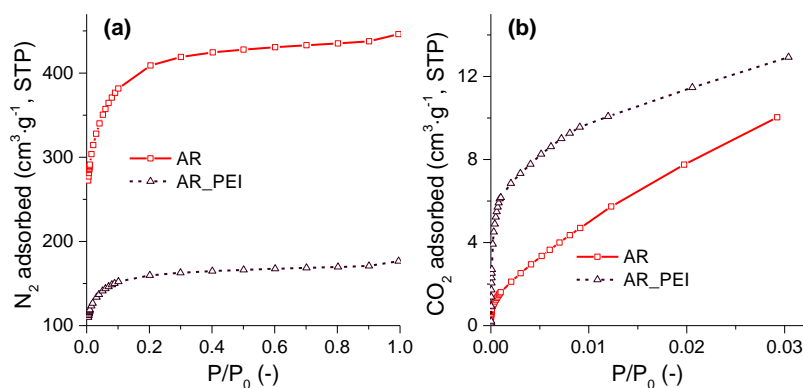


Figure 6-32 N_2 (a) and CO_2 (b) adsorption isotherms for virgin and optimally PEI-impregnated carbons

The Scanning Electron Microscope (SEM) micrographs in Figure 6-33 depict the cross sections of virgin carbon and polymer-impregnated carbon. Although the overall morphology is maintained, it is noticeable that some of the macropores of the carbon substrate were partially blocked by PEI impregnation.

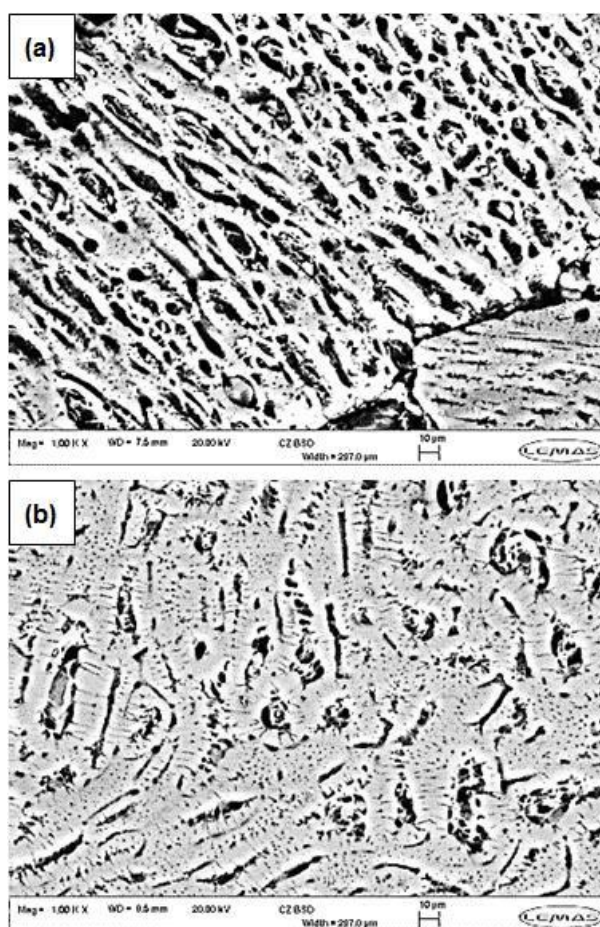


Figure 6-33 Back-scattered SEM micrographs at 1 Kx magnification of the cross-section of (a) virgin and (b) optimally PEI-impregnated carbons

Figure 6-34 shows significant differences in the Thermogravimetric Analysis (TGA) of virgin and PEI-impregnated carbons. First, as seen in Figure 6-34(a), the PEI-modified sample experienced a more pronounced weight loss occurring at lower temperature. This might be due to liberation of a higher amount of trapped moisture due to the hygroscopic nature of the polymer [217]. The peak shown by the Differential Thermogravimetric Analysis (DTGA) curve indicates that the highest mass loss occurs at ca. 100 °C (see Figure 6-34 (b)). Secondly, the TGA profile of the PEI-loaded sample revealed a much larger weight loss between 150 °C and 500 °C.

This can be ascribed to the polymer decomposition [310] with the liberation of volatile material and / or volatilization although the polymer can nevertheless be regarded as being relatively thermally stable. According to the DTG curve of the PEI-impregnated carbon, the polymer started this process at around 175 °C [311] as shown by the additional peak. No significant weight loss was observed above 600 °C, suggesting that evolution of volatile material was completed by this stage.

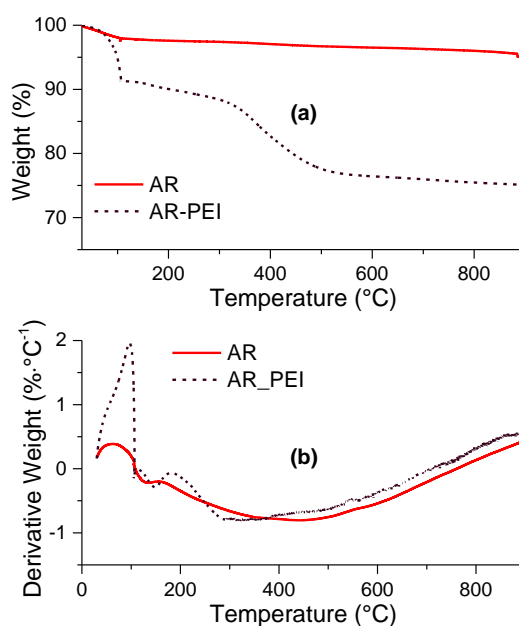


Figure 6-34 (a) TGA and (b) DTGA of virgin and optimally PEI-impregnated carbons

As shown by Figure 6-35, the carbon's basicity significantly increased after the impregnation of polyethyleneimine. This is due to the incorporation of N-containing functionalities present within the polymer. Conversely, a seemingly negative concentration of acidic groups was found for the PEI-impregnated carbon. Acidic groups, which were present in already very small quantities for the parent carbon, might have been neutralized by the polymer. Nevertheless, in addition to this, after mixing the PEI-impregnated carbon with the alkaline

standard solution (0.05 M NaOH) used to neutralize acidic groups, some of the polymer's basic groups might have actually been transferred into the liquid phase (supernatant), thereby increasing its alkalinity. This would result in a seemingly negative quantity of acidic groups since this is assayed by difference between the concentrations of alkaline species in the supernatant before and after exposure to the PEI-impregnated carbon.

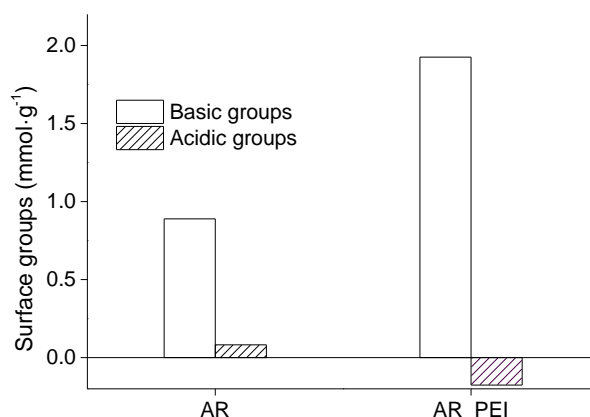


Figure 6-35 Surface functional group concentrations assayed for virgin and optimally PEI-impregnated carbon

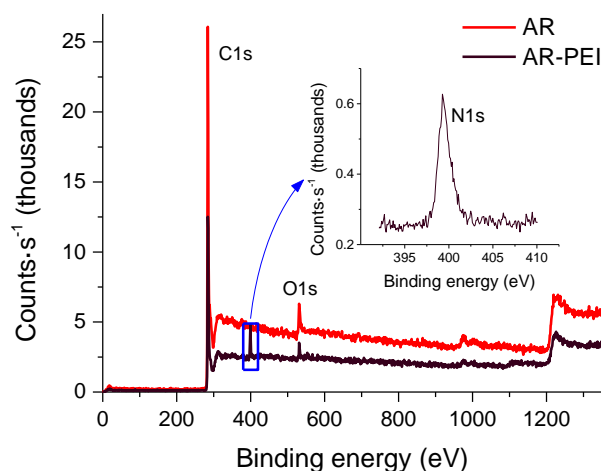


Figure 6-36 Comparison of X-ray Photoelectron Spectroscopy (XPS) survey scan spectra measured for virgin and optimally PEI-impregnated carbons. C/S indicates the counts per second. Inset shows the deconvoluted N1s spectra for the PEI-modified carbon.

Conclusive evidence of the successful impregnation of PEI onto the carbon support was given by XPS (see Figure 6-36). Indeed, from the survey scan spectra shown in Figure 6-36 it is possible to observe a well-defined N1s peak at ca. 399.2 eV for the PEI-loaded carbon. This is typical of N functionalities of PEI as reported by Drage *et al.* [234], who measured a N1s peak at ca. 400 eV for a PEI-modified mesoporous silica. In addition to that, Thi

Le *et al.* [312] reported a N1s peak at 398.2 eV for a PEI-coated mesoporous silicate (MCM-41). The slight shift in the position of the N1s peak measured in this study might be ascribed to a different interaction between PEI and the carbon support compared to that occurring with silica-based substrates. It is worth mentioning that Maroto-Valer *et al.* [313] reported a predominant presence of pyridine and imine groups on a PEI-impregnated carbon derived from anthracite, whereas no amino groups were identified by these authors. This is in contrast with results found in this work, as in this case N1s peak could be reasonably attributable to the amino groups of the PEI chain.

C1s and O1s peaks were recorded at ca. 284 eV and 532 eV respectively for both samples. Note that the dramatic decrease of the intensity of all the peaks (with particular regard to the carbon peak) in the PEI-impregnated sample seemed to corroborate the presence of the polymer within the pores of the carbon support.

6.4 Sorption kinetics modeling

The CO₂ sorption kinetics measured for the virgin (AR) and the PEI-modified commercial carbon (AR-PEI) were fitted to two models, i.e. pseudo first order and pseudo second order, whose equations can be found elsewhere [314]. Model parameters were calculated with the aid of Origin Pro software by minimizing the square of residuals (SOR).

As clearly shown both in Figure 6-37(a) and Figure 6-37(b), both models failed at predicting the early stage of the CO₂ adsorption process occurring onto the sorbents tested. However, the absence of CO₂ uptake observed for $t < \text{ca. } 1$ min might be attributed to an artefact due to the experimental measurement conducted using TGA. [315]. Specifically, when switching the atmosphere from nitrogen to carbon dioxide (see Chapter 4 for further details), CO₂ does not instantaneously displace the N₂ present within the TGA chamber and surrounding the sample. Accordingly, the adsorption of CO₂ onto the solid material is delayed.

Nonetheless, as concerns AR, both models exhibited a poorer fit of the experimental data over the entire equilibration time (see Figure 6-37). This was likely because of the fast kinetics exhibited by AR at the early stage of the adsorption process, which does not agree with the model's predictions. In addition to this, the lack of agreement between experimental and model kinetics is caused by the decreasing trend of AR's sorption capacity with increasing time. These results seem to suggest that pseudo first order and pseudo second order models are not suitable for interpreting pure physisorption.

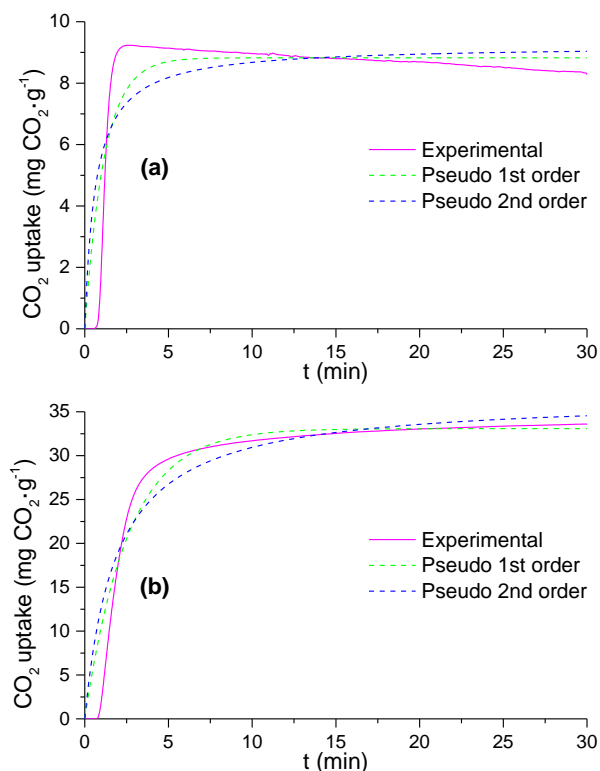


Figure 6-37 Sorption kinetics fitting for (a) virgin commercial carbon (AR) and (b) PEI-modified commercial carbon (AR-PEI)

In contrast, a relatively better fit was observed when correlating models to the experimental CO₂ sorption kinetic measured for AR-PEI (see Figure 6-37(b)), with higher values of R^2 than those determined for AR (see Table 6-16). The improved fitting of the experimental data may be attributed to the presence of a chemisorption contribution in AR-PEI's sorption process. In addition to this, it is worth noting that AR-PEI's sorption kinetic was better interpreted by the pseudo first order model (see R^2 values in Table 6-16). This is in contrast with what reported by Aroua *et al.* [316], who measured the Pb²⁺ adsorption kinetics for PEI-impregnated AC. Indeed, these authors found that experimental sorption data were best fitted by the pseudo second order model. This might be due to a different interaction between PEI and Pb²⁺ in comparison with that between the polymer and CO₂.

Table 6-16 Kinetic model parameters for CO₂ sorption onto virgin (AR) and PEI-modified commercial carbon (AR-PEI)

Sample ID	Pseudo 1 st order				Pseudo 2 nd order		
	$q_{e, \text{exp}}^{60}$ mg CO ₂ ·g ⁻¹	$q_{e, \text{mod}}^{61}$ mg CO ₂ ·g ⁻¹	K_1^{62} min ⁻¹	R^2 -	$q_{e, \text{mod}}$ mg CO ₂ ·g ⁻¹	K_2^{63} g·mgCO ₂ ⁻¹ ·s ⁻¹	R^2 -
AR	8.28	8.83	0.86	0.80	9.23	0.17	0.65
AR-PEI	33.60	33.08	0.39	0.95	36.68	0.01	0.90

⁶⁰ CO₂ adsorbed capacity at equilibrium measured experimentally

⁶¹ CO₂ adsorbed capacity at equilibrium predicted from the model

⁶² Rate constant of pseudo-first-order adsorption

⁶³ Rate constant of pseudo-second-order adsorption

6.5 Assessment of CO₂ capture performance of the optimally PEI-impregnated carbon

6.5.1 Comparison with virgin AC and benchmark sorbent (Z13X)

6.5.1.1 35 °C, 100 % CO₂

As seen in Figure 6-38, at high partial pressure of CO₂ both AR and zeolite Z-13X attained larger CO₂ uptakes than that exhibited by the PEI-modified carbon. The latter was evidently hindered compared to the parent carbon because the polymer took up the pore space, thus deactivating part of the (physi)sorption sites.

N₂ adsorption data reported in Table 6-2 highlighted a far more developed porous structure for AR compared to that of zeolite. Nevertheless, the higher uptake of CO₂ achieved by Z13X could be ascribed to the larger ultramicropore volume (0.105 cm³·g⁻¹) measured for this material by CO₂ adsorption at 0 °C, compared to that found for AR (0.026 cm³·g⁻¹).

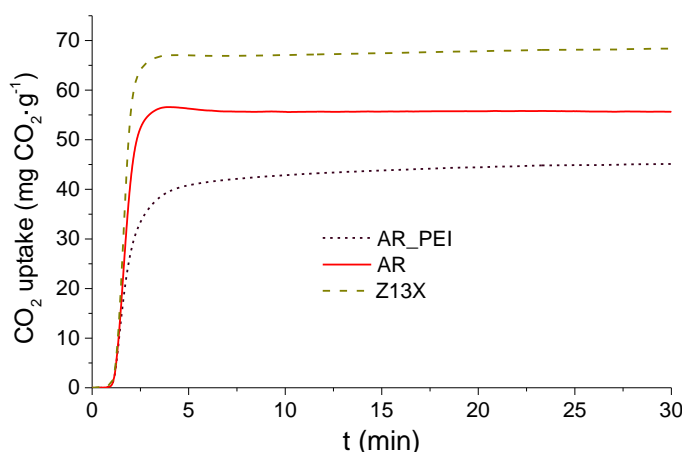


Figure 6-38 CO₂ uptakes measured at 35 °C and 1 bar (total pressure of 1 bar): comparison of virgin carbon, optimally PEI-impregnated carbon and Z13X

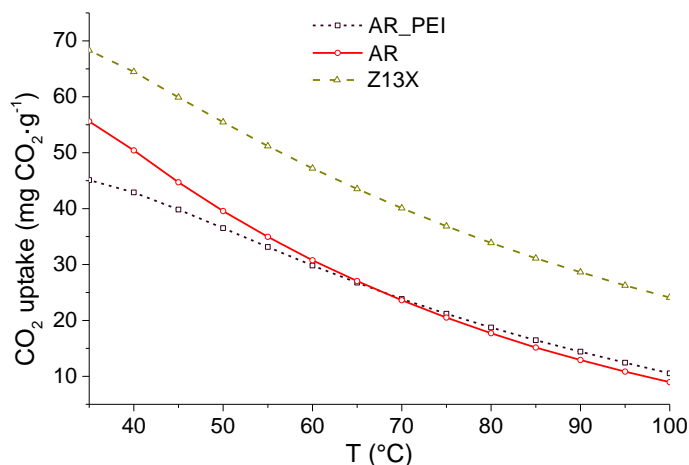


Figure 6-39 Regeneration (RTSA, 35-100 °C): comparison of virgin carbon, optimally PEI-impregnated carbon and Z13X

As shown in Figure 6-39, both AR and Z13X released CO₂ more easily than AR-PEI during the desorption step. Nonetheless, especially for zeolite, regeneration was not fully accomplished, as samples exhibited residual adsorbed CO₂ at 100 °C. Figure 6-39 also shows a higher retention of CO₂ (see less steep slope) for AR-PEI, especially at lower temperature (see cross over between AR-PEI and AR desorption profiles at ca. 65 °C). This seems to indicate a stronger interaction (i.e. chemisorption) between CO₂ and the PEI-coated carbon, which could be attributed to the basic character of the N functionalities incorporated onto the carbon structure.

6.5.1.2 Simulated post-combustion performance

As shown by Figure 6-40, when measuring CO₂ uptakes under simulated post-combustion conditions (53 °C and 0.15 bar CO₂ partial pressure (total pressure of 1 bar)), the PEI-impregnated carbon showed the largest CO₂ sorption capacity. In particular, a capability improvement of ca. 4 times compared to the parent carbon was recorded (see also Table 6-3). Moreover, the CO₂ uptake of the modified carbon was even higher than that measured for Z13X. Furthermore, the CO₂ sorption kinetic observed for PEI-loaded carbon is much faster than that measured for zeolite. In fact, after 5 min, AR-PEI achieved most of its CO₂ uptake, which was nearly 2 times larger than that attained by Z13X at the same stage. In contrast, the zeolite had not reached saturation after 30 min. This suggests PEI-modified carbon to be a more promising CO₂ sorbent under real world operating conditions when fast sorption kinetics are required [58].

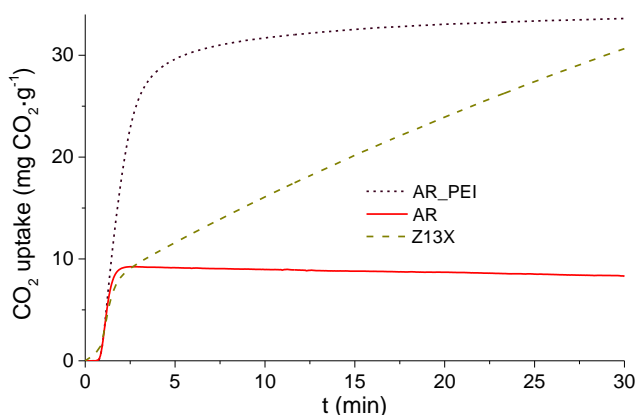


Figure 6-40 CO₂ uptakes at 53 °C and 0.15 bar (total pressure of 1 bar): comparison of virgin carbon, optimally PEI-impregnated carbon and Z13X

In addition to faster sorption rates, the optimally PEI-impregnated carbon also exhibited a higher selectivity toward carbon dioxide compared to that observed for Z13X. Indeed, as shown in Figure 6-41, when exposing samples to pure nitrogen at 53 °C (total pressure of 1 bar), both virgin and PEI-modified carbons did not exhibit any gas uptake. In addition, the weight of the unmodified carbon (AR) seems to decrease slightly, thereby suggesting desorption of some of the nitrogen previously adsorbed. Conversely, despite a very slow sorption rate, zeolite appeared to adsorb a significant amount of nitrogen. The slow uptake of N₂ might be explained through the hydrophilicity of this sorbent [214]. In particular, as samples were not stored in a desiccator, zeolite might have adsorbed more water from the air compared to carbon, which is normally more hydrophobic. Thus, apparently, nitrogen may be slowly displacing the moisture molecules pre-adsorbed onto the zeolite porous framework. On this basis, it is possible that the sorption capacity previously exhibited by Z13X in Figure 6-40 may not be entirely ascribed to uptake of CO₂.

However, results related to the measurement of samples' sorption kinetics under pure N₂ seem to agree with the sorbents' behaviour during the cooling stage performed under nitrogen (see Figure 6-42) immediately before measuring adsorption under 15% CO₂/85% N₂. Indeed, sample weights recorded for AR and AR-PEI exhibit a low plateau at saturation, whereas Z13X's sample weight continuously increases with increasing time without equilibrating.

Overall, these findings highlighted that the affinity between sorbents and nitrogen followed the sequence Z13X>AR>AR-PEI, thus suggesting that not only PEI-modified carbon was less sensitive to N₂ compared to zeolite, but also that the presence of polymer within AR's porous structure ensured an increased selectivity towards capturing CO₂.

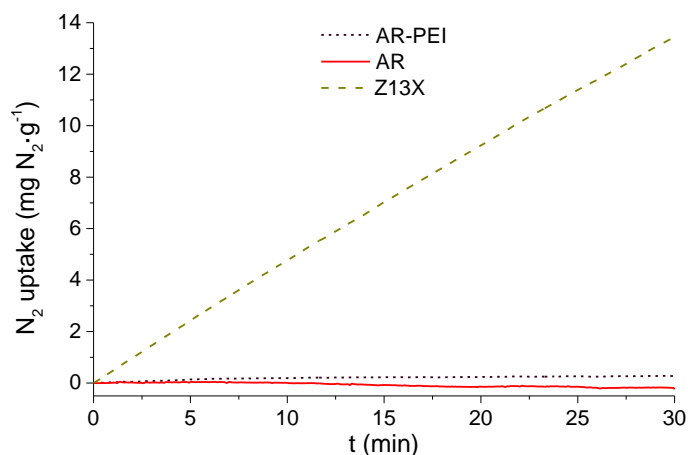


Figure 6-41 Pure N₂ uptakes measured at 53 °C and 1 bar: comparison of virgin carbon, optimally PEI-impregnated carbon and Z13X

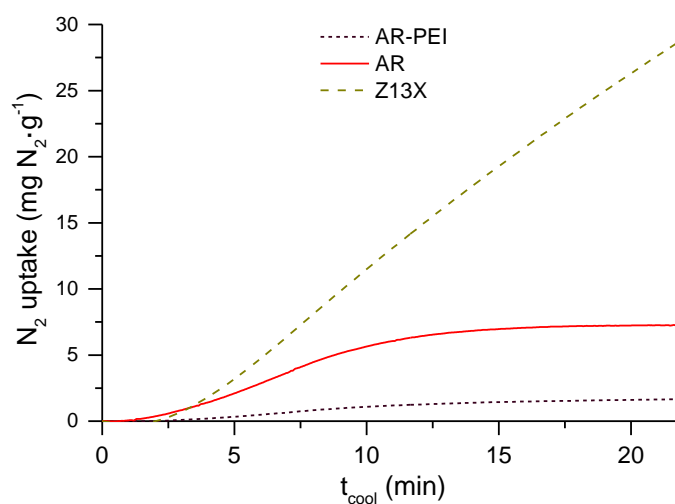


Figure 6-42 Preliminary adsorption of nitrogen during 22 min cooling stage prior to measuring CO₂ uptakes at 53 °C and 0.15 bar (total pressure of 1 bar)

As shown by Figure 6-43, the very low amount of CO₂ adsorbed onto the virgin carbon was completely removed at ca. 85 °C. Conversely, the regeneration of zeolite and PEI-modified carbon was not efficient at 100 °C probably because of the stronger interaction between CO₂ and these materials. This dictates the need for a higher temperature to effectively regenerate the sorbents. In particular, the amount of CO₂ adsorbed by Z13X remained nearly unaltered until temperature was ca. 75 °C. Note that the slight apparent increase in uptake at lower temperatures was probably due to buoyancy effects when increasing the system temperature. Nonetheless, the stronger bond between Z13X and CO₂ could be attributed to the interaction between the permanent quadrupole moment of carbon dioxide and the electric field induced by the cations present within the zeolite network [58, 69, 317]. This electrostatic

force outweighs Van der waals interactions [59] typical of activated carbons. In addition to that, Z13X's desorption behaviour might be explained by the formation of carbonates and carboxylates on the surface of the zeolite after reaction with CO_2 , which are regenerated only at high temperature ($350\text{ }^\circ\text{C}$) [12].

The stronger bond between PEI-loaded carbon and CO_2 led to the far more intense exothermic peak exhibited by the modified carbon's heat flow compared to that observed for AR (see Figure 6-44). This clearly indicated a chemisorption of CO_2 as also suggested by the value of heat of adsorption ($69\text{ kJ}\cdot\text{mol}^{-1}$, see Table 6-17) calculated for the PEI-coated carbon, which falls in the range of values usually associated with chemisorbents [58]. It is worth pointing out that it was possible to quantify a reliable figure of the adsorption enthalpy (i.e. integral of heat flow curve) for AR and AR-PEI because these exhibited a distinct peak as atmosphere was changed to 15% CO_2 (see Figure 6-44). On the other hand, samples did not attain any well-defined peak during desorption stage, thus not discrimination between contributions from nitrogen and carbon dioxide.

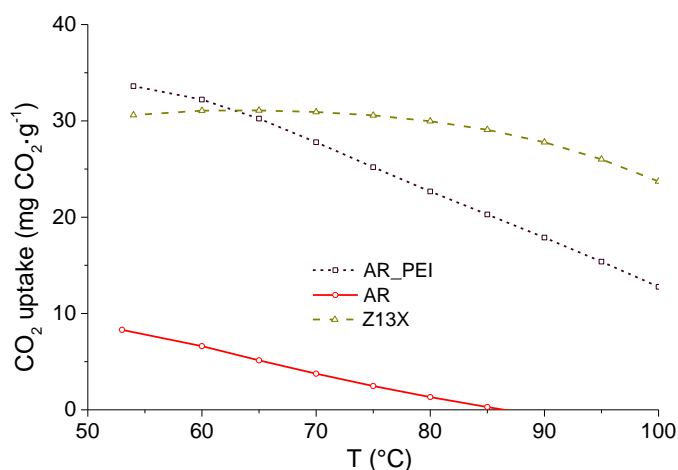


Figure 6-43 Regeneration (RTSA, 53-100 °C): comparison of virgin carbon, optimally PEI-impregnated carbon and Z13X

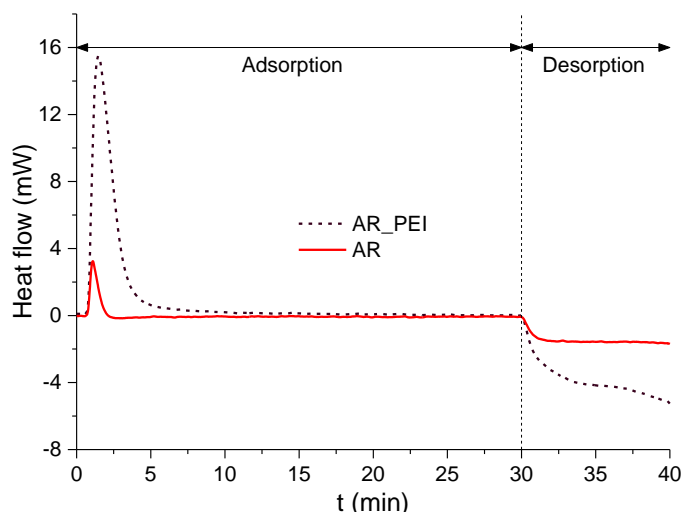


Figure 6-44 Heat flow related to adsorption and desorption of CO₂ under simulated post-combustion conditions: comparison of virgin carbon and optimally PEI-impregnated carbon

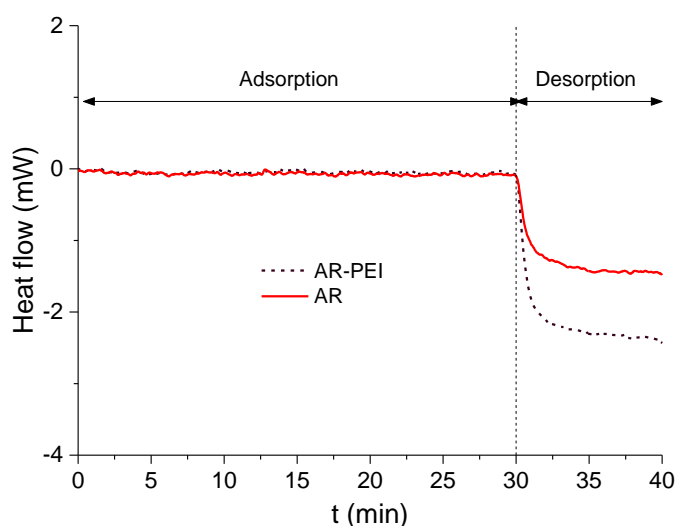


Figure 6-45 Heat flow related to adsorption and desorption of N₂ under simulated post-combustion conditions: comparison of virgin carbon and optimally PEI-impregnated carbon

However, in an attempt to disentangle the influence of the two gases on the heat flow related to the desorption process, values reported in Table 6-18 were corrected for the contribution associated with desorption of pure nitrogen (see methodology description in Chapter 3). In particular, the integral of the heat flow measured under pure nitrogen (Figure 6-45) was subtracted from the integral value obtained under 15% CO₂/85% N₂ mixture (Figure 6-44) over the same interval (30-40 min). In addition to this, the actual moles of desorbed CO₂ were assumed to be yielded by the (CO₂ + N₂) moles desorbed from the sample under 15% CO₂/85% minus the (N₂) moles desorbed from the sample under

pure nitrogen (see Figure 6-45). The heat of adsorption/desorption was then calculated as total enthalpy of adsorption/desorption divided by the adsorbed/desorbed moles of CO₂.

Table 6-17 Differential Scanning Calorimetry (DSC) data related to the adsorption of CO₂ - Total enthalpy was calculated as the integral of heat flow for 0<t<30 min. Heat of adsorption was calculated as total enthalpy divided by adsorbed moles of gas.

Sample ID	Adsorption		
	Total enthalpy	Adsorbed CO ₂	Heat of adsorption (ΔH_{ads})
	mJ	mol	kJ·mol ⁻¹
AR	137	3.9E-06	35
AR_PEI	1717	2.5E-05	69

Table 6-18 DSC data related to desorption of CO₂ and pure N₂. Total enthalpy was calculated as the integral of heat flow for 30<t<40 min. Heat of desorption was calculated as total enthalpy divided by desorbed moles of gas.

Sample ID	Desorption		
	Total enthalpy	Desorbed CO ₂	Heat of desorption (ΔH_{des})
	mJ	mol	kJ·mol ⁻¹
AR_tot ⁶⁴	833	5.2E-06	159
AR_N ₂ ⁶⁵	721	2.5E-06	-
AR_CO ₂ ⁶⁶	112	2.7E-06	41
AR-PEI_tot	2306	1.6E-05	145
AR-PEI_N ₂	1232	1.8E-06	-
AR-PEI_CO ₂	1073	1.4E-05	76

Corrected values of the heat of desorption approximately agree with the heat of adsorption figures (see Table 6-17 and Table 6-18 respectively) for both samples. Note that, the slightly higher heat of desorption data obtained might be

⁶⁴ Run under 15% CO₂/85% N₂ mixture (see Figure 6-44)

⁶⁵ Run under pure N₂ (see Figure 6-45)

⁶⁶ Corrected estimation. Values of total enthalpy and desorbed moles of CO₂ were calculated by difference (¹⁹⁻²⁰)

explained through a higher amount of N₂ adsorbed onto the samples under pure nitrogen atmosphere (no competition from CO₂). The extra moles of adsorbed nitrogen would then imply an underestimation of the actual moles of adsorbed CO₂, and therefore resulting in slightly higher values of the corrected heat of desorption. As given in Table 6-18, the heat of desorption measured for the PEI-loaded carbon was ca. 76 kJ·mol⁻¹ is in agreement with the less easy regeneration observed for this sample in comparison to AR (see Figure 6-43). This further corroborates the existence of a chemisorption contribution in the CO₂ uptake process for AR-PEI. Interestingly, the desorption enthalpy required for the regeneration of the PEI-modified carbon was much lower than the energy consumption needed to regenerate a 30% MEA solution (209 kJ·mol⁻¹) [30].

6.5.2 Cyclic post combustion capture for the optimally PEI-impregnated carbon

Figure 6-46 illustrates the main steps of the cyclic run performed for the optimally PEI-impregnated carbon. In particular, after degassing the sample for 30 min under N₂, the material was subjected to multiple cycles. Each cycle consisted of three main stages. First, sample was cooled down from 120 °C (degassing/regeneration temperature) to ca. 53 °C (sorption temperature). During this stage (ca. 22 min) the sample weight increased, thus indicating a minor uptake of nitrogen onto the material. After this (at ca. 52 min), the atmosphere was switched to 15% CO₂/85% N₂ and the sorption kinetic was measured for 30 min. Finally, the solid sorbent was regenerated by swinging the temperature up to 120 °C. This step was quite fast (ca. 14 min) in order to simulate RTSA as the regeneration strategy. At the end of the regeneration step, atmosphere was then switched back to pure nitrogen in order to start the second cycle.

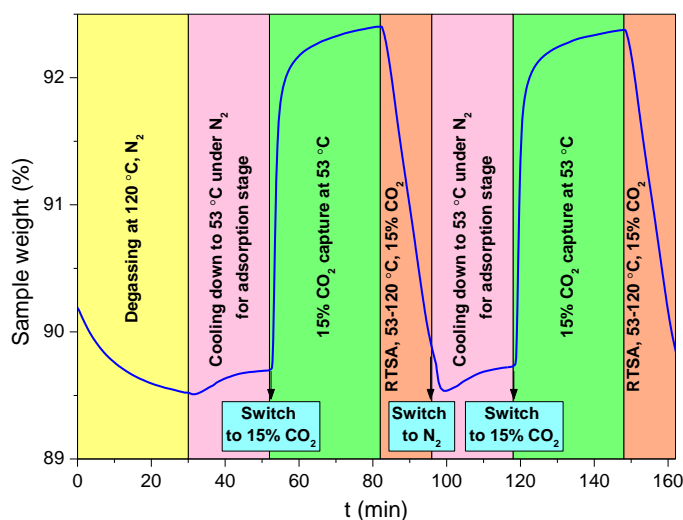


Figure 6-46 Illustration of RTSA cycling experiment (first 2 cycles only) carried out for the optimally PEI-impregnated carbon under simulated post-combustion conditions ($T \approx 53\text{ }^{\circ}\text{C}$, $P_{\text{CO}_2} = 0.15\text{ bar}$, $P_{\text{tot}} = 1\text{ bar}$).

Figure 6-47 illustrated the energetic processes occurring during the first RTSA cycle of the CO_2 sorption test. The upward (exothermic) DSC peak was associated with the adsorption of CO_2 as also shown by the increase of sample weight. The position of the heat flow peak indicates that the highest CO_2 uptake rate was achieved at ca. 2.5 min. Indeed, the speed of adsorption appeared to become slower and slower with increasing time. During the desorption stage the sample was heated up in order to remove CO_2 from the sorption sites. This endothermic process caused a negative heat flow from the sample as reflected by the heat flow profile which starts to decline at $t = 30\text{ min}$.

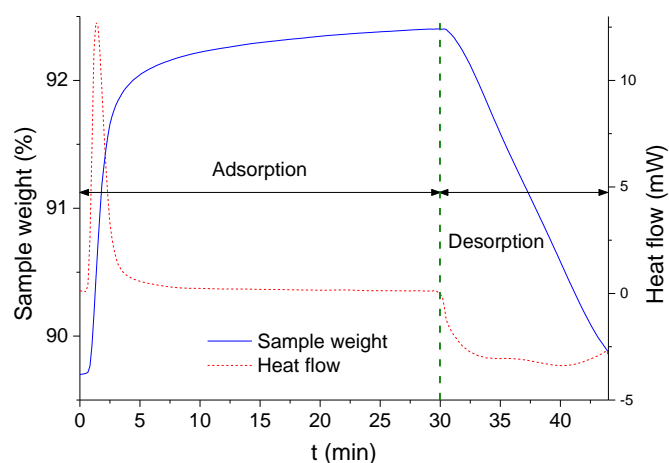


Figure 6-47 Heat flow related to adsorption and desorption of CO_2 under simulated post combustion conditions during the first RTSA cycle

The regeneration performance of the best performing PEI-impregnated carbon over 10 cycles is reported in Figure 6-48(a). Despite the sample's high

heat of desorption (see Table 6-17), CO₂ was fully desorbed after each cycle at a relatively low temperature (120 °C). Moreover, the desorption kinetics exhibited by AR-PEI were quite rapid, with sorbent being regenerated in ca. 14 minutes. This suggests that RTSA could be successfully applied as the regeneration strategy in a real world application.

Furthermore, as seen in Figure 6-48(b), the maximum CO₂ capacity of the sample remained nearly constant over ten adsorption-desorption cycles, thus demonstrating a potential long lifetime for the PEI-modified carbon. The slightly decreasing trend might be due to urea formation, as this is not removed at 120 °C [214]. Additionally, it is worth mentioning that the sorption capacity of the polymer-loaded carbon would probably be even larger under real post-combustion conditions because the presence of moisture in the flue gas (not considered in this study) is believed to enhance the chemisorption of CO₂ onto amines [230].

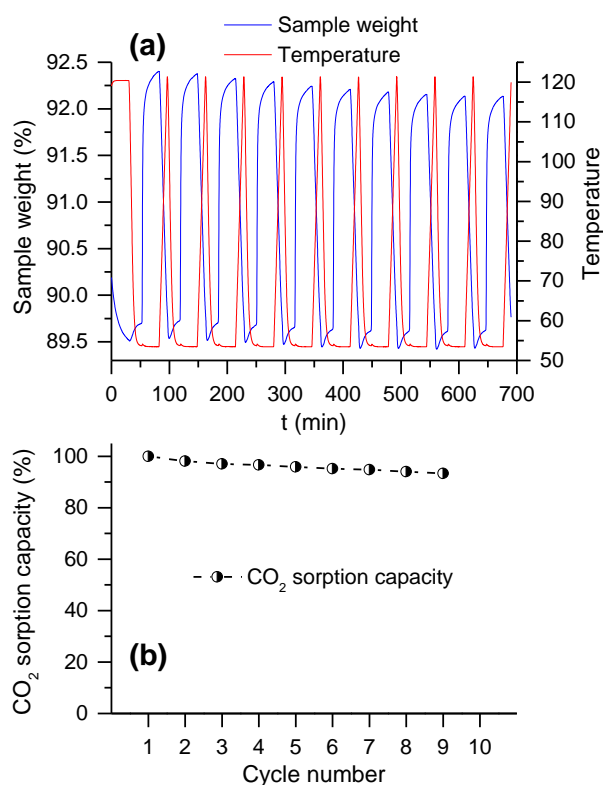


Figure 6-48 (a) Regeneration performance and (b) Cyclic capacity over ten RTSA cycles for the optimally PEI-impregnated carbon

6.6 Chapter Conclusions

The CO₂ sorption capacity of an activated carbon under simulated post-combustion conditions was successfully enhanced through wet impregnation of amines. Polyethyleneimine was initially chosen as the main impregnating agent.

The PEI impregnation was systematically optimized. The characterization of the optimally PEI-impregnated carbon confirmed that PEI was successfully loaded onto the porous network of the virgin carbon support.

A primary optimization was performed by maximizing post combustion CO₂ uptakes at 53 or 77 °C as a function of the polymer loading, the stirring time of the polymer/solvent/carbon mixture and the solvent type used to dissolve the polymer.

Interestingly, for the same (optimal) polymer loading and for any solvent and sorption temperature, a prolonged agitation (i.e. stirring time > 0.5 h) during polymer impregnation led to a general improvement of the CO₂ sorption capacity of the PEI-impregnated samples. However, the value of the stirring time that maximized CO₂ uptake varied depending upon the solvent type and the sorption temperature. Overall, it was noticed that, under identical conditions of polymer loading and solvent type, the fraction of pore volume filled with polymer increased with increasing stirring time. Therefore, the increase of CO₂ uptake, despite decreasing pore volume, was attributed to the beneficial effect of a thorough agitation at engendering a good dispersion of the polymer into the pore channels, thus leading to an optimized exploitation of the carbon support. Moreover, the positive effect of the stirring time on the CO₂ capture capacity of PEI-impregnated samples (using methanol as solvent) measured at 53 °C was independent of the polymer loadings examined (i.e. the same trend was observed for PEI loadings other than the optimal value).

A more complex discussion is required to explain the effect of the remaining parameters on the optimization of the CO₂ capture performance of the PEI-loaded carbons. This was because of a mutual dependency of these factors. In particular, the solvent type seemed to affect the amount of polymer loaded onto the carbon-based supports. Specifically, for a given value of stirring time, higher amounts of PEI were generally loaded onto the carbon when water was used as solvent. In addition, for a given nominal loading of PEI, the optimal solvent could thus vary because the actual PEI loading which resulted in maximum CO₂ uptake varied depending upon sorption temperature.

For instance, when measuring CO₂ uptakes at 53 °C, the impregnation conditions that maximized sorption capacity were: a nominal loading of 44 wt% (actual loading of ca. 29.6 wt%), a stirring time of 8 h and methanol as solvent. These conditions also gave rise to fast sorption kinetics, thus not implying significant diffusion limitations. In contrast, under identical conditions of nominal PEI loading and stirring time, lower CO₂ uptakes accompanied by slower kinetics were observed when using water as solvent. This was because of the higher impregnation efficiency in aqueous solvent (i.e. actual loading up to 34.3 wt%). Although this seems to suggest water as a better carrier for polymer dispersion, the higher amount of PEI actually introduced within the porous channels of the carbon during aqueous impregnation reduced the CO₂

diffusivity through the polymer film at low temperature (i.e. 53 °C). In fact, when high amounts of polymer are coated onto the pores of the carbon support, CO₂ uptake is a diffusion-controlled process, which entails a trade-off in terms of CO₂ capacity at lower temperatures (i.e. 53 °C). However, the more environmentally friendly (i.e. aqueous) impregnation resulted in CO₂ uptakes (32.1 mg CO₂·g⁻¹) nearly as large as the optimal uptake (33.6 mg CO₂·g⁻¹) attained when methanol was used, but using a lower amount of polymer (nominal loading of 38 wt%, corresponding to an actual loading of 28.6 wt%) and shorter impregnation durations (2 h).

Nevertheless, when measuring CO₂ uptakes at higher temperature (77 °C), the CO₂ sorption capacity decreased for most of the impregnated samples. This was attributed to a more dominant desorption process occurring at higher temperature. In spite of this, for either of the solvents used (methanol or water), the CO₂ sorption capability was now maximized by a higher PEI loading (50 wt%). In addition to this, for identical optimal conditions of nominal PEI loading (50 wt%) and stirring time (4 h), the more environmentally sound (i.e. aqueous) impregnation led to larger uptakes (27.3 mg CO₂·g⁻¹) than those achieved when solvent was methanol (22.5 mg CO₂·g⁻¹). This was because water facilitated higher actual PEI loading which, at this higher temperature, enabled higher CO₂ uptake due to a combination of more amine groups (from more polymer), which were more accessible to CO₂ due to its enhanced diffusivity at 77°C. In addition, for these reasons, AR_PEI_50%_W_4h was the only sample experiencing an improvement of the CO₂ sorption capacity when temperature was raised from 53 to 77 °C because the higher temperature allowed the sample to exploit its high polymer loadings (an actual loading of up to 38.8 wt% was measured for AR_PEI_50%_W_4h) as CO₂ diffusion capability increased. Specifically, when increasing temperature from 53 to 77 °C, the CO₂ transport from the external surface of the support toward the polymer bulk loaded inside the pores was accelerated. Therefore, more (chemi)sorption sites (i.e. amino groups) could become accessible to participate in CO₂ capture.

Therefore, if capture is to be accomplished at 77 °C, the more sustainable solvent (i.e. water) is preferred to methanol for preparing PEI-impregnated sorbents. Moreover, this higher temperature regime would require less cooling, as the flue gas would only need to be cooled down to 77 °C rather than 53 °C prior to entering the capture unit. Accordingly, cost associated with RTSA cycling would be potentially reduced.

Under optimal conditions of nominal PEI loading, stirring time and solvent, the use of a more porous carbon support (OW800CA) allowed the loading of a much higher amount of polymer. On the other hand, this resulted in a complete blockage of the support porosity, thus increasing diffusional limitations. Accordingly, PEI-impregnation of OW800CA led to a very limited improvement of the CO₂ sorption capacity at 53 °C. This was also ascribed to the higher number of acidic groups measured for the oak wood-based support.

Acidic functionalities are expected to react with amino groups, thus neutralizing their CO₂ chemisorption potential.

Interestingly, the impregnation of TEPA onto the commercial carbon led to larger uptakes (39.2 mg CO₂·g⁻¹) than those attained when loading PEI (33.6 mg CO₂·g⁻¹). This was ascribed to the more favourable physical properties featured by the tetraethylenepentamine molecule. In spite of this, PEI was selected as optimal impregnating agent because of its higher thermal stability, which was believed to be a key factor for minimizing amine leaching during RTSA cycling. In contrast, impregnation with MEA did not lead to any improvement of the CO₂ sorption capacity of the unmodified carbon.

The addition of glycerol to the mixture PEI/carbon/solvent did not bring any enhancement of the CO₂ sorption capacity. However, a moderate increase of speed of adsorption/desorption was observed. This was likely caused by the change of the chemisorption mechanism in presence of hydroxyl groups.

Under simulated post-combustion conditions (i.e. 53 °C and 0.15 bar partial pressure of CO₂), the best-performing PEI-impregnated sample attained a CO₂ sorption capability nearly 4 times larger than that achieved by the parent material. Amine-functionalization caused an increase of the heat of adsorption/desorption to values typical of a chemisorption process, which accounted for the improved selectivity of the sorbent for capturing CO₂ at higher temperatures and lower pressure. The optimally PEI-impregnated carbon also exhibited larger uptakes and more rapid sorption kinetics than a benchmark sorbent (i.e. Z13X). In spite of this, the CO₂ uptake attained by the best sorbent synthesized in this work (ca. 0.75 mmol·g⁻¹) is still lower than the target value (3 mmol·g⁻¹) to be reached in order to make sorption process more convenient than chemical absorption onto liquid amines. Moreover, the highest post-combustion capacity for CO₂ measured in this study falls short of the largest CO₂ uptakes reported in the literature under similar conditions (see Appendix C).

Nevertheless, the best PEI-loaded carbon fabricated in the present work was easily regenerated at a relatively low temperature (120 °C) through the RTSA strategy. In addition, the energy demand associated with the regeneration of the best performing chemisorbent was found to be only one third of that required for the state of the art technology (i.e. 30% MEA solution). Amine leaching was minimal, as the CO₂ sorption capacity remained nearly unaltered over ten working cycles. The durability of the sorbent appears to be due the thermal stability of the PEI/carbon support blend.

7 Conclusions

7.1 Biomass feedstocks

The application of *Laminaria hyperborea* (LH_S) for preparing CO₂ sorbents has been presented for the first time in this report. Novel activated carbons (ACs) were successfully synthesized through carbonization of the unconventional biomass feedstock and subsequent activation of seaweed-based biochars. Nonetheless, the traditional biomass, i.e. oak wood (OW), revealed to be a more suitable raw material for the preparation of highly porous carbons. This was mostly due to the lower percentage of inorganics contained within wood-based feedstock (1.9 wt%) compared to that found for macroalgae (18.1 wt%). As a result, carbonization (in particular pyrolysis) of wood gave rise to biochars with higher carbon purity than those obtained after seaweed processing.

However, especially after CO₂ activation, wood-derived carbons presented a higher extent of porosity. The higher amount of inorganics featured by *Laminaria hyperborea* hindered the formation of pores when mild activation (i.e. physical activation) was applied. On the other hand, regardless of the feedstock used, when chars were chemically treated (i.e. KOH activation followed by HCl washing), resulting ACs had higher purity and larger porosity in comparison to physically-activated counterparts. This was ascribed to the demineralization occurred upon acid washing. Nonetheless, under the same conditions, chemical activation of *Laminaria hyperborea* implied much lower product yields than those measured after chemical treatment of oak wood. This seems to suggest that the production of chemically-activated macroalgae on an industrial scale would be uneconomical.

Pyrolysis of wood followed by chemical activation was found to be a good compromise between product yield and porosity enhancement. Moreover, AC obtained through this preparation route attained the highest CO₂ uptake (ca. 70 mg CO₂·g⁻¹) at 35 °C, P_{CO₂}=1 bar and P_{tot}=1 bar. This result appears to indicate chemically-activated wood as a promising sorbent for pre-combustion applications (e.g. P_{tot}=30 bar).

Chemical characterization of wood-based materials revealed a predominant presence of Ca-containing compounds (e.g. calcium hydroxide, calcium carbonate) within inorganic matter. Conversely, investigations on the chemistry of *Laminaria hyperborea*-derived products allowed identifying a major presence of Na and K chlorides along with magnesium oxide on macroalgae-based char and physically activated counterpart. It is worth noting that, due to the demineralization occurred after HCl washing, the greater part of the

inorganic species present onto raw biomass, chars and physically-activated carbons were not found within the structure of chemically-ACs. Nevertheless, the presence of alkaline species onto biomass-derived samples was reflected by the high basicity of the materials, which was proved to play a key role in the CO₂ uptake process under post-combustion conditions (53 °C, 0.15 bar). In fact, in-house ACs outperformed a commercial carbon having better textural properties but significantly lower inorganic fractions. However, the effect of inorganic matter was more pronounced for seaweed-derived products, showing a CO₂ (chemi)sorption behaviour similar to that observed for magnesium oxide.

Interestingly, the exploitation of alkali metals intrinsically contained within the structure of macroalgae enabled achieving a greener and cheaper fabrication of alkali-based sorbents compared to procedures previously reported in the literature. Moreover, the use of a widely available raw material (i.e. seaweed) for the manufacture of CO₂ sorbents promoted the environmental sustainability of the entire process.

7.2 Carbonization routes

Hydrothermal carbonization (HTC) of biomass used in this work gave rise to poorly carbonized chars compared to pyrolysis-derived counterparts. Hydrochars had negligible porosity, entirely composed by macropores. In contrast, a moderately larger porosity development was achieved after pyrolysis, with the creation of microporosity to some extent. The milder heat-treatment (250 °C) entailed by HTC did not properly devolatilize the raw materials. As a result, hydrochars presented a well higher fraction of volatiles (up to 58.5 wt%) within their structure compared to that found for pyrolyzed derivatives (below 21 wt%). Consequently, further removal of volatiles occurred during activation treatments of hydrochars. This was reflected in a more dramatic texture development experienced by HTC-derived chars. In addition to this, ACs obtained from the chemical activation of hydrochars exhibited higher surface area than those obtained after chemically-treating pyrolyzed analogues. In particular, the highest surface area herein reported (2757 m²·g⁻¹) was attained after (optimal) chemical activation of *Laminaria hyperborea*-derived hydrochar. Nevertheless, the best textural properties achieved by chemically-activated hydrochars corresponded to lowest product yields (<3 wt%), which would impede the commercialization of these materials. By contrast, physical activation of hydrochars led to much higher carbon yields (in excess of 50 wt%). Also, CO₂-activated hydrochars attained relatively high CO₂ uptakes (around 40 mg CO₂·g⁻¹) at 35 °C and 1 bar (total pressure of 1 bar), thereby indicating potential application for pre-combustion capture.

Unexpectedly, hydrothermal synthesis of *Laminaria hyperborea* yielded to a slightly higher proportion of fixed carbon and to a much lower ash content

compared to those recorded for pyrolyzed macroalgae. This result was ascribed to the dissolution of inorganic species within the aqueous HTC process, thus causing a relatively higher purity in carbon for hydrochars in comparison to that of pyrolysis-derived samples. Moreover, although HTC of *Laminaria hyperborea* and oak wood led to hydrochars containing a similar fraction of fixed carbon (33.5 wt% and 32.9 wt% respectively), carbonization yield obtained after HTC of *Laminaria hyperborea* (ca. 34 wt%) was substantially lower than that obtained for hydrothermally carbonized wood (ca. 58.5 wt%). This finding was attributed to the higher levels of lignin usually contained by wood-based biomass, which are believed to favour biomass conversion into char. Interestingly, pyrolysis of *Laminaria hyperborea* implied higher carbonization yield (ca. 27 wt%) compared to that measured for pyrolyzed wood (21.50 wt%). This was ascribed to the catalytic effect of inorganic fractions (especially K) contained within macroalgae, which seems to increase char production. However, pyrolyzed *Laminaria hyperborea* had a much lower proportion of fixed carbon (27.5 wt%) than that exhibited by pyrolyzed wood (66.1 wt%). This was probably due to the lack of ash-free organic matter contained within *Laminaria hyperborea*, which could not be converted into ash-free carbon.

Overall, pyrolysis seems to be the recommended route for the fabrication of chars when further treatment (activation) needs to be pursued. Indeed, with particular regard to oak wood, pyrolytical process created a more stable product with a larger amount of fixed carbon available for porosity formation. By contrast, HTC could be potentially cheaper (less energy demanding) than pyrolysis for the production of functionalized biochars, especially when starting from wet feedstock, as no pre-drying would be required. In addition to this, the amount of char formed after HTC was generally larger (in excess of 55 wt%) than that produced through dry pyrolysis (up to ca. 27 wt%), thus suggesting a more cost-effective production of biochars. These may be suggested for use in applications other than that studied in this work, such as soil amendments.

7.3 Activation methods

Porosity of biochars was enhanced through the application of two activation methodologies, i.e. physical (CO₂) and chemical (KOH) activation.

CO₂ activation generally implied a limited development of the textural properties of carbonized materials. This was particularly true for seaweed-based chars and was mostly due to the mildness of the physical treatment. In fact, controlled oxidation under CO₂ did not remove inorganic particles, which were left within the pore cavities.

Procedure optimization led to a maximum surface area of ca. 627 m²·g⁻¹ achieved after activation of pyrolyzed oak wood at 800 °C for 1 h. As concerns

pyrolyzed *Laminaria hyperborea*, the highest surface area ($189 \text{ m}^2\cdot\text{g}^{-1}$) was attained at a slightly lower temperature ($700 \text{ }^\circ\text{C}$) held for a dwell time of 30 min. Maximum surface areas corresponded to optimal burn-offs of 34 wt% and 13 wt% respectively. The lower surface per unit of burn off obtained for *Laminaria hyperborea*-derived AC was attributed to the lower proportion of fixed carbon featured by carbonized *Laminaria hyperborea*. Higher intensities (i.e. temperatures/residence times) of activation resulted to be detrimental for the texture of the carbons.

The effect of the activation temperature on the variation of textural parameters of the final carbons was more drastic compared to that of holding time when considering a 30 min increment. However, when increasing time step from 30 to 60 min (see activation of OW800 in Chapter 4), a more dramatic influence of the residence time on the activation burn-off was observed, which was reflected in a higher variation of the textural parameters.

Regarding CO_2 activation of HTC-derived products, surface area was maximized when temperature was $600 \text{ }^\circ\text{C}$ and dwell time was 30 min. Optimal burn-offs (46 wt% and 48 wt% for oak wood and *Laminaria hyperborea*-based carbons respectively) were larger than those found for pyrolyzed analogues. This was likely due to the additional devolatilization experienced by hydrochars during heat-treatment under carbon dioxide. Observations also indicated $550 \text{ }^\circ\text{C}$ as the probable onset temperature for an efficient reaction between carbon dioxide and hydrochars. On the other hand, when increasing the intensity of activation (i.e. $T > 650 \text{ }^\circ\text{C}$, burn-off $> 46 \text{ wt}\%$), damage of porous structure was observed.

In contrast, chemical method (KOH activation and subsequent HCl rinsing) enabled a more dramatic enhancement of porosity. Apparently, the use of KOH as activating agent resulted in a more intense attack to the carbon structure. In addition to this, acid washing step was essential not only for removing any residual potassium-based compounds deposited within the pores, but also for etching other mineral matter, which might have functioned as an in-situ template for the creation of additional pores. Accordingly, chemically-activated carbons generally exhibited higher carbon purity and far more developed porous network than their physically-activated analogues. Surface area optimization performed for *Laminaria hyperborea*-derived chars led to identical optimal conditions in terms of temperature ($750 \text{ }^\circ\text{C}$) and KOH:char ratio (4:1). Nevertheless, it is worth noticing that when activation conditions were severe ($T > 550 \text{ }^\circ\text{C}$, KOH:char ratio > 1), carbons exhibited a more heterogeneous distribution of pores, with contributions from different pore widths but predominant proportion of larger pores (meso and macropores). Conversely, a milder chemical treatment ($T = 550 \text{ }^\circ\text{C}$, KOH:char ratio = 1) as well as physical activation revealed to be more suitable for tailoring the manufacture of carbons with narrower pore size distributions, featuring mostly microporosity, with major contribution from ultramicropores ($d < 0.7 \text{ nm}$).

Chemical treatment allowed producing carbons that exhibited superior surface areas and larger sorption capacities at 35 °C and pure CO₂ ($P_{\text{CO}_2}=1$ bar) than those attained by CO₂-ACs. Nonetheless, chemical method implied much lower carbon yields than those obtained for physical activation, in particular for hydrochars-derived ACs. In addition to that, ACs obtained after chemical activation were in the form of a very fine powder, especially when applying severe conditions. The low mechanical strength of the chemically-ACs particles impedes their application in industry (e.g. adsorption column). Thus, milder KOH activation or physical treatment might represent a more suitable option for producing CO₂ sorbents suitable for pre-combustion capture, as higher carbon yield, stronger particles and larger ultramicroporosity will be obtained.

Conversely, physical treatment resulted to be more beneficial for CO₂ sorption performance of the carbons under post-combustion conditions. Indeed, most of (alkali metal-containing) inorganic species incorporated within chars were largely retained after heat-treatment under CO₂. Alkali metal-based functionalities were evidently responsible for selective sorption of CO₂ under reduced pressure ($P_{\text{CO}_2}=0.15$ bar). In contrast, most of inorganic matter was removed after chemical treatment of the chars, thus causing a lower sorption capability under post-combustion conditions.

In addition to this, CO₂ activation represents a more eco-friendly and cheaper methodology for the manufacture of ACs, as this route poses a lower cost and environmental impact in comparison to that implied by the chemical treatment (i.e. no use of chemicals such as KOH and HCl).

7.4 Chemical modification of carbons

Optimized impregnation of polyethileneimine (PEI) dramatically improved the CO₂ sorption capacity of a commercial carbon (defined as AR) under post-combustion conditions (i.e. 53 °C, $P_{\text{CO}_2}=0.15$ bar, and $P_{\text{tot}}=1$ bar). The sorption capacity of the impregnated carbon prepared under optimized conditions was ca. 4 times larger than that observed for the parent support, and more than 3 times higher than that achieved by the best performing virgin carbon examined in this study. The maximum uptake (up to 33.6 mg CO₂·g⁻¹) was attained for a nominal loading of 44 wt% (actual loading of 31 wt%), a stirring time of the solvent/polymer/carbon mixture of 8 h and methanol as solvent. A series of characterization techniques performed on the optimally-impregnated carbon proved that PEI was successfully loaded onto the porous support.

Overall, optimization of the chemical impregnation procedure led to infer that, for a common amount of polymer loaded onto the porous support and for any type of carrier (methanol or water), longer agitations of the solvent/polymer/carbon blend generally enhanced the post-combustion CO₂

capture performance of the PEI-coated carbons. This behaviour was associated with a more facile dispersion of the polymer into the pore channels when longer agitations were applied, thereby leading to an optimized utilization of the porous support.

Importantly, the effects of solvent type, PEI loading and sorption temperature appeared to be mutually related. In the first place, regardless of the stirring time, using water as solvent always allowed loading larger amounts of polymer onto the carbon support, thus indicating aqueous solvent as a better carrier for polymer dispersion. Secondly, the optimal PEI loading (and therefore the kind of solvent) resulted to be temperature-dependent. In essence, at lower temperature (i.e. 53 °C), a lower actual PEI loading (31 wt%), coupled with methanol as solvent, enabled achieving the absolute maximum CO₂ sorption capacity (33.6 mg CO₂·g⁻¹) and the fastest CO₂ kinetics.

Irrespective of the impregnation conditions, except for one sample (AR_PEI_50%_W_4h), CO₂ sorption capacity always decreased when increasing temperature from 53 to 77 °C, thus indicating that CO₂ uptake process was mostly governed by thermodynamic (sorption) effects. However, the higher temperature (77 °C) implied a change in the optimal conditions maximizing CO₂ uptakes. Specifically, the largest CO₂ sorption capacity (27.3 mg CO₂·g⁻¹) exhibited by AR_PEI_50%_W_4h was obtained for a nominal loading of 50 wt% and using water as solvent. In addition to this, AR_PEI_50%_W_4h was the only sample exhibiting an increase of CO₂ sorption capacity when temperature was raised from 53 to 77 °C. The increase of sorption capability with increasing temperature was explained through the enhancement of the CO₂ diffusion mechanism at higher temperature, which governs the CO₂ uptake process (kinetically-diffusion controlled) when high amount of PEI are loaded onto the pore channels of the carbon support. Indeed, the increased temperature favoured the CO₂ transport through the PEI film/pore channels, thus increasing the number of CO₂-capturing sites that actually contribute to the chemisorption process. Hence, a more environmentally sound (aqueous) impregnation is the ideal solution for the preparation of chemisorbents when capturing CO₂ at 77 °C. In fact, this would also imply a lower energy penalty due to the regeneration of the sorbents when using rapid temperature swing adsorption (RTSA) cycling as strategy, because the cooling step of the flue gas prior to entering the capture unit would be less energy-intensive.

The set of optimal conditions determined at 53 °C was used for assessing the effect of further parameters. In particular, the use of the chemically-activated oak wood (i.e. OW800CA) as an alternative porous support did not improve the sorption capacity attained by PEI-modified AR. This was likely due to the higher amount of acidic functionalities present onto the surface of the oak wood-based support in comparison to those measured for

the commercial substrate. Indeed, acid groups might have neutralized most of the amino groups present within the PEI chain.

At 53 °C, CO₂ uptakes attained an absolute maximum (39.2 mg CO₂·g⁻¹) when impregnating agent was tetraethylenepentamine (TEPA), while monoethanolamine (MEA) did not lead to any improvement of the capacity of the parent carbon. The more efficient impregnation of TEPA was probably due to the lower viscosity and density featured by this molecule compared to those typical of PEI. On the other hand, PEI was preferred to TEPA because of its higher thermal stability, which was considered a priority when testing recyclability of the sorbents through RTSA.

Although lower CO₂ uptakes were measured when adding glycerol to the PEI/carbon/solvent blend, adsorption and desorption kinetics were found to be slightly faster. In addition to this, glycerol-containing and glycerol-free samples exhibited comparable “amine efficiency” (CO₂ captured:N molar ratio). These findings were ascribed to the introduction of hydroxyl groups, which appeared to change the chemisorption mechanism.

In general, amine-functionalization allowed having a significant chemisorption contribution, which accounted for improving the selectivity of the sorbents at capturing CO₂ at higher temperatures and lower pressure (post-combustion scenario). Best performing PEI-loaded carbon exhibited larger sorption capacity and faster sorption kinetics than a benchmark sorbent (i.e. zeolite Z-13X (Z13X)). In addition to this, best solid chemisorbent fabricated in this work showed easiness of regeneration at a relatively low temperature (120 °C) when applying RTSA as strategy. Although a minor part of amines leached from the sorbent, the CO₂ sorption capacity was found to remain approximately constant over ten adsorption/desorption cycles, thereby indicating good durability.

The optimal chemisorbent synthesized in this work exhibited a less energy-intensive regeneration compared to that of the state-of-the-art technology (30% MEA solution). This may compensate the lower chemisorption capacity possessed by PEI-modified AC in comparison to that of 30% MEA solution. Therefore, the industrial implementation of a CO₂ capture unit based on the solution proposed in this study (adsorption onto solid sorbents) might be potentially more convenient than the conventional post-combustion technology (absorption onto liquid amines), if used in a combustion-based power plant.

7.5 The mechanism of CO₂ uptake onto virgin and chemically-modified activated carbons

Oak wood-derived ACs, with specific regard to the chemically-activated sample (OW800CA), generally exhibited sorption performance typical of physisorbents. CO₂ uptake process appeared to be mostly due to physical adsorption (Van der Waals forces) of carbon dioxide onto the pores surface, especially at lower temperature (35 °C) and higher partial pressure of CO₂ (1 bar). This was corroborated by very fast sorption kinetics and significant decline of sorption capacity with increasing temperature. Nevertheless, under post-combustion conditions (53 °C, P_{CO₂}=1 bar and P_{tot}=1 bar), physically-activated oak wood (OW800PA) showed a higher sorption capacity than that of samples having more developed texture but lower basicity (i.e. OW800CA and GAC). This was explained through a weak chemisorption contribution given by alkali (Ca)-based surface functionalities present within the structure of OW800PA. The latter's stronger interaction with CO₂ was corroborated by the higher energy of adsorption obtained from the measurement of CO₂ adsorption isotherms at 0 °C, following the sequence OW800PA>OW800CA>GAC. Results highlighted that basicity outweighed texture contribution in terms of CO₂ capture potential when increasing sorption temperature and decreasing the CO₂ partial pressure. Despite the relatively low sorption temperature (53 °C), findings seemed to suggest that carbonation reaction between Ca-containing compounds (i.e. calcium hydroxide) and carbon dioxide might have occurred to a minor extent.

Conversely, stronger evidence of a chemisorption mechanism was reported for seaweed-based sorbents. In particular, at higher temperature and lower pressure (post-combustion conditions), pyrolyzed *Laminaria hyperborea* (LH_S800) and its physically (CO₂)-activated derivative (LH_S800PA) exhibited a larger CO₂ sorption capacity than that measured for chemically-activated macroalgae (LH_S800CA). The latter sorbent had much larger surface areas but lower level of alkali metals compared to the former materials, and its sorption behaviour was typical of physisorbents. Moreover, under post-combustion conditions, sorption kinetics measured for LH_S800 and LH_S800PA were found to be similar to that observed for magnesium oxide. This agreed with the presence of MgO crystals onto the seaweed-derived sorbents. On the other hand, CO₂-activated *Laminaria* exhibited higher sorption potential and faster kinetics in comparison both to the parent char and to pure magnesium oxide. This was ascribed to the slight increase of porosity after physical activation of macroalgae-based char. The improved porous network exhibited by LH_S800PA not only ensured a higher physisorption contribution, but it might have also favoured the migration of CO₂ toward the chemisorption sites (MgO crystallites). These observations led to infer that uptake of CO₂ onto LH_S800PA was due to a synergetic contribution of chemisorption (carbonation

reaction between magnesium oxide crystals and CO₂) and physisorption (increased porosity) processes. Furthermore, the strength in the CO₂ sorption process occurring onto macroalgae-derived sorbents agreed with the calculated energy of adsorption at 0 °C, which followed the order LH_S800>LH_S800PA>LH_S800CA. Nonetheless, sorbents were partly (LH_S800) or fully (LH_S800PA) regenerated at very low temperature (100 °C), thus revealing a relatively weak intensity of the chemisorption process. The reconversion of MgCO₃ into MgO was attributed to a weak interaction between CO₂ and the MgO particles not embedded within the framework of the carbon-based sorbent (i.e. magnesium oxide crystals anchored onto the carbon surface). However, it is worth mentioning that, the more facile regeneration observed for LH_S800PA seemed to suggest a change in the sorption mechanism of CO₂ following to physical activation of pyrolyzed *Laminaria hyperborea*. In particular, Na and/or K-based carbonates might have formed. These can absorb CO₂ under moist conditions, giving rise to alkali-metals bicarbonates, which can be easily regenerated at low temperature (100-200 °C).

Unlike virgin carbons, a distinct chemisorption behaviour was observed for amine-modified sorbents. In fact, the incorporation of PEI onto the commercial carbon (AR) used as support caused an increase of the heat of adsorption/desorption to values typically measured for chemisorbents (69-74 kJ·mol⁻¹). This proved that CO₂ uptake process changed from physisorption to chemisorption. In addition, in this case chemisorption mechanism was due to the typical two-step reaction occurring between amines and carbon dioxide. In contrast to results reported in the literature, the addition of an OH-containing guest (glycerol) to the polymer/solvent/AC system did not lead to any increase of the CO₂ chemisorbed onto amine-containing sorbents. This was likely due to additional pore blockage and resistance to gas diffusion involved by the presence of glycerol. Nonetheless, glycerol-containing samples exhibited nearly as large amine efficiency as that calculated for glycerol-free sorbents. Furthermore, slightly higher adsorption/desorption rates were measured for glycerol-doped materials. These results seemed to suggest that the introduction of hydroxyl groups promoted CO₂ conversion but to a low extent.

As already mentioned, findings reported in this work also highlighted that CO₂ uptake process occurring onto amine-modified carbons was influenced by the sorption temperature and by the amount of PEI actually loaded onto the porous support. In particular, when sorption temperature was 53 °C, the highest CO₂ uptake was achieved for relatively lower PEI actual loading, and thermodynamic (sorption) effect was the predominant feature of the capture process. Conversely, when loading a higher concentration of PEI, uptake process was mostly governed by diffusion mechanism, which adversely affected CO₂ capture performance (i.e. slower uptake rate and lower capacity) at lower temperature. However, with increasing sorption temperature (77 °C), the

maximum uptake was attained when loading higher amount of polymer (i.e. kinetically-diffusion controlled process) as diffusion effects became more dominant. This was ascribed to the increase of the CO₂ diffusivity through the PEI gel with increasing temperature.

7.6 Directions for future work

- This work shows that inorganics (i.e. alkali metal-based functionalities) resulted to be more influential than texture in the post-combustion capture of CO₂. This is particularly true for *Laminaria hyperborea*-derived products, as these materials exhibited a significant (chemi)sorption potential, which was mostly attributed to the presence of magnesium oxide particles within their structure. Therefore, in order to optimize the sorption potential of alkali metals-containing carbon materials, it might be worth testing alternative precursors having a higher amount of ash (with particular regard to Mg-containing fractions) than that measured for *Laminaria hyperborea*. For instance, *Laminaria hyperborea* usually has a higher concentration of inorganics when collected in winter season. However, it may be also worthwhile synthesizing carbons starting directly from Mg-alginates, which might be potentially lead to even larger CO₂ chemisorption capacities of the final sorbents.
- Activation of hydrochars was generally found to be an inconvenient route for the fabrication of activated carbons. In fact, physical treatment did not significantly develop the porosity of the hydrochars, whereas chemical treatment resulted in very low activation yields. On this basis, in an attempt to obtain larger surface areas along with higher carbon yields, it would be interesting to develop a one-step treatment, which would entail blending the raw material with an appropriate activating agent prior to running HTC (i.e. carbonization and activation occur simultaneously).
- Correlations between textural parameters and CO₂ uptakes at 35 °C and 1 bar reported in this work indicate that both surface area and ultramicropore volume are affecting the CO₂ sorption capacity of the carbons at high gas partial pressure and relatively low temperature. However, in an attempt to further investigate on this correlation, a wider range of samples should be included. Additionally, it would be interesting to determine activation treatments' optimal conditions for maximum ultramicropore volume rather than for largest surface area. This could potentially lead to even larger CO₂ uptakes at 35 °C and 1 bar.
- Results reported in Chapter 5 reveal a (chemi)sorption potential for some of the seaweed-derived sorbents. In particular, the sorption performance of pyrolyzed *Laminaria hyperborea* was improved after CO₂ activation, which caused a moderate development of the texture without implying a significant demineralization. However, it would be worth trying to refine

the intensity/type of activation treatments in an attempt find a trade-off between porosity and concentration/form (e.g. MgO, NaCO₃, K₂CO₃) of alkali metal-containing functionalities. In this regard, it may be worth studying the CO₂ sorption performance of the KOH-activated counterpart submitted to water-washing only. Indeed, in contrast to acid-washing, aqueous rinsing might free the pore structure from the majority of the K salts without eliminating most of the inorganic content (alkali metals). Therefore, given that the CO₂ uptake seems to be optimized by a synergistic effect of textural development and chemisorption on the inorganic content, water-washed sample might be proven to be an even more optimal CO₂ sorbent than that deemed in this study.

- In this work, highly porous carbons were obtained when pursuing chemical activation. Chemically(KOH)-activated carbons attained the highest CO₂ uptakes at 35 °C, P_{CO2}=1 bar and P_{tot}=1 bar. These findings suggest that these materials could be promising for pre-combustion capture of CO₂. However, in order to be applicable in a pressure swing adsorption (PSA) unit for CO₂/H₂ separation, the CO₂/H₂ selectivity of the sorbents needs to be assessed. Thus, further adsorption tests at higher total pressure (i.e. 5-40 bar) and under multi-component gas phase typical of the shifted-syngas for pre-combustion capture would be required.

List of References

1. Quadrelli, R. and S. Peterson, *The energy–climate challenge: Recent trends in CO₂ emissions from fuel combustion*. Energy Policy, 2007. **35**(11): p. 5938-5952.
2. Jacobson, M.Z., *Correction to “Control of fossil-fuel particulate black carbon and organic matter, possibly the most effective method of slowing global warming”*. Journal of Geophysical Research, 2005. **110**(D14): p. D14105-D14105.
3. Açıkyıldız, M., A. Gürses, and S. Karaca, *Preparation and characterization of activated carbon from plant wastes with chemical activation*. Microporous and Mesoporous Materials, 2014. **198**: p. 45-49.
4. CAIT Climate Data Explorer. 2015. Washington, DC: World Resources Institute. Total CO₂ Emissions Excluding Land-Use Change and Forestry (MtCO₂). [Online]. 2015 [Accessed 15 September 2015]; Available from: <http://cait.wri.org>.
5. Dhillon, R.S.S. and G. von Wuehlisch, *Mitigation of global warming through renewable biomass*. Biomass and Bioenergy, 2013. **48**: p. 75-89.
6. Adelodun, A.A., Y.-H. Lim, and Y.-M. Jo, *Effect of UV-C on pre-oxidation prior amination for preparation of a selective CO₂ adsorbent*. Journal of Analytical and Applied Pyrolysis, 2014. **105**: p. 191-198.
7. *United Nations framework convention on climate change (UNFCCC). Kyoto Protocol to the United Nations Framework Convention on Climate Change*. [Online]. 1998 [Accessed 15 September 2015]; Available from: <http://unfccc.int/resource/docs/convkp/kpeng.pdf>.
8. *United Nations framework convention on climate change (UNFCCC). Copenhagen Accord. Draft decision -/CP.15*. [Online]. 2009 [Accessed 15 September 2015]; Available from: <http://unfccc.int/resource/docs/2009/cop15/eng/l07.pdf>.
9. Lau, L.C., K.T. Lee, and A.R. Mohamed, *Global warming mitigation and renewable energy policy development from the Kyoto Protocol to the Copenhagen Accord - A comment*. Renewable and Sustainable Energy Reviews, 2012. **16**(7): p. 5280-5284.
10. Council, E., *Conclusions on 2030 Climate and Energy Policy Framework*. 2014.
11. Arent, D.J., A. Wise, and R. Gelman, *The status and prospects of renewable energy for combating global warming*. Energy Economics, 2011. **33**(4): p. 584-593.
12. Spigarelli, B.P. and S.K. Kawatra, *Opportunities and challenges in carbon dioxide capture*. Journal of CO₂ Utilization, 2013. **1**: p. 69-87.
13. Feron, P. and C. Hendriks, *Les différents procédés de capture du CO₂ et leurs coûts*. Oil Gas Sci Technol, 2005. **60**(3): p. 451-459.
14. B. Metz, O.D., H.d. Coninck, M. Loos, L. Meyer, *Intergovernmental Panel on Climate Change (IPCC) Special Report on Carbon Dioxide Capture and Storage*, 2005: Cambridge, United Kingdom and New York. p. pp. 107–171.
15. Gibbins, J. and H. Chalmers, *Carbon capture and storage*. Energy Policy, 2008. **36**(12): p. 4317-4322.
16. Padurean, A., C.-C. Cormos, and P.-S. Agachi, *Pre-combustion carbon dioxide capture by gas–liquid absorption for Integrated Gasification*

- Combined Cycle power plants*. International Journal of Greenhouse Gas Control, 2012. **7**: p. 1-11.
17. Berstad, D., P. Nekså, and G.A. Gjøvåg, *Low-temperature syngas separation and CO₂ capture for enhanced efficiency of IGCC power plants*. Energy Procedia, 2011. **4**: p. 1260-1267.
 18. Scholes, C.A., K.H. Smith, S.E. Kentish, and G.W. Stevens, *CO₂ capture from pre-combustion processes - Strategies for membrane gas separation*. International Journal of Greenhouse Gas Control, 2010. **4**(5): p. 739-755.
 19. Drage, T.C., A. Arenillas, K. Smith, and C.E. Snape. *Comparison of pre and postcombustion CO₂ adsorbent technologies*.
 20. García, S., M. Gil, C. Martín, J. Pis, F. Rubiera, and C. Pevida, *Breakthrough adsorption study of a commercial activated carbon for pre-combustion CO₂ capture*. Chemical Engineering Journal, 2011. **171**(2): p. 549-556.
 21. Lee, A., G. Xiao, P. Xiao, K. Joshi, R. Singh, and P.A. Webley, *High temperature adsorption materials and their performance for pre-combustion capture of carbon dioxide*. Energy Procedia, 2011. **4**: p. 1199-1206.
 22. Jansen, D., M. Gazzani, G. Manzolini, E.v. Dijk, and M. Carbo, *Pre-combustion CO₂ capture*. International Journal of Greenhouse Gas Control, 2015. **40**: p. 167-187.
 23. Casas, N., J. Schell, L. Joss, and M. Mazzotti, *A parametric study of a PSA process for pre-combustion CO₂ capture*. Separation and Purification Technology, 2013. **104**: p. 183-192.
 24. Herzog, H. and D. Golomb, *Carbon capture and storage from fossil fuel use*. Encyclopedia of energy, 2004. **1**: p. 1-11.
 25. Kanniche, M., R. Gros-Bonnivard, P. Jaud, J. Valle-Marcos, J.-M. Amann, and C. Bouallou, *Pre-combustion, post-combustion and oxy-combustion in thermal power plant for CO₂ capture*. Applied Thermal Engineering, 2010. **30**(1): p. 53-62.
 26. Wang, M., A. Lawal, P. Stephenson, J. Sidders, and C. Ramshaw, *Post-combustion CO₂ capture with chemical absorption: A state-of-the-art review*. Chemical Engineering Research and Design, 2011. **89**(9): p. 1609-1624.
 27. Merkel, T.C., H. Lin, X. Wei, and R. Baker, *Power plant post-combustion carbon dioxide capture: An opportunity for membranes*. Journal of Membrane Science, 2010. **359**(1-2): p. 126-139.
 28. Leci, C., *Financial implications on power generation costs resulting from the parasitic effect of CO₂ capture using liquid scrubbing technology from power station flue gases*. Energy Conversion and Management, 1996. **37**(6): p. 915-921.
 29. Goeppert, A., S. Meth, G.K.S. Prakash, and G.A. Olah, *Nanostructured silica as a support for regenerable high-capacity organoamine-based CO₂ sorbents*. Energy and Environmental Science, 2010. **3**(12): p. 1949-1960.
 30. Qi, G., L. Fu, and E.P. Giannelis, *Sponges with covalently tethered amines for high-efficiency carbon capture*. Nature communications, 2014. **5**.
 31. Olajire, A.a., *CO₂ capture and separation technologies for end-of-pipe applications – A review*. Energy, 2010. **35**(6): p. 2610-2628.

32. Goto, K., K. Yogo, and T. Higashii, *A review of efficiency penalty in a coal-fired power plant with post-combustion CO₂ capture*. Applied Energy, 2013. **111**: p. 710-720.
33. Lepaumier, H., E.F. da Silva, A. Einbu, A. Grimstvedt, J.N. Knudsen, K. Zahlse, and H.F. Svendsen, *Comparison of MEA degradation in pilot-scale with lab-scale experiments*. Energy Procedia, 2011. **4**(0): p. 1652-1659.
34. Rao, A.B. and E.S. Rubin, *A Technical, Economic, and Environmental Assessment of Amine-Based CO₂ Capture Technology for Power Plant Greenhouse Gas Control*. Environmental Science & Technology, 2002. **36**(20): p. 4467-4475.
35. Kittel, J., R. Idem, D. Gelowitz, P. Tontiwachwuthikul, G. Parrain, and A. Bonneau, *Corrosion in MEA units for CO₂ capture: Pilot plant studies*. Energy Procedia, 2009. **1**(1): p. 791-797.
36. Songolzadeh, M., M. Soleimani, M. Takht Ravanchi, and R. Songolzadeh, *Carbon dioxide separation from flue gases: a technological review emphasizing reduction in greenhouse gas emissions*. The Scientific World Journal, 2014. **2014**: p. 828131-828131.
37. S. Darling, A.L., F. Kluger, P. Monckert, G. Heinz, B. Prodhomme. *Oxy-combustion: a sound CCS solution built from pilot operation*. in *Powergen International*. 2010. Orlando, Florida, USA.
38. L. Parker, P.F. *Capturing CO₂ from Coal Fired Power Plants: Challenges for a Comprehensive Strategy*. in *Congressional Research Service*. 2010. Washington, DC.
39. Buhre, B.J.P., L.K. Elliott, C.D. Sheng, R.P. Gupta, and T.F. Wall, *Oxy-fuel combustion technology for coal-fired power generation*. Progress in Energy and Combustion Science, 2005. **31**(4): p. 283-307.
40. Yang, H., Z. Xu, M. Fan, R. Gupta, R.B. Slimane, A.E. Bland, and I. Wright, *Progress in carbon dioxide separation and capture: A review*. Journal of Environmental Sciences, 2008. **20**(1): p. 14-27.
41. Rydén, M. and A. Lyngfelt, *Using steam reforming to produce hydrogen with carbon dioxide capture by chemical-looping combustion*. International Journal of Hydrogen Energy, 2006. **31**(10): p. 1271-1283.
42. Adanez, J., A. Abad, F. Garcia-Labiano, P. Gayan, and L.F. de Diego, *Progress in Chemical-Looping Combustion and Reforming technologies*. Progress in Energy and Combustion Science, 2012. **38**(2): p. 215-282.
43. Hossain, M.M. and H.I. de Lasa, *Chemical-looping combustion (CLC) for inherent separation - a review*. Chemical Engineering Science, 2008. **63**(18): p. 4433-4451.
44. Cao, Y. and W.-P. Pan, *Investigation of Chemical Looping Combustion by Solid Fuels. 1. Process Analysis*. Energy & Fuels, 2006. **20**(5): p. 1836-1844.
45. Lyngfelt, A., B. Leckner, and T. Mattisson, *A fluidized-bed combustion process with inherent CO₂ separation; application of chemical-looping combustion*. Chemical Engineering Science, 2001. **56**(10): p. 3101-3113.
46. Moghtaderi, B., *Review of the Recent Chemical Looping Process Developments for Novel Energy and Fuel Applications*. Energy & Fuels, 2012. **26**(1): p. 15-40.
47. Adánez, J., L.F. de Diego, F. García-Labiano, P. Gayán, A. Abad, and J.M. Palacios, *Selection of Oxygen Carriers for Chemical-Looping Combustion*. Energy & Fuels, 2004. **18**(2): p. 371-377.

48. Boot-Handford, M.E., J.C. Abanades, E.J. Anthony, M.J. Blunt, S. Brandani, N. Mac Dowell, J.R. Fernández, M.-C. Ferrari, R. Gross, J.P. Hallett, R.S. Haszeldine, P. Heptonstall, A. Lyngfelt, Z. Makuch, E. Mangano, R.T.J. Porter, M. Pourkashanian, G.T. Rochelle, N. Shah, J.G. Yao, and P.S. Fennell, *Carbon capture and storage update*. Energy & Environmental Science, 2014. **7**(1): p. 130-130.
49. Race, J.M., B. Wetenhall, P.N. Seevam, and M.J. Downie, *Towards a CO₂ pipeline specification: defining tolerance limits for impurities*. Journal of Pipeline Engineering, 2012. **11**(3).
50. Leung, D.Y.C., G. Caramanna, and M.M. Maroto-Valer, *An overview of current status of carbon dioxide capture and storage technologies*. Renewable and Sustainable Energy Reviews, 2014. **39**: p. 426-443.
51. De Visser, E., C. Hendriks, M. Barrio, M.J. Mølnvik, G. de Koeijer, S. Liljemark, and Y. Le Gallo, *Dynamis CO₂ quality recommendations*. International Journal of Greenhouse Gas Control, 2008. **2**(4): p. 478-484.
52. Oldenburg, C.M., *Why we need the and in CO₂ utilization and storage*. Greenhouse Gases: Science and Technology, 2, 1-2, 2012, 2013.
53. MacDowell, N., N. Florin, A. Buchard, J. Hallett, A. Galindo, G. Jackson, C.S. Adjiman, C.K. Williams, N. Shah, and P. Fennell, *An overview of CO₂ capture technologies*. Energy & Environmental Science, 2010. **3**(11): p. 1645-1669.
54. Lackner, K.S., *A Guide to CO₂ Sequestration*. Science, 2003. **300**(5626): p. 1677-1678.
55. Herzog, H., *Carbon sequestration via mineral carbonation: overview and assessment*. Cambridge, Massachusetts: Massachusetts Institute of Technology, Laboratory for Energy and the Environment, 2002.
56. Szulczewski, M.L., C.W. MacMinn, H.J. Herzog, and R. Juanes, *Lifetime of carbon capture and storage as a climate-change mitigation technology*. Proceedings of the National Academy of Sciences, 2012. **109**(14): p. 5185-5189.
57. Mangano, E., S. Brandani, M.C. Ferrari, H. Ahn, D. Friedrich, M.L. Lozinska, P.A. Wright, J. Kahr, R. Morris, M. Croad, N. McKeown, H. Shamsipour, and P. Budd, *Efficient and Rapid Screening of Novel Adsorbents for Carbon Capture in the UK IGSCC Project*. Energy Procedia, 2013. **37**: p. 40-47.
58. Samanta, A., A. Zhao, G.K.H. Shimizu, P. Sarkar, and R. Gupta, *Post-Combustion CO₂ Capture Using Solid Sorbents: A Review*. Industrial & Engineering Chemistry Research, 2012. **51**(4): p. 1438-1463.
59. Margenau, H., *Van der waals forces*. Reviews of Modern Physics, 1939. **11**(1): p. 1-35.
60. Ruthven, D.M., *Principles of adsorption and adsorption processes*. John Wiley & Sons, 1984.
61. Breck, D.W., *Zeolite molecular sieves: structure, chemistry, and use*. Vol. 4. Wiley New York, 1973.
62. Chester, A.W. and E.G. Derouane, *Zeolite characterization and catalysis*. Springer, 2009.
63. Csicsery, S.M., *Shape-selective catalysis in zeolites*. Zeolites, 1984. **4**(3): p. 202-213.
64. De Luca, P., T. Poulsen, A. Salituro, A. Tedeschi, D. Vuono, Z. Kònya, D. Madaràsz, and J. Nagy, *Evaluation and comparison of the ammonia adsorption capacity of titanosilicates ETS-4 and ETS-10 and*

- aluminotitanosilicates ETAS-4 and ETAS-10*. Journal of Thermal Analysis and Calorimetry. **122**(3): p. 1257-1267.
65. Hargreaves, J.S.J., V.S. Batra, J.-E. Park, H.-K. Youn, S.-T. Yang, and W.-S. Ahn, *CO₂ capture and MWCNTs synthesis using mesoporous silica and zeolite 13X collectively prepared from bottom ash*. Catalysis Today, 2012. **190**(1): p. 15-22.
 66. Yu, L., J. Gong, C. Zeng, and L. Zhang, *Synthesis of binderless zeolite X microspheres and their CO₂ adsorption properties*. Separation and Purification Technology, 2013. **118**: p. 188-195.
 67. Li, G., P. Xiao, P. Webley, J. Zhang, R. Singh, and M. Marshall, *Capture of CO₂ from high humidity flue gas by vacuum swing adsorption with zeolite 13X*. Adsorption, 2008. **14**(2-3): p. 415-422.
 68. Cavenati, S., C.A. Grande, and A.E. Rodrigues, *Adsorption Equilibrium of Methane, Carbon Dioxide, and Nitrogen on Zeolite 13X at High Pressures*. Journal of Chemical & Engineering Data, 2004. **49**(4): p. 1095-1101.
 69. Bonenfant, D., M. Kharoune, P. Niquette, M. Mimeault, and R. Hausler, *Advances in principal factors influencing carbon dioxide adsorption on zeolites*. Science and Technology of Advanced Materials, 2008. **9**(1): p. 013007.
 70. Brandani, F. and D.M. Ruthven, *The Effect of Water on the Adsorption of CO₂ and C₃H₈ on Type X Zeolites*. Industrial & Engineering Chemistry Research, 2004. **43**(26): p. 8339-8344.
 71. D'Alessandro, D.M., B. Smit, and J.R. Long, *Carbon Dioxide Capture: Prospects for New Materials*. Angewandte Chemie International Edition, 2010. **49**(35): p. 6058-6082.
 72. Yaghi, O.M., M. O'Keeffe, N.W. Ockwig, H.K. Chae, M. Eddaoudi, and J. Kim, *Reticular synthesis and the design of new materials*. Nature, 2003. **423**(6941): p. 705-714.
 73. Lee, S.-Y. and S.-J. Park, *A review on solid adsorbents for carbon dioxide capture*. Journal of Industrial and Engineering Chemistry, 2015. **23**(0): p. 1-11.
 74. Bao, Z., L. Yu, Q. Ren, X. Lu, and S. Deng, *Adsorption of CO₂ and CH₄ on a magnesium-based metal organic framework*. Journal of Colloid and Interface Science, 2011. **353**(2): p. 549-556.
 75. Caskey, S.R., A.G. Wong-Foy, and A.J. Matzger, *Dramatic Tuning of Carbon Dioxide Uptake via Metal Substitution in a Coordination Polymer with Cylindrical Pores*. Journal of the American Chemical Society, 2008. **130**(33): p. 10870-10871.
 76. Dietzel, P.D.C., R.E. Johnsen, H. Fjellvag, S. Bordiga, E. Groppo, S. Chavan, and R. Blom, *Adsorption properties and structure of CO₂ adsorbed on open coordination sites of metal-organic framework Ni₂(dhtp) from gas adsorption, IR spectroscopy and X-ray diffraction*. Chemical Communications, 2008(41): p. 5125-5127.
 77. Omri, A., M. Benzina, and N. Ammar, *Preparation, modification and industrial application of activated carbon from almond shell*. Journal of Industrial and Engineering Chemistry, 2013. **19**(6): p. 2092-2099.
 78. Diaz-Terán, J., D. Nevskaja, J. Fierro, A. Lopez-Peinado, and A. Jerez, *Study of chemical activation process of a lignocellulosic material with KOH by XPS and XRD*. Microporous and mesoporous materials, 2003. **60**(1): p. 173-181.

79. Franklin, R.E. *Crystallite growth in graphitizing and non-graphitizing carbons*. in *Proceedings of the Royal Society of London, Series A, Mathematical and Physical Sciences*. 1951. The Royal Society.
80. H., M., *Introduction to carbon science*. London: Butterworths, 1989.
81. Stoeckli, H.F., *Microporous carbons and their characterization: the present state of the art*. Carbon, 1990. **28**(1): p. 1-6.
82. Zhang, Z.-l., R. Brydson, Z. Aslam, S. Reddy, A. Brown, A. Westwood, and B. Rand, *Investigating the structure of non-graphitising carbons using electron energy loss spectroscopy in the transmission electron microscope*. Carbon, 2011. **49**(15): p. 5049-5063.
83. Boehm, H., *Some aspects of the surface chemistry of carbon blacks and other carbons*. Carbon, 1994. **32**(5): p. 759-769.
84. Rodriguez-Reinoso, F., *Activated Carbon: Structure, characterisation, preparation and applications*. In: Marsh, H., Rodriguez-Reinoso, F. and Heintz, E.A.(eds) *Introduction to Carbon Technologies*. University of Alicante, Secretariado de Publicaciones, 1997.
85. Md Dali, A., A. Saadi Ibrahim, and A. Hadi, *General study about activated carbon for adsorption carbon dioxide*. Journal of Purity, Utility Reaction and Environment, 2012. **1**(5): p. 236-251.
86. Sarkar, S. and A. Bose, *Role of activated carbon pellets in carbon dioxide removal*. Energy conversion and management, 1997. **38**: p. S105-S110.
87. Kadirvelu, K., K. Thamaraiselvi, and C. Namasivayam, *Removal of heavy metals from industrial wastewaters by adsorption onto activated carbon prepared from an agricultural solid waste*. Bioresource Technology, 2001. **76**(1): p. 63-65.
88. Dastgheib, S.A., T. Karanfil, and W. Cheng, *Tailoring activated carbons for enhanced removal of natural organic matter from natural waters*. Carbon, 2004. **42**(3): p. 547-557.
89. Bashkova, S. and T.J. Bandosz, *The effects of urea modification and heat treatment on the process of NO₂ removal by wood-based activated carbon*. Journal of colloid and interface science, 2009. **333**(1): p. 97-103.
90. Rubio, B., M. Teresa Izquierdo, M. Carmen Mayoral, M. Teresa Bona, and J.M. Andres, *Unburnt carbon from coal fly ashes as a precursor of activated carbon for nitric oxide removal*. Journal of Hazardous Materials, 2007. **143**(1-2): p. 561-566.
91. Aworn, A., P. Thiravetyan, and W. Nakbanpote, *Preparation and characteristics of agricultural waste activated carbon by physical activation having micro- and mesopores*. Journal of Analytical and Applied Pyrolysis, 2008. **82**(2): p. 279-285.
92. Yang, R., G. Liu, M. Li, J. Zhang, and X. Hao, *Preparation and N₂, CO₂ and H₂ adsorption of super activated carbon derived from biomass source hemp (*Cannabis sativa L.*) stem*. Microporous and Mesoporous Materials, 2012. **158**: p. 108-116.
93. Sevilla, M. and A.B. Fuertes, *Sustainable porous carbons with a superior performance for CO₂ capture*. Energy & Environmental Science, 2011. **4**(5): p. 1765-1765.
94. Plaza, M.G., S. García, F. Rubiera, J.J. Pis, and C. Pevida, *Post-combustion CO₂ capture with a commercial activated carbon: Comparison of different regeneration strategies*. Chemical Engineering Journal, 2010. **163**(1-2): p. 41-47.

95. Lively, R.P., R.R. Chance, B.T. Kelley, H.W. Deckman, J.H. Drese, C.W. Jones, and W.J. Koros, *Hollow Fiber Adsorbents for CO₂ Removal from Flue Gas*. Industrial & Engineering Chemistry Research, 2009. **48**(15): p. 7314-7324.
96. Hedin, N., L. Andersson, L. Bergström, and J. Yan, *Adsorbents for the post-combustion capture of CO₂ using rapid temperature swing or vacuum swing adsorption*. Applied Energy, 2013. **104**: p. 418-433.
97. Hao, W., E. Björkman, M. Lilliestråle, and N. Hedin, *Activated carbons prepared from hydrothermally carbonized waste biomass used as adsorbents for CO₂*. Applied Energy, 2013. **112**: p. 526-532.
98. Sun, Y. and P.a. Webley, *Preparation of Activated Carbons with Large Specific Surface Areas from Biomass Corncob and Their Adsorption Equilibrium for Methane, Carbon Dioxide, Nitrogen, and Hydrogen*. Industrial & Engineering Chemistry Research, 2011. **50**(15): p. 9286-9294.
99. Mohamad Nor, N., L.C. Lau, K.T. Lee, and A.R. Mohamed, *Synthesis of activated carbon from lignocellulosic biomass and its applications in air pollution control - a review*. Journal of Environmental Chemical Engineering, 2013. **1**(4): p. 658-666.
100. Olivares-Marin, M. and M. Maroto-Valer, *Development of adsorbents for CO₂ capture from waste materials: a review*. Greenhouse Gases-Science and Technology, 2012. **2**(1): p. 20-35.
101. Ioannidou, O. and a. Zabaniotou, *Agricultural residues as precursors for activated carbon production - A review*. Renewable and Sustainable Energy Reviews, 2007. **11**(9): p. 1966-2005.
102. Do, D.D. and K. Wang, *A new model for the description of adsorption kinetics in heterogeneous activated carbon*. Carbon, 1998. **36**(10): p. 1539-1554.
103. Su, F., C. Lu, A.-J. Chung, and C.-H. Liao, *CO₂ capture with amine-loaded carbon nanotubes via a dual-column temperature/vacuum swing adsorption*. Applied Energy, 2014. **113**: p. 706-712.
104. Shen, W. and W. Fan, *Nitrogen-containing porous carbons: synthesis and application*. Journal of Materials Chemistry A, 2013. **1**(4): p. 999-999.
105. Maria-Magdalena, T., R. J.White, and Z. Li, *Nitrogen-doped Hydrothermal Carbons*. 2012.
106. Sevilla, M., C. Falco, M.-M. Titirici, and A.B. Fuertes, *High-performance CO₂ sorbents from algae*. RSC Advances, 2012. **2**(33): p. 12792-12792.
107. Zhang, Z., K. Wang, J.D. Atkinson, X. Yan, X. Li, M.J. Rood, and Z. Yan, *Sustainable and hierarchical porous Enteromorpha prolifera based carbon for CO₂ capture*. Journal of hazardous materials, 2012. **229-230**: p. 183-91.
108. Falco, C., M. Sevilla, R.J. White, R. Rothe, and M.-M. Titirici, *Renewable nitrogen-doped hydrothermal carbons derived from microalgae*. ChemSusChem, 2012. **5**(9): p. 1834-40.
109. Przepiórski, J., M. Skrodzewicz, and a.W. Morawski, *High temperature ammonia treatment of activated carbon for enhancement of CO₂ adsorption*. Applied Surface Science, 2004. **225**(1-4): p. 235-242.
110. Zhang, Z., M. Xu, H. Wang, and Z. Li, *Enhancement of CO₂ adsorption on high surface area activated carbon modified by N₂, H₂ and ammonia*. Chemical Engineering Journal, 2010. **160**(2): p. 571-577.

111. Shafeeyan, M.S., W.M.A.W. Daud, A. Houshmand, and A. Shamiri, *A review on surface modification of activated carbon for carbon dioxide adsorption*. Journal of Analytical and Applied Pyrolysis, 2010. **89**(2): p. 143-151.
112. Shafeeyan, M.S., W.M.A.W. Daud, A. Houshmand, and A. Arami-Niya, *Ammonia modification of activated carbon to enhance carbon dioxide adsorption: Effect of pre-oxidation*. Applied Surface Science, 2010. **257**(9): p. 3936-3942.
113. Plaza, M.G., F. Rubiera, J.J. Pis, and C. Pevida, *Ammonia modification of carbon materials for CO₂ capture*. Applied Surface Science, 2010. **256**(22): p. 6843-6849.
114. Plaza, M.G.G., C. Pevida, B. Arias, J. Feroso, M.D.D. Casal, C.F.F. Martín, F. Rubiera, and J.J.J. Pis, *Development of low-cost biomass-based adsorbents for postcombustion CO₂ capture*. Fuel, 2009. **88**(12): p. 2442-2447.
115. Wang, J., H. Chen, H. Zhou, X. Liu, W. Qiao, D. Long, and L. Ling, *Carbon dioxide capture using polyethylenimine-loaded mesoporous carbons*. Journal of Environmental Sciences, 2013. **25**(1): p. 124-132.
116. Gibson, J.A.A., A.V. Gromov, S. Brandani, and E.E.B. Campbell, *The effect of pore structure on the CO₂ adsorption efficiency of polyamine impregnated porous carbons*. Microporous and Mesoporous Materials, 2015. **208**: p. 129-139.
117. Pevida, C., M.G. Plaza, B. Arias, J. Feroso, F. Rubiera, and J.J. Pis, *Surface modification of activated carbons for CO₂ capture*. Applied Surface Science, 2008. **254**(22): p. 7165-7172.
118. Plaza, M.G., C. Pevida, B. Arias, M.D. Casal, C.F. Martín, J. Feroso, F. Rubiera, and J.J.P. Pis, *Different Approaches for the Development of Low-Cost CO₂ Adsorbents*. Journal of Environmental Engineering, 2009. **135**(6): p. 426-432.
119. Sayari, A. and Y. Belmabkhout, *Stabilization of Amine-Containing CO₂ Adsorbents: Dramatic Effect of Water Vapor*. Journal of the American Chemical Society, 2010. **132**(18): p. 6312-6314.
120. Xu, X., C. Song, J.M. Andresen, B.G. Miller, and A.W. Scaroni, *Novel Polyethylenimine-Modified Mesoporous Molecular Sieve of MCM-41 Type as High-Capacity Adsorbent for CO₂ Capture*. Energy & Fuels, 2002. **16**(18): p. 1463-1469.
121. Sanz-Pérez, E.S., M. Olivares-Marín, A. Arencibia, R. Sanz, G. Calleja, and M.M. Maroto-Valer, *CO₂ adsorption performance of amino-functionalized SBA-15 under post-combustion conditions*. International Journal of Greenhouse Gas Control, 2013. **17**: p. 366-375.
122. Sanz, R., G. Calleja, A. Arencibia, and E.S. Sanz-Pérez, *Development of high efficiency adsorbents for CO₂ capture based on a double-functionalization method of grafting and impregnation*. Journal of Materials Chemistry A, 2013. **1**(6): p. 1956-1956.
123. Xu, X., C. Song, J.M. Andrésen, B.G. Miller, and A.W. Scaroni, *Preparation and characterization of novel CO₂ "molecular basket" adsorbents based on polymer-modified mesoporous molecular sieve MCM-41*. Microporous and Mesoporous Materials, 2003. **62**(1-2): p. 29-45.

124. Houshmand, A., W. Daud, M.G. Lee, and M.S. Shafeeyan, *Carbon Dioxide Capture with Amine-Grafted Activated Carbon*. Water Air and Soil Pollution, 2012. **223**(2): p. 827-835.
125. Zhao, Y., Y. Shen, and L. Bai, *Effect of chemical modification on carbon dioxide adsorption property of mesoporous silica*. Journal of colloid and interface science, 2012. **379**(1): p. 94-100.
126. Zhao, C., X. Chen, E.J. Anthony, X. Jiang, L. Duan, Y. Wu, W. Dong, and C. Zhao, *Capturing CO₂ in flue gas from fossil fuel-fired power plants using dry regenerable alkali metal-based sorbent*. Progress in Energy and Combustion Science, 2013. **39**(6): p. 515-534.
127. Yu, F.-C., N. Phalak, Z. Sun, and L.-S. Fan, *Activation strategies for calcium-based sorbents for CO₂ capture: a perspective*. Industrial & Engineering Chemistry Research, 2011. **51**(4): p. 2133-2142.
128. Gupta, H. and L.-S. Fan, *Carbonation-calcination cycle using high reactivity calcium oxide for carbon dioxide separation from flue gas*. Industrial & engineering chemistry research, 2002. **41**(16): p. 4035-4042.
129. Han, K.K., Y. Zhou, Y. Chun, and J.H. Zhu, *Efficient MgO-based mesoporous CO₂ trapper and its performance at high temperature*. Journal of Hazardous Materials, 2012. **203–204**: p. 341-347.
130. Liu, M., C. Vogt, A.L. Chaffee, and S.L.Y. Chang, *Nanoscale Structural Investigation of Cs₂CO₃-Doped MgO Sorbent for CO₂ Capture at Moderate Temperature*. The Journal of Physical Chemistry C, 2013. **117**(34): p. 17514-17520.
131. Bhagiyalakshmi, M., P. Hemalatha, M. Ganesh, P.M. Mei, and H.T. Jang, *A direct synthesis of mesoporous carbon supported MgO sorbent for CO₂ capture*. Fuel, 2011. **90**(4): p. 1662-1667.
132. Bansal, R.P., Donnet, J.B. and Stoeckli, F., "Active Carbon". New York: Marcell Dekker, 1988.
133. Song, M.Y., H.Y. Park, D.S. Yang, D. Bhattachariya, and J.S. Yu, *Seaweed-Derived Heteroatom-Doped Highly Porous Carbon as an Electrocatalyst for the Oxygen Reduction Reaction*. ChemSusChem, 2014. **7**(6): p. 1755-1763.
134. Ross, A.B., J.M. Jones, M.L. Kubacki, and T. Bridgeman, *Classification of macroalgae as fuel and its thermochemical behaviour*. Bioresource technology, 2008. **99**(14): p. 6494-504.
135. Milledge, J.J., B. Smith, P.W. Dyer, and P. Harvey, *Macroalgae-derived biofuel: A review of methods of energy extraction from seaweed biomass*. Energies, 2014. **7**(11): p. 7194-7222.
136. McHugh, D.J., *A guide to the seaweed industry*. Rome, Italy: Food and Agriculture Organization of the United Nations, 2003.
137. Qin, S., P. Jiang, and C. Tseng, *Transforming kelp into a marine bioreactor*. Trends in biotechnology, 2005. **23**(5): p. 264-268.
138. Bae, Y.J., C. Ryu, J.-K. Jeon, J. Park, D.J. Suh, Y.-W. Suh, D. Chang, and Y.-K. Park, *The characteristics of bio-oil produced from the pyrolysis of three marine macroalgae*. Bioresource Technology, 2011. **102**(3): p. 3512-3520.
139. Aravindhan, R., J. Raghava Rao, and B. Unni Nair, *Preparation and characterization of activated carbon from marine macro-algal biomass*. Journal of Hazardous Materials, 2009. **162**(2-3): p. 688-694.
140. Pintor, M.J., C. Jean-Marius, V. Jeanne-Rose, P.L. Taberna, P. Simon, J. Gamby, R. Gadiou, and S. Gaspard, *Preparation of activated carbon*

- from *Turbinaria turbinata* seaweeds and its use as supercapacitor electrode materials. *Comptes Rendus Chimie*, 2013. **16**(1): p. 73-79.
141. Ferrera-Lorenzo, N., E. Fuente, I. Suárez-Ruiz, and B. Ruiz, *Sustainable activated carbons of macroalgae waste from the Agar–Agar industry. Prospects as adsorbent for gas storage at high pressures*. *Chemical Engineering Journal*, 2014. **250**: p. 128-136.
 142. Ferrera-Lorenzo, N., E. Fuente, I. Suárez-Ruiz, and B. Ruiz, *KOH activated carbon from conventional and microwave heating system of a macroalgae waste from the Agar–Agar industry*. *Fuel Processing Technology*, 2014. **121**: p. 25-31.
 143. Maschio, G., C. Koufopoulos, and A. Lucchesi, *Pyrolysis, a promising route for biomass utilization*. *Bioresource technology*, 1992. **42**(3): p. 219-231.
 144. Bridgwater, A.V., *IEA Bioenergy 27th update*. *Biomass and Bioenergy*, 2007. **31**(4): p. VII-XVIII.
 145. Onay, O. and O.M. Kockar, *Slow, fast and flash pyrolysis of rapeseed*. *Renewable Energy*, 2003. **28**(15): p. 2417-2433.
 146. Wigmans, T., *Industrial aspects of production and use of activated carbons*. *Carbon*, 1989. **27**(1): p. 13-22.
 147. Peterson, A.A., F. Vogel, R.P. Lachance, M. Fröling, M.J. Antal Jr, and J.W. Tester, *Thermochemical biofuel production in hydrothermal media: a review of sub-and supercritical water technologies*. *Energy & Environmental Science*, 2008. **1**(1): p. 32-65.
 148. Funke, A. and F. Ziegler, *Hydrothermal carbonization of biomass: a summary and discussion of chemical mechanisms for process engineering*. *Biofuels Bioproducts and Biorefining*, 2010(4): p. 160-177.
 149. Libra, J.A., K.S. Ro, C. Kammann, A. Funke, N.D. Berge, Y. Neubauer, M.-M. Titirici, C. Fühner, O. Bens, and J. Kern, *Hydrothermal carbonization of biomass residuals: a comparative review of the chemistry, processes and applications of wet and dry pyrolysis*. *Biofuels*, 2011. **2**(1): p. 71-106.
 150. Ahmadpour, A. and D. Do, *The preparation of active carbons from coal by chemical and physical activation*. *Carbon*, 1996. **34**(4): p. 471-479.
 151. Tay, T., S. Ucar, and S. Karagöz, *Preparation and characterization of activated carbon from waste biomass*. *Journal of hazardous materials*, 2009. **165**(1-3): p. 481-5.
 152. Rodríguez-Reinoso, F., M. Molina-Sabio, and M.T. González, *The use of steam and CO₂ as activating agents in the preparation of activated carbons*. *Carbon*, 1995. **33**(1): p. 15-23.
 153. Molina-Sabio, M., M.T. Gonzalez, F. Rodriguez-Reinoso, and A. Sepúlveda-Escribano, *Effect of steam and carbon dioxide activation in the micropore size distribution of activated carbon*. *Carbon*, 1996. **34**(4): p. 505-509.
 154. González, J.F., J.M. Encinar, C.M. González-García, E. Sabio, A. Ramiro, J.L. Canito, and J. Gañán, *Preparation of activated carbons from used tyres by gasification with steam and carbon dioxide*. *Applied Surface Science*, 2006. **252**(17): p. 5999-6004.
 155. Jüntgen, H., *Entstehung des porensystems bei der teilvergasung von koksen mit wasserdampf*. *Carbon*, 1968. **6**(3): p. 297-308.

156. Thrower, P., J. Bogner, and G. Mathew, *The influence of oxidation on the structure and strength of graphite-I: materials of different structure*. Carbon, 1982. **20**(6): p. 457-464.
157. Kühl, H., M. Kashani-Motlagh, H.-J. Mühlen, and K. Van Heek, *Controlled gasification of different carbon materials and development of pore structure*. Fuel, 1992. **71**(8): p. 879-882.
158. Pastor-Villegas, J. and C.J. Durán-Valle, *Pore structure of activated carbons prepared by carbon dioxide and steam activation at different temperatures from extracted rockrose*. Carbon, 2002. **40**(3): p. 397-402.
159. San Miguel, G., G.D. Fowler, and C.J. Sollars, *A study of the characteristics of activated carbons produced by steam and carbon dioxide activation of waste tyre rubber*. Carbon, 2003. **41**(5): p. 1009-1016.
160. Sánchez, A.R., A.A. Elguézabal, and L. de La Torre Saenz, *CO₂ activation of char from Quercus agrifolia wood waste*. Carbon, 2001. **39**(9): p. 1367-1377.
161. Zhang, T., W. Walawender, L. Fan, M. Fan, D. Daugaard, and R. Brown, *Preparation of activated carbons from forest and agricultural residues through CO₂ activation*. Chemical Engineering Journal, 2004. **105**(1-2): p. 53-59.
162. Lua, A.C. and J. Guo, *Microporous oil-palm-shell activated carbon prepared by physical activation for gas-phase adsorption*. Langmuir, 2001. **17**(22): p. 7112-7117.
163. Molina-Sabio, M. and F. Rodríguez-Reinoso, *Role of chemical activation in the development of carbon porosity*. Colloids and Surfaces A: Physicochemical and Engineering Aspects, 2004. **241**(1-3): p. 15-25.
164. Jankowska, H., A. Świątkowski, and J. Choma, *Active carbon*. Ellis Horwood Ltd, 1991.
165. Wu, F.-C. and R.-L. Tseng, *High adsorption capacity NaOH-activated carbon for dye removal from aqueous solution*. Journal of Hazardous Materials, 2008. **152**(3): p. 1256-1267.
166. Hayashi, J., A. Kazehaya, K. Muroyama, and A.P. Watkinson, *Preparation of activated carbon from lignin by chemical activation*. Carbon, 2000. **38**(13): p. 1873-1878.
167. Lozano-Castello, D., M. Lillo-Rodenas, D. Cazorla-Amoros, and A. Linares-Solano, *Preparation of activated carbons from Spanish anthracite: I. Activation by KOH*. Carbon, 2001. **39**(5): p. 741-749.
168. Illingworth, J.M., *Chemical activation of biomass fibre with alkali metal salts*. Ph.D. thesis, Institute of Materials Research and the Energy and Resources Research Institute, University of Leeds, 2005.
169. Fierro, V., V. Torné-Fernández, and A. Celzard, *Highly microporous carbons prepared by activation of kraft lignin with KOH* in 7th International Symposium on the Characterization of Porous Solids (COPS-VII)2007, Elsevier: Aix-en-Provence, 26-28 May 2005, France. p. 607-614.
170. Cho, H.J., K. Baek, J.-K. Jeon, S.H. Park, D.J. Suh, and Y.-K. Park, *Removal characteristics of copper by marine macro-algae-derived chars*. Chemical Engineering Journal, 2013. **217**: p. 205-211.
171. Dehkhoda, A.M. and N. Ellis, *Biochar-based catalyst for simultaneous reactions of esterification and transesterification*. Catalysis Today, 2013. **207**: p. 86-92.

172. A.H. Basta, V.F., H. El-Saied, A. Celzard, *2-Steps KOH activation of rice straw: An efficient method for preparing high-performance activated carbons*. *Bioresource Technology*, 2009. **100**(17): p. 3941-7.
173. Lillo-Ródenas, M., J. Juan-Juan, D. Cazorla-Amorós, and A. Linares-Solano, *About reactions occurring during chemical activation with hydroxides*. *Carbon*, 2004. **42**(7): p. 1371-1375.
174. McKee, D.W., *Mechanisms of the alkali metal catalysed gasification of carbon*. *Fuel*, 1983. **62**(2): p. 170-175.
175. Evans, M., E. Halliop, and J. MacDonald, *The production of chemically-activated carbon*. *Carbon*, 1999. **37**(2): p. 269-274.
176. Carvalho, A., B. Cardoso, J. Pires, and M.B. de Carvalho, *Preparation of activated carbons from cork waste by chemical activation with KOH*. *Carbon*, 2003. **41**(14): p. 2873-2876.
177. Oh, G.H. and C.R. Park, *Preparation and characteristics of rice-straw-based porous carbons with high adsorption capacity*. *Fuel*, 2002. **81**(3): p. 327-336.
178. Guo, J. and A.C. Lua, *Textural and chemical characterizations of adsorbent prepared from palm shell by potassium hydroxide impregnation at different stages*. *Journal of colloid and interface science*, 2002. **254**(2): p. 227-233.
179. Jindo, K., H. Mizumoto, Y. Sawada, M.A. Sanchez-Monedero, and T. Sonoki, *Physical and chemical characterization of biochars derived from different agricultural residues*. *Biogeosciences*, 2014. **11**(23): p. 6613-6621.
180. López, F.A., T.A. Centeno, I. García-Díaz, and F.J. Alguacil, *Textural and fuel characteristics of the chars produced by the pyrolysis of waste wood, and the properties of activated carbons prepared from them*. *Journal of Analytical and Applied Pyrolysis*, 2013. **104**: p. 551-558.
181. Carpenter, D., T.L. Westover, S. Czernik, and W. Jablonski, *Biomass feedstocks for renewable fuel production: a review of the impacts of feedstock and pretreatment on the yield and product distribution of fast pyrolysis bio-oils and vapors*. *Green Chemistry*, 2014. **16**(2): p. 384-406.
182. Karagöz, S., T. Bhaskar, A. Muto, Y. Sakata, and M.A. Uddin, *Low-temperature hydrothermal treatment of biomass: effect of reaction parameters on products and boiling point distributions*. *Energy & fuels*, 2004. **18**(1): p. 234-241.
183. Sevilla, M., J.A. Maciá-Agulló, and A.B. Fuertes, *Hydrothermal carbonization of biomass as a route for the sequestration of CO₂: Chemical and structural properties of the carbonized products*. *Biomass and Bioenergy*, 2011. **35**(7): p. 3152-3159.
184. Kang, S., X. Li, J. Fan, and J. Chang, *Characterization of hydrochars produced by hydrothermal carbonization of lignin, cellulose, D-xylose, and wood meal*. *Industrial & Engineering Chemistry Research*, 2012. **51**(26): p. 9023-9031.
185. Hoekman, S.K., A. Broch, and C. Robbins, *Hydrothermal Carbonization (HTC) of Lignocellulosic Biomass*. *Energy & Fuels*, 2011. **25**(4): p. 1802-1810.
186. Hoekman, S.K., A. Broch, C. Robbins, B. Zielinska, and L. Felix, *Hydrothermal carbonization (HTC) of selected woody and herbaceous biomass feedstocks*. *Biomass Conversion and Biorefinery*, 2013. **3**(2): p. 113-126.

187. Reza, M.T., J.G. Lynam, V.R. Vasquez, and C.J. Coronella, *Pelletization of biochar from hydrothermally carbonized wood*. Environmental Progress & Sustainable Energy, 2012. **31**(2): p. 225-234.
188. Inoue, S., T. Hanaoka, and T. Minowa, *Hot Compressed Water Treatment for Production of Charcoal from Wood*. Journal of chemical engineering of Japan, 2002. **35**(10): p. 1020-1023.
189. Ishibashi, N., H. Wakizaka, K. Yamamoto, and Y. Kawahara, *Carbonization behavior of hydrothermally treated woody biomass*. Sen'i Gakkaishi, 2012. **68**(12): p. 323-326.
190. Carrasco, J., M.C. Sáiz, A. Navarro, P. Soriano, F. Saez, and J. Martinez, *Effects of dilute acid and steam explosion pretreatments on the cellulose structure and kinetics of cellulosic fraction hydrolysis by dilute acids in lignocellulosic materials*. Applied biochemistry and biotechnology, 1994. **45**(1): p. 23-34.
191. Szczodrak, J., Z. Liczuk, J. Rogalski, and A. Leonowicz, *Intensification of oak sawdust enzymatic hydrolysis by chemical or hydrothermal pretreatment*. Biotechnology and bioengineering, 1986. **28**(4): p. 504-510.
192. Salvador, F., Sánchez-Montero, M. Jesús Izquierdo, Carmen, *C/H₂O Reaction under Supercritical Conditions and Their Repercussions in the Preparation of Activated Carbon*. The Journal of Physical Chemistry C, 2007. **111**(37): p. 14011-14020.
193. Mourao, P., P. Carrott, and M.R. Carrott, *Application of different equations to adsorption isotherms of phenolic compounds on activated carbons prepared from cork*. Carbon, 2006. **44**(12): p. 2422-2429.
194. Ishibashi, N., K. Yamamoto, H. Wakisaka, and Y. Kawahara, *Influence of the Hydrothermal Pre-treatments on the Adsorption Characteristics of Activated Carbons from Woods*. Journal of Polymers and the Environment, 2014. **22**(2): p. 267-271.
195. Zyzlila Figueroa-Torres, M., A. Robau-Sánchez, L. De la Torre-Sáenz, and A. Aguilar-Elguézabal, *Hydrogen adsorption by nanostructured carbons synthesized by chemical activation*. Microporous and Mesoporous Materials, 2007. **98**(1-3): p. 89-93.
196. Cardoso, B., A.S. Mestre, A.P. Carvalho, and J. Pires, *Activated carbon derived from cork powder waste by KOH activation: preparation, characterization, and VOCs adsorption*. Industrial & Engineering Chemistry Research, 2008. **47**(16): p. 5841-5846.
197. Mourão, P.A., I.P. Cansado, P.J. Carrott, and M.M. Ribeiro Carrott. *Designing activated carbons from natural and synthetic raw materials for pollutants adsorption*. in *Materials Science Forum*. 2010. Trans Tech Publ.
198. Ross, A.B., K. Anastasakis, M. Kubacki, and J.M. Jones, *Investigation of the pyrolysis behaviour of brown algae before and after pre-treatment using PY-GC/MS and TGA*. Journal of Analytical and Applied Pyrolysis, 2009. **85**(1-2): p. 3-10.
199. Shekhar, S.H.S., G. Lyons, C. McRoberts, D. McCall, E. Carmichael, F. Andrews, and R. McCormack, *Brown seaweed species from Strangford Lough: Compositional analyses of seaweed species and biostimulant formulations by rapid instrumental methods*. Journal of Applied Phycology, 2012. **24**(5): p. 1141-1157.

200. Haykiri-Acma, H., S. Yaman, and S. Kucukbayrak, *Production of biobriquettes from carbonized brown seaweed*. Fuel Processing Technology, 2013. **106**: p. 33-40.
201. Antal, M.J. and M. Grønli, *The art, science, and technology of charcoal production*. Industrial & Engineering Chemistry Research, 2003. **42**(8): p. 1619-1640.
202. Stratford, J.P.H., Tony R. de Leij, Frans A. A. M., *Intrinsic activation: The relationship between biomass inorganic content and porosity formation during pyrolysis*. Bioresource Technology, 2014. **159**(0): p. 104-111.
203. Ferrera-Lorenzo, N., E. Fuente, I. Suárez-Ruiz, R.R. Gil, and B. Ruiz, *Pyrolysis characteristics of a macroalgae solid waste generated by the industrial production of Agar–Agar*. Journal of Analytical and Applied Pyrolysis, 2014. **105**: p. 209-216.
204. Cherad, R., J.A. Onwudili, P.T. Williams, and A.B. Ross, *A parametric study on supercritical water gasification of Laminaria hyperborea: A carbohydrate-rich macroalga*. Bioresource Technology, 2014. **169**: p. 573-580.
205. Zhou, D., L. Zhang, S. Zhang, H. Fu, and J. Chen, *Hydrothermal Liquefaction of Macroalgae Enteromorpha prolifera to Bio-oil*. Energy & Fuels, 2010. **24**(7): p. 4054-4061.
206. Anastasakis, K. and A.B. Ross, *Hydrothermal liquefaction of the brown macro-alga Laminaria Saccharina: Effect of reaction conditions on product distribution and composition*. Bioresource Technology, 2011. **102**(7): p. 4876-4883.
207. Xu, Q., Q. Qian, A. Quek, N. Ai, G. Zeng, and J. Wang, *Hydrothermal Carbonization of Macroalgae and the Effects of Experimental Parameters on the Properties of Hydrochars*. ACS Sustainable Chemistry & Engineering, 2013. **1**(9): p. 1092-1101.
208. Xu, Y.-P., P.-G. Duan, and F. Wang, *Hydrothermal processing of macroalgae for producing crude bio-oil*. Fuel Processing Technology, 2015. **130**: p. 268-274.
209. Gao, Y., Q.Y. Yue, Y.Y. Sun, J.N. Xiao, B.Y. Gao, P. Zhao, and H. Yu, *Optimization of high surface area activated carbon production from Enteromorpha prolifera with low-dose activating agent*. Fuel Processing Technology, 2015. **132**: p. 180-187.
210. Nasri, N.S., U.D. Hamza, S.N. Ismail, M.M. Ahmed, and R. Mohsin, *Assessment of porous carbons derived from sustainable palm solid waste for carbon dioxide capture*. Journal of Cleaner Production, 2013.
211. Creamer, A.E., B. Gao, and M. Zhang, *Carbon dioxide capture using biochar produced from sugarcane bagasse and hickory wood*. Chemical Engineering Journal, 2014. **249**: p. 174-179.
212. Heidari, A., H. Younesi, A. Rashidi, and A. Ghoreyshi, *Adsorptive removal of CO₂ on highly microporous activated carbons prepared from Eucalyptus camaldulensis wood: Effect of chemical activation*. Journal of the Taiwan Institute of Chemical Engineers, 2014. **45**(2): p. 579-588.
213. Zhu, X.-L., P.-Y. Wang, C. Peng, J. Yang, and X.-B. Yan, *Activated carbon produced from paulownia sawdust for high-performance CO₂ sorbents*. Chinese Chemical Letters, 2014. **25**(6): p. 929-932.
214. Labreche, Y., Y. Fan, F. Rezaei, R.P. Lively, C.W. Jones, and W.J. Koros, *Poly(amide-imide)/silica supported PEI hollow fiber sorbents for*

- postcombustion CO₂ capture by RTSA*. ACS Applied Materials and Interfaces, 2014. **6**(21): p. 19336-19346.
215. Li, F.S., W. Qiu, R.P. Lively, J.S. Lee, A.A. Rownaghi, and W.J. Koros, *Polyethyleneimine-functionalized polyamide imide (Torlon) hollow-fiber sorbents for post-combustion CO₂ capture*. ChemSusChem, 2013. **6**(7): p. 1216-23.
216. Yue, M.B., L.B. Sun, Y. Cao, Z.J. Wang, Y. Wang, Q. Yu, and J.H. Zhu, *Promoting the CO₂ adsorption in the amine-containing SBA-15 by hydroxyl group*. Microporous and Mesoporous Materials, 2008. **114**(1): p. 74-81.
217. Arenillas, A., K.M. Smith, T.C. Drage, and C.E. Snape, *CO₂ capture using some fly ash-derived carbon materials*. Fuel, 2005. **84**(17): p. 2204-2210.
218. Satyapal, S., T. Filburn, J. Trela, and J. Strange, *Performance and properties of a solid amine sorbent for carbon dioxide removal in space life support applications*. Energy & Fuels, 2001. **15**(2): p. 250-255.
219. Aschenbrenner, O., S. Supasitmongkol, M. Taylor, and P. Styring, *Measurement of vapour pressures of ionic liquids and other low vapour pressure solvents*. Green Chemistry, 2009. **11**(8): p. 1217-1221.
220. Zhang, Y., M.M. Maroto-Valer, and Z. Tang, *Microporous activated carbons produced from unburned carbon in fly ash and their application for CO₂ capture*. Prepr. Pap.-Am. Chem. Soc., Div. Fuel, 2004.
221. M. G. Plaza, C.P., A. Arenillas, F. Rubiera, J. J. Pis, *CO₂ capture by adsorption with nitrogen enriched carbons*. Fuel, 2007. **86**(14): p. 2204-2212.
222. Wang, D., X. Wang, X. Ma, E. Fillerup, and C. Song, *Three-dimensional molecular basket sorbents for CO₂ capture: Effects of pore structure of supports and loading level of polyethylenimine*. Catalysis Today, 2014. **233**: p. 100-107.
223. Son, W.-J., J.-S. Choi, and W.-S. Ahn, *Adsorptive removal of carbon dioxide using polyethyleneimine-loaded mesoporous silica materials*. Microporous and Mesoporous Materials, 2008. **113**(1-3): p. 31-40.
224. Chen, C., S.-T. Yang, W.-S. Ahn, and R. Ryoo, *Amine-impregnated silica monolith with a hierarchical pore structure: enhancement of CO₂ capture capacity*. Chemical Communications, 2009(24): p. 3627-3629.
225. Wang, X., H. Li, H. Liu, and X. Hou, *As-synthesized mesoporous silica MSU-1 modified with tetraethylenepentamine for CO₂ adsorption*. Microporous and Mesoporous Materials, 2011. **142**(2): p. 564-569.
226. Wang, X., X. Ma, C. Song, D.R. Locke, S. Siefert, R.E. Winans, J. Möllmer, M. Lange, A. Möller, and R. Gläser, *Molecular basket sorbents polyethyleneimine-SBA-15 for CO₂ capture from flue gas: Characterization and sorption properties*. Microporous and Mesoporous Materials, 2013. **169**: p. 103-111.
227. Egbebi, A., S. Hammache, and M.L. Gray. *Effect of preparation parameters on mixed amine functionalized silica sorbents for CO₂ capture*. in *Spring Meeting and 9th Global Congress on Process Safety*. 2013. Pittsburgh: AIChE.
228. Marques, L.M., P.J.M. Carrott, and M.M.L. Ribeiro Carrott, *Amine-modified carbon aerogels for CO₂ Capture*. Adsorption Science and Technology, 2013. **31**(2-3): p. 223-232.

229. Labreche, Y., R.P. Lively, F. Rezaei, G. Chen, C.W. Jones, and W.J. Koros, *Post-spinning infusion of poly(ethyleneimine) into polymer/silica hollow fiber sorbents for carbon dioxide capture*. Chemical Engineering Journal, 2013. **221**: p. 166-175.
230. Xu, X., C. Song, B.G. Miller, and A.W. Scaroni, *Influence of Moisture on CO₂ Separation from Gas Mixture by a Nanoporous Adsorbent Based on Polyethylenimine-Modified Molecular Sieve MCM-41*. Industrial & Engineering Chemistry Research, 2005. **44**(21): p. 8113-8119.
231. Zhang, Z., X. Ma, D. Wang, C. Song, and Y. Wang, *Development of silica-gel-supported polyethylenimine sorbents for CO₂ capture from flue gas*. AIChE Journal, 2012. **58**(8): p. 2495-2502.
232. Delaney, S.W., G.P. Knowles, and A.L. Chaffee, *Hybrid mesoporous materials for carbon dioxide separation*. Fuel Chem Div. Preprints, 2002. **47**: p. 65.
233. Dao, D.S., H. Yamada, and K. Yogo, *Large-Pore Mesostructured Silica Impregnated with Blended Amines for CO₂ Capture*. Industrial & Engineering Chemistry Research, 2013. **52**(38): p. 13810-13817.
234. Drage, T.C., A. Arenillas, K.M. Smith, and C.E. Snape, *Thermal stability of polyethylenimine based carbon dioxide adsorbents and its influence on selection of regeneration strategies*. Microporous and Mesoporous Materials, 2008. **116**(1-3): p. 504-512.
235. Wang, J., H. Huang, M. Wang, L. Yao, W. Qiao, D. Long, and L. Ling, *Direct Capture of Low-Concentration CO₂ on Mesoporous Carbon-Supported Solid Amine Adsorbents at Ambient Temperature*. Industrial & Engineering Chemistry Research, 2015. **54**(19): p. 5319-5327.
236. Patience, G.S., *Experimental Methods and Instrumentation for Chemical Engineers*, Elsevier.
237. Wang, W., J. Xiao, X. Wei, J. Ding, X. Wang, and C. Song, *Development of a new clay supported polyethylenimine composite for CO₂ capture*. Applied Energy, 2013. **113**: p. 334-341.
238. Zhao, W., Z. Zhang, Z. Li, and N. Cai, *Investigation of Thermal Stability and Continuous CO₂ Capture from Flue Gases with Supported Amine Sorbent*. Industrial & Engineering Chemistry Research, 2013. **52**(5): p. 2084-2093.
239. Dow Chemical Company. *DOW Specialty Amines - Typical Properties of Ethanolamines from Dow*. [Online]. 2003. [Accessed 21 December 2015]; Available from: http://www.dow.com/amines/prod/tpp_ethano.htm.
240. Huntsman Corporation. *Technical bulletin tetraethylenepentamine (TEPA)*. [Online]. 2007. [Accessed 21 December 2015]; Available from: <http://www.huntsman.com>.
241. Tucker, M., *Recommendation about degassing process*, 2012.
242. Singh, K.S.W., D.H. Everett, R.A.W. Haul, L. Moscou, R.A. Pierotti, J. Rouquerol, and T. Siemieniowska, *IUPAC, Reporting physisorption data for gas/solid systems with special reference to the determination of surface area and porosity*. Pure Appl Chem, 1985. **57**(4): p. 603-619.
243. Thommes, M., K. Kaneko, V. Neimark Alexander, P. Olivier James, F. Rodriguez-Reinoso, J. Rouquerol, and S.W. Sing Kenneth, *Physisorption of gases, with special reference to the evaluation of surface area and pore size distribution (IUPAC Technical Report)*, in *Pure and Applied Chemistry* 2015.
244. Quantachrome Instruments. *Autosorb-1/ASWin Operating Manual*, 2008.

245. Lozano-Castelló, D., D. Cazorla-Amorós, and a. Linares-Solano, *Usefulness of CO₂ adsorption at 273 K for the characterization of porous carbons*. Carbon, 2004. **42**(7): p. 1233-1242.
246. Cazorla-Amorós, D., J. Alcañiz-Monge, M.A. de la Casa-Lillo, and A. Linares-Solano, *CO₂ As an Adsorptive To Characterize Carbon Molecular Sieves and Activated Carbons*. Langmuir, 1998. **14**(16): p. 4589-4596.
247. Cazorla-Amorós, D., J. Alcaniz-Monge, and A. Linares-Solano, *Characterization of activated carbon fibers by CO₂ adsorption*. Langmuir, 1996. **12**(11): p. 2820-2824.
248. Brunauer, S., P.H. Emmett, and E. Teller, *Adsorption of Gases in Multimolecular Layers*. Journal of the American Chemical Society, 1938. **60**(2): p. 309-319.
249. *Internation Standard Organisation. ISO-FDIS 9277:2010. Determination of the specific surface area of solids by gas adsorption - BET method*, 2010, ISO, 2010: Switzerland.
250. *Quantachrome Instruments. BET Surface Area Analyzer. Seminar and Practical Training Short Course*. [Online]. 2006 [Accessed 4 September 2015]; Available from: <http://slideplayer.com/slide/4216174/>.
251. Sing, K., *The use of nitrogen adsorption for the characterisation of porous materials*. Colloids and Surfaces A: Physicochemical and Engineering Aspects, 2001. **187-188**(0): p. 3-9.
252. Gurvitsch, L.G., *Physicochemical attractive force*. Russ. J. Phys. Chem., 1915. **47**: p. 805-827.
253. Barrett, E.P., L.G. Joyner, and P.P. Halenda, *An example of a method of analysis based on the assumption of cylindrical pores is found in J. Am. Chem. Soc*, 1951. **73**: p. 373-373.
254. J. Rouquérol, D.A., C. W. Fairbridge, D. H. Everett, J. H. Haynes, N. Pernicone, J. D. F. Ramsay, K. S. W. Sing, K. K. Unger, *IUPAC, Recommendations*. Pure & Appl. Chem, 1994. **66**: p. 1739-1739.
255. Kruk, M., M. Jaroniec, and A. Sayari, *Application of Large Pore MCM-41 Molecular Sieves To Improve Pore Size Analysis Using Nitrogen Adsorption Measurements*. Langmuir, 1997. **13**(23): p. 6267-6273.
256. Gregg, S.J., *Adsorption, surface area and porosity*. 2nd ed., London: Academic Press, 1982.
257. Rouquerol, J., F. Rouquerol, P. Llewellyn, G. Maurin, and K.S. Sing, *Adsorption by powders and porous solids : principles, methodology and applications*. London: Academic Press, 1999.
258. Polanyi, M., *Adsorption from the point of view of the Third Law of Thermodynamics*. Verh. Deut. Phys. Ges, 1914. **16**: p. 1012-1016.
259. Dubinin, M. and L. Radushkevich, *On the characteristic curve equation for active carbons*. Doklady Akademii Nauk SSSR, Ser. Khim, 1947. **55**: p. 331.
260. Lastoskie, C., K.E. Gubbins, and N. Quirke, *Pore size heterogeneity and the carbon slit pore: a density functional theory model*. Langmuir, 1993. **9**(10): p. 2693-2702.
261. Neimark, A.V., P.I. Ravikovitch, M. Grün, F. Schüth, and K.K. Unger, *Pore size analysis of MCM-41 type adsorbents by means of nitrogen and argon adsorption*. Journal of colloid and interface science, 1998. **207**(1): p. 159-169.

262. Ravikovitch, P.I., A. Vishnyakov, R. Russo, and A.V. Neimark, *Unified approach to pore size characterization of microporous carbonaceous materials from N₂, Ar, and CO₂ adsorption isotherms*. Langmuir, 2000. **16**(5): p. 2311-2320.
263. *British Standards Institution (BSI). BS ISO 15901-3:2007. Pore size distribution and porosity of solid materials by mercury porosimetry and gas adsorption - Part 3: Analysis of micropores by gas adsorption*, 2007, BSI, 2007: London, United Kingdom.
264. Guo, S., J. Peng, W. Li, K. Yang, L. Zhang, S. Zhang, and H. Xia, *Effects of CO₂ activation on porous structures of coconut shell-based activated carbons*. Applied Surface Science, 2009. **255**(20): p. 8443-8449.
265. Jagiello, J. and M. Thommes, *Comparison of DFT characterization methods based on N₂, Ar, CO₂, and H₂ adsorption applied to carbons with various pore size distributions*. Carbon, 2004. **42**(7): p. 1227-1232.
266. *Quantachrome Instruments. Powder Tech Note 35. Micropore size analysis of porous carbons using CO₂ adsorption at 273.15 K (0 °C)*.
267. *British Standards Institution (BSI). Draft BS EN ISO 18134-3 Solid biofuels - Determination of moisture content*, 2013, BSI, 2013: London, United Kingdom.
268. *British Standards Institution (BSI). Draft BS EN ISO 18123 Solid biofuels - Determination of the content of volatile matter*, 2013, BSI, 2013: London, United Kingdom.
269. *British Standards Institution (BSI). Draft BS EN ISO 18122 Solid biofuels - Determination of ash content*, 2013, BSI, 2013: London, United Kingdom.
270. *American Society for Testing and Materials (ASTM). Section 15. General products, chemical specialties, and end use products; Volume 15.01 Refractories, Activated Carbon; Advanced Ceramics*, 2010: West Conshohocken, Pennsylvania, United States, 2010.
271. Cullity, B., *Elements of X-ray Diffraction*. 2nd ed. Adisson-Wesley Publishing. USA. 1978.
272. Bragg, W.L. *The structure of some crystals as indicated by their diffraction of X-rays*. in *Proceedings of the Royal Society of London. Series A, Containing Papers of a Mathematical and Physical Character*. 1913. The Royal Society.
273. Moore, Z., *Application of X-ray Diffraction Methods and Molecular Mechanics Simulations to Structure Determination and Cotton Fiber Analysis*. Ph.D. thesis, University of New Orleans Theses and Dissertations. Paper 888, 2008.
274. Salari, Z., F. Danafar, S. Dabaghi, and S.A. Ataei, *Sustainable synthesis of silver nanoparticles using macroalgae Spirogyra varians and analysis of their antibacterial activity*. Journal of Saudi Chemical Society, 2014.
275. *Carl Zeiss Microscopy. Electron and Ion Beam Microscopes*.
276. *Oxford Instruments. Silicon Drift Detectors Explained*.
277. Bagreev, A., J. Angel Menendez, I. Dukhno, Y. Tarasenko, and T.J. Bandosz, *Bituminous coal-based activated carbons modified with nitrogen as adsorbents of hydrogen sulfide*. Carbon, 2004. **42**(3): p. 469-476.
278. Oickle, A.M., S.L. Goertzen, K.R. Hopper, Y.O. Abdalla, and H.A. Andreas, *Standardization of the Boehm titration: Part II. Method of*

- agitation, effect of filtering and dilute titrant*. Carbon, 2010. **48**(12): p. 3313-3322.
279. Goertzen, S.L., K.D. Thériault, A.M. Oickle, A.C. Tarasuk, and H.a. Andreas, *Standardization of the Boehm titration. Part I. CO₂ expulsion and endpoint determination*. Carbon, 2010. **48**(4): p. 1252-1261.
280. Smith, B.C., *Infrared spectral interpretation: a systematic approach*. 1998.
281. Casa Software Ltd. [Online]. 2005 [Accessed 10 September 2015]; Available from: <http://www.casaxps.com>.
282. Cunliffe, A.M., *The Pyrolysis of Scrap Tyres. Ph.D. thesis*, Dept. Fuel and Energy, University of Leeds, 1998.
283. Rouquerol, J., F. Rouquerol, P. Llewellyn, G. Maurin, and K.S. Sing, *Adsorption by powders and porous solids: principles, methodology and applications*. London: Academic press, 1999.
284. Silvestre-Albero, A.M., J.M. Juárez-Galán, J. Silvestre-Albero, and F. Rodríguez-Reinoso, *Low-pressure hysteresis in adsorption: an artifact?* The Journal of Physical Chemistry C, 2012. **116**(31): p. 16652-16655.
285. Presser, V., J. McDonough, S.-H. Yeon, and Y. Gogotsi, *Effect of pore size on carbon dioxide sorption by carbide derived carbon*. Energy & Environmental Science, 2011. **4**(8): p. 3059-3059.
286. Kwon, S.-M., N.-H. Kim, and D.-S. Cha, *An investigation on the transition characteristics of the wood cell walls during carbonization*. Wood science and technology, 2009. **43**(5-6): p. 487-498.
287. Zhang, J.-h., Q.-m. Lin, and X.-r. Zhao, *The Hydrochar Characters of Municipal Sewage Sludge Under Different Hydrothermal Temperatures and Durations*. Journal of Integrative Agriculture, 2014. **13**(3): p. 471-482.
288. Zhu, Q., J. Jones, A. Williams, and K. Thomas, *The predictions of coal/char combustion rate using an artificial neural network approach*. Fuel, 1999. **78**(14): p. 1755-1762.
289. Sevilla, M., A. Fuertes, and R. Mokaya, *High density hydrogen storage in superactivated carbons from hydrothermally carbonized renewable organic materials*. Energy & Environmental Science, 2011. **4**(4): p. 1400-1410.
290. Tushar, M.S.H.K., N. Mahinpey, A. Khan, H. Ibrahim, P. Kumar, and R. Idem, *Production, characterization and reactivity studies of chars produced by the isothermal pyrolysis of flax straw*. biomass and bioenergy, 2012. **37**: p. 97-105.
291. Scherrer, P., *Göttinger Nachrichten Gesell*. Search PubMed, 1918. **2**: p. 98-100.
292. Hyatt, E.P., I.B. Cutler, and M.E. Wadsworth, *Calcium carbonate decomposition in carbon dioxide atmosphere*. Journal of the American Ceramic Society, 1958. **41**(2): p. 70-74.
293. Arenillas, A., F. Rubiera, J.B. Parra, C.O. Ania, and J.J. Pis, *Surface modification of low cost carbons for their application in the environmental protection*. Applied Surface Science, 2005. **252**(3): p. 619-624.
294. González, A.S., M.G. Plaza, J.J. Pis, F. Rubiera, and C. Pevida, *Post-combustion CO₂ capture adsorbents from spent coffee grounds*. Energy Procedia, 2013. **37**: p. 134-141.

295. Sevilla, M., J.B. Parra, and A.B. Fuertes, *Assessment of the role of micropore size and N-doping in CO₂ capture by porous carbons*. ACS applied materials & interfaces, 2013. **5**(13): p. 6360-8.
296. Berge, N.D., K.S. Ro, J. Mao, J.R.V. Flora, M.a. Chappell, and S. Bae, *Hydrothermal carbonization of municipal waste streams*. Environmental science & technology, 2011. **45**(13): p. 5696-703.
297. Otawa, T., M. Yamada, R. Tanibata, and M. Kawakami. *Preparation, pore analysis and adsorption behavior of high surface area active carbon from coconut shell*. in *Proceeding of the international symposium on gas separation technology*. 1990. Antwerp (Belgium).
298. Wang, S., X.M. Jiang, N. Wang, L.J. Yu, Z. Li, and P.M. He, *Fusing characteristic analysis on seaweed biomass ash*. Zhongguo Dianji Gongcheng Xuebao/Proceedings of the Chinese Society of Electrical Engineering, 2008. **28**(5): p. 96-101.
299. Ross, A., C. Hall, K. Anastasakis, A. Westwood, J. Jones, and R. Crewe, *Influence of cation on the pyrolysis and oxidation of alginates*. Journal of Analytical and Applied Pyrolysis, 2011. **91**(2): p. 344-351.
300. Lee, S.C., H.J. Chae, S.J. Lee, B.Y. Choi, C.K. Yi, J.B. Lee, C.K. Ryu, and J.C. Kim, *Development of Regenerable MgO-Based Sorbent Promoted with K₂CO₃ for CO₂ Capture at Low Temperatures*. Environmental Science & Technology, 2008. **42**(8): p. 2736-2741.
301. Kumar, S. and S.K. Saxena, *A comparative study of CO₂ sorption properties for different oxides*. Materials for Renewable and Sustainable Energy, 2014. **3**(3): p. 1-15.
302. Stark, J.V., D.G. Park, I. Lagadic, and K.J. Klabunde, *Nanoscale metal oxide particles/clusters as chemical reagents. Unique surface chemistry on magnesium oxide as shown by enhanced adsorption of acid gases (sulfur dioxide and carbon dioxide) and pressure dependence*. Chemistry of Materials, 1996. **8**(8): p. 1904-1912.
303. Song, G., X. Zhu, R. Chen, Q. Liao, Y.D. Ding, and L. Chen, *An investigation of CO₂ adsorption kinetics on porous magnesium oxide*. Chemical Engineering Journal, 2016. **283**: p. 175-183.
304. Lee, J.B., C.K. Ryu, J.-I. Baek, J.H. Lee, T.H. Eom, and S.H. Kim, *Sodium-Based Dry Regenerable Sorbent for Carbon Dioxide Capture from Power Plant Flue Gas*. Industrial & Engineering Chemistry Research, 2008. **47**(13): p. 4465-4472.
305. Wang, S., S. Yan, X. Ma, and J. Gong, *Recent advances in capture of carbon dioxide using alkali-metal-based oxides*. Energy & Environmental Science, 2011. **4**(10): p. 3805-3819.
306. Lee, S., T.P. Filburn, M. Gray, J.-W. Park, and H.-J. Song, *Screening test of solid amine sorbents for CO₂ capture*. Industrial & Engineering Chemistry Research, 2008. **47**(19): p. 7419-7423.
307. Gray, M., Y. Soong, K. Champagne, H. Pennline, J. Baltrus, R. Stevens, R. Khatri, S. Chuang, and T. Filburn, *Improved immobilized carbon dioxide capture sorbents*. Fuel Processing Technology, 2005. **86**(14): p. 1449-1455.
308. Satyapal, S., T. Filburn, H.H. Michels, and J. Graf, *A unique solid amine sorbent useful for capturing low concentrations of carbon dioxide*. Greenhouse Gas Control Technologies, ed. B. Eliasson, P. Riemer, and A. Wokaun. Amsterdam: Elsevier Science Bv, 1999. 113-118.

309. Drese, J.H., S. Choi, R.P. Lively, W.J. Koros, D.J. Fauth, M.L. Gray, and C.W. Jones, *Synthesis–structure–property relationships for hyperbranched aminosilica CO₂ adsorbents*. *Advanced Functional Materials*, 2009. **19**(23): p. 3821-3832.
310. Yan, X., L. Zhang, Y. Zhang, K. Qiao, Z. Yan, and S. Komarneni, *Amine-modified mesocellular silica foams for CO₂ capture*. *Chemical Engineering Journal*, 2011. **168**(2): p. 918-924.
311. Witton, T., *Polyethyleneimine-loaded bimodal porous silica as low-cost and high-capacity sorbent for CO₂ capture*. *Materials Chemistry and Physics*, 2012. **137**(1): p. 235-245.
312. Thi Le, M.U., S.-Y. Lee, and S.-J. Park, *Preparation and characterization of PEI-loaded MCM-41 for CO₂ capture*. *International Journal of Hydrogen Energy*, 2014.
313. Maroto-Valer, M.M., Z. Tang, and Y. Zhang, *CO₂ capture by activated and impregnated anthracites*. *Fuel Processing Technology*, 2005. **86**(14-15): p. 1487-1502.
314. Serna-Guerrero, R. and A. Sayari, *Modeling adsorption of CO₂ on amine-functionalized mesoporous silica. 2: Kinetics and breakthrough curves*. *Chemical Engineering Journal*, 2010. **161**(1): p. 182-190.
315. Abdollahi-Govar, A., A.D. Ebner, and J.A. Ritter, *New Kinetic Model That Describes the Reversible Adsorption and Desorption Behavior of CO₂ in a Solid Amine Sorbent*. *Energy and Fuels*, 2015. **29**(7): p. 4492-4502.
316. Aroua, M.K., C.Y. Yin, F.N. Lim, W.L. Kan, and W.M.A.W. Daud, *Effect of impregnation of activated carbon with chelating polymer on adsorption kinetics of Pb²⁺*. *Journal of Hazardous Materials*, 2009. **166**(2–3): p. 1526-1529.
317. Zhang, J., R. Singh, and P.A. Webley, *Alkali and alkaline-earth cation exchanged chabazite zeolites for adsorption based CO₂ capture*. *Microporous and Mesoporous Materials*, 2008. **111**(1–3): p. 478-487.

List of abbreviations and symbols

A	Ash
ACs	Activated carbons
AL	Actual loading
ASTM	American Society for Testing and Materials
ASU	Air separation unit
ATR	Attenuated total reflection
AY	Activation Yield
BET	Brunauer-Emmett-Teller
BJH	Barrett-Joyner-Halenda
BO	Burn-off
BSI	British Standards Institution
CA	Chemically activated
CAIT	Climate Analysis Indicators Tool
CCS	Carbon capture and storage
CDR	Carbon dioxide re-use
CLC	Chemical-looping combustion
$CO_{2, ads}(t)$	CO_2 adsorption capacity at a given time t
$CO_{2, ads max}$	Maximum CO_2 adsorption capacity
$CO_{2, ads pro}(t)$	CO_2 adsorption progress at a given time t
$CO_{2, des}(t)$	CO_2 desorption capacity at a given time t
$CO_{2, des pro}(t)$	CO_2 desorption progress at a given time t
COP	Conference of Parties
CR	Chemical ratio
CY	Carbon Yield
d	Interplanar spacing
db	Dry basis
DEA	Diethanolamine
DF	Dilution factor
DFT	Density functional theory
DR	Dubinin-Radushkevich

DSC	Differential Scanning Calorimetry
DTGA	Differential Thermogravimetric Analysis
E_0	Energy of adsorption
EDX	Energy-Dispersive X-ray
EOR	Enhanced oil recovery
ESP	Electrostatic precipitator
FC	Fixed carbon
FGD	Flue gas desulfurization
FTIR	Fourier Transform Infrared
FWHM	Full width at half maximum
GAI	Generalized adsorption isotherm
GHGs	Greenhouse gases
Gly	Glycerol
HAS	Hemispherical analyser
HR	Heating rate
HTC	Hydrothermal carbonization
IAE	Integral adsorption equation
IEA	International Energy Agency
IGCC	Integrated gasification combined cycle
IPCC	Intergovernmental Panel on Climate Change
ISO	International Standard Organization
K_1	Rate constant of pseudo-first-order adsorption
K_2	Rate constant of pseudo-second-order adsorption
LH_S	<i>Laminaria hyperborea</i> summer
LHP	Low-pressure hysteresis phenomena
M	Moisture
Me	Methanol
MEA	Monoethanolamine
m_{initial}	Mass of water initially added to HTC rig
m_{lost}	Mass of water lost after HTC process
MOFs	Metal organic frameworks
$m_{\text{recovered}}$	Mass of water recovered after HTC process

MSW	Municipal solid waste
MW	Molecular weight
N*	Amount of nitrogen actually incorporated after impregnation of PEI
ND	Not detected
NEXUS	National EPSRC XPS Users Service
NL	Nominal loading
NLDFT	Non-local density functional theory
NM	Not measured
OW	Oak wood
PA	Physically activated
PEG	Polyethylene glycol
PEI	Polyethyleneimine
PSA	Pressure swing adsorption
$q_{e, \text{exp}}$	CO ₂ adsorbed capacity at equilibrium measured experimentally
$q_{e, \text{mod}}$	CO ₂ adsorbed capacity at equilibrium predicted from the model
RETS	Renewable energy technologies
RTSA	Rapid temperature swing adsorption
S_{BET}	BET surface area
SCW	Supercritical water
SD	Standard deviation
SDD	Silicon Drift Detector
SEM	Scanning Electron Microscope
SOR	Square of residuals
TCD	Thermal conductivity detector
t_{cool}	Cooling time
t_{des}	Desorption time
TEPA	Tetraethylenepentamine
TGA	Thermogravimetric Analysis
TSA	Temperature swing adsorption
UNFCCC	United Nations Framework Convention on Climate Change
V_{ads}	Volume of adsorbate
VM	Volatile matter

V_{ma}	Macroporous volume
V_{me}	Mesoporous volume
V_{mi}	Microporous volume
VOCs	Volatile organic compounds
V_{tot}	Total pore volume
V_{umi}	Ultramicroporous volume
W	Water
WGS	Water-gas shift
WRI	World Resources Institute
wt%	Weight percentage
XPS	X-ray Photoelectron Spectroscopy
XRD	X-Ray Diffraction
Z13X	Zeolite Z-13X
ΔH_{ads}	Heat of adsorption
ΔH_{des}	Heat of desorption
θ	Angle of incidence of an X-ray
λ	X-ray wavelength

Appendix A

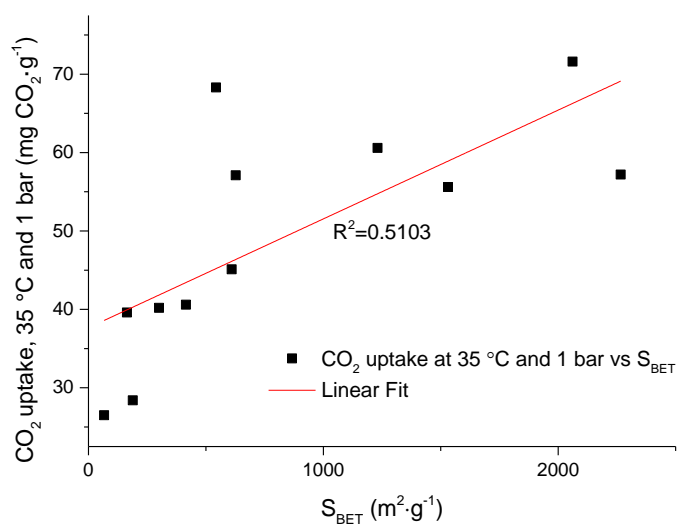


Figure A 1 Correlation between CO₂ uptakes measured at 35 °C and 1 bar and BET surface area

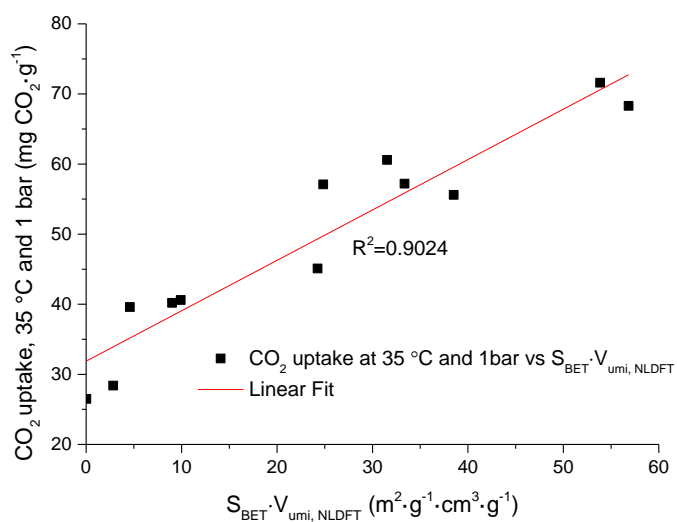


Figure A 2 Correlation between CO₂ uptakes measured at 35 °C and 1 bar and textural factor. The latter was determined as BET surface area times the ultramicropore volume calculated by applying NLDFT model to the CO₂ adsorption isotherms measured at 0 °C.

Table A 1 Main textural parameters and CO₂ uptakes at 35 °C and 1 bar for selected samples

Sample ID	CO ₂ uptake, 35 °C and 1 bar	V _{umi, NLDFT}	S _{BET}	S _{BET} ·V _{umi, NLDFT}
	mg CO ₂ ·g ⁻¹	cm ³ ·g ⁻¹	m ² ·g ⁻¹	m ² ·g ⁻¹ ·cm ³ ·g ⁻¹
AR	55.6	0.025	1531	38.51
AR_PEI	45.1	0.040	610	24.24
GAC	60.6	0.026	1231	31.53
LH_S250PA	40.2	0.030	301	9.01
LH_S800	26.5	0.000	66	0.03
LH_S800CA	57.2	0.015	2266	33.37
LH_S800PA	28.4	0.015	189	2.84
OW250PA	40.6	0.024	415	9.91
OW800	39.6	0.028	164	4.59
OW800CA	71.6	0.026	2061	53.85
OW800PA	57.1	0.040	627	24.85
Z13X	68.3	0.105	543	56.84

Appendix B

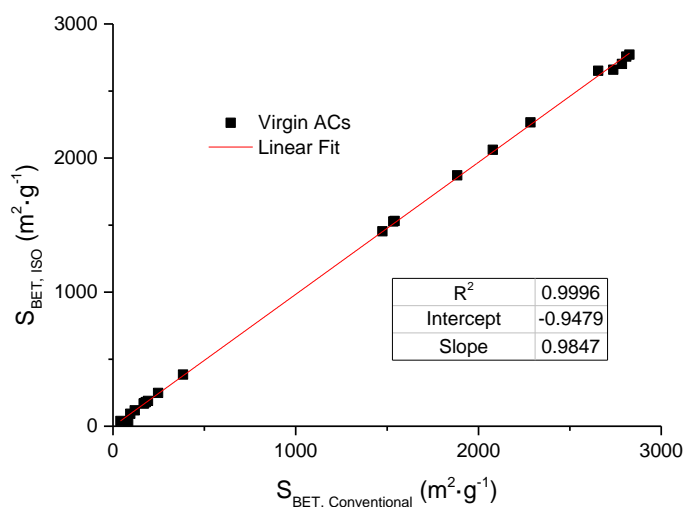


Figure B 1 Correlation between S_{BET} values calculated by applying BET method over Conventional ($P/P_0 = 0.05-0.3$) or ISO ($P/P_0 = 0.01-0.1$) pressure range for Virgin Activated Carbons (ACs)

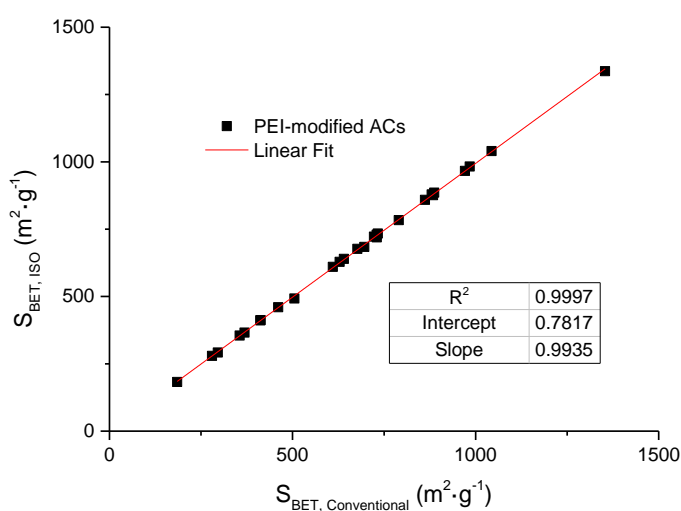


Figure B 2 Correlation between S_{BET} values calculated by applying BET method over Conventional ($P/P_0 = 0.05-0.3$) or ISO ($P/P_0 = 0.01-0.1$) pressure range for PEI-modified Activated Carbons (ACs)

Table B 1 S_{BET} values in $\text{m}^2\cdot\text{g}^{-1}$ calculated by applying BET method over Conventional ($P/P_0 = 0.05\text{-}0.3$) or ISO ($P/P_0 = 0.01\text{-}0.1$) pressure range for Virgin Activated Carbons (ACs)

Sample ID	ISO	Conventional
AR	1531	1541
OW800CA	2061	2078
OW250CA	2757	2809
LH_S800PA	189	192
LH_S800CA	2266	2285
LH_S250CA	2771	2826
OW800PA_800_2h	385	383
OW250PA_500_0.5h	39	41
OW250PA_600_0h	169	168
LH_S250PA_550_0.5h	248	247
LH_S250PA_600_0h	118	119
LH_S250PA_600_1h	180	179
LH_S800PA_750_0.5h	21	83
LH_S800PA_700_0h	171	171
LH_S800PA_700_1h	93	94
LH_S800CA_650_4-1	1454	1475
LH_S800CA_750_1-1	1527	1534
LH_S800CA_750_2-1	1871	1884
LH_S250CA_650_4-1	2659	2738
LH_S250CA_750_1-1	2702	2785
LH_S250CA_750_2-1	2651	2655

Table B 2 S_{BET} values in $\text{m}^2\cdot\text{g}^{-1}$ calculated by applying BET method over Conventional ($P/P_0 = 0.05\text{-}0.3$) or ISO ($P/P_0 = 0.01\text{-}0.1$) pressure range for PEI-modified Activated Carbons (ACs)

Sample ID	ISO	Conventional
AR_PEI_29%_Me_0.5h	1336	1354
AR_PEI_38%_Me_0.5h	1040	1044
AR_PEI_44%_Me_0.5h	966	971
AR_PEI_44%_Me_2h	783	790
AR_PEI_44%_Me_4h	729	730
AR_PEI_44%_Me_6h	677	677
AR_PEI_44%_Me_8h	610	610
AR_PEI_38%_Me_2h	983	984
AR_PEI_38%_Me_4h	876	884
AR_PEI_38%_Me_6h	720	730
AR_PEI_38%_Me_8h	684	696
AR_PEI_50%_Me_2h	879	880
AR_PEI_50%_Me_4h	492	505
AR_PEI_50%_Me_6h	411	412
AR_PEI_50%_Me_8h	412	413
AR_PEI_38%_W_0.5h	886	887
AR_PEI_38%_W_2h	734	733
AR_PEI_38%_W_4h	640	640
AR_PEI_38%_W_6h	460	461
AR_PEI_38%_W_8h	628	629
AR_PEI_44%_W_0.5h	859	862
AR_PEI_44%_W_8h	355	355
AR_PEI_50%_W_0.5h	722	722
AR_PEI_50%_W_2h	292	296
AR_PEI_50%_W_4h	366	369
AR_PEI_50%_W_6h	279	280
AR_PEI_50%_W_8h	183	185

Appendix C

Table C 1 CO₂ sorption capacities (mmol-CO₂-g⁻¹) measured for best performing sample in this work versus values reported by literature for other sorbents under similar temperature/CO₂ partial pressure conditions

Sample ID	CO ₂ sorption capacity
PEI-AC ⁶⁷ (this work)	0.75
PEI-AC ([115])	3.98
PEI-silica ⁶⁸ ([122])	5.34
Z13X ⁶⁹ (this work)	0.52
Z13X ([57])	3.03
MOF ⁷⁰ (Mg-CPO-27, [57])	6.55

⁶⁷ Polyethyleneimine-modified activated carbon

⁶⁸ Polyethyleneimine-modified silica

⁶⁹ Zeolite-13X

⁷⁰ Metal organic framework